



THE HONG KONG
POLYTECHNIC UNIVERSITY

香港理工大學

Pao Yue-kong Library

包玉剛圖書館

Copyright Undertaking

This thesis is protected by copyright, with all rights reserved.

By reading and using the thesis, the reader understands and agrees to the following terms:

1. The reader will abide by the rules and legal ordinances governing copyright regarding the use of the thesis.
2. The reader will use the thesis for the purpose of research or private study only and not for distribution or further reproduction or any other purpose.
3. The reader agrees to indemnify and hold the University harmless from and against any loss, damage, cost, liability or expenses arising from copyright infringement or unauthorized usage.

IMPORTANT

If you have reasons to believe that any materials in this thesis are deemed not suitable to be distributed in this form, or a copyright owner having difficulty with the material being included in our database, please contact lbsys@polyu.edu.hk providing details. The Library will look into your claim and consider taking remedial action upon receipt of the written requests.

**INFLUENCES OF ANISOTROPIC SPATIAL
VARIATION OF SOILS AND SAMPLING
STRATEGY ON SLOPE RELIABILITY
EVALUATION**

HUANG LEI

PhD

The Hong Kong Polytechnic University

2021

The Hong Kong Polytechnic University
Department of Civil and Environmental Engineering

**Influences of Anisotropic Spatial Variation of Soils
and Sampling Strategy on Slope Reliability
Evaluation**

HUANG LEI

A thesis submitted in partial fulfillment of the requirements for
the degree of Doctor of Philosophy

October 2020

CERTIFICATE OF ORIGINALITY

I hereby declare that this thesis is my own work and that, to the best of my knowledge and belief, it reproduces no material previously published or written, nor material that has been accepted for the award of any other degree or diploma, except where due acknowledgement has been made in the text.

_____ (Signed)

_____ HUANG Lei (Name of student)

*To my dearest mother in heaven
for her forever love and care*

Abstract

In nature, soils are spatially variable. In the context of soil spatial variability, anisotropic spatial variation of soils is a significant topic, which has been widely investigated for horizontally deposited soils. However, rotated transverse anisotropy can often be observed in natural slopes with tilted stratification. Previous studies mainly considered rotated transverse anisotropy in two-dimensional (2D) probabilistic slope stability analyses using stationary random field (RF). However, in-situ observations usually show the non-stationarity of soils, where the trends of soil properties are not constant. Besides, the three-dimensional (3D) rotated transverse anisotropy of soil spatial variability has not been considered in probabilistic slope stability analyses up to the present. In practice, three-dimensional slope models often exhibit rotated transverse anisotropy associated with various stratigraphic occurrences, which can significantly influence the slope stability. The sampling effect is another important topic considering soil spatial variability, as the spatial uncertainty can be reduced by sampling points (i.e., known points) in a domain. Previous probabilistic slope stability analyses only considered the sampling effect in soils with horizontal bedding, while most of the studies were based on 2D slope models. In the few existing 3D studies related to the sampling effect, the influences of end boundary conditions and slope length (L) have not been investigated. This thesis aims to investigate those issues in probabilistic slope stability analyses and provide guidelines for engineering practice.

The influence of rotated transverse anisotropy is first investigated in 2D probabilistic slope stability analyses, where the non-stationarity in soil property is also considered. In the study, two soil scenarios are simulated, where the undrained shear strength increases along depth or the direction perpendicular to bedding. The results show that when considering soil strength with an increasing trend with depth, the slope reliability is higher than that considering stationary random field. Meanwhile, when undrained shear strength increases along the direction perpendicular to bedding, the estimated slope reliability and sliding consequence are sensitive to the change of dip angle of strata (α). The rotated transverse anisotropy is then investigated in 3D probabilistic slope stability analyses, associated with three slope scenarios (i.e., cross-dip slope, reverse-dip slope and dip slope). In a cross-dip slope, the observations on the changes of slope reliability and failure patterns with spatial autocorrelation distance (θ) are different from those considering horizontally deposited soils. On the other hand, the changes of slope reliability with θ for a dip slope or a reverse-dip slope are similar to those under horizontal transverse anisotropy.

In 2D probabilistic slope stability analyses considering the sampling effect, two conditional RF models are considered with various sampling strategies and dip angles of strata, the residual parts of which are simulated by Kriging interpolation and decomposing the conditional autocorrelation matrix, respectively. The method based

on Sobol sensitivity index is also adopted. It is found that the conditional random field simulation method based on Kriging interpolation may result in higher standard deviation (σ) of factor of safety (FS) than that by unconditional random field simulation method. This issue may occur when sample points are distributed sparsely or the angle of the drilling direction of the borehole is near the dip angle of the strata, while such a problem cannot be found when using the conditional RF simulation method by decomposing conditional autocorrelation matrix and the Sobol index method. Besides, it is observed that the magnitude of uncertainty reduction by the various methods would decrease when the angle of the drilling direction of the borehole approaches the dip angle of the strata. For 3D probabilistic slope stability analyses considering the sampling effect, the computation effort would be quite demanding using conditional random field simulation method, as many trial sampling patterns need to be considered. Therefore, the Sobol index method is adopted to quantify the sampling efficiency. It is found that when the ratio of θ / L increases, the sampling efficiency increases. In the meantime, the optimal sampling efficiency for slopes with fixed end boundary condition would be higher than that with smooth end boundary condition, except for the cross-dip slope, where the smooth end boundary condition would indicate higher optimal sampling efficiency. This study reveals the significance of characteristics in 3D slope model [e.g., slope length (L) and end boundary conditions] in the reliability evaluation incorporating sampling effects, which cannot be explicitly considered in the 2D slope model.

Publications Arising from the Thesis

Huang, L., Cheng, Y.M., Leung, Y.F., and Li, L. 2019. Influence of rotated anisotropy on slope reliability evaluation using conditional random field. *Computers and Geotechnics*, 115: 103133.

Huang, L., Zhang, Y., Lo, M.K., and Cheng, Y.M. 2020. Comparative study of conditional methods in slope reliability evaluation. *Computers and Geotechnics*, 127: 103762.

Huang, L., and Leung, Y.F. 2020. Reliability assessment of slopes with three-dimensional rotated transverse anisotropy in soil properties. *Canadian Geotechnical Journal*, DOI: <https://doi.org/10.1139/cgj-2019-0611>.

Huang, L., Leung, Y.F., Liu, W.F., and Pan, Q.J. 2020. Reliability of an engineered slope considering the regression Kriging based conditional random field. *HKIE Transactions*, 27(4): 183 - 194.

Huang, L., Cheng, Y.M., Li, L., and Yu, S. 2021. Reliability and failure mechanism of a slope with non-stationarity and rotated transverse anisotropy in undrained soil strength. *Computers and Geotechnics*, 132: 103970.

Acknowledgements

I would like to express the deepest gratitude to my supervisors, Dr. Yat-Fai Leung and Prof. Yung-Ming Cheng for their valuable guidelines and supports during my Ph.D study. Without their helps and encouragements, this thesis could not be eventuated.

In the meantime, I would like to thank my seniors, Dr. Man-Kong Lo, Dr. Wen-Fei Liu, Dr. Lei-Lei Liu and Dr. Qiu-Jing Pan, for their great supports to my researches. My thanks also give to the other members in Dr. Leung's and Prof. Cheng's groups and all my friends in the university for their warm friendship and constant encouragements to help me overcome the difficulties encountered in my life.

The research is financially support by Research Grants Council of the Hong Kong Special Administrative Region (Projects No. 15220415 and 15217517). The support is greatly acknowledged.

Table of Contents

Abstract.....	i
Publications Arising from the Thesis.....	iv
Acknowledgements.....	vi
Table of Contents.....	viii
List of Figures.....	xiv
List of Tables.....	xxi
Notations and Abbreviations.....	xxiii
CHAPTER 1 Introduction.....	1
1.1 Research Motivation.....	1
1.2 Research Objectives.....	8
1.3 Thesis Outline.....	9
CHAPTER 2 Literature Review.....	15
2.1 Introduction.....	15
2.2 Deterministic Slope Stability Analysis.....	16
2.2.1 Factor of Safety (FS).....	16
2.2.2 Limit Equilibrium Method.....	18
2.2.3 Finite Element Method.....	22
2.2.4 Other Slope Stability Analysis Methods.....	24
2.2.5 3D Slope Stability Analysis.....	26
2.3 Probabilistic Slope Stability Analysis.....	30
2.3.1 Probability of Failure and Reliability Index.....	30

2.3.2	Approximate Method.....	32
2.3.3	Probabilistic Method Assuming Perfect Autocorrelation.....	35
2.3.4	Random Field Based Method.....	36
2.3.5	Surrogate Model.....	42
2.4	Spatial Variability in Soils.....	44
2.4.1	Characterisation of Spatial Variability.....	45
2.4.2	Spatially Correlated Random Variables.....	46
2.4.3	Spatial Variability in Soils with Increasing Trend.....	47
2.5	Spatial Autocorrelation.....	49
2.5.1	Autocorrelation Distance.....	50
2.5.2	Autocorrelation Function.....	52
2.5.3	Anisotropic Spatial Variation.....	55
2.6	Random Field Generation.....	57
2.6.1	Cholesky Decomposition Method.....	57
2.6.2	Local Average Subdivision.....	59
2.6.3	Cross-correlated Random Field.....	61
2.7	Conditional Random Field Simulation and Sobol Index Method.....	62
2.7.1	Conditional Random Field.....	63
2.7.2	Sobol Sensitivity Index.....	66
2.7.3	Discussion on Methods Considering Sampling effect.....	71
2.8	Summary.....	74

CHAPTER 3 2D Probabilistic Slope Stability Analyses with Rotated

Transverse Anisotropy and Non-stationarity in Soil Properties.....	103
3.1 Introduction.....	103
3.2 Methodology.....	105
3.2.1 Random Limit Equilibrium Method (RLEM).....	105
3.2.2 Non-stationarity and Rotated Transverse Anisotropy.....	106
3.2.3 Implementation Procedure of Non-stationary Random Field Generation	107
3.3 Case Description.....	109
3.4 Results.....	110
3.4.1 Slope Reliability and Sliding Area.....	110
3.4.2 Depth and Distribution of Slip Surface.....	114
3.5 Summary.....	118
 CHAPTER 4 3D Probabilistic Slope Stability Analyses with Rotated Transverse Anisotropy in Soil Properties.....	 136
4.1 Introduction.....	136
4.2 Methodology.....	138
4.2.1 3D Random Finite Element Method.....	138
4.2.2 Soil Spatial Variability Considering 3D Rotated Transverse Anisotropy	139
4.3 Case Description.....	140
4.4 Results.....	144
4.4.1 Statistical Characteristics of FS.....	144

4.4.2 Reliability Index.....	147
4.4.3 Mean of Slide Length.....	150
4.5 Discussion.....	153
4.6 Summary.....	154
CHAPTER 5 Sampling Effects in 2D Probabilistic Slope Stability Analyses..	172
5.1 Introduction.....	172
5.2 Methodology.....	174
5.2.1 Conditional Random Field Modelling and Stationarity Assumptions	174
5.2.2 Polynomial Chaos Expansion.....	175
5.2.3 Sobol Index Method.....	177
5.3 Case Description.....	178
5.4 Results.....	180
5.4.1 Influence of Sampling Strategy on Magnitude of Uncertainty Reduction	181
5.4.2 Influence of Rotated Transverse Anisotropy on Magnitude of Uncertainty Reduction.....	185
5.4.3 Discussion.....	187
5.5 Summary.....	191
CHAPTER 6 Sampling Effects in 3D Probabilistic Slope Stability Analyses..	202
6.1 Introduction.....	202
6.2 Methodology.....	205

6.2.1 Quantification on Sampling Efficiency in Three-dimensional Problem	205
6.2.2 Differential Evolution	207
6.3 Case Description	209
6.4 Results	210
6.4.1 Sampling Strategies Considering Two and Three Boreholes	212
6.4.2 Sampling Efficiency Considering Single Borehole	213
6.4.3 Optimal Sampling Location and Uncertainty Reduction Considering Single Borehole	215
6.4.4 Sampling Effects under Rotated Transverse Anisotropy Considering Single Borehole	217
6.5 Discussion	219
6.6 Summary	220
CHAPTER 7 Conclusion and Recommendations	239
7.1 Conclusion	239
7.1.1 Influence of Non-stationarity and Rotated Transverse Anisotropy in Slope Reliability Evaluation	240
7.1.2 Influence of 3D Rotated Transverse Anisotropy in Slope Reliability Evaluation	242
7.1.3 Influence of Sampling Strategies in 2D Slope Reliability Evaluation	243
7.1.4 Influence of Sampling Strategies in 3D Slope Reliability Evaluation	

.....	245
7.1.5 Suggestions for Engineering Practice.....	247
7.2 Recommendations.....	250
7.2.1 Recommendations on Study of Non-stationarity in Soil Properties....	250
7.2.2 Recommendations on Study of Anisotropic Patterns of Soil Spatial Variability.....	251
7.2.3 Recommendations on Study of Sampling Effects in Probabilistic Slope Stability Analyses.....	253
7.2.4 Recommendations on Study of the Influence of Groundwater Level in Probabilistic Slope Stability Analyses.....	254
References.....	256

List of Figures

Figure 1.1 Typical patterns of soil spatial variability in nature: (a) isotropy; (b) horizontal transverse anisotropy; (c) rotated transverse anisotropy; (d) general anisotropy (the direction of the minor autocorrelation distance, θ_1 , is horizontal); (e) general rotated transverse anisotropy (the direction of the minor autocorrelation distance is not horizontal); (f) combination (Zhu and Zhang 2013)..... **13**

Figure 1.2 Displacement contours at failure of a slope in spatially variable soils under different boundary conditions at the two end sections: (a) preventing the movement in y - direction; (b) preventing the movement in (x, y, z) - direction.....**14**

Figure 2.1 Areas for the entry and exit points (GEO-SLOPE International Ltd. 2012).
.....**87**

Figure 2.2 Definitions of D and l for the correction factor f_0 (Janbu 1972; Cheng and Lau 2008)..... **88**

Figure 2.3 Various shapes of $f(x)$ (Cheng and Lau 2008).....**88**

Figure 2.4 Progressive formation of the continuous plastic zone..... **89**

Figure 2.5 (a) Multiple failure surfaces in a slope with think weak layer under undrained conditions by SRM; (b) multiple failure surfaces in a slope with weak foundation layer under undrained conditions by SRM (Griffiths and Lane 1999)..... **90**

Figure 2.6 Taylor’s stability chart for cohesive slope (Taylor 1937; Barnes 1995).
.....**91**

Figure 2.7 Implementation procedure of DLO: (a) define problem domain; (b) discretise the domain by nodes; (c) interconnect the nodes to produce discontinuities;

(d) find the critical mechanism with the minimum energy dissipation by optimization (Smith and Gilbert 2010).....	92
Figure 2.8 The end sections in a 3D slope model.....	93
Figure 2.9 Slope reliability versus slope length using random finite element method (RFEM) and the method based on the probability theory (Hicks and Spencer 2010).	93
Figure 2.10 Limit state surface and design point in FORM: (a) in the normal space; (b) in the space of original variable (Ji <i>et al.</i> 2019).....	94
Figure 2.11 Typical realisations of random fields in a slope under undrained conditions and the analysis results by Bishop method ($\theta_h = 20$ m and $\theta_v = 2$ m): (a) FS = 0.905; (b) FS=0.927; (c) FS=0.834; (d) FS=0.983 (Cho 2010).....	95
Figure 2.12 Analysis results for the same realisations of random fields in Figure 2.11 by SRM using FLAC: (a) FS = 0.881; (b) FS = 0.889; (c) FS = 0.811; (d) FS = 0.9575 (Cho 2010).....	95
Figure 2.13 Isotropic random fields in a square domain of length = 20 m with different spatial autocorrelation distances: (a) $\theta = 15$ m; (b) $\theta = 0.5$ m.....	96
Figure 2.14 Typical realisations of 2D random fields using different autocorrelation functions with $\theta_x = 20$ m and $\theta_z = 2$ m: (a) exponential function; (b) separated single exponential function; (d) Gaussian function.....	97
Figure 2.15 Typical realisations of 3D random fields using different autocorrelation functions with $\theta_x = \theta_y = 20$ m and $\theta_z = 1$ m: (a) exponential function; (b) separated single exponential function; (d) Gaussian function.....	98

Figure 2.16	Spatial autocorrelation structure: (a) ellipse for 2D soil anisotropy; (b) ellipsoid for 3D soil anisotropy (Liu 2018).....	99
Figure 2.17	Subdivision process in LAS (Fenton and Vanmarcke 1990).....	100
Figure 2.18	Realisations of cross-correlated random fields by Gaussian function with $\rho_{c,\phi} = -0.5$: (a) cohesion; (b) friction angle.....	101
Figure 2.19	A slope under drained conditions and layout of the sampling points (Liu <i>et al.</i> 2017b).....	102
Figure 2.20	Standard deviation of FS by conditional random field simulation method and unconditional random field simulation method versus various cross-correlation coefficients $\rho_{c,\phi}$ (Liu <i>et al.</i> 2017b).....	102
Figure 3.1	Two orientations of the trend for mean shear strength with rotational angle of soil bedding = 45° : (a) Type 1; (b) Type 2.....	122
Figure 3.2	Geometry of the slope model.....	123
Figure 3.3	Flowchart of non-intrusive RLEM.....	124
Figure 3.4	Typical realisations of random fields with $\alpha = 30^\circ$: (a) stationary RF; (b) RF Type 1; (c) RF Type 2.....	125
Figure 3.5	Reliability index versus major autocorrelation distance by Eq. (2.11) with $\theta_2 = 2$ m: (a) $\alpha = 0^\circ$; (b) $\alpha = 45^\circ$; (c) $\alpha = -45^\circ$	126
Figure 3.6	Reliability index versus minor autocorrelation distance by Eq. (2.11) with $\theta_1 = 20$ m: (a) $\alpha = 0^\circ$; (b) $\alpha = 45^\circ$; (c) $\alpha = -45^\circ$	127
Figure 3.7	Reliability index versus rotational angle of soil bedding using Eq. (2.11).	128

Figure 3.8	Mean of sliding area versus rotational angle of soil bedding.....	129
Figure 3.9	Histograms and probability distributions of h_c : (a) stationary RF ($\alpha = 0^\circ$); (b) non-stationary RF ($\alpha = 0^\circ$); (c) stationary RF ($\alpha = 45^\circ$); (d) RF Type 1 ($\alpha = 45^\circ$); (e) RF Type 2 ($\alpha = 45^\circ$); (f) stationary RF ($\alpha = -45^\circ$); (g) RF Type 1 ($\alpha = -45^\circ$); (h) RF Type 2 ($\alpha = -45^\circ$).....	131
Figure 3.10	Consequences (failure scales) caused by shallow slip surfaces passing through slope face and slope toe, respectively.....	132
Figure 3.11	1000 slip surfaces within the slope in horizontally deposited soils ($\alpha =$ 0°): (a) stationary RF; (b) non-stationary RF.....	133
Figure 3.12	1000 slip surfaces within the dip slope ($\alpha = 45^\circ$): (a) stationary RF; (b) RF Type 1; (c) RF Type 2.....	134
Figure 3.13	1000 slip surfaces within the reverse slope ($\alpha = -45^\circ$): (a) stationary RF; (b) RF Type 1; (c) RF Type 2.....	135
Figure 4.1	(a) Strata rotating around the x axis (cross-dip slope); (b) strata rotating around the y axis (dip slope); (c) strata rotating around the y axis (reverse-dip slope); (d) strata rotating around the z axis.....	158
Figure 4.2	Flowchart of non-intrusive 3D RFEM using ABAQUS.....	159
Figure 4.3	Typical realisations of random fields of undrained shear strength under rotation around the x axis: (a) $\alpha = 30^\circ$; (b) $\alpha = 90^\circ$	160
Figure 4.4	Typical realisations of random fields of undrained shear strength under rotation around the y axis: (a) $\alpha = 45^\circ$; (b) $\alpha = 90^\circ$	161
Figure 4.5	Slope geometry and finite element mesh: (a) cross-section through mesh;	

(b) finite element mesh for a 3D slope model.....	162
Figure 4.6 Standard deviation of FS versus angle of rotation.....	163
Figure 4.7 Mean of FS versus angle of rotation under: (a) rotated anisotropy around the x axis; (b) rotated anisotropy around the y axis; (c) rotated anisotropy around the z axis.....	164
Figure 4.8 (a) Two slopes under rotated anisotropy around the x axis with the same degrees of rotation and opposite rotational directions; (b) two slopes under rotated anisotropy around the z axis with the same degrees of rotation and opposite rotational directions.....	165
Figure 4.9 Reliability index versus angle of rotation: (a) $\theta_1 = 2$ m; (b) $\theta_1 = 12$ m; (c) $\theta_1 = 24$ m; (d) $\theta_1 = 60$ m.....	166
Figure 4.10 Reliability index β versus major autocorrelation distance.....	167
Figure 4.11 Reliability index β with $\theta_1 = 24$ m versus: (a) slope length; (b) angle of rotation.....	168
Figure 4.12 Slide length of a slope.....	169
Figure 4.13 Relationship between displacement δ_0 and the volume of soil mass with displacements exceeding δ_0	170
Figure 4.14 Slip surface and plastic strain contour (darker parts indicate higher shear strain).....	170
Figure 4.15 Mean of slide length versus angle of rotation considering the threshold of 32 % of the maximum computed displacement: (a) rotated anisotropy around the x axis; (b) rotated anisotropy around the y axis; (c) rotated anisotropy around the z axis.	

.....	171
Figure 5.1 Geometry of the slope model and random field discretisation.....	194
Figure 5.2 $\sigma_{\text{cond}}(\text{FS}) / \sigma_{\text{uncond}}(\text{FS})$ versus minor autocorrelation distance: (a) $n = 2$; (b) $n = 3$; (c) $n = 5$	195
Figure 5.3 Magnitude of uncertainty reduction for each borehole location: (a) $n = 2$; (b) $n = 5$	196
Figure 5.4 The two sampling patterns.....	197
Figure 5.5 Standard deviation of FS versus angle of rotation of strata under: (a) vertical sampling pattern; (b) inclined sampling pattern.....	198
Figure 5.6 Original vertical lag distance τ_y , and lag distance in the rotated coordinate system $\tau_{y\alpha}$	199
Figure 5.7 $\sigma_{\text{cond}}(\text{FS}) / \sigma_{\text{uncond}}(\text{FS})$ versus angle of rotation of strata under: (a) vertical sampling pattern; (b) inclined sampling pattern.....	200
Figure 5.8 The unconditional random field z_{ur} and the prediction field by ordinary Kriging z_{kr} with $\theta_1 = 20$ m and $\theta_2 = 2$ m (the sample points are marked by black circles): (a) the field z_{ur} ; (b) the prediction field considering single sample point; (c) the prediction field considering two very close sample points; (d) the prediction field considering two sparse sample points.....	201
Figure 6.1 (a) Geometry of the 3D slope model; (b) the cross-section of finite element mesh.....	229
Figure 6.2 Sobol index using 1,000 simulations and 2,000 simulations for constructing PCE.....	230

Figure 6.3	Distance between the optimal borehole location and the nearer end boundary divided by θ versus θ / L considering two sampling boreholes.....	231
Figure 6.4	Distance between the optimal borehole location and the nearer end boundary divided by θ versus θ / L considering three sampling boreholes.....	232
Figure 6.5	Sobol index along the slope length under different boundary conditions: (a) smooth boundary; (b) boundary fixed in (x, y) direction; (c) fully fixed boundary.	233
Figure 6.6	Comparison of Sobol index under the three boundary conditions with $L = 40$ m.....	234
Figure 6.7	Optimal sampling location with one borehole.....	235
Figure 6.8	Multiple potential sliding volumes.....	236
Figure 6.9	Magnitude of uncertainty reduction considering the optimal sampling pattern versus θ / L	237
Figure 6.10	Sobol index along the slope length considering anisotropic patterns of soil spatial variability under different end boundary conditions: (a) slope with horizontal bedding; (b) dip slope ($\alpha = 30^\circ$); (c) reverse-dip slope ($\alpha = -30^\circ$); (d) cross-dip slope ($\alpha = 30^\circ$)	238

List of Tables

Table 1.1	Number of landslide incidents from 2008 to 2016 in Hong Kong.....	12
Table 2.1	Recommended thresholds of FS in Hong Kong (GEO, Hong Kong 1984; Cheng and Lau 2008).....	76
Table 2.2	Various types of $f(x)$ (Cheng and Lau 2008).....	76
Table 2.3	Reliability index β , probability of failure P_f and corresponding expected performance level (U.S. Army Corps of Engineers 1997).....	77
Table 2.4	P_f by RLEM and RFEM with mean and COV of s_u equal 25 kPa and 0.7 respectively considering isotropic random fields by 1,000 Monte Carlo simulations.	78
Table 2.5	Non-stationary random field models (Jiang and Huang 2018).....	79
Table 2.6	Autocorrelation distance for shear strength parameters (part 1) (Li <i>et al.</i> 2015; Liu 2018).....	80
Table 2.6	Autocorrelation distance for shear strength parameters (part 2) (Li <i>et al.</i> 2015; Liu 2018).....	81
Table 2.7	Theoretical 2D autocorrelation functions (Li <i>et al.</i> 2015).....	82
Table 2.8	Theoretical 3D autocorrelation functions.....	83
Table 2.9	Exponential autocorrelation functions for anisotropic spatial variation of soils (Zhu and Zhang 2013).....	84
Table 2.10	Gaussian autocorrelation functions for anisotropic spatial variation of soils (Zhu and Zhang 2013).....	85
Table 2.11	Standard deviation of FS after conditioning when $N_d = 2$ (Liu <i>et al.</i>	

2017b).....	86
Table 3.1 Proportion of h_c within each depth range with $\theta_1 = 20$ m and $\theta_2 = 2$ m.	121
Table 4.1 Comparison of mean slide lengths of slopes in horizontally deposited soils under undrained conditions with $\theta_2 = 1$ m.....	157
Table 5.1 $\sigma_{\text{cond}}(\text{FS}) / \sigma_{\text{uncond}}(\text{FS})$ by the various methods considering sampling effects with $\theta_2 = 10$ m.....	193
Table 6.1 Depth of samples according to the borehole location.....	223
Table 6.2 Parametric settings, the optimal sampling location and the optimal Sobol index value.....	224
Table 6.3 Difference of Sobol index for any two symmetrical boreholes considering two different simulation sizes in Figure 6.2.....	225
Table 6.4 Simulation size for each setting.....	226
Table 6.5 Difference of Sobol index by the two approaches.....	227
Table 6.6 Magnitude of uncertainty reduction, $\sigma_{\text{cond}}(\text{FS}) / \sigma_{\text{uncond}}(\text{FS})$, considering the optimal sampling pattern under different slope scenarios.....	228

Notations and Abbreviations

a	rate of change of the increasing spatial variables
$a_0, a_j, a_{j_1j_2}$	PCE coefficients
a_{0p}, b_i, c_i	coefficients in a quadratic function
c	cohesion
c'	effective cohesion
CR	crossover constant taken from 0 to 1
$\hat{C}(\tau_k)$	covariance at τ_k
D	maximum thickness of the failure mass with reference to the line connecting the entry and exit points of the slip surface for the correction factor in Janbu simplified method
\mathbf{D}	diagonal matrix formed by the n_u terms in σ_z^2
d	number of elements in a random field
d_0	depth below the ground surface
d_e	distance in the direction of trend of soil property in RF Type 2
E	Young's modulus
E_0	Inter-slice normal force
\mathbf{E}	matrix equal to $\mathbf{H}\mathbf{\Lambda}^{1/2}$ corresponding to all the elements in the mesh
\mathbf{E}_s	matrix equal to $\mathbf{H}\mathbf{\Lambda}^{1/2}$ corresponding to the sample locations
\mathbf{e}	residual
\mathbf{e}_n	residual for sample points

F	strength reduction factor in SRM
\mathbf{F}	matrix equal to inverse of \mathbf{E}_s times inverse of \mathbf{R}_s
F_a	mutation amplification factor taken from 0 to 2
F_d	driving force
F_r	resisting force
f_0	correction factor in Janbu simplified method
f_s	threshold value for defining the failure of a slope
$FS_i(\mathbf{X}_0)$	FS of the i th potential slip surface
$f(x)$	inter-slice force function
$f_{\mathbf{x}}(\mathbf{X}_0)$	joint probability density function
$g(\mathbf{X}_0)$	performance function
H	slope height
\mathbf{H}	matrix of M retained eigenvectors
\mathbf{H}_d	matrix of d retained eigenvectors
h_c	depth of slip surface
$I(\cdot)$	indicator function
\mathbf{I}_r	identity matrix to ensure the crossover occurs on each initial sampling pattern in Differential Evolution
L	slope length
\mathbf{L}	Cholesky factor
l	distance between the left and right exit points of the slip surface for the correction factor in Janbu simplified method

M	the retained number of eigenvectors
M_d	driving moment
M_r	resisting moment
mu	vector containing three random samples in Differential Evolution
N_d	number of sampling points in Figure 2.20
N_{de}	dimension of the variable in Differential Evolution
N_k	number of pairs of the observed samples
N_{pop}	size of the initial population in Differential Evolution
N_T	number of simulations of Monte Carlo process
n	number of sample locations
n_p	number of soil parameters in mean-value FOSM
n_u	number of unsampled locations
P_f	probability of failure
p	number of coefficients in the trend
PAR₀	matrix containing the initial population of patterns of different combinations of two boreholes
PAR_C	matrix containing the population by crossover
PAR_M	matrix containing the mutated population of sampling patterns
pl	lower bound of the population in Differential Evolution
pu	upper bound of the population in Differential Evolution
q_c	cone tip resistance
R	spatial autocorrelation matrix

\mathbf{R}_s	spatial autocorrelation matrix between the sampling locations
Rand	matrix containing random samples taken from 0 to 1
$s_{fs=1}$	shear strength indicating FS=1
\mathbf{s}_i	independent standard Gaussian random vector
s_u	undrained shear strength
$S(\mathbf{X})$	Sobol index value
\mathbf{u}^*	design point in FORM in the normal space
\mathbf{V}	covariance matrix
\mathbf{V}_s	covariance matrix between sampling points
\mathbf{V}_{su}	covariance matrix between sampling points and unknown points
v	user defined parameter in Fredlund-Wilson-Fan force function
$V(\text{FS})$	coefficient of variation of FS
W	slope width
w_n	fluctuating component of non-stationary random field
\mathbf{X}	spatial coordinates of the sample locations
\mathbf{X}_0	set of random variables
\mathbf{x}	spatial coordinates of a point
\mathbf{x}^*	design point in FORM in the space of original variable
\mathbf{x}_0	vector representing a set of random variables
y_0	distance between the borehole location and the nearer end section in y – direction

\mathbf{z}	vector for spatially random variables in various locations
z_0	soil property at the top surface
\mathbf{z}_c	cross-correlated random field for cohesion
\mathbf{z}_{c_0}	random field for cohesion
\mathbf{z}_{cr}	simulated conditional random field
\mathbf{z}_j	spatially random variable at location j
$\mathbf{z}_{k,i}$	Kriging predictor of the i th point
\mathbf{z}_{km}	Kriging field based on the measured values at the sampling locations
\mathbf{z}_{ks}	Kriging field based on the simulated values by the unconditional random field simulation at the sampling locations
\mathbf{z}_{logcr}	logarithm of the simulated conditional random field
\mathbf{z}_{logkm}	Kriging field based on the logarithm of the measured values
\mathbf{z}_{logks}	Kriging field based on the simulated values of the logarithmic unconditional random field at the sampling locations
\mathbf{z}_{logur}	logarithm of the unconditional random field
\mathbf{z}_m	vector that contains sampled values at the sampling locations
z_n	spatially variable soil property with increasing trend
\mathbf{z}_{ur}	simulated unconditional random field
\mathbf{z}_φ	cross-correlated random field for friction angle
\mathbf{z}_{φ_0}	random field for friction angle
α	rotational angle / dip angle of strata

α_0	rotational angle of the increasing direction of soil property
β	reliability index
$\mathbf{\beta}^{(i)}$	vector representing weights of the known points to the i th unknown point
γ	unit weight of soil
γ_{sat}	saturated unit weight of soil
Δ_y	distance between the location and the end section in y – direction
Δ_{y_0}	distance between one of the symmetrical boreholes and the nearer boundary
δ_0	a certain displacement expressed as percentage of the maximum nodal x -displacement
$\delta_{j_1 j_2}$	Kronecker delta
$\boldsymbol{\varepsilon}$	standard Gaussian random field
$\boldsymbol{\varepsilon}_j^{(i)}$	element in the i th realisation of standard Gaussian random field corresponding to location j
η	angle between the two principal scales of fluctuation
$\boldsymbol{\eta}$	vector containing FS obtained by Monte Carlo simulation
Θ	matrix containing polynomials constructed by ξ
θ	spatial autocorrelation distance
θ_1	major autocorrelation distance
θ_2	minor autocorrelation distance
θ_h	horizontal autocorrelation distance

θ_p	vector containing the parameters in Matérn function
θ_v	vertical autocorrelation distance
θ_x	autocorrelation distance in x - direction
θ_y	autocorrelation distance in y - direction
θ_z	autocorrelation distance in z - direction
κ	normalised dimensional factor in Fredlund-Wilson-Fan force function
Λ	diagonal matrix of M retained eigenvalues
Λ_d	diagonal matrix of d retained eigenvalues
λ	Lagrange multiplier
λ_i	i th eigenvalue in the diagonal matrix Λ_d
λ_0	directional factor for inter-slice force $\lambda_0 f(x) E_n$
μ	deterministic trend structure
μ_a	mean of the increasing rate in the non-stationary random field
μ_c	mean of cohesion
μ_j	value of the trend at location j
μ_{k_0}	vector containing expected values of the trend at the sampled locations.
$\mu_{\ln c_u}$	mean of logarithm of undrained shear strength
μ_φ	mean of friction angle
$\mu_n(d_0)$	mean of the non-stationary random field in the depth d_0
$\mu(\text{FS})$	mean of FS

$\mu[X_i]$	mean of the i th soil parameter in mean-value FOSM
$\mu_k(\mathbf{x})$	trend value at a location with spatial coordinate \mathbf{x}
ν	Poisson's ratio
ν_p	preserved percentage of total variance
ξ	vector containing independent components that represent the random field
ρ	spatial correlation coefficient
$\rho_{c,\varphi}$	cross-correlation coefficient between cohesion and friction angle
ρ_X	correlation between soil parameters in mean-value FOSM
σ	standard deviation
σ'	effective normal stress
σ_a	standard deviation of the increasing rate in the non-stationary random field
$\sigma_{\ln c_u}$	standard deviation of the logarithm of undrained shear strength
σ_z^2	vector containing Kriging prediction variance
$\sigma_n(d_0)$	standard deviation of the non-stationary random field in the depth d_0
$\sigma(\text{FS})$	standard deviation of FS
$\sigma_{\text{cond}}(\text{FS})$	standard deviation of FS after conditioning
$\sigma_{\text{cond1}}(\text{FS})$	standard deviation of FS after conditioning with optimal sampling

	pattern considering one borehole
$\sigma_{\text{cond2}}(\text{FS})$	standard deviation of FS after conditioning with optimal sampling pattern considering two boreholes
$\sigma_{\text{uncond}}(\text{FS})$	standard deviation of FS by the unconditional random field simulation method
$\sigma[X_i], \sigma[X_j]$	mean of the i th and j th soil parameter in mean-value FOSM, respectively
τ'	effective shear strength
$\bar{\tau}$	average sample separation distance
τ_k	lag distance for observed samples
τ_v	vertical lag distance
$\tau_{v\alpha}$	lag distance in the rotational coordinate system
τ_x	lag distance between any two points in x - direction
τ_y	lag distance between any two points in y - direction
τ_z	lag distance between any two points in z - direction
$\Phi(\cdot)$	cumulative standard normal distribution function
φ	friction angle
φ'	effective friction angle
Ψ	user defined parameter in Fredlund-Wilson-Fan force function
2D	two-dimensional
3D	three-dimensional
BINX	binary noise

<i>COV</i>	coefficient of variation
CPT	cone penetration test
CSX	cosine exponential
DLO	discontinuity layout optimization
DST	direct shear test
FDM	finite difference method
FEM	finite element method
FORM	first order reliability method
FOSM	first order second moment method
FS	factor of safety
LAS	local average subdivision
LEM	limit equilibrium method
OK	ordinary Kriging
PCE	polynomial chaos expansion
RF	random field
RFDM	random finite difference method
RFEM	random finite element method
RLEM	random limit equilibrium method
SMX	second-order Markov
SNX	single exponential
SQX	squared exponential
SRM	strength reduction method

Var	variance
VST	vane shear test

CHAPTER 1 Introduction

1.1 Research Motivation

From 2008 to 2016, the average number of landslide incidents reported by the local authorities in Hong Kong is around 250 per year (Table 1.1), which caused severe economic losses and even consequences to human lives. In order to assess the safety of slopes, deterministic slope stability analysis is commonly used, which is well established for engineers and the authorities. However, in Hong Kong, landslides occasionally happen on slopes that are assessed to be ‘safe’ by the deterministic slope stability analysis. As shown in Table 1.1, the average number of such events is around 13 per year from 2008 to 2016. One of the reasons for this phenomenon is that the conventional deterministic slope stability analysis techniques assume homogeneous soil properties within each soil profile. Such an assumption does not consider the soil spatial variability, which is a significant source of geotechnical uncertainty. Inherent soil spatial variability has been found to be influential to slope reliability and the failure mechanism in many previous studies. For example, Griffiths *et al.* (2004) and Griffiths *et al.* (2009a) proposed that in probabilistic slope stability analysis, the simplified probabilistic analysis, where soil spatial variability is ignored by assuming perfect autocorrelation, can result in much higher probability of failure (P_f) than that

obtained considering soil spatial variability.

In recent years, soil spatial variability has been considered in probabilistic slope stability analyses using random field (RF) theory (Griffiths and Fenton 2004; Griffiths *et al.* 2009a; Griffiths *et al.* 2009b; Griffiths *et al.* 2009c; Cho 2010; Wang *et al.* 2011; Hicks and Spencer 2010; Huang *et al.* 2010; Li *et al.* 2013; Jha and Ching 2013; Jiang *et al.* 2014; Hicks *et al.* 2014; Jiang *et al.* 2015; Li *et al.* 2015; Li and Chu 2015; Jiang and Huang 2016; Jiang and Huang 2018; Li *et al.* 2016a; Liu *et al.* 2017a; Liu *et al.* 2017b; Liu *et al.* 2018; Zhu *et al.* 2019; Varkey *et al.* 2019). In these studies, soils that display isotropic spatial variability features or anisotropic horizontal fabric patterns were considered. However, in nature, various fabric patterns of soils are often observed. Figure 1.1 shows five typical patterns of soil spatial variability presented by Zhu and Zhang (2013), including isotropy, horizontal transverse anisotropy, rotated transverse anisotropy, general anisotropy and general rotated anisotropy. Herein, the rotated transverse anisotropy of soil spatial variability can usually be found for natural slopes, where the two principal directions of spatial autocorrelation distance (θ) are orthogonal and rotate by an angle to the coordinate axes. Griffiths *et al.* (2009c) considered rotated transverse anisotropy in two-dimensional (2D) probabilistic slope stability analysis, but the spatial autocorrelation distance in one of the orthogonal directions is assumed to be infinite. This means the one-dimensional random field is essentially considered. Meanwhile, Zhu *et al.* (2019) used a 2D random field to investigate the effects of rotated transverse anisotropy on the reliability and failure

pattern of a slope. Although the rotated transverse anisotropy is considered in probabilistic slope stability analyses in these studies, the random field is assumed to be stationary and only two-dimensional slope problems are investigated.

Many observations revealed that the spatial variation of soil property highly depends on depth (Asaoka and A-Grivas 1982; Kulatilake and Um 2003; Foye *et al.* 2004; Sivakumar *et al.* 2006; Ching *et al.* 2010). Usually, soil shear strength tends to increase with depth, and increasing trend functions are often adopted in modelling spatially variable soils (Phoon *et al.* 1999; Phoon *et al.* 2003; Li *et al.* 2014). Therefore, a stationary random field with a constant mean and standard deviation (σ) may not always be applicable to simulate in-situ soils. A non-stationary random field was used by Li *et al.* (2014) in the probabilistic stability analyses of an infinite slope, and the non-stationarity was found to be influential to slope reliability and the depth of critical slip surfaces. Meanwhile, Jiang and Huang (2018) compared the performance of different non-stationary random field models (Table 2.5) in slope reliability analysis, where the assumptions on the soil property at the top surface and the increasing rate of soil strength are different between different non-stationary RF models. In these studies, the soils are assumed to be horizontally deposited. For a more realistic simulation of spatially variable soils, other patterns of anisotropic spatial variation should be investigated.

In practice, 2D slope stability analysis is usually considered as a more conservative

approach than the three-dimensional (3D) analyses (Hutchinson and Sarma 1985; Hungr 1987). Thus, engineers are often reluctant to use the more time-consuming 3D methods. However, some investigators have observed that sometimes 3D slope stability analysis may result in a more critical factor of safety (FS), in certain cases of slopes with cohesion-less soils (Chen and Chameau 1982). That is because in cohesion-less soils, the unit weight of the soils, shear forces on the ends and sides of each column, pore-water pressures and slope geometry would have significant influences on the resisting force. Therefore, the end effects of the ellipsoidal sliding mass might indicate a negative change in FS, resulting in FS by 3D analysis less than that by 2D analysis. Considering soil spatial variability, Griffiths *et al.* (2009b) found that 3D slope reliability analysis would result in a higher probability of failure than that by 2D analysis when the slope length (L) or the spatial correlation distance are large enough. Therefore, for more realistic assessments of slope reliability, the use of 3D approach is desirable. Although there are many existing studies that are related to the effects of soil spatial variability on the slope reliability and failure pattern in 3D probabilistic slope stability analyses, only isotropic spatial variation of soils or horizontal transverse anisotropy have been considered (Griffiths *et al.* 2009a; Hicks and Spencer 2010; Hicks *et al.* 2014; Hicks and Li 2018).

In probabilistic slope stability analyses considering soil spatial variability, another issue that needs to be investigated further is the effect of sampling strategy on slope reliability. This corresponds to the known points in the random field and their effects

on reducing uncertainty. In engineering practice, discrete soil samples are usually obtained from site investigation, which can be adopted as known points to simulate conditional random fields. After conditioning, the performance uncertainty will reduce, while the probability of failure would also be affected. For example, Kim and Sitar (2013) found that the conditional random field simulation method can result in lower P_f compared with that by the unconditional random field simulation method. Liu *et al.* (2017b) studied the sampling effects on the uncertainty reduction and probability of failure of a $c - \phi$ slope in 2D probabilistic slope stability analyses using a conditional random field. They found that the ratio of the sample distance to the autocorrelation distance is a significant factor for effective reduction in the performance uncertainty. These previous studies only considered horizontal transverse anisotropy of soils. However, the sampling effects are expected to be affected by anisotropic spatial variation of soils. This is because the orientation of the principal axes under anisotropy is changed, as shown in Figure 1.1, and thus the lag distance in the direction of the spatial autocorrelation distance would be changed in the rotated coordinate system.

Sampling effects are seldom investigated in 3D probabilistic slope stability analyses. In the literature, Li *et al.* (2016b) is the only one to consider the sampling effects in 3D probabilistic slope stability analyses up to the present. They found that the performance uncertainty in relation to FS can be effectively reduced by the conditional random field simulation method, and they also identified an optimal

sampling distance of half of the horizontal autocorrelation distance (θ_h) along the slope length. However, some limitations should be noted in their research. First, they used the conditional random field simulation method to determine the optimal sample locations with the best sampling efficiency. When simulating the conditional random field, the locations of known points should be given as prior information. This means, to determine an optimal distributed pattern of sampling points, trial patterns should be used in the simulation to cover all the possible sampling locations, and each trial pattern indicates hundreds to thousands of realisations under the Monte Carlo framework. In this case, the computational effort would be significantly increased in 3D problems not only because the computational effort of a 3D program is demanding, but also because the larger geometry of a 3D slope can lead to a large increase in the number of trial sampling patterns. When multiple boreholes need to be considered, the computational demands would be dramatically increased, as the number of trial patterns is based on permutation. Therefore, in Li *et al.* (2016b), the best sampling pattern is selected from a number of sampling patterns defined by the authors, which is not obtained by an optimal search. Second, the effect of ratio of autocorrelation distance to slope length (θ / L) on the sampling efficiency is not resolved, as the length of the slope investigated is fixed at 100 m by Li *et al.* (2016b). However, it is well recognised that in 3D probabilistic slope stability analyses, the slope length is influential to slope reliability (Griffiths *et al.* 2009b; Hicks and Li 2018). The influences of boundary conditions at the two end sections on sampling efficiency are also not resolved by Li *et al.* (2016b). As shown in Figure 1.2, the boundary

conditions at the end sections can influence the shape and location of the critical failure zone in a slope with spatially variable soils. This may affect the location of the best sampling point (i.e., the point with the maximum uncertainty reduction magnitude), as the optimal sampling location corresponds to the location of critical failure zone.

The research motivation of this thesis is to resolve the limitations mentioned above in the previous studies. In the current study, through combining the non-stationary random field with rotated transverse anisotropy, slope reliability and failure mechanisms are investigated. In addition, the effects of 3D rotated transverse anisotropy on slope reliability are studied in consideration of the dip angle of the strata. Besides, the sampling effects are studied in 2D probabilistic slope stability analyses using conditional random field simulation methods and the method based on the Sobol sensitivity index (Lo and Leung 2018), considering various sampling strategies and rotated transverse anisotropy. Regarding the sampling effects in 3D probabilistic slope stability analyses, the Sobol sensitivity index is adopted to quantify the sampling efficiency. With the use of the Sobol index method, trial sampling patterns are not necessary when determining the optimal sampling pattern, as the optimal sampling strategy can be obtained by finding the sampling pattern with the maximum Sobol index value. This would significantly decrease the computational effort for the 3D problem, and thus various slope lengths and the boundary conditions at the two end sections are considered in the 3D probabilistic slope stability analyses

considering sampling effects.

1.2 Research Objectives

The main research objectives of this thesis are presented in this section:

1. To incorporate a non-stationary random field with a rotated transverse anisotropy in slope reliability evaluation. In this case, three scenarios of spatially variable soils (i.e., stationary RF, RF with increasing trend with depth, and RF with increasing trend along the direction perpendicular to the bedding) are considered, while the effects of these scenarios on slope reliability and failure mechanisms are investigated and compared.
2. To study the effects of 3D rotated transverse anisotropy on slope reliability and failure patterns. Through considering the 3D rotated transverse anisotropy of soils, three slope scenarios are considered (i.e., dip slope, reverse-dip slope and cross-dip slope). As the orientation of bedding is no longer horizontal, previous findings regarding the change of slope reliability and failure pattern with θ under 3D horizontal transverse anisotropy may not be valid. These are discussed under rotated transverse anisotropy.

3. To study the sampling effects in 2D probabilistic slope stability analyses considering various sampling strategies and rotated transverse anisotropy. Three slope reliability analysis methods (i.e., two conditional random field simulation methods and Sobol index method) that can incorporate sample points under the context of soil spatial variability are used. The influence of rotated transverse anisotropy on the sampling efficiency is investigated. In addition, a comparative study on the three methods is conducted.

4. To study the sampling effects in 3D probabilistic slope stability analyses using Sobol index method. Various combinations of slope length L and autocorrelation distance θ are considered to find the relation between θ / L ratio and the sampling efficiency. Different boundary conditions at the end sections are considered in this study. In addition, sampling patterns with one borehole and two boreholes are both considered.

1.3 Thesis Outline

There are seven chapters in this thesis:

CHAPTER 1 is a general introduction of the proposed research including the research motivation and research objectives.

CHAPTER 2 reviews previous studies in the literature that are related to the present research. Both deterministic slope stability analysis approaches and probabilistic slope stability analysis approaches are reviewed. Previous findings on soil spatial variability are reviewed and discussed. In addition, reviews on the conditional random field and Sobol sensitivity index are also presented.

CHAPTER 3 presents the investigation on the effects of rotated transverse anisotropy on slope reliability and failure pattern using 2D non-stationary random field. Three scenarios of spatially variable soils are considered combining non-stationarity with rotated transverse anisotropy of soils: (1) the mean and standard deviation of undrained shear strength (s_u) are constant (i.e., stationary random field); (2) the mean and standard deviation of undrained shear strength increase with depth; (3) the mean and standard deviation of undrained shear strength increase along the direction perpendicular to the bedding. Slope reliability is investigated under three scenarios of soil spatial variability, while the distributions of slip surfaces obtained by Monte Carlo simulations are also presented.

CHAPTER 4 presents the investigation on 3D probabilistic slope stability analyses considering rotated transverse anisotropy of soils. Three slope scenarios (i.e., dip slope, reverse-dip slope and cross-dip slope) are constructed through random field simulation considering rotated transverse anisotropy. In addition, previous findings on

the 3D failure modes under isotropy and horizontal transverse anisotropy are presented and compared with the current findings considering rotated transverse anisotropy. The statistical characteristics of FS, slope reliability and mean of slide length are also investigated in this chapter.

CHAPTER 5 presents the investigation on sampling effects in 2D probabilistic slope stability analysis. In this chapter, a comparative study is conducted among two conditional random field simulation methods and the Sobol index method, through investigating the sampling efficiency under various sampling patterns and rotational angles of the strata. The influence of rotated transverse anisotropy on the sampling efficiency is also investigated and discussed.

CHAPTER 6 presents the investigation on sampling effects in 3D probabilistic slope stability analyses by the Sobol index method. In consideration of various θ and L , the influences of θ / L ratio on the sampling efficiency and optimal sampling pattern are investigated. In addition, three types of boundary conditions at the two end sections are considered. In this chapter, the investigations are conducted considering sampling strategies with one borehole and two boreholes.

CHAPTER 7 summarises the main findings of this thesis and proposes recommendations for future works.

Table 1.1 Number of landslide incidents from 2008 to 2016 in Hong Kong.

Year	No. of landslides involving slopes that are assessed to be safe and stabilized	Total no. of reported landslides	References
2008	29	863	Li <i>et al.</i> (2012)
2009	12	101	Li <i>et al.</i> (2013)
2010	8	206	Li <i>et al.</i> (2014)
2011	7	77	Lam <i>et al.</i> (2014)
2012	17	163	Lee <i>et al.</i> (2015)
2013	14	241	Lee and Lo (2017)
2014	8	237	Lee <i>et al.</i> (2017)
2015	9	161	Wai <i>et al.</i> (2018a)
2016	13	226	Wai <i>et al.</i> (2018b)
Average	13	253	

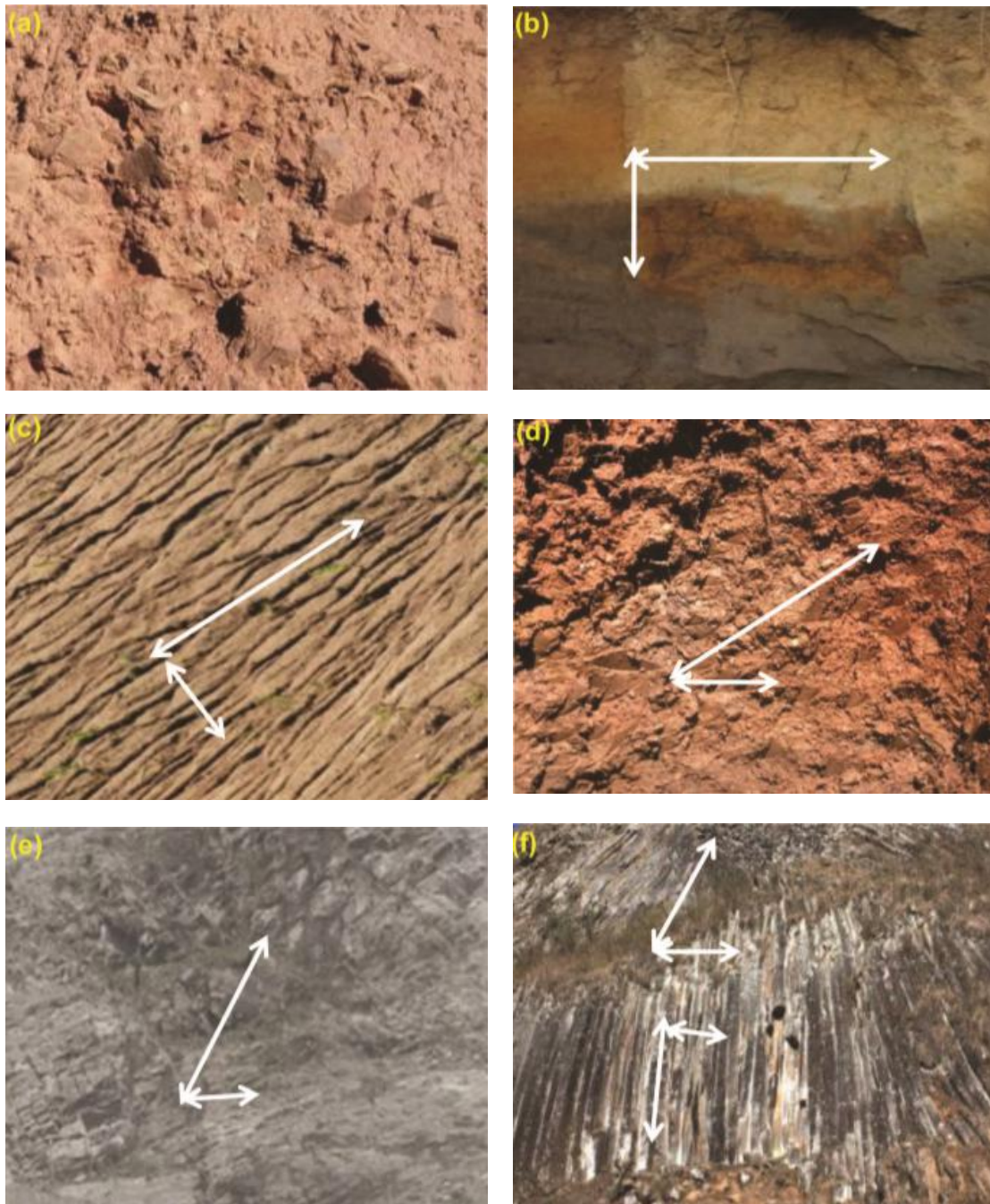


Figure 1.1 Typical patterns of soil spatial variability in nature: (a) isotropy; (b) horizontal transverse anisotropy; (c) rotated transverse anisotropy; (d) general anisotropy (the direction of the minor autocorrelation distance, θ_1 , is horizontal); (e) general rotated transverse anisotropy (the direction of the minor autocorrelation distance is not horizontal); (f) combination (Zhu and Zhang 2013).

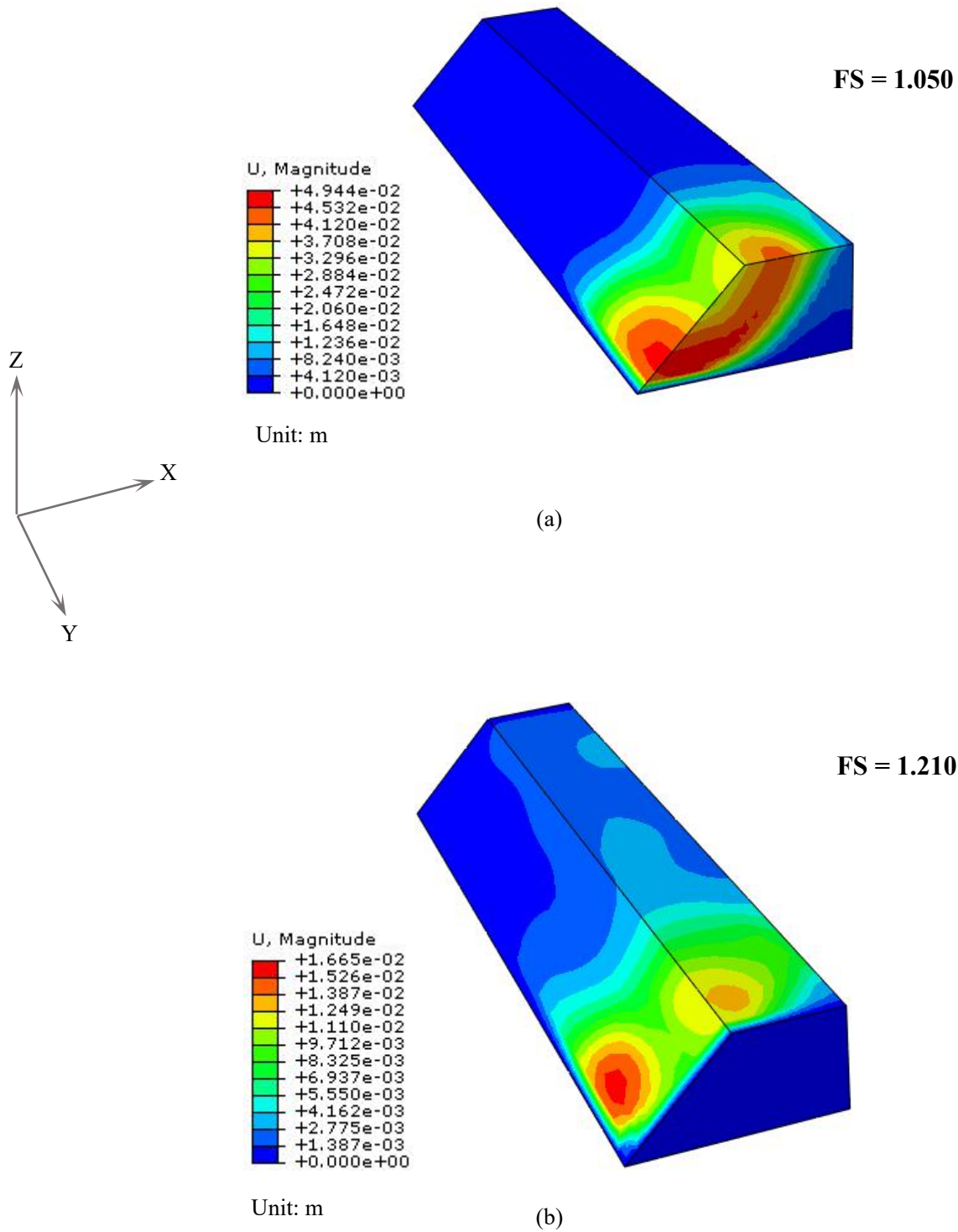


Figure 1.2 Displacement contours at failure of a slope in spatially variable soils under different boundary conditions at the two end sections: (a) preventing the movement in y - direction; (b) preventing the movement in (x, y, z) - direction.

CHAPTER 2 Literature Review

2.1 Introduction

An overview of the literature relevant to this thesis is presented in this chapter, which in particular concentrates on slope stability analysis and soil spatial variability. Probabilistic slope stability analysis is the main focus of this thesis. When conducting probabilistic slope stability analyses, deterministic slope stability analysis techniques are usually combined with probability theories. Therefore, this chapter firstly presents a review of the conventional deterministic slope stability analysis methods. The review of probabilistic slope stability analysis methods are subsequently presented in Section 2.3, where the reliability index and probability of failure are also introduced. Another important topic of this thesis is the soil spatial variability. In Section 2.4, previous studies on soil spatial variability are reviewed, and the formulations related to soil spatial variability are discussed. Subsequently, the parameters describing the spatial variation of soils (i.e., autocorrelation distance and autocorrelation function) are demonstrated in Section 2.5. Random field theory is often used to simulate spatially variable soils, which is discussed in Section 2.6. In engineering practice, soil samples are usually obtained from a site investigation, which can provide known information for simulating spatially variable soils and thus reduce the spatial uncertainty. In Section 2.7, the methods that can incorporate the sampling effects in probabilistic slope stability analysis are discussed.

2.2 Deterministic Slope Stability Analysis

Soils are assumed to be homogeneous within each soil layer in traditional deterministic slope stability analyses, where geotechnical uncertainties are not explicitly modeled. A deterministic FS is usually adopted to assess the safety of a slope in the deterministic method. In this section, different definitions for FS are presented, while methods for determining FS are reviewed.

2.2.1 Factor of Safety (FS)

Generally, FS can be defined by the the following two formulations (Cheng and Lau 2008) :

$$FS_m = \frac{M_r}{M_d} \quad (2.1)$$

Eq. (2.1) is based on moment equilibrium, where M_r represents the resisting moment and M_d denotes the driving moment.

$$FS_f = \frac{F_r}{F_d} \quad (2.2)$$

Eq. (2.2) is based on force equilibrium, where F_r represents the resisting force and F_d denotes the driving force.

These two definitions may result in slightly different FS values, and it is often difficult to satisfy both definitions simultaneously using the method of slices, since the inter-slice force function, $f(x)$, is not uniquely defined. Actually, most design codes do not have a clear requirement for the selection of these two equations, and a single definition for FS is usually specified in many design codes (Cheng and Lau 2008). An extremum method developed by Cheng *et al.* (2010) can give a FS considering the force and moment equilibrium simultaneously. In the extremum method, a range of $f(x)$ is considered into the two equations for FS. A global optimization method is then implemented to find the minimum and maximum extremum values for FS that can satisfy both the force and moment equilibrium with a unique $f(x)$. Cheng *et al.* (2010) proved that the maximum values of FS is acceptable to describe the safety of a slope by numerical analyses.

Theoretically, $FS < 1.0$ indicates failure of a slope, but sufficient safety margin has to be considered in practice. For example, Table 2.1 shows the required FS of slopes in Hong Kong (GEO, 1984). This table is based on a groundwater table for a ten-year return period rainfall. It should be noted that when the safety of a slope is assessed under the predicted worst groundwater conditions, the recommended FS can be decreased. Statistical characteristics of FS are significant indicators in slope reliability evaluation. For example, the cumulative distribution function of FS is usually adopted to assess the slope performance for different safety margins in reliability analysis. Besides, the probability of failure of a slope is usually given by the percentage of FS

< 1 in a suite of FS obtained by Monte Carlo simulations.

2.2.2 Limit Equilibrium Method

The limit equilibrium method (LEM) is commonly used to obtain the FS in engineering practice. In LEM, slope problems are statically indeterminate, while the sliding mass is divided into slices. The Mohr-Coulomb failure criterion is used in LEM, and progressive failure is not considered. In the early implementation of LEM, the shape and location of the slip surface were fixed, meaning that the minimum FS and the most critical slip surface may not be correctly obtained. With the use of modern optimization techniques, the shape and location of slip surface do not have to be restricted. The "Entry and Exit" method (Figure 2.1) is incorporated in many commercial software packages to search for the critical failure surface [e.g., SLOPE/W (GEO-SLOPE International Ltd. 2012)]. In the "Entry and Exit" method (GEO-SLOPE International Ltd. 2012), the locations where the trial slip surfaces will enter the slope body and where they are likely to exit are specified, as shown in Figure 2.1 by the two red lines. Usually, the number of entry and exit points is determined as the number of increments along the two lines. For the circular failure surface, many trial slip surfaces are formed by connecting the entry and exit points through arc lines. The trial slip surface with the minimum FS can then be determined as the critical failure surface. For a non-circular failure surface, an optimization

method named “segmental technique” (GEO-SLOPE International Ltd. 2012) can be adopted. In the segmental technique, the circular critical failure surface is first determined, and then the slip surface is divided into many line segments. After that, the end points of those segments will move to probe lower values of FS. This process starts from the entry point of the predetermined circular surface. The entry point would randomly move backwards and forwards on the ground surface to find a position in relation to the lowest value of FS. Such a process is repeated for all the end points of line segments, one by one, and a new pattern of slip surface with many line segments can be obtained (the end points of line segments in the slope body can move in every direction within a range). After that, the longest line segment within the slip surface will be divided into two portions by adding a new point to the middle, and then the added point will move randomly to probe a new solution. This process would be repeated until the final critical slip surface is found with an acceptable tolerance.

Assumptions of static equilibrium between inter-slice forces are required in LEM, and many approaches related to LEM were developed based on the different assumptions (Fellenius 1936; Bishop 1955; Janbu 1956; Lowe and Karafiath 1960; Morgenstern and Price 1965; Spencer 1967; Fan *et al.* 1986; Corps of Engineers 2003). The Bishop method (Bishop 1955) is often used in engineering practice, as the computational cost is low and the result is close to that obtained by more advanced LEMs. The failure surface is assumed to be circular in the Bishop method, while the vertical inter-slice force is assumed to be zero, and the horizontal force equilibrium is not considered. In

the Bishop method, the moment equilibrium about the center of the circle is often used to determine FS. However, this method can only satisfy the global moment equilibrium, and the local moment equilibrium is not enforced. The Janbu simplified method (Janbu 1957) adopts the force equilibrium definition for FS, and the failure surface can be non-circular. Usually, FS obtained by the Janbu simplified method would be smaller than that by the Bishop and Morgenstern-Price methods (Morgenstern and Price 1965). In addition, FS by the Bishop method can yield better agreement with FS by the Morgenstern-Price method than that by the Janbu simplified method. Janbu (1973) proposed a correction factor, f_0 , for the simplified method, which can be given as follows (Cheng and Lau 2008) :

$$\begin{aligned}
 \text{For } c, \varphi > 0, \quad f_0 &= 1 + 0.5 \left[\frac{D}{l} - 1.4 \left(\frac{D}{l} \right)^2 \right] \\
 \text{For } c = 0, \quad f_0 &= 1 + 0.3 \left[\frac{D}{l} - 1.4 \left(\frac{D}{l} \right)^2 \right] \\
 \text{For } \varphi = 0, \quad f_0 &= 1 + 0.6 \left[\frac{D}{l} - 1.4 \left(\frac{D}{l} \right)^2 \right]
 \end{aligned} \tag{2.3}$$

In the above equations, l denotes the distance between the left and right exit points of the slip surface, and D denotes the maximum thickness of the failure mass with reference to the line connecting the entry and exit points, as shown in Figure 2.2. With the use of the correction factor, f_0 , FS by the Janbu simplified method can yield better agreement with FS obtained by the Bishop and Morgenstern-Price methods. The inter-slice force function, $f(x)$, should be used in the Morgenstern-Price method, while the inter-slice force is equal to $\lambda_0 f(x) E_0$, where E_0 is the inter-slice normal force and λ_0 is a directional factor. Assumptions on $f(x)$ are usually made. Some commonly used types of $f(x)$ are represented in Table 2.2. The functions of $f(x) = 1$ and $f(x) = \sin(x)$ are

popular in engineering practice, and when $f(x) = 1$, the Morgenstern-Price method is equivalent to the Spencer method (Spencer 1967). Using these two functions, the force equilibrium and global moment equilibrium are satisfied in the Morgenstern-Price method, but the local moment equilibrium equation is not considered. Alternatively, other more complex types of $f(x)$ can also be adopted. The trapezoidal shape function shown in Figure 2.3 can be reduced to $f(x) = 1$, but this function is seldom adopted in practice. The Fredlund-Wilson-Fan force function [$f(x) = \Psi \exp(-0.5v^n \kappa^n)$ (Figure 2.3)] is obtained by an elastic finite element stress analysis (Fan *et al.* 1986), where Ψ , v , and κ are defined by the users, and κ is a normalised dimensional factor. Since the LEM is based on the ultimate condition, which is different from the elastic stress analysis by Fan *et al.* (1986), this inter-slice force function cannot be justified using elastic analysis (Cheng and Lau 2008). In addition, for a slope with soil nails, water table and external loading, the parameters in the Fredlund-Wilson-Fan force function are difficult to define (Cheng and Lau 2008). The Corps of Engineers method (Corps of Engineers 2003) assumes that $\lambda_0 f(x)$ is the value of the slope angle, while in the Lowe-Karafiath method (Lowe and Karafiath 1960), $\lambda_0 f(x)$ is equal to the average of the angle of the slice top (ground surface) and the base inclination. These two methods cannot satisfy moment equilibrium, since $\lambda_0 f(x)$ is prescribed.

2.2.3 Finite Element Method

Compared with LEM, the finite element method (FEM) has the following advantages when obtaining FS and the critical failure surface (Griffiths and Lane 1999): (a) assumption on inter-slice force function, $f(x)$, is unnecessary; (b) it is possible to consider the progressive failure; and (c) deformation can be given. Although the stress and strain of soils in a slope domain can be obtained using finite element method, FS cannot be directly determined. In slope stability analysis, the strength reduction method (SRM) is often used to determine FS in the context of FEM (Ugai and Leshchinsky 1995; Griffiths and Lane 1999; Dawson *et al.* 1999; Zheng *et al.* 2005). In SRM, FS is represented by the strength reduction factor F which is given as follows:

$$\frac{\tau'}{F} = \frac{c'}{F} + \sigma' \frac{\tan \varphi'}{F} \quad (2.4)$$

which can also be expressed by

$$\frac{\tau'}{F} = c^* + \sigma' \tan \varphi^* \quad (2.5)$$

where τ' = effective shear strength; σ' = effective normal stress; c' = effective cohesion; φ' = effective friction angle; $c^* = \frac{c'}{F}$ and $\varphi^* = \arctan\left(\frac{\tan \varphi'}{F}\right)$. The procedure for obtaining FS in SRM can be summarised as follows: (1) compute the stress and strain of soils in the slope domain based on the original input parameters; (2) increase the strength reduction factor, while Eq. (2.4) or Eq. (2.5) are implemented to reduce the shear strength (new stress and strain conditions are obtained in this stage); (3) repeat step (2) until the slope failure occurs, while the strength reduction factor F

can be considered as FS for the slope. The definition of slope failure is discussed in the following paragraph.

In SRM, FS should be determined when slope failure occurs. For the definition of slope failure in SRM, there are mainly three criteria (Cheng and Lau 2008): (1) a sudden increase in the nodal displacement; (2) non-convergence of the finite element solution; and (3) a plastic zone, indicating the potential failure surface, is formed continuously (Figure 2.4). Xiao *et al.* (2014) discussed the applicability of the above criteria in probabilistic slope stability analysis under the framework of Monte Carlo simulation. In general, among these criteria, the physical significance of (1) and (3) are clear, but sometimes they are not very practical, especially in probabilistic slope stability analysis. For example, the continuous plastic zone should be decided manually, which cannot be realistically implemented when using Monte Carlo simulation associated with hundreds to thousands of models. Also, the nodal displacement needs to be observed on some feature points, but the feature points are difficult to select. In 3D probabilistic slope stability analysis with spatially variable soils, some selected feature points may not involve information for displacements, as localised and discrete failures can occur. In contrast, criterion (2) is relatively easy to implement in both 2D and 3D probabilistic slope stability analyses, which is often incorporated in many commercial software packages (e.g., FLAC and FLAC3D). However, the results obtained by criterion (2) may be slightly affected by the solver setting in the SRM procedure.

Zienkiewicz *et al.* (1970) was the first to use FEM in slope analyses. SRM was subsequently developed by Naylor (1982) in the finite element framework to obtain FS. After that, many attempts have been made to further investigate SRM. For example, nodal strains have been used to determine FS by Donald and Giam (1988). Matsui and San (1992) used the stress condition to determine the critical failure surface and FS. Griffiths and Lane (1999) investigated many slope models using LEM and SRM, including a homogeneous soil slope without a foundation, a slope with a thin weak layer under undrained conditions, two side earth embankment, etc. It was found that SRM is a more powerful alternative to LEM, as the failure surface determined by SRM is naturally formed without defining the shape of slip surface prior to the analyses. This advantage of SRM is particularly significant in probabilistic slope stability analyses with spatially variable soils, as the spatially heterogeneous distribution of the soil properties would indicate the pronounced non-circular failure mechanism of the slope. Using the modern optimization technique, it is unnecessary to assume the shape of slip surface in LEM, but only one slip surface can be determined in a slope. That means when it comes to a slope failure with more than one slip surfaces (Figure 2.5), the performance of LEM may not be adequate.

2.2.4 Other Slope Stability Analysis Methods

For simple estimation of slope stability, Taylor's stability chart (Taylor 1937) (Figure

2.6) can be used. Taylor's stability chart is formed by considering the relation between slope stability, the soil parameters and slope geometry. Therefore, given the soil parameters and slope geometry, the slope stability number can be readily estimated using the stability chart. Duncan (1996) suggested that within a total stress analysis framework, the accuracy of the slope stability number obtained from Taylor's stability chart is generally acceptable.

Apart from LEM and FEM, limit analysis (Druker and Prager 1952) is also a popular method for slope stability analysis, where soils are assumed to be elastic-perfectly plastic with the use of the associated flow rule (Chen 1970). This method can consider the soil stress associated with soil strain, but it is necessary to define the shape of the sliding mass prior to the analyses. To randomly search for the slip surface based on limit analysis, Smith and Gilbert (2007) developed a method named "Discontinuity Layout Optimization" (DLO). In the DLO method, many discontinuities are formed by connecting the discrete points in a domain, after which many potential slip paths can be formed through combining the discontinuities. The path with the minimum energy dissipation is considered as the critical failure surface. The procedure for the implementation of DLO is shown in Figure 2.7 [Smith and Gilbert (2010)].

In addition, the rigid element method (Zhang and Qian 1993) and the distinct (or discrete) element method (Chang 1992; Itasca 1999) can also be adopted to calculate FS and estimate the failure mechanism. Unlike LEM and FEM, the material is

discontinuous in the rigid element and distinct element methods. In the rigid element method, the elements are assumed to be rigid, and the problem domain is divided into a number of rigid bodies that are connected at inter-surfaces. The solution and processing procedures for the rigid element method resemble that used in FEM. In recent distinct element method implementations (Itasca 1999), soils are represented by circular particles in 2D problems or spherical particles in 3D problems. The elements in the distinct element method interact through frictional sliding contacts. The main disadvantage of the distinct element method is the high computational cost compared with LEM and SRM when performing slope stability analysis. However, this method is more suitable to simulate progressive slope failure and the flow of a failed mass after the initiation of slope failure.

2.2.5 3D Slope Stability Analysis

Slope stability is generally a three-dimensional phenomenon. In engineering practice, 2D slope stability techniques are popular due to their low computational costs. Another reason for the common use of 2D slope stability analysis is that conservative results of FS are obtained in most cases. However, Griffiths and Marquez (2008) found that some cross-sections within a 3D slope may give higher two-dimensional FS than the three-dimensional FS, which can occur on a slope with an oblique layer of weak soil intersecting with the slope section. Therefore, it should be noted that

although the three-dimensional slope stability analysis usually results in a higher FS due to the support from the boundary, the slope failure mechanism might be more critical in 3D slope stability analysis under some unusual geological settings (e.g., non-uniform loading, spatially variable soils, irregular geometry) (Griffiths *et al.* 2009b).

Earlier investigations on 3D LEM were based on a simple extension of the 2D approaches (Baligh and Azzouz 1975; Leshchinsky *et al.* 1985; Hungr *et al.* 1987). During recent decades, more advanced 3D LEMs were developed considering the sliding direction and asymmetric failure mechanism (Jiang and Yamagami 1999; Huang and Tsai 2000; Cheng *et al.* 2005; Cheng and Yip 2007). Jiang and Yamagami (1999) was the first to develop the 3D LEM method to consider an asymmetric failure mechanism, where the sliding direction is not incorporated in the classical LEM equations. In their study, the sliding direction is obtained by rotating the axes until the minimum FS is found. Huang and Tsai (2000) derived the equations incorporating the sliding direction for a 3D Bishop method, which can consider the asymmetrical problem. Cheng *et al.* (2005) proposed a method for determining an arbitrary failure mechanism for 3D slope problems. Later, Cheng and Yip (2007) proposed the 3D LEM equations for the Bishop, Janbu simplified and Morgenstern-Price methods, where the sliding direction is obtained from the 3D force/moment equilibrium function.

The finite element investigations on 3D slope stability analysis were usually based on SRM (Griffiths and Marquez 2007; Wei *et al.* 2009; Detournay *et al.* 2011; Stianson *et al.* 2011; Gharti *et al.* 2012; Nian *et al.* 2012; Zhang *et al.* 2013). In 3D finite element analysis of slope stability, boundary conditions of the two end sections along the y - direction (Figure 2.8) are significant. Generally, the following three kinds of boundary conditions are usually adopted in practice (Chugh 2003; Shen and Karakus 2014): (1) only preventing movement in the y – direction, which is adopted when there is no side shear resistance of a contact (i.e., smooth boundary); (2) preventing movement in the (x, y) – directions that considers the side shear resistance in the x - direction [i.e., boundary is fixed in the (x, y) – directions]; (3) preventing movement in the (x, y, z) – directions that represents a contact without movements (i.e., fully fixed boundary). The smooth boundary condition is analogous to the implicit boundary condition in 3D limit equilibrium method (Chugh 2003), as in the 3D LEM the slope body is divided into rigid columns and there is no shear force on the side at the boundary. For the boundary condition preventing movement in the (x, y) – directions, it has been used by Arellano and Stark (2000) to simulate side shear resistance in 3D slope stability analysis. The fully fixed boundary condition is often adopted in 3D finite element analysis of slopes. That is because considering homogeneous soils and symmetrical 3D slope geometry, only half of a slope needs to be simulated using the fixed boundary condition, and hence the computing time can be reduced (Jian and Chan 2014). In addition, Griffiths (2009b) pointed out that the fixed boundary condition would be the most appropriate boundary condition for the

abutment of an earth dam.

On the other hand, some investigators have different opinions towards the selection of the end boundary condition. Ji and Chan (2014) pointed out that the slope failure would be affected by the boundary condition, and the portion of a 3D slope investigated is often cut from a long slope. Therefore, the use of a fixed boundary condition may not be appropriate, and a smooth boundary condition would be better. However, in the context of spatially variable soil properties, Spencer (2007) found that slope failures tend to occur around the two end sections with a smooth boundary condition, and thus biases may occur at this situation. Based on these considerations, Hicks and Spencer (2010) proposed that the boundary condition without movements in the (x, y) – directions would be a better choice in 3D probabilistic slope stability analysis. Meanwhile, the validation of this boundary condition was also implemented in an investigation analysing slopes of different lengths. Hicks and Spencer (2010) conducted comparative studies between the numerical method with the boundary condition fixed in the (x, y) - directions and the method based on simple probability theory, where the probability of failure of a long slope is a function of that of a shorter slope. As shown in Figure 2.9, considering spatially variable soils and various slope lengths, the results by the numerical method are in good agreement with the results by the method based on the probability theory. Considering soil spatial variability, Griffiths *et al.* (2009b) found that the boundary conditions are influential to the estimated P_f . Generally, under the fixed boundary condition, the estimated P_f is

increased with a larger slope length. However, under the smooth boundary condition, the P_f would generally decrease with an increase in the slope length, when the slope length is less than the “average preferred failure mechanism width”, which is equal to the average of the widths of the sliding masses in the out-of-plane direction over a suite of Monte Carlo simulations. By contrast, when the slope length is larger than that, the P_f would increase with larger slope lengths.

2.3 Probabilistic Slope Stability Analysis

Deterministic slope stability analysis does not explicitly model the geotechnical uncertainties when assessing the safety of a slope. In order to consider geotechnical uncertainties in slope stability analysis, probabilistic slope stability analysis was developed. The probability of failure P_f or reliability index β are often adopted to assess the reliability of a slope in the context of probabilistic slope stability analysis. The definitions for P_f and β are presented in this section. Moreover, some probabilistic approaches are reviewed.

2.3.1 Probability of Failure and Reliability Index

In probabilistic slope stability analysis, the probability of failure P_f is usually adopted to assess the safety margin of a slope. Theoretically, the P_f is given by

$$P_f = P[g(\mathbf{X}_0) \leq 0] = \int \dots \int_{g(\mathbf{X}_0) \leq 0} f_{\mathbf{X}_0}(\mathbf{X}_0) d\mathbf{X}_0 \quad (2.6)$$

where $f_{\mathbf{X}}(\mathbf{X}_0)$ denotes the joint probability density function of \mathbf{X}_0 that represents a set of random variables, and $g(\mathbf{X}_0)$ is the performance function defined as

$$g(\mathbf{X}_0) = \min_{i=1,2,\dots,n} FS_i(\mathbf{X}_0) - 1 \quad (2.7)$$

where $FS_i(\mathbf{X}_0)$ is FS of the i th potential slip surface. The integration in Eq. (2.7) is difficult to obtain, but following Monte Carlo process, P_f can be easily estimated as

$$P_f \approx \frac{1}{N_T} \sum_{i=1}^{N_T} I(FS_i < fs) \quad (2.8)$$

where fs is the threshold value for defining the failure of a slope, which is usually taken as 1; N_T is the number of simulations in Monte Carlo process; and $I(\cdot)$ is an indicator function that is equal to 1 when the failure of a slope occurs, and 0 otherwise. In Monte Carlo simulation, the sampling size influences the accuracy of P_f . Usually, for achieving a desired level of accuracy, the N_T is suggested to be larger than 10 times the reciprocal of P_f of interest (Roberts and Casella 1999). The coefficient of variation (COV) of P_f can be given as follows in consideration of the sampling size N_T :

$$COV_{P_f} = \sqrt{\frac{1 - P_f}{N_T P_f}} \quad (2.9)$$

The reliability index β can also be used to express the safety of a slope in probabilistic slope stability analysis. For simplicity, assuming the evaluated factors of safety are normally distributed, β can be given as follows (Chowdhury and Xu 1993; Christian *et al.* 1994) :

$$\beta = \frac{\mu(\text{FS})-1}{\sigma(\text{FS})} \quad (2.10)$$

If FS is assumed to be log-normally distributed, the reliability index is given by

$$\beta = \frac{\ln \left[\frac{\mu(\text{FS})}{\sqrt{1+V(\text{FS})^2}} \right]}{\sqrt{\ln[1+V(\text{FS})^2]}} \quad (2.11)$$

In Eqs. (2.10) and (2.11), $\mu(\text{FS})$ denotes the mean of FS; $\sigma(\text{FS})$ represents the standard deviation of FS; and $V(\text{FS}) = \sigma(\text{FS}) / \mu(\text{FS})$. Low (2014) proposed various computational approaches for determining the reliability index, while a comparative study was also implemented in the investigation. The approximate methods corresponding to different definitions of the reliability index are reviewed in the following section. The expected performance levels of a structure under different values of β and corresponding P_f are shown in Table 2.3.

2.3.2 Approximate Method

Methods for obtaining probability of failure and reliability index can generally be divided into two categories (Ji *et al.* 2012): (1) approximate methods including first-order reliability method (FORM), second-order reliability method (SORM) and first-order second moment method (FOSM); and (2) simulation methods based on Monte Carlo simulation. Compared with the Monte Carlo simulation based methods, the computational costs for the approximate methods are lower.

FORM is a commonly used approximate method, and the Hasofer - Lind (Hasofer and Lind 1974) reliability index is often adopted in FORM. The main advantage of the Hasofer - Lind reliability index is its invariance with respect to different formulations of performance function (Ji 2012). However, this method assumes the performance function is linear, meaning that errors would occur when the actual performance function or the failure criteria are non-linear. Physically, the Hasofer-Lind reliability index indicates the minimum distance between the design point for the mean value of the random variables and the limit state surface (Figure 2.10). The formulation of Hasofer-Lind reliability index can be given as follows:

$$\beta = \min_{\mathbf{x}_0 \in \Omega} \sqrt{(\mathbf{x}_0 - \boldsymbol{\mu})^T \mathbf{V}^{-1} (\mathbf{x}_0 - \boldsymbol{\mu})} \quad (2.12)$$

In Eq. (2.12), \mathbf{x}_0 is a vector containing a set of random variables; \mathbf{V} denotes the covariance matrix; $\boldsymbol{\mu}$ represents the mean of \mathbf{x}_0 ; and Ω denotes the failure domain. FORM has been extensively studied considering correlated normal random variables (Hasofer and Lind 1974; Ditlevsen 1981; Shinozuka 1983; Ang and Tang 1984; Melchers 1999; Haldar and Mahadevan 1999; Baecher and Christian 2003). In these studies, the soils are assumed to be homogeneous. To consider the spatial variability of soil properties, some researchers combined random field theory with FORM (Ji *et al.* 2012; Low 2014). In their studies, LEM is used, and \mathbf{x}_0 is considered as autocorrelated random variables of soil properties along the failure surface, where the number of random variables in \mathbf{x}_0 is equal to the number of slices. At the same time, FORM had also been developed to consider the system reliability of slopes (Zhang *et*

al. 2011; Cho 2013). Since using FORM is less time-consuming than using Monte Carlo simulation based methods, such methods are often adopted in 3D probabilistic slope stability analysis (Auvinet and Gonzalez 2000; Vanmarcke 2011; Ji 2014; Ji and Chan 2014), where soil spatial variability is considered.

On the other hand, FOSM uses another definition of reliability index, where the first two moments of FS (i.e., mean and standard deviation of FS) are used to compute the reliability index [i.e., Eq. (2.10)]. The mean-value first order second moment method is often adopted to calculate the reliability index, where the performance functions and limit states are considered. The formulation for mean-value FOSM is given as follows (Hassan and Wolff 1999):

$$\beta = \frac{\mu(\text{FS}) - 1}{\sigma(\text{FS})} = \frac{\text{FS}\{\mu[X_i]\} - 1}{\sqrt{\sum_{i=1}^{n_p} \left(\frac{\partial \text{FS}}{\partial X_i}\right)^2 \sigma^2[X_i] + 2 \sum_{i,j=1}^n \left(\frac{\partial \text{FS}}{\partial X_i}\right) \left(\frac{\partial \text{FS}}{\partial X_j}\right) \rho_X \sigma[X_i][X_j]}} \quad (2.13)$$

In Eq. (2.13), n_p denotes the number of soil parameters; X_i is the i th soil parameter; $\sigma[X_i]$ and $\sigma[X_j]$ represent the standard deviation of the i th and j th soil parameter, respectively; $\mu[X_i]$ represents the mean of the i th soil parameter; and ρ_X denotes the correlation between the i th and j th soil parameters. FOSM has also been widely studied in slope stability problems (Wu and Kraft 1970; Cornell 1971; Alnoso 1976; Tang *et al.* 1976; Vanmarcke 1977; Samui *et al.* 2011; Samui *et al.* 2013). When using FOSM to estimate the reliability of a slope, the performance function should be given. Samui *et al.* (2011) considered the relevance vector machine in FOSM, where the

relevance machine was used to construct the implicit performance function. Meanwhile, the response surface method (Wong 1985; Bucher and Bourgund 1990) and artificial neural network technique (Gomes and Awruch 2004; Deng *et al.* 2005; Deng 2006) can also be used to predict the performance function in FOSM.

2.3.3 Probabilistic Method Assuming Perfect Autocorrelation

The probabilistic methods assuming infinite autocorrelation distance are discussed in this section. That means soils within each layer are assumed to be homogeneous, while values of soil parameters are selected randomly from a probability distribution (e.g., normal distribution and lognormal distribution). When considering a slope with single layer under undrained conditions, P_f can be simply obtained using the following equation, where the undrained shear strength is normally distributed:

$$P_f = P[s_u < s_{fs=1}] = \Phi\left(\frac{s_{fs=1} - \mu_{s_u}}{\sigma_{s_u}}\right) \quad (2.14)$$

In Eq. (2.14), s_u = undrained shear strength; $s_{fs=1}$ = shear strength indicating FS=1; and $\Phi(\cdot)$ = cumulative standard normal distribution function. When the undrained shear strength is log-normally distributed, the equation is given by:

$$P_f = P[\ln(s_u) < \ln(s_{fs=1})] = \Phi\left(\frac{\ln(s_{fs=1}) - \mu_{\ln s_u}}{\sigma_{\ln s_u}}\right) \quad (2.15)$$

where $\mu_{\ln s_u}$ = mean of logarithm of s_u ; and $\sigma_{\ln s_u}$ = standard deviation of

logarithm of s_u .

When there are multiple soil profiles within a slope or more than one soil property is assumed to vary random variably, Eqs. (2.14) and (2.15) cannot be used. In these cases, Monte Carlo simulation can be used in the probabilistic method assuming perfect autocorrelation (Ji and Low 2012; Zhang *et al.* 2013a; Zhang *et al.* 2013b; Liu and Cheng 2016; Liu *et al.* 2017c), which is actually equivalent to the random field based approach with an infinite spatial autocorrelation distance. Herein, the spatial autocorrelation distance represents the distance within which the correlation between the spatially random variables is significant. Griffiths *et al.* (2004) and Griffiths *et al.* (2009a) conducted comparative studies between the method assuming perfect autocorrelation and the method considering soil spatial variability. The results show that the method assuming perfect autocorrelation would overestimate P_f when COV of soil property < 1 , which would be more pronounced with a smaller mean of the soil property. That is because the stronger parts of the spatially variable soils would make it difficult to form a continuous weak path for a critical failure surface.

2.3.4 Random Field Based Method

Soils are spatially variable in reality, which is not explicitly modeled in the probabilistic method discussed in Section 2.3.3. Random field theory (Vanmarcke

1984) can be adopted to simulate the spatially variable soils of a slope, where the soil properties at any locations are considered random variables following a specific probability distribution and correlated spatially. The simulated random fields can then be mapped onto slope stability models, while within a Monte Carlo framework, the probability of slope can be obtained using Eq. (2.8). The slope stability model can be constructed using different slope stability techniques (e.g., LEM and FEM). Based on the adopted slope stability technique, the random field based approaches are presented as follows: (a) random limit equilibrium method (RLEM) that combines traditional limit equilibrium method with a random field (Cho 2010; Wang *et al.* 2011; Li *et al.* 2013; Jiang *et al.* 2015; Li *et al.* 2015; Li and Chu 2015; Jiang and Huang 2016; Liu *et al.* 2018); (b) random finite element method that combines traditional finite element method with a random field (RFEM) (Griffiths and Fenton 2004; Griffiths *et al.* 2009a; Griffiths *et al.* 2009b; Griffiths *et al.* 2009c; Hicks and Spencer 2010; Huang *et al.* 2010; Jha and Ching 2013; Jiang *et al.* 2014; Hicks *et al.* 2014; Li *et al.* 2016b); (c) random finite difference method (RFDM) that combines traditional finite difference method (FDM) with a random field (Lo and Leung 2017, 2018). These methods are usually implemented in a non-intrusive manner, where the existing slope stability analysis procedures do not have to be modified. As a result, many commercial software packages (e.g., FLAC, ABAQUS, and SLOPE/W) can be used. The implementation procedure for the non-intrusive RFEM is summarised as follows, while RLEM and RFDM are conducted in a similar manner (Jiang *et al.* 2014):

Step 1: Define the statistical characteristics for the soil property (e.g., mean, standard

deviation and probability distribution), and determine the autocorrelation function and autocorrelation distance of the spatially variable soils.

Step 2: Build the slope stability model through finite element procedure (e.g., ABAQUS). Discretise the domain into elements and extract the coordinates for each element (e.g., centroid coordinate for each element).

Step 3: The extracted coordinates are adopted to generate N_T random fields.

Step 4: Map the N_T random fields onto the slope stability model to generate N_T slope models with spatially variable soils.

Step 5: Compute the FS of each of the N_T slope model, and calculate the probability of failure using Eq. (2.8) or reliability index using Eqs. (2.10) and (2.11).

Tabarrokhi *et al.* (2013) compared the performance of random limit equilibrium method (RLEM) with that of RFDM in probabilistic slope stability analysis. In the study, various LEMs (e.g, Bishop, Spencer and Morgenstern-Price methods) are considered. It was found that the non-circular LEM may encounter two main issues with random fields: (a) the global optimization search of the critical slip surface is difficult; and (b) solutions may fail to converge. The reason for the convergence problem is that the assumption on inter-slice force function $f(x)$ is made for all the slope stability models with spatially variable soils, but each of the slope models should correspond to a specified $f(x)$ for ensuring the convergence of the FS solution. Although a unique definition of $f(x)$ can be obtained by the extremum method by Cheng *et al.* (2010) for each Monte Carlo simulation, the computational effort would

be quite demanding with hundreds to thousands of calculations. When the convergence issue occurs, the actual critical failure surface may not be properly considered. The Bishop method would not have such a problem, but the failure surface cannot be represented by a circular slip surface in some cases in reality (e.g., failure of slopes in sandy soil). Considering an inter-slice force function of $f(x) = 1/2 \sin(x)$ in the Morgenstern-Price method, the influence of the convergence issue on the resulting P_f is modest. On the contrary, the methods considering SRM can yield reliable results without the above issues, and the failure mechanism can be obtained naturally in each Monte Carlo simulation (Griffiths *et al.* 2004; Griffiths *et al.* 2009a). However, the computational effort is relatively extensive. On the other hand, Cheng *et al.* (2007) identified the limitations of SRM when analysing a slope with a thin weak layer, and such problems need to be investigated considering soil spatial variability in the future, as this scenario can occur in spatially soils simulated by an anisotropic random field. Furthermore, Cheng *et al.* (2007) proposed that the settings of the tolerance for stress analysis and the maximum number of iterations in the SRM procedures might have significant influences on the FS, when the geological conditions are complex.

Due to the low computational cost, the Bishop method is often used in probabilistic slope stability analysis considering random fields (Cho 2010; Li *et al.* 2013; Jiang *et al.* 2015; Li *et al.* 2015; Li and Chu 2015; Jiang and Huang 2016; Liu *et al.* 2017a; Liu *et al.* 2017b; Jiang and Huang 2018). Cho (2010) proposed that, for a cohesive

slope with spatially variable soils under undrained conditions, the accuracy for the use of circular slip surface is acceptable. The failure mechanism and FS of slopes in spatially variable soils by LEM and SRM are shown in Figures (2.11) and (2.12) by Cho (2010). Javankhoshdel *et al.* (2017) conducted the comparative studies of RLEM (the Bishop method) and RFEM considering cohesive soil slopes with the depth factor = 2. They found that when considering isotropic random fields, the results of P_f obtained by RLEM and RFEM can yield good agreements for the slope with a small angle (slope angle = 27°), and the influence of the cross-correlation between the undrained soil strength and unit weight is insignificant. However, when the slope is steep (slope angle = 67°), the results obtained by RFEM would be significantly different from those obtained by RLEM. On the other hand, when considering anisotropic random fields, the influence of the cross-correlation between the undrained soil strength and unit weight would be significant. Herein, when the magnitude of the cross-correlation increases, the differences between the results obtained by RFEM and RLEM would generally increase. Li and Chu (2019) conducted the comparative studies between the LEMs (the Bishop, Spencer and Morgenstern-Price methods), FDM and FEM in calculating FS considering a cohesive soil slope with spatially variable soils. They found that the FS and failure mechanism obtained by the Bishop method are close to those obtained by FDM and FEM. In addition, they also pointed out the global optimization and convergence issues in the Spencer and Morgenstern-Price methods, which echos the previous findings proposed by Tabarrokhi *et al.* (2013). To obtain the non-circular failure surface accurately in

RLEM, Mafi *et al.* (2020) proposed a novel optimization method termed surface altering optimization, which can indicate accurate results of FS and failure mechanism in comparison to those obtained by RFEM with less computational time. Besides, Lo and Leung (2017) conducted the comparison analyses between RLEM (the Bishop method) and RFDM considering a slope under drained conditions. They found that the results of P_f obtained by RFDM are higher than those obtained by RLEM, because the non-circular slip surface determined by FDM can represent the actual failure surface better and indicate the smaller FS in each MCS simulation. The author of this thesis also conducted comparison analyses between RLEM and RFEM incorporating the Bishop and Janbu methods, where the slope under undrained conditions investigated in Cho (2010) (Figures 2.11 and 2.12) was considered. The RFEM procedure used in the analyses was developed by Griffiths and Fenton (2004), which is open-source and can be downloaded at <http://courses.engmath.dal.ca/rfem/>. The comparison results are shown in Table 2.4. It can be found that the results obtained by RLEM with the Bishop method and RFEM yield good agreements, while the results obtained by RLEM with the Janbu method are significantly higher. As proposed by Cheng and Lau (2008), the Janbu method can produce the significantly smaller FS than that by the Bishop and Morgenstern - Price methods in cohesive soils, which may indicate the higher value of P_f .

When it comes to 3D problems, the computational cost would be a significant problem for RFDM and RFEM. Besides, Cheng and Lau (2008) pointed out that 3D

SRM by FLAC3D may lead to inaccurate results when considering soil nails, and they suggested that 3D SRM may not be mature for engineering use. 3D RLEM may be an alternative approach in 3D probabilistic slope stability analysis considering spatially variable soils, and lower computational cost can be achieved using a spherical failure surface. However, 3D RLEM is seldom investigated up to now. Furthermore, the random search of the arbitrary failure shape using 3D LEM is time-consuming even for a single deterministic analysis (Cheng *et al.* 2005), meaning that it may not be applicable within a Monte Carlo framework with hundreds to thousands of slope stability models.

2.3.5 Surrogate Model

The large computational demand is a significant issue in probabilistic slope stability analysis using Monte Carlo simulation. To save computation time, surrogate models are often adopted. The surrogate model can be used to define the functional relation between the system response and the input parameters. The accuracy of a surrogate model heavily relies on the process of experiment design. In the stage of experiment design, sampling techniques (e.g., Monte Carlo simulation and Latin hyper-cube sampling) are often adopted to generate training samples for developing the surrogate model. Usually, when the number of training samples increases, the accuracy of a surrogate model improves. However, to obtain additional training samples, more

simulations need to be conducted, increasing its computational effort. Therefore, a balance between the accuracy and computational effort should be considered when developing a surrogate model.

In probabilistic slope stability analysis, the response surface method is often adopted to construct the surrogate model (Ying 2012; Li and Chu 2015; Jiang and Huang 2016; Li *et al.* 2016c; Li and Chu 2016). Li *et al.* (2016c) reviewed the recent developments of the response surface methods. To construct the response surface, quadratic functions [Eq. (2.16)] (Bucher and Bourgund 1990; Zhang *et al.* 2013b) are usually adopted:

$$FS = a_{0p} + \sum_{i=1}^{n_i} b_i x_i + \sum_{i=1}^{n_i} c_i x_i^2 \quad (2.16)$$

where n_i denotes the number of input random variables, and a_{0p} , b_i and c_i are the unknown coefficients. In order to determine these coefficients, regression methods are often adopted in consideration of $(2n_i+1)$ points: $(\mu_{x1}, \mu_{x2}, \dots, \mu_{xn})$, $(\mu_{x1}, \mu_{x2} \pm k\sigma_{x2}, \dots, \mu_{xn}), \dots, (\mu_{x1}, \mu_{x2}, \dots, \mu_{xn} \pm k\sigma_{xn})$, where k is usually taken as 2 (Li *et al.* 2016c).

Meanwhile, the 2nd order polynomial chaos expansion (PCE) function is also popular (e.g., Huang *et al.* 2009; Jiang *et al.* 2014, 2015), which is given as follows:

$$FS = a_0 + \sum_{i=1}^{n_i} a_i \xi_i + \sum_{i_1=1}^{n_i} \sum_{i_2=i_1}^{n_i} a_{i_1 i_2} (\xi_{i_1} \xi_{i_2} - \delta_{i_1 i_2}) \quad (2.17)$$

where $(a_0, a_i, a_{i_1 i_2})$ are the PCE coefficients, which can also be determined through a regression analysis based on the simulated FS, and ξ denotes the independent components representing the random field; and $\delta_{i_1 i_2}$ is the Kronecker delta. Li *et al.* (2016c) proposed that, for a single layer slope with soils assuming perfect

autocorrelation, the accuracy of P_f by Eq. (2.16) is sufficient. Since the computational cost using Eq. (2.16) is lower than that using Eq. (2.17), Eq. (2.16) is suggested to be used in this scenario. However, when considering a slope with multiple soil layers or a slope with spatially variable soils, the accuracy by Eq. (2.16) is significantly worse than that by Eq. (2.17), and Eq. (2.17) is suggested to be adopted.

In addition, the Kriging method (Zhang *et al.* 2013a; Yi *et al.* 2015; Liu *et al.* 2017c), artificial neural networks (e.g., Cho 2009) and support vector machines (Samui *et al.* 2011; Samui *et al.* 2013; Kang and Li 2016; Kang *et al.* 2016) can also be used to generate surrogate models. Zhang *et al.* (2013a) proposed that the Kriging method would yield better performance than the response surface method with the quadratic function when considering system reliability of a soil slope. Samui *et al.* (2013) compared the least square support vector machine method with the artificial neural network method for constructing the surrogate model in slope reliability analysis. The comparative results showed that when the performance function is non-linear, the least square support vector machine performs better than the artificial neural network method.

2.4 Spatial Variability in Soils

Soil spatial variability is a significant source of uncertainties in probabilistic slope

stability analysis. As mentioned in the previous section, random field theory is often used to simulate spatially variable soils. In this section, previous studies on characterising soil spatial variability are reviewed, while the model representing spatially correlated random variables is discussed. This section also presents and discusses the formulations for simulating spatially correlated random variables with increasing trend by depth (i.e., non-stationary random field).

2.4.1 Characterisation of Spatial Variability

Soil properties (e.g., cohesion, friction angle, undrained shear strength and coefficient of permeability) are spatially variable in nature. To characterise soil spatial variability, geostatistical methods can be adopted (Georgakakos *et al.* 1990; Mateu *et al.* 2007; Shahid *et al.* 2013; Liu *et al.* 2017d; Liu and Leung 2018). For example, Georgakakos *et al.* (1990) presented a number of geostatistical approaches, and then used those approaches to predict the spatially variable soil properties. Liu *et al.* (2017d) proposed an integrated framework to characterise spatially correlated variables for two-dimensional problems, where the stationary assumptions are checked and the trend order is determined in a data-driven manner. To characterise the spatially anisotropic soils for three-dimensional problems, the framework is further extended by Liu and Leung (2018).

The procedure for characterising soil spatial variability mainly includes the following steps (Liu 2018): (1) obtaining known samples and determining the autocorrelation structure; (2) predicting the soil properties at unsampled locations considering the autocorrelation structure; and (3) checking the prediction accuracy. Kriging interpolation techniques are often used to predict spatially variable soil properties (the formulations for Kriging interpolation are presented in Section 2.7.1). Generally, larger number of sample values can result in more accurate predictions using the Kriging methods. However, the sample values by site investigation are usually limited, especially when the sample values need to be obtained by laboratory experiments. With limited sample values, the accuracy of soil characterisation is difficult to guarantee. In this case, the spatially variable soil properties can be simulated as spatially correlated random variables, where the autocorrelation structure obtained in the soil characterisation stage can also be adopted. The simulation of spatially correlated random variables is treated in the following sections.

2.4.2 Spatially Correlated Random Variables

Generally, spatially correlated random variables can be represented by the following linear function with a deterministic trend structure plus a residual:

$$\mathbf{z} = \boldsymbol{\mu} + \mathbf{e} \quad (2.18)$$

In Eq. (2.18), \mathbf{z} denotes a vector for spatially random variables in various locations;

and $\boldsymbol{\mu}$ represents the deterministic trend. When the prevalent trend cannot be found in the data $\boldsymbol{\mu}$, the trend structure is often assumed to be constant. The parameter \mathbf{e} represents the residual, which is a random vector with a constant variance under second-order stationarity assumptions. The mean of \mathbf{e} is 0, while the covariance matrix \mathbf{V} of \mathbf{e} can be factored as $\mathbf{V}=\sigma^2\mathbf{R}$. The parameter \mathbf{R} represents the spatial autocorrelation matrix formed by correlation coefficient between any two points, which is discussed in Section 2.6. The random variable at a specified location j can also be represented by the following equation:

$$\mathbf{z}_j^{(i)} = \boldsymbol{\mu}_j + \sqrt{\sigma^2} \boldsymbol{\varepsilon}_j^{(i)} \quad (2.19)$$

where $\mathbf{z}_j^{(i)}$ = spatially correlated random variables at location j corresponding to the i th realisation; $\boldsymbol{\mu}_j$ = value of the trend at location j ; σ = standard deviation of the Gaussian random field; and $\boldsymbol{\varepsilon}_j^{(i)}$ = an element in the i th realisation of standard Gaussian random field at location j . The parameter $\boldsymbol{\varepsilon}$ can be obtained using random field generators, which are presented in Section 2.6.

2.4.3 Spatial Variability in Soils with Increasing Trend

A constant trend structure may not be appropriate to simulate in-situ soils in some cases, as the soil strength usually increases with depth (Jaksa *et al.* 1997; Phoon and Kulhawy 1999; Hicks and Samy 2002; Elkateb *et al.* 2003; Kulatilake and Um 2003; Wu *et al.* 2012; Wilson *et al.* 2013). In-situ overburden stress is the main cause for the

increasing trend, while other geotechnical processes (e.g., desiccation, tectonic movements, deltaic deposits and soil deposition) can also affect the trend structure.

The equation proposed by Li *et al.* (2014) is presented as follows:

$$z_n = a(\mathbf{x})\gamma d_0 + z_0 \quad (2.20)$$

where z_n = spatially variable soil property with increasing trend at a certain location; $a(\mathbf{x})$ = rate of change of z_n at a location with spatial coordinates \mathbf{x} , which can be simulated using Eq. (2.19); γ = unit weight of soil; d_0 = depth below the ground surface; and z_0 = soil property at the ground surface. The mean and standard deviation of z_n are corresponding to the depth, which are given as follows:

$$\mu_n(d_0) = z_0 + \gamma d_0 \mu_a \quad (2.21)$$

$$\sigma_n(d_0) = \gamma d_0 \sigma_a \quad (2.22)$$

In the above equations, $\mu_n(d_0)$ and $\sigma_n(d_0)$ denote the mean and standard deviation of z_n in the depth d_0 , respectively, while μ_a and σ_a are the mean and standard deviation of a , respectively.

It should be noted that z_0 is assumed to be constant in Eq. (2.20). However, due to rainfalls, vegetation, traffic loading, etc., uncertainties should be considered in z_0 .

Table 2.5 presents various models for simulating non-stationary random fields summarised by Jiang and Huang (2018). To modify the limitation of the model by Li *et al.* (2014), z_0 is simulated as a lognormal random variable in Eq. (2.20) (Model 3).

For Model 2 proposed by Griffiths *et al.* (2015), the soil property at ground surface, z_0 , is simulated as a 1D lognormal random field, while the rate of increase a is assumed

to be constant. This formulation ignores the uncertainty in the rate of increase. To consider the uncertainty of a in the formulation by Griffiths *et al.* (2015), a is assumed to be a lognormal random variable in a modified model (Model 4). However, it is clear that the above models do not incorporate the uncertainty of the trend component of z_n . To consider the uncertainty in the trend component, Jiang and Huang (2018) developed a new formulation, where a fluctuating component w_n is explicitly considered and simulated as a stationary Gaussian random field. Comparative studies were also conducted among the non-stationary random field models in Table 2.5 in slope reliability analysis by Jiang and Huang (2018). It was found that considering the uncertainty in the trend component, P_f of the slope is marginally influenced by the vertical autocorrelation distance θ_v , while the influences of θ_v on P_f are more pronounced when using other non-stationary RF models without considering the fluctuation of trend.

2.5 Spatial Autocorrelation

When simulating spatially variable soils, spatial autocorrelation of soils should be considered. The spatial autocorrelation can be represented by the autocorrelation function. In the meantime, the autocorrelation distance involved in the autocorrelation function denotes the distance over which the spatially random values would be significantly correlated. In this section, spatial autocorrelation distances for different shear strength parameters of soils are summarised from literature. Some widely used

theoretical autocorrelation functions and autocorrelation functions indicating anisotropic spatial variation are also presented.

2.5.1 Autocorrelation Distance

The autocorrelation distance θ is an essential parameter for simulating spatially variable soils. The correlation between spatial variables at different locations relies on the separation distance. Generally, with larger separation distance, the correlation between spatial variables at any two locations would decrease. As the distance exceeds a threshold, the correlation can be negligible. Such a threshold distance is named “autocorrelation distance” (Vanmarcke 1977). The autocorrelation distance can be obtained using the traditional space average method, where the variance reduction function is considered (Vanmarcke 1977). The formulation for the space average method is given as follows:

$$\theta = \lim_{\bar{\tau} \rightarrow \infty} \bar{\tau} \times \Gamma^2(\bar{\tau}) \quad (2.23)$$

where $\bar{\tau}$ denotes the average sample separation distance; and $\Gamma^2(\bar{\tau})$ represents the variance reduction function, which is given by

$$\Gamma^2(\bar{\tau}) = \frac{2}{\bar{\tau}} \int_0^{\bar{\tau}} \left(1 - \frac{\tau}{\bar{\tau}}\right) \rho(\tau) d\tau \quad (2.24)$$

where τ is the lag distance between two points; and $\rho(\tau)$ is the autocorrelation function, which is discussed in Section 2.5.2. Meanwhile, many modern techniques [e.g., maximum likelihood method (Santra *et al.* 2012) and restricted maximum

likelihood method (Liu *et al.* 2017d; Liu and Leung 2018)] have been developed to obtain more accurate results with small sampling data-sets. For a random field, a larger autocorrelation distance indicates a smoother field. With a smaller autocorrelation distance, the random field would be more ragged. Figure 2.13 shows two typical realisations of isotropic random field with different autocorrelation distances. In Figure 2.13, the darker elements indicate smaller values, while the lighter elements indicate larger values.

The autocorrelation distance of soil properties has been estimated by many researchers (Phoon and Kulhawy 1999; Hicks and Samy 2002; Ching *et al.* 2011), where various methods [e.g., vane shear test (VST); direct shear test (DST); cone penetration test (CPT); and laboratory test] have been used to obtain the sampling values for different soil types. Associated with this, when determining the autocorrelation distance, various theoretical autocorrelation functions are adopted [e.g., single exponential (SNX); squared exponential (SQX); second-order Markov (SMX); cosine exponential (CSX); binary noise (BINX)]. The discussions on autocorrelation function are presented in Section 2.5.2. In this section, the autocorrelation distances for various shear strength parameters [e.g., undrained shear strength (s_u), cohesion (c), friction angle (φ), and cone tip resistance (q_c)] are summarised from literature and presented in Table 2.6 (Li *et al.* 2015; Liu 2018). As can be seen in the table, the horizontal autocorrelation distance for each soil parameter is much higher than the vertical autocorrelation distance, while the vertical

autocorrelation distance is generally in the range of 0.1 m - 6.0 m. This is because the depositional direction of in situ soils is often horizontal, leading to smoother variations of the soil properties in the horizontal direction.

2.5.2 Autocorrelation Function

The autocorrelation function is often adopted to express the autocorrelation between spatially variable soils, which can be obtained from site investigation data using site characterisation techniques [e.g., method of moments (Phoon and Kulhawy 1999a; Baecher and Christian 2003), maximum likelihood method (DeGroot and Baecher 1993), and restricted maximum likelihood method (Lark 2000; Liu *et al.* 2017d)]. The Method of moments is a traditional technique for obtaining the autocorrelation structure of spatially variable soils, the formulation of which is given by

$$\hat{C}(\tau_k) = \frac{1}{2N_k} \sum_{i=1}^{N_k} [z_m(x_i) - \hat{\mu}_z][z_m(x_i + \tau_k) - \hat{\mu}_z] \quad (2.25)$$

where $\hat{C}(\tau_k)$ denotes covariance at τ_k , and the correlation coefficient $\hat{\rho}(\tau_k) = \hat{C}(\tau_k) / \hat{C}(0)$; N_k represents the number of pairs of the observed samples; $z_m(x_i)$ denotes the sample value at location x_i ; and τ_k is the lag distance of the observed samples. When the sample points are distributed irregularly, a binning process can be used, where the separation distance is partitioned into a series of intervals. In this case, an appropriate bin size, τ_k , can be given by

$$\tau_k = \frac{1}{N_k} \sum_{(x_i, x_j) \in N_k} |x_i - x_j| \quad (2.26)$$

The sample size is influential to the estimation of autocorrelation function. Lark (2000) proposed that with a small sample size, the estimated autocorrelation function would be significantly different from the actual one. Especially, as proposed by Kerry and Oliver (2007), when using the method of moments, the required sampling size would be demanding. Besides, in the method of moments, the semivariogram can be influenced by the bin size, which would be more pronounced when the sampling points are irregularly distributed (Liu 2018).

In order to obtain a more accurate autocorrelation structure with a smaller sampling size and irregular sampling space, Liu and Leung (2017d) proposed a framework, where a stationarity check and treatment of site-specific data are implemented. In the framework by Liu and Leung (2017d), the autocorrelation structure is represented by a Matérn autocorrelation model (Matérn 1960), which is a flexible form of autocorrelation function. The Matérn function can be interpreted as an autocorrelation function with a flexible form, where the shape of the function is controlled by a shape parameter ν . For example, when $\nu = 0.5$, the Matérn autocorrelation function would be equivalent to an exponential function, while when ν approaches infinity, a Gaussian function can be obtained (Liu *et al.* 2017d). The parameters in the Matérn autocorrelation function are then obtained by using the restricted maximum likelihood method by Liu and Leung (2017d), the formulation of which is given as follows:

$$L(\theta_p | \mathbf{y}) = -\frac{n_0 - p}{2} \log(2\pi) - \frac{1}{2} \log|\mathbf{V}| - \frac{1}{2} \log|\mathbf{W}| - \frac{1}{2} \mathbf{y}^T \mathbf{V}^{-1} \mathbf{Q} \mathbf{y} \quad (2.27)$$

In Eq. (2.27), $\mathbf{W} = \mathbf{XV}^{-1}\mathbf{X}$ and $\mathbf{Q} = \mathbf{I} - \mathbf{XW}^{-1}\mathbf{X}^T\mathbf{V}^{-1}$, in which \mathbf{I} is the identity matrix and \mathbf{X} is the matrix that contains information on spatial coordinates; θ_p represents the parameters in Matérn function; n_0 denotes the number of sample points, and p represents the number of coefficients in the trend; and $\mathbf{y} = (\mathbf{I} - \mathbf{X}(\mathbf{X}^T\mathbf{X})^{-1}\mathbf{X}^T)\mathbf{z}_m$ is considered for filtering out the trend components so that the covariance estimates of restricted maximum likelihood method are separated from the estimates of the trend structure.

This section also presents some theoretical autocorrelation functions. The theoretical autocorrelation functions can be adopted in geotechnical designs, when the correlation coefficient of the site investigation data by Eq. (2.26) can show an approximate form to a certain theoretical function. Li *et al.* (2015) compared the performance of various theoretical autocorrelation functions in estimating P_f of slopes, where the same settings of autocorrelation distances were considered in every autocorrelation function. They found that the difference of the resulting P_f is small. Table 2.7 shows different 2D theoretical autocorrelation functions, and Figure 2.14 shows different 2D random field patterns generated using various autocorrelation functions. In addition, Table 2.8 shows some 3D theoretical autocorrelation functions, and Figure 2.15 presents different 3D random field patterns. In these figures, the elements indicating higher values are lighter, while the elements indicating smaller values are darker. Li *et al.* (2015a) proposed that the patterns of random fields simulated by exponential function

[Figures 2.14(a) and 2.15(a)], separated single exponential function [Figures 2.14(b) and 2.15(b)], cosine exponential function, and binary noise function are relatively rough, especially in the vertical direction. In contrast, the random fields generated by the Gaussian function [Figures 2.14(c) and 2.15(c)] and the second order Markov function are smoother. The patterns of random fields by different autocorrelation functions can generally reflect the different scenarios of spatially variable soils on site.

2.5.3 Anisotropic Spatial Variation

An isotropic random field is one where the spatial variation patterns in different directions are the same. Such an assumption may not always be realistic, as layered fabric patterns are often observed in natural soils. The autocorrelation distance for anisotropic random fields varies in different directions, which can generally be shown by an ellipse and ellipsoid [Figures 2.16(a) and (b)] for 2D and 3D anisotropy, respectively (Liu 2018). Herein, the autocorrelation represented by the ellipse (or ellipsoid) indicates that anisotropic fields can be obtained through stretching and rotating the coordinates axes of isotropic fields [the autocorrelation can be represented by a circle in two dimensions (or sphere in three dimensions) for isotropic fields].

.

The autocorrelation functions presented in Tables 2.7 and 2.8 are based on

horizontally deposited soils. However, in nature, soils often exhibit various anisotropy patterns of spatial variability. This means, when simulating spatially variable soils, other anisotropy patterns should be considered. As shown previously in Figures 1.1 (b)-(e), there are mainly four types of anisotropic patterns (i.e., horizontal transverse anisotropy, rotated transverse anisotropy, general anisotropy, and general rotated transverse anisotropy). Zhu and Zhang (2013) discussed the significance for considering anisotropic spatial variation of soils and rocks. In their study, the spatial autocorrelation distance was developed as a function of directional angle by modifying the coordinate system, and the 3D autocorrelation functions associated with different anisotropy patterns were then derived. For example, through rotating the coordinate system, the directional spatial autocorrelation distance and the corresponding autocorrelation function can be obtained for rotated transverse anisotropy. The procedures and details in deriving the autocorrelation functions are given by Zhu and Zhang (2013). The 2D exponential autocorrelation functions and Gaussian autocorrelation functions for various anisotropy patterns derived by Zhu and Zhang (2013) are presented in Tables 2.9 and 2.10, respectively. Those formulations have been implemented through random field generation by Zhu and Zhang (2013).

For the 3D anisotropic autocorrelation function, the formulation should be extended from an expression of ellipses to expression of ellipsoids, while the anisotropic autocorrelation function can also be obtained through modification of the coordinate system (Liu 2018). Details for the derivation of 3D anisotropic autocorrelation

functions are given by Liu (2018) and Liu and Leung (2018).

2.6 Random Field Generation

When simulating spatially correlated random variables, $\boldsymbol{\varepsilon}$ in Eq. (2.19) can be generated using many random field generation techniques [e.g., Cholesky decomposition (e.g., Deodatis 1996), the local average subdivision (LAS) method (Fenton and Vanmarcke 1990), the Karhunen - Loeve expansion method (Sudret and Der Kiureghian 2002), and the fast Fourier transform method (Cooley and Tukey 1965)]. In this thesis, the Cholesky decomposition and local average subdivision methods are discussed, as these methods have been adopted in the present research.

2.6.1 Cholesky Decomposition Method

Covariance matrix decomposition methods (e.g., eigen decomposition and Cholesky decomposition) can be used to simulate random fields. The Cholesky decomposition method is a popular method for random field generation in slope reliability analysis (Li *et al.* 2015; Jiang and Huang 2016; Liu *et al.* 2017a; Liu *et al.* 2017b). In the Cholesky decomposition method, the spatial autocorrelation matrix \mathbf{R} is decomposed into a lower triangular matrix and an upper triangular matrix:

$$\mathbf{R} = \mathbf{L}\mathbf{L}^T \quad (2.28)$$

$$\boldsymbol{\varepsilon} = \mathbf{L}\mathbf{s}_i \quad (2.29)$$

where \mathbf{L} is the Cholesky factor of \mathbf{R} ; and \mathbf{s}_i denotes an independent standard Gaussian random vector corresponding to the i th random field realisation. The spatial autocorrelation matrix can be obtained as follows:

$$\mathbf{R}_{d \times d} = \begin{bmatrix} 1 & \rho_{12} & \cdots & \rho_{1d} \\ \rho_{21} & 1 & \cdots & \rho_{2d} \\ \vdots & \vdots & \ddots & \vdots \\ \rho_{d1} & \rho_{d2} & \cdots & 1 \end{bmatrix} \quad (2.30)$$

where d denotes the number of elements in a random field, and ρ_{12} is the spatial correlation coefficient between locations 1 and 2. The correlation coefficient can be obtained by the autocorrelation function, which was discussed in Section 2.5 and shown in Tables 2.7 - 2.10.

The Cholesky decomposition method is relatively simple to implement, especially when anisotropic spatial variation needs to be considered (Zhu *et al.* 2019). That is because using the Cholesky decomposition method, the spatial autocorrelation matrix can be directly involved in random field generation. However, this method may suffer from a computational effort issue when generating a very large spatial autocorrelation matrix with a large domain with many elements (e.g., a very large 3D slope model with a large section and a long slope length).

2.6.2 Local Average Subdivision

The LAS method was first developed by Fenton and Vanmarcke (1990), which is extensively used to simulate random fields in probabilistic slope stability analysis (Griffiths *et al.* 2004; Griffiths *et al.* 2009a; Griffiths *et al.* 2009b; Hicks and Spencer 2010; Hicks *et al.* 2014). LAS can be adopted when the element averaging effect (Griffiths *et al.* 2004) needs to be considered. A subdivision process, in a top-down recursive fashion (Fenton 1990), is involved in LAS, which is simply expressed in Figure 2.17. As shown in the figure, each cell in the domain is divided into two parts at every stage. During the process of LAS, the average of the values of sub-cells is the same to that of the parent cell, meaning that the statistical mean of the random field is maintained. The general procedure for LAS is presented as follows (Fenton and Vanmarcke 1990):

1. Define the global statistics of the global cell Z_1^0 , where the mean is usually set to zero and variance is obtained using local averaging theory (Fenton and Vanmarcke 1990).
2. Divide Z_1^0 into two equal parts (i.e., Z_1^1 and Z_2^1). The mean and variance of the two parts should follow three criteria: (a) local averaging theory should be adopted to obtain the variance for each cell; (b) the two parts need to be correlated; (c) the

average of the two parts is equal to Z_1^0 (i.e., $\frac{(Z_1^1 + Z_2^1)}{2} = Z_1^0$).

3. Divide the two cells obtained in the above step into four equal parts (i.e., Z_1^2 , Z_2^2 , Z_3^2 , and Z_4^2). The mean and variance of these cells should follow four criteria: (a) local averaging theory should be adopted to obtain the variance of each cell; (b) the two sub-cells from a parent cell need to be correlated; (c) the average of the two sub-cells is equal the parent cell (i.e., $\frac{(Z_1^2 + Z_2^2)}{2} = Z_1^1$ and $\frac{(Z_3^2 + Z_4^2)}{2} = Z_2^1$); (d) Z_1^2 and Z_2^2 should be correlated to Z_3^2 and Z_4^2 .

4. Subdivide each cell, until the desired number of elements for the random field is achieved.

Compared with the Cholesky decomposition method, LAS is performed more efficiently when it comes to a very large problem domain with a large covariance matrix. In addition, in LAS, the statistics (e.g., mean and standard deviation) are consistent with the field resolution, while the local averaging effect can be considered. However, the subdivision algorithm itself in LAS is unable to preserve anisotropy, and the directional scales of fluctuation tend to be the minimum for the field during the subdivision process. Therefore, although global anisotropy can be achieved for the field, small neighborhoods of cells tend to be correlated in an isotropic manner at the final resolution of the field (Fenton 1994). This problem can be solved with no loss of

efficiency through extending, compressing or rotating a isotropic field to obtain an anisotropic field (Spencer 2007). The details of LAS is given by Fenton and Vanmarcke (1990), where the formulations for LAS in one, two and three dimensions are presented.

2.6.3 Cross-correlated Random Field

In slope design, many soil properties need to be incorporated, meaning that cross-correlation between different soil properties should be considered. In the literature, the cross-correlation coefficient of cohesion and friction angle, $\rho_{c,\phi}$, observed by Lumb (1970) is in the range of $-0.7 < \rho_{c,\phi} < -0.37$. Yucemen *et al.* (1973), observed it to be $-0.49 < \rho_{c,\phi} < -0.24$, whereas Rackwitz (2000) suggested it around -0.5 . Cross-correlation needs to be incorporated in generating a $c - \phi$ random field.

The corresponding equation is given as follows (Fenton and Griffiths 2003):

$$\begin{bmatrix} \mathbf{z}_c(\mathbf{x}) \\ \mathbf{z}_\phi(\mathbf{x}) \end{bmatrix} = \begin{bmatrix} 1 & 0 \\ \rho_{c,\phi} & \sqrt{1 - \rho_{c,\phi}^2} \end{bmatrix} \begin{bmatrix} \mathbf{z}_{c_0}(\mathbf{x}) \\ \mathbf{z}_{\phi_0}(\mathbf{x}) \end{bmatrix} \quad (2.31)$$

where \mathbf{x} represents spatial coordinates; \mathbf{z}_c and \mathbf{z}_ϕ denote the cross-correlated random fields for cohesion and friction angle, respectively; and \mathbf{z}_{c_0} and \mathbf{z}_{ϕ_0} represent the two independent random fields for cohesion and friction angle, respectively. The details of the procedure for generating cross-correlated random fields is given by Fenton and Griffiths (2003). Figure 2.18 shows a typical example of cross-correlated random fields of cohesion and friction angle with negative

cross-correlation, where a portion with higher values of cohesion tends to correlate with a portion with lower values of friction angle. The influence of cross-correlation between cohesion and friction angle on probabilistic slope stability analyses has been investigated previously (Cho 2010; Jiang *et al.* 2015; Liu *et al.* 2017b; Lo and Leung 2017), and it was found that the probability of failure would increase when the negative cross-correlation coefficient approaches zero.

2.7 Conditional Random Field Simulation and Sobol Index Method

The previous sections have mainly discussed the simulation of unconditional random fields, where the sample values are not considered. In ground investigation, sample values of soil properties are usually obtained. Those sample points can be adopted to generate conditional random fields in probabilistic slope stability analysis. Using such a random field simulation method, the performance uncertainty (e.g., the uncertainty of FS of slopes, footing settlement, and displacement of retaining walls) can be reduced. The performance uncertainty reduction caused by sampling effects is a popular topic in the geotechnical profession in recent years (Li *et al.* 2016; Lo and Leung 2017, 2018). In this section, two conditional random field models are discussed. In addition, a recently developed technique using the Sobol sensitivity index is presented, where the formulations of the traditional Sobol sensitivity index are

extended to consider soil spatial variability by Lo and Leung (2018). Formulations for conditional random field modelling and the Sobol index method are presented, while the benefits and limitations of each method are discussed.

2.7.1 Conditional Random Field

In recent years, many researchers have considered conditional random fields in geotechnical reliability analysis (Lloret-Cabot *et al.* 2012; Kim and Sitar 2013; Lloret-Cabot *et al.* 2014; Li *et al.* 2016b; Liu *et al.* 2017b; Lo and Leung 2017). Kim and Sitar (2013) compared the performance of the conditional random field simulation method with other two methods in slope reliability analysis (i.e., the random value approach that assumes perfect autocorrelation in soils and the unconditional random field simulation method), and found that the conditional random field simulation method can result in lower probabilities of failure than that by the unconditional methods. Li *et al.* (2016b) used the conditional random field simulation method to quantify the magnitude of uncertainty reduction considering different sampling patterns in a 3D slope model, where each of the sampling patterns contains a number of sampling boreholes. It was found that the performance uncertainty can reduce after conditioning, as the known points can provide information to the random field generation and thus reduce the spatial uncertainty.

In this section, two conditional random field models are discussed. The first one is proposed by Frimpong and Achireko (1998), where the Kriging interpolation technique is employed to predict the soil properties at each spatial point, and the corresponding prediction error is simulated by Monte Carlo simulation. Liu *et al.* (2017b) pointed out that, when using this conditional random field model, the relation between sampling space and autocorrelation distance is significant for reduction in performance uncertainty. In some cases, uncertainty reduction may not be achieved with an improper combination of sampling space and autocorrelation distance. This problem is discussed in details in Section 2.7.3. The second conditional random field model was proposed by Lo and Leung (2017) that is based on the matrix decomposition technique, where the spatial autocorrelation matrix after conditioning is considered.

Conditional random field model 1

The conditional random field model proposed by Frimpong and Achireko (1998) is commonly used in geotechnical reliability analyses (Fenton and Griffiths 2008; Lloret-Cabot *et al.* 2012; Lloret-Cabot *et al.* 2014; Li *et al.* 2016b; Liu *et al.* 2017b), which is given as follows:

$$\mathbf{z}_{\text{cr}} = \mathbf{z}_{\text{km}} + (\mathbf{z}_{\text{ur}} - \mathbf{z}_{\text{ks}}) \quad (2.32)$$

where \mathbf{z}_{cr} = simulated conditional random field; \mathbf{z}_{km} = Kriging field based on the measured values (known values) at sampling locations; \mathbf{z}_{ur} = simulated unconditional random field; and \mathbf{z}_{ks} = Kriging field based on the simulated values of the

unconditional random field, \mathbf{z}_{ur} , at sampling locations.

Kriging interpolation techniques can provide unbiased predictions for the unknown spatial points. In Kriging interpolation, the spatial autocorrelation of soil properties can be represented by the autocorrelation function (Tables 2.7 - 2.10). Equations for determining the Kriging predictor in a specific location, $\mathbf{z}_{kr,j}$, are as follows (Odeh *et al.* 1995):

$$\begin{bmatrix} \mathbf{V}_s & \mathbf{1} \\ \mathbf{1}^T & 0 \end{bmatrix} \begin{bmatrix} \boldsymbol{\beta}^{(i)} \\ \lambda \end{bmatrix} = \begin{bmatrix} \mathbf{V}_{su}^{(i)} \\ 1 \end{bmatrix} \quad (2.33)$$

$$\mathbf{z}_{kr,j} = \boldsymbol{\mu}_k(\mathbf{x}) + (\mathbf{z}_m - \boldsymbol{\mu}_{k0})^T \boldsymbol{\beta}^{(j)} \quad (2.34)$$

In the above equations, \mathbf{V}_s denotes the covariance matrix between sampled points; $\mathbf{1}$ is a column vector of all ones; $\boldsymbol{\beta}^{(i)}$ represents the vector of weights of the known data to the i th element with $\sum_{j=1}^n \boldsymbol{\beta}_j^{(i)} = 1$, and λ is a Lagrange multiplier; \mathbf{V}_{su} is the spatial covariance matrix between sampled points and unsampled points; \mathbf{z}_m is a vector containing the values of sampled points; $\boldsymbol{\mu}_{k0}$ represents the expected values of the trend at the sampled locations; and $\boldsymbol{\mu}_k(\mathbf{x})$ is the trend structure with spatial coordinates \mathbf{x} . Within the framework of regression Kriging, the trend structure is determined through regression analysis. When the trend structure is assumed to be a constant value, Eq. (2.34) can be reduced as follows, which is the formulation of ordinary Kriging (OK):

$$\mathbf{z}_{kr,j} = \mathbf{z}_m^T \boldsymbol{\beta}^{(i)} \quad (2.35)$$

Conditional random field model 2

The conditional random field model proposed by Lo and Leung (2017) is based on the matrix decomposition method. In this thesis, the Cholesky decomposition method [i.e., Eqs. (2.28) and (2.29)] is adopted. When the random field \mathbf{z} is conditioned into \mathbf{z}_{cr} , the conditional covariance matrix \mathbf{V}_{cond} and the conditional spatial autocorrelation matrix \mathbf{R}_{cond} can be given as follows:

$$\mathbf{V}_{\text{cond}} = \text{cov}[\mathbf{z} | \mathbf{z}_{\text{cr}}] = \mathbf{V}_{\text{u}} - \mathbf{V}_{\text{su}}^{\text{T}} \mathbf{V}_{\text{s}}^{-1} \mathbf{V}_{\text{su}} \quad (2.36)$$

$$\mathbf{R}_{\text{cond}} = \mathbf{D}^{-1/2} \mathbf{V}_{\text{cond}} \mathbf{D}^{-1/2} \quad (2.37)$$

In Eq. (2.36), \mathbf{V}_{u} represents the covariance matrix between unsampled points. Within the framework of OK, the diagonal term of \mathbf{V}_{cond} , σ_z^2 , represents Kriging prediction variance at unsampled points. In Eq. (2.37), \mathbf{D} is a $n_u \times n_u$ diagonal matrix formed by the n_u terms in σ_z^2 (n_u denotes the number of unsampled locations). When simulating a conditional random field by this model, \mathbf{R} in Eq. (2.28) is replaced by \mathbf{R}_{cond} , $\boldsymbol{\mu}_j$ in Eq. (2.19) is replaced by the Kriging predictor, $\mathbf{z}_{\text{km},j}$, and $\sqrt{\sigma^2}$ in Eq. (2.19) is replaced by $\sqrt{\sigma_{z,j}^2}$. The difference between the two conditional random field simulation methods will be elaborated upon Chapter 5.

2.7.2 Sobol Sensitivity Index

The contribution of each input parameter to the variance of system response can be

quantified using the Sobol sensitivity index (Sobol 2001) in a physical model, where each input is considered as a random variable (Lo and Leung; Lo 2019). In recent years, the Sobol sensitivity index has been adopted in geotechnical probabilistic analysis (Mollon *et al.* 2011; Houmadi *et al.* 2012; Miro *et al.* 2014). In these studies, soils are assumed to be homogeneous in each profile, meaning that the spatial variability of soil property is not considered. Since the original Sobol index formulation should be based on independent random variables, soil spatial variability cannot be incorporated. To solve this issue, Lo and Leung (2018) extended the original formulation of the Sobol index to consider the cross-correlation between random variables, where the response surface method is adopted to represent the model response. Using the Sobol index method by Lo and Leung (2018), the spatially variable soil properties can be represented by cross-correlated random variables at different spatial points. Based on this concept, the Sobol index value at each location can then be calculated, leading to a Sobol index map in a problem domain. In a Sobol index map, the location associated with the maximum Sobol index value indicates the most influential point to the variance of the system response (i.e., the optimal sampled location). Furthermore, with the use of Sobol index, the magnitude of uncertainty reduction associated with a certain sampling pattern can be obtained, while the mean and standard deviation of the system response can also be calculated (Lo and Leung 2018; Lo 2019).

Definition of Sobol index

In the context of geotechnical engineering, the Sobol index can quantify the contribution of soil properties at certain locations to the variance of a system response (e.g., FS of slopes). In slope reliability analysis, the definition of the Sobol index, $S(\mathbf{X})$, is (Sobol 2001; Lo and Leung 2018; Lo 2019):

$$S(\mathbf{X}) = \frac{\text{Var}_{\mathbf{e}_n} [\text{E}_{-\mathbf{e}_n}(\text{FS} | \mathbf{e}_n)]}{\text{Var}(\text{FS})} = 1 - \frac{\text{E}_{\mathbf{e}_n} [\text{Var}_{-\mathbf{e}_n}(\text{FS} | \mathbf{e}_n)]}{\text{Var}(\text{FS})} \quad (2.38)$$

where $\mathbf{e}_n = (e_1, e_2, \dots, e_n)$ is a vector of residual values corresponding to soil samples from n locations; and $\mathbf{X} = (x_1, x_2, \dots, x_n)$ represents the spatial coordinates of n sample locations. $S(\mathbf{X})$ can be defined as the variance reduction of system response, when the n sample points are given. Subsequently, the reduction is averaged considering all the possible values of soil properties in the n sample locations.

Based on $S(\mathbf{X})$, the magnitude of uncertainty reduction can be given by (Lo and Leung 2018; Lo 2019):

$$\frac{\sigma_{\text{cond}}(\text{FS})}{\sigma_{\text{uncond}}(\text{FS})} = \sqrt{1 - S(\mathbf{X})} \quad (2.39)$$

where $\sigma_{\text{uncond}}(\text{FS})$ denotes the standard deviation of FS by unconditional random field simulation method; and $\sigma_{\text{cond}}(\text{FS})$ denotes the standard deviation of FS after conditioning.

Eigen decomposition

By the formulation of Lo and Leung (2018), the residual \mathbf{e} should be transformed to independent components (denoted by ξ) that represent the random field. This step is necessary because ξ is used to construct the response surface for the system response. The transformation can be achieved through eigen decomposition of the spatial autocorrelation matrix (Lo and Leung 2018). The autocorrelation matrix \mathbf{R} is built using Eq. (2.30). Through eigen decomposition of \mathbf{R} , d eigenvectors and positive eigenvalues could be obtained (the obtained eigenvalues are in descending order in this case), where d is the total number of elements in a random field mesh:

$$\mathbf{R} = \mathbf{H}_d \mathbf{\Lambda}_d \mathbf{H}_d^T \quad (2.40)$$

where \mathbf{H}_d is a matrix of d eigenvectors, and $\mathbf{\Lambda}$ is a diagonal matrix of d eigenvalues. In practice, only $M \ll d$ eigenvectors are retained, which depends on the percentage of total variance that needs to be preserved. \mathbf{e} is related to ξ by the following equation:

$$\mathbf{e} = \mathbf{H} \mathbf{\Lambda}^{\frac{1}{2}} \xi = \mathbf{E} \xi \quad (2.41)$$

where \mathbf{H} is a matrix of retained eigenvectors; and $\mathbf{\Lambda}$ is a diagonal matrix of retained eigenvalues. \mathbf{E} is a $(d \times M)$ matrix, where each row of \mathbf{E} corresponds to all the elements in a random field mesh.

Model response

In order to consider the soil spatial variability, the response surface method is adopted to represent the model response of Lo and Leung (2018). For each setting (slope

geometry, spatial autocorrelation distance, mean and standard deviation of soil property, etc.), hundreds of realisations of random fields are simulated, with the corresponding FS evaluated. The system FS is then represented through a response surface based on the soil strength variation. A 2nd order PCE function [Eq. (2.17)] can be adopted as the response surface. From the PCE coefficients (a_0 , a_i , $a_{i_1 i_2}$) in Eq. (2.17), the variance of FS is given by:

$$\text{Var}(\text{FS}) = \sum_{i=1}^M a_i^2 + \sum_{i_1=1}^M \sum_{i_2=1}^M a_{i_1 i_2}^2 (1 + \delta_{i_1 i_2}) \quad (2.42)$$

Variance after conditioning

Through representing the system FS as a 2nd order PCE, the conditional mean response can be evaluated as a quadratic function (Lo and Leung 2018; Lo 2019):

$$E_{-\mathbf{e}_n}(\text{FS} | \mathbf{e}_n) = r_0 + \sum_{j=1}^n r_j \mathbf{e}_j + \sum_{j_1=1}^n \sum_{j_2=j_1}^n r_{j_1 j_2} \mathbf{e}_{j_1} \mathbf{e}_{j_2}$$

$$\text{where } r_0 = a_0 - \sum_{i_1=1}^M \sum_{i_2=i_1}^M a_{i_1 i_2} G_{i_1 i_2}$$

$$r_j = \sum_{i=1}^M a_i F_{ij}$$

$$r_{j_1 j_2} = \begin{cases} P_{jj} & \text{if } j_1 = j_2 = j \\ P_{j_1 j_2} + P_{j_2 j_1} & j_1 \neq j_2 \end{cases}$$

$$\mathbf{F} = \mathbf{E}_s^T \mathbf{R}_s^{-1}$$

$$\mathbf{G} = \mathbf{F} \mathbf{E}_s$$

$$\mathbf{P} = \sum_{i_1=1}^M \sum_{i_2=i_1}^M a_{i_1 i_2} \mathbf{F}_{i_1}^T \mathbf{F}_{i_2} \quad (2.43)$$

In Eq. (2.43), (a_0 , a_i , $a_{i_1 i_2}$) are coefficients of the 2nd order PCE. \mathbf{E}_s is a ($n \times M$)

matrix consisting of n rows of \mathbf{E} , which corresponds to sample locations. \mathbf{R}_s is a $(n \times n)$ matrix of autocorrelation between sample locations. The variance of the conditional mean is given by:

$$\begin{aligned} & \text{Var}_{\mathbf{e}_n} [E_{-\mathbf{e}_n}(\text{FS} | \mathbf{e}_n)] \\ &= \sum_{i=1}^n \sum_{j=1}^n r_i r_j R_{ij} + \sum_{i_1=1}^n \sum_{i_2=i_1}^n \sum_{j_1=1}^n \sum_{j_2=j_1}^n r_{i_1 i_2} r_{j_1 j_2} (R_{i_1 j_1} R_{i_2 j_2} + R_{i_1 j_2} R_{i_2 j_1}) \end{aligned} \quad (2.44)$$

where R_{ij} is the ij th element of \mathbf{R}_s . The Sobol index, $S(\mathbf{X})$, is then determined by $\text{Var}[E_{-\mathbf{e}}(\text{FS} | \mathbf{e})]$ dividing $\text{Var}(\text{FS})$ [Eq. (2.38)].

2.7.3 Discussion on Methods Considering Sampling effect

The conditional random field simulation and Sobol index methods can be used to quantify the uncertainty reduction after conditioning for a given sampling pattern. The main disadvantage of the conditional random field simulation method is the demanding computational effort when determining the optimal sampling strategy. That is because Monte Carlo simulation should be conducted for all the possible trial sampling patterns in the conditional random field simulation method, and each trial sampling pattern corresponds to hundreds to thousands of calculations. The issue of extensive computational effort would be more pronounced when considering multiple sampling boreholes, as permutations need to be considered. In 3D problems, the computational effort would further increase, due to the long computation time of a 3D slope stability analysis procedure and the larger geometry which results in far more

trial sampling patterns. The Sobol index method by Lo and Leung (2018) is more efficient than the conditional random field simulation method when determining the optimal sampling pattern, especially when more than one sampling borehole or a large problem domain need to be considered. Also, the mean and standard deviation of FS after conditioning can be obtained easily using the Sobol index method. With the mean and standard deviation of FS, the reliability index can be simply estimated using Eqs. (2.10) and (2.11). However, such a method cannot be adopted to obtain the probability of failure and investigate the failure scale and failure mechanism directly, since the response surface involved in the method is constructed by unconditional random field simulation. In engineering practice, quantifying the failure scale is essential in risk assessment, which corresponds to the estimation of potential failure consequence (Li *et al.* 2016a; Liu *et al.* 2017a). In addition, estimating the failure mechanism is significant in controlling the risk caused by landslides (Zhu *et al.* 2015). In this aspect, the conditional random field simulation method is a better option.

On the other hand, Liu *et al.* (2017b) observed that, when the sampling points are quite sparse with small autocorrelation distance ($\theta_v = 2$ m in their study) in a $c - \phi$ slope (Figure 2.19), the standard deviation of FS by the conditional random field model proposed by Frimpong and Achireko (1998) would be higher than that by the unconditional approach. This problem is shown in Figure 2.20, where N_d denotes the number of sampling points, and $N_d = 0$ means the unconditional random field is used. When $N_d = 2$ (points A and E in Figure 2.19), the standard deviation of FS by the

conditional random field simulation method is larger than that by the unconditional random field simulation method. As illustrated by Liu *et al.* (2017b), the reason for this issue is that the Kriging interpolation used in the conditional random field model [Eq. (2.32)] is effective only when at least two known points can be adopted to predict other unknown points within the range of autocorrelation distance. Therefore, as presented in Table 2.11, when the vertical autocorrelation distance increases, the standard deviation of FS by the conditional random field simulation method considering $N_d = 2$ would be smaller than that by the unconditional random field simulation method ($N_d = 0$). This is because with a higher vertical autocorrelation distance, more unknown points can be predicted effectively by the known points. Hence, Liu *et al.* (2017b) concluded that the problem of $\sigma_{\text{cond}}(\text{FS}) > \sigma_{\text{uncond}}(\text{FS})$ by the conditional random field model (Eq. 2.32) is caused by the improper establishment of the sample distance to autocorrelation distance. Liu *et al.* (2017b) did not investigate this issue systematically, and the reasons for such a problem were not discussed in detail. The horizontal transverse anisotropy and single exponential autocorrelation function were considered in their research. It is expected that other patterns of soil spatial variability may affect the sampling effects and thus their conclusions. Besides, other reliability analysis methods that can consider sampling effects should be conducted to find out whether this issue can only occur when using the conditional random field model by Frimpong and Achireko (1998). Theoretically, if the conditioning effect is not effective, there should be no uncertainty reduction of system response, meaning that the standard deviation of FS by conditional random field

simulation method would be equal to that by the unconditional random field simulation method. The issue of $\sigma_{\text{cond}}(\text{FS}) > \sigma_{\text{uncond}}(\text{FS})$ by the conditional random field model proposed by Frimpong and Achireko (1998) will be further investigated and discussed in Chapter 5.

2.8 Summary

Geotechnical uncertainty is a well known topic in the civil engineering profession, which cannot be explicitly modeled in traditional deterministic slope stability analysis. In order to consider the uncertainties, probabilistic slope stability analysis methods have been developed by combining probability theories with slope stability analysis techniques. Soil spatial variability is a significant source of geotechnical uncertainties, and its influence on slope reliability has been extensively investigated. To simulate spatially variable soils, unconditional random fields are widely used in the literature (Griffiths and Fenton 2004; Griffiths *et al.* 2009a; Griffiths *et al.* 2009b; Griffiths *et al.* 2009c; Cho 2010; Hicks and Spencer 2010; Huang *et al.* 2010; Li *et al.* 2013; Jha and Ching 2013; Jiang *et al.* 2014; Hicks *et al.* 2014; Jiang *et al.* 2015; Jiang and Huang 2016; Li *et al.* 2016a; Liu *et al.* 2017a; Liu *et al.* 2017b; Liu *et al.* 2018; Varkey *et al.* 2019). In addition, conditional random fields and the sampling effect have been considered in slope reliability analysis in recent years (Kim and Sitar 2013; Li *et al.* 2016b; Liu *et al.* 2017b, etc.).

Non-stationarity and anisotropic spatial variation of soils are often observed. Non-stationary random field models proposed by Li *et al.* (2014), Griffiths *et al.* (2015) and Jiang and Huang (2018) can be adopted to simulate spatially variable soils with an increasing trend with depth. For anisotropic spatial variation of soils, Zhu and Zhang (2013) proposed formulations for various 2D patterns of anisotropic soil spatial variability. Later, Liu (2018) proposed that the 3D anisotropic autocorrelation structure can be obtained through modifying the coordinate system.

To incorporate sampling data in slope reliability analysis, the conditional random field simulation and Sobol index methods can be used. However, both methods have their limitations. For example, the computational effort of the conditional random field simulation method is extensive when determining the optimal sampling pattern. Such an issue would be more pronounced for a 3D slope problem or a problem considering multiple sampling boreholes. In these situations, the Sobol index method is a more efficient alternative. However, the Sobol index method cannot indicate the probability of failure and information on the failure mass after conditioning. Therefore, the selection of methods should be based on different objectives. The previous study (Liu *et al.* 2017b) observed that the conditional random field simulation method [Eq. (2.32)] may produce the standard deviation of FS higher than that by the unconditional random field simulation method. This finding is contrary to the theoretical basis of conditional random field simulation, and thus it should be further investigated using other methods that can consider sampling effects.

Table 2.1 Recommended thresholds of FS in Hong Kong (GEO, Hong Kong 1984; Cheng and Lau 2008).

		Potential human losses		
		Negligible	Average	High
Potential economic losses	Negligible	1.1	1.2	1.4
	Average	1.2	1.3	1.4
	High	1.4	1.4	1.5

Table 2.2 Various types of $f(x)$ (Cheng and Lau 2008).

Type No.	$f(x)$
1	1
2	$\sin(x)$
3	Trapezoidal shape function
4	Fredlund-Wilson-Fan inter-slice force function (Fan <i>et al.</i> 1986)
5	Corps of Engineering inter-slice force function (Corps of Engineering 2003)
6	Lowe-Karafiath inter-slice force function (Lowe and Karafiath 1960)

Table 2.3 Reliability index β , probability of failure P_f and corresponding expected performance level (U.S. Army Corps of Engineers 1997).

Reliability index β	Probability of failure P_f	Expected performance level
1.0	0.16	Hazardous
1.5	0.07	Unsatisfactory
2.0	0.023	Poor
2.5	0.006	Below average
3.0	0.001	Above average
4.0	0.00003	Good
5.0	0.0000003	High

Table 2.4 P_f by RLEM and RFEM with mean and COV of s_u equal 25 kPa and 0.7 respectively considering isotropic random fields by 1,000 Monte Carlo simulations.

θ (m)	RLEM (Bishop method)	RLEM (Janbu method)	RFEM	Difference between RLEM (Bishop method) and RFEM	Difference between RLEM (Janbu method) and RFEM
3	0.4140	0.5530	0.4380	5.8 %	20.8 %
6	0.4195	0.5210	0.4110	2.0 %	21.1 %
10	0.4120	0.4850	0.4050	1.7 %	16.5 %
50	0.3960	0.4490	0.4070	2.8 %	9.4 %

Table 2.5 Non-stationary random field models (Jiang and Huang 2018).

Model No.	Formulations	Parameters	Assumption on parameters	References
1	$z_n = z_0 + a\gamma d_0$	z_0 a	Constant Stationary random field	Li <i>et al.</i> (2014)
2	$z_n = z_0 \frac{\mu_{z_0} + a\gamma d_0}{\mu_{z_0}}$	z_0 a	Stationary random field Constant	Griffiths <i>et al.</i> (2015)
3	$z_n = z_0 + a\gamma d_0$	z_0 a	Random variable Stationary random field	Modified from Li <i>et al.</i> (2014)
4	$z_n = z_0 \frac{\mu_{z_0} + a\gamma d_0}{\mu_{z_0}}$	z_0 a	Stationary random field Random variable	Modified from Griffiths <i>et al.</i> (2015)
5	$z_n = z_0 + a\gamma d_0 \exp(w_n)$	z_0 a w_n	Random variable Stationary Gaussian random field	Jiang and Huang (2018)

Table 2.6 Autocorrelation distance for shear strength parameters (part 1) (Li *et al.* 2015; Liu 2018).

Soil property	Soil type	Horizontal Autocorrelation distance θ_h (m)	Vertical Autocorrelation distance θ_v (m)	References
s_u	Marine clay, Japan	-	1.3 - 2.7	Matsuo (1976)
	New Liskeard varved caly Clay	46	5	Vanmarcke (1977)
	Sensitive clay, soft clay	20 - 80	2.0 - 6.0	El-Ramly <i>et al.</i> (2003)
	Chicago clay	-	0.79 - 1.25	Xie (2009)
	Saturated clay, Japan	-	1.25 - 2.86	Xie (2009)
	Ankara Clay	-	1.0 - 3.0	Akbas and Kulhawy (2010)
	In situ soils	30 - 60	1.0 - 6.0	Ji <i>et al.</i> (2012)
	s_u by DST	Clay	92.4	1.19 - 1.23
s_u by VST	Marine clay	46	-	DeGroot and Baecher (1993)
	Clay	46 - 60	2.0 - 6.2	Phoon and Kulhawy (1999)
	Clay	46 - 60	2.0 - 6.2	Ching <i>et al.</i> (2011)
	Desiccated Clay	5.83	0.27	Stuedlein <i>et al.</i> (2012b)
q_c	North sea clay	60	-	Hoeg and Tang (1977)
	Sand and Clay	3.0 - 80.0	-	Phoon and Kulhawy (1999)
	Sandy soil	-	0.1 - 1.0	Cheng <i>et al.</i> (2000)
	Clay	-	0.1 - 1.8	Cheng <i>et al.</i> (2000)
	Soft clay	-	0.2 - 2.0	Cheng <i>et al.</i> (2000)
	Taranto clay	-	0.287 - 0.401	Cafaro and Cherubini (2002)
	Sand, clay	-	0.13 - 1.11	Uzielli <i>et al.</i> (2005)
	Tianjin port clay	8.37	0.132 - 0.322	Yan <i>et al.</i> (2009)
	Tianjin port silty clay	9.65	0.095 - 0.426	Yan <i>et al.</i> (2009)
	Tianjin port silt	12.7	0.140 - 1.0	Yan <i>et al.</i> (2009)
	Desiccated Clay	2.97 - 9.90	0.16 - 1.17	Stuedlein <i>et al.</i> (2012a)
	Silty clay	-	0.8 - 6.1	Haldar and Sivakumar Babu (2009)
	Silty clay	1.2 - 2.0	0.45 - 0.5	Firouzianbandpey <i>et al.</i> (2014)
	Clay	10 - 62	1.3 - 4.0	Salgado and Kim (2014)
Sand	35 - 75	2.2 - 3.0	Salgado and Kim (2014)	

Table 2.6 Autocorrelation distance for shear strength parameters (part 2) (Li *et al.* 2015; Liu 2018).

Soil property	Soil type	Horizontal Autocorrelation distance θ_h (m)	Vertical Autocorrelation distance θ_v (m)	References
c	Yan'an silty clay	-	1.47	Ni <i>et al.</i> (2002)
	Jiangzhang silty clay	-	6.47	
	Tongguan silt	-	7.19	
c by DST	Taiyuan silty clay	36.2 - 41.7	0.37 - 0.58	Li <i>et al.</i> (2003)
	Taiyuan silt	41.5 - 45.1	0.6 - 0.84	
	Hangzhou silty clay	40.5 - 45.4	0.52 - 0.75	
	Hangzhou clay	-	0.5 - 0.77	
φ	Yan'an silty clay	-	1.44	Ni <i>et al.</i> (2002)
	Jiangzhang silty clay	-	2.96	
	Tongguan silt	-	1.2	
φ by DST	Taiyuan silty clay	36 - 41.4	0.35 - 0.49	Li <i>et al.</i> (2003)
	Taiyuan silt	41.8 - 45.5	0.54 - 0.92	
	Hangzhou silty clay	40.4 - 45.2	0.49 - 0.71	
	Hangzhou clay	-	0.59 - 0.73	

Note: c and φ represent the cohesion and friction angle under total stress, respectively.

Table 2.7 Theoretical 2D autocorrelation functions (Li *et al.* 2015).

Name	Autocorrelation function
Exponential function	$\rho(\tau_x, \tau_z) = \exp\left(-2\sqrt{\frac{\tau_x^2}{\theta_x^2} + \frac{\tau_z^2}{\theta_z^2}}\right)$
Separated single exponential function	$\rho(\tau_x, \tau_z) = \exp\left[-2\left(\frac{ \tau_x }{\theta_x} + \frac{ \tau_z }{\theta_z}\right)\right]$
Gaussian function (squared exponential function)	$\rho(\tau_x, \tau_z) = \exp\left[-\left(\frac{\tau_x^2}{\theta_x^2} + \frac{\tau_z^2}{\theta_z^2}\right)\right]$
Second order Markov	$\rho(\tau_x, \tau_z) = \exp\left[-4\left(\frac{ \tau_x }{\theta_x} + \frac{ \tau_z }{\theta_z}\right)\right]\left(1 + \frac{4 \tau_x }{\theta_x}\right)\left(1 + \frac{4 \tau_z }{\theta_z}\right)$
Cosine exponential	$\rho(\tau_x, \tau_z) = \exp\left[-\left(\frac{ \tau_x }{\theta_x} + \frac{ \tau_z }{\theta_z}\right)\right]\cos\left(\frac{ \tau_x }{\theta_x}\right)\cos\left(\frac{ \tau_z }{\theta_z}\right)$
Binary noise	$\rho(\tau_x, \tau_z) = \begin{cases} \left(1 - \frac{ \tau_x }{\theta_x}\right)\left(1 - \frac{ \tau_z }{\theta_z}\right) & \tau_x \leq \theta_x \text{ and } \tau_z \leq \theta_z \\ 0 & \text{otherwise} \end{cases}$

Note: τ_x = lag distance between any two points in x - direction; τ_z = lag distance between any two points in z - direction; θ_x = autocorrelation distance in x - direction; θ_z = autocorrelation distance in z - direction

Table 2.8 Theoretical 3D autocorrelation functions.

Name	Autocorrelation function
Exponential function	$\rho(\tau_x, \tau_y, \tau_z) = \exp\left(-2\sqrt{\frac{\tau_x^2}{\theta_x^2} + \frac{\tau_y^2}{\theta_y^2} + \frac{\tau_z^2}{\theta_z^2}}\right)$
Separated single exponential function	$\rho(\tau_x, \tau_y, \tau_z) = \exp\left[-2\left(\frac{ \tau_x }{\theta_x} + \frac{ \tau_y }{\theta_y} + \frac{ \tau_z }{\theta_z}\right)\right]$
Partly separated single exponential function	$\rho(\tau_x, \tau_y, \tau_z) = \exp\left[-2\left(\frac{\sqrt{\tau_x^2 + \tau_y^2}}{\theta_h} + \frac{ \tau_z }{\theta_v}\right)\right]$
Gaussian function	$\rho(\tau_x, \tau_y, \tau_z) = \exp\left[-\left(\frac{\tau_x^2}{\theta_x^2} + \frac{\tau_y^2}{\theta_y^2} + \frac{\tau_z^2}{\theta_z^2}\right)\right]$

Note: τ_y = lag distance between any two points in y - direction; θ_y = autocorrelation distance in y - direction

Table 2.9 Exponential autocorrelation functions for anisotropic spatial variation of soils (Zhu and Zhang 2013).

Patterns	Autocorrelation function
Isotropy	$\rho(\tau_x, \tau_y) = \exp\left(-2\sqrt{\frac{\tau_x^2 + \tau_y^2}{\theta^2}}\right)$
Horizontal transverse anisotropy	$\rho(\tau_x, \tau_y) = \exp\left(-2\sqrt{\frac{\tau_x^2}{\theta_1^2} + \frac{\tau_y^2}{\theta_2^2}}\right)$
Rotated transverse anisotropy	$\rho(\tau_x, \tau_y) = \exp\left\{-2\sqrt{\frac{(\tau_x \cos\alpha + \tau_y \sin\alpha)^2}{\theta_1^2} + \frac{(-\tau_x \cos\alpha + \tau_y \sin\alpha)^2}{\theta_2^2}}\right\}$
General anisotropy	$\rho(\tau_x, \tau_y) = \exp\left\{-2\sqrt{\frac{[\tau_x + \tau_y \tan(\pi/2 - \eta)]^2}{\theta_1^2} + \frac{\tau_y^2}{\theta_2^2}}\right\}$
General rotated transverse anisotropy	$\rho(\tau_x, \tau_y) = \exp\left\{-2\sqrt{\frac{[\tau_x + \tau_y \tan(\pi/2 - \eta) \cos\alpha] + \tau_y \sin\alpha}{\theta_1^2} + \frac{-[\tau_x + \tau_y \tan(\pi/2 - \eta) \cos\alpha] + \tau_y \sin\alpha}{\theta_2^2}}\right\}$

Note: θ_1 represents the major autocorrelation distance, the direction of which is along the bedding orientation. θ_2 represents the minor autocorrelation distance, the direction of which is perpendicular to the bedding. α denotes the rotational angle of strata. η denotes angle between the two principal scales of fluctuation.

Table 2.10 Gaussian autocorrelation functions for anisotropic spatial variation of soils (Zhu and Zhang 2013).

Patterns	Autocorrelation function
Isotropy	$\rho(\tau_x, \tau_y) = \exp\left(-\frac{\tau_x^2 + \tau_y^2}{\theta^2}\right)$
Horizontal transverse anisotropy	$\rho(\tau_x, \tau_y) = \exp\left[-\left(\frac{\tau_x^2}{\theta_1^2} + \frac{\tau_y^2}{\theta_2^2}\right)\right]$
Rotated transverse anisotropy	$\rho(\tau_x, \tau_y) = \exp\left[-\left(\frac{(\tau_x \cos\alpha + \tau_y \sin\alpha)^2}{\theta_1^2} + \frac{(-\tau_x \cos\alpha + \tau_y \sin\alpha)^2}{\theta_2^2}\right)\right]$
General anisotropy	$\rho(\tau_x, \tau_y) = \exp\left\{-\frac{[\tau_x + \tau_y \tan(\pi/2 - \eta)]^2}{\theta_1^2} + \frac{\tau_y^2}{\theta_2^2}\right\}$
General rotated transverse anisotropy	$\rho(\tau_x, \tau_y) = \exp\left\{-\frac{[\tau_x + \tau_y \tan(\pi/2 - \eta) \cos\alpha] + \tau_y \sin\alpha}{\theta_1^2} - \frac{-[\tau_x + \tau_y \tan(\pi/2 - \eta) \cos\alpha] + \tau_y \sin\alpha}{\theta_2^2}\right\}$

Table 2.11 Standard deviation of FS after conditioning when $N_d = 2$ (Liu *et al.* 2017b).

θ_h (m)	θ_v (m)	$N_d = 0$	$N_d = 2$
20	2	0.1033	0.1549
20	12	0.1527	0.1128
20	20	0.1584	0.1025

Entry area for the trial slip surfaces

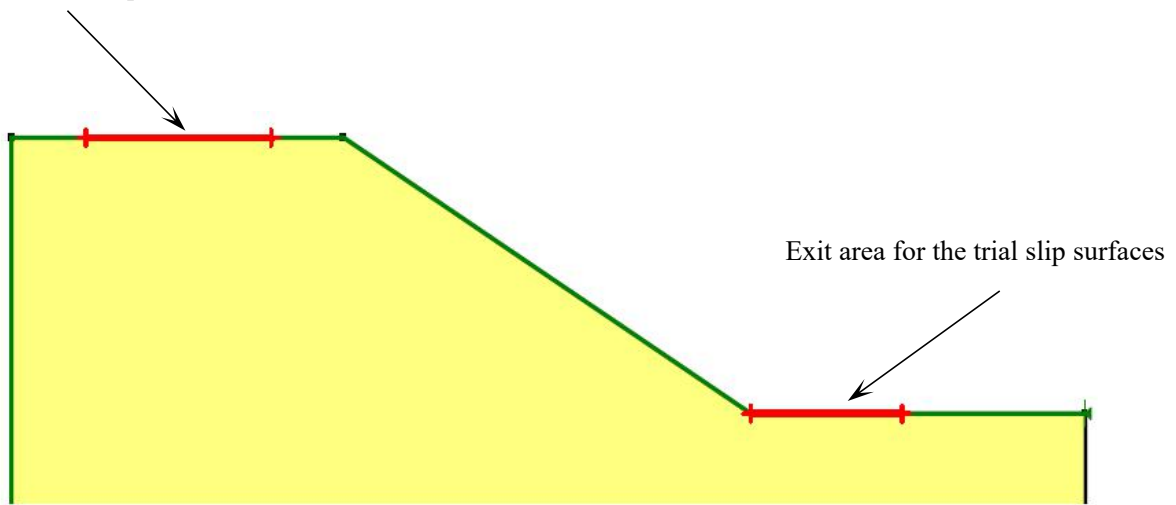


Figure 2.1 Areas for the entry and exit points (GEO-SLOPE International Ltd. 2012).

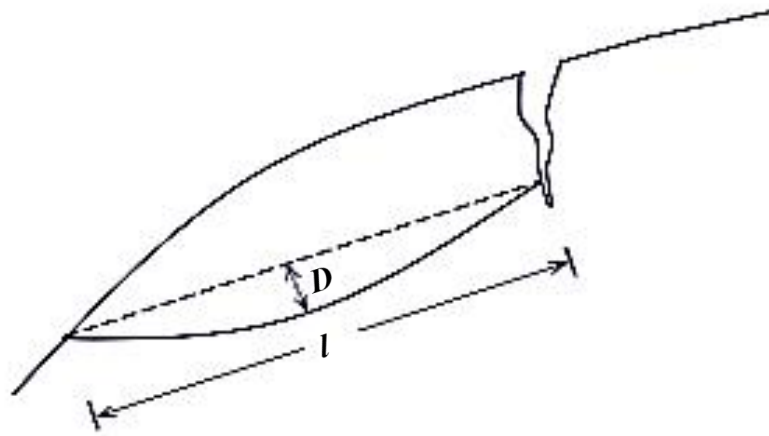


Figure 2.2 Definitions of D and l for the correction factor f_0 (Janbu 1972; Cheng and Lau 2008).

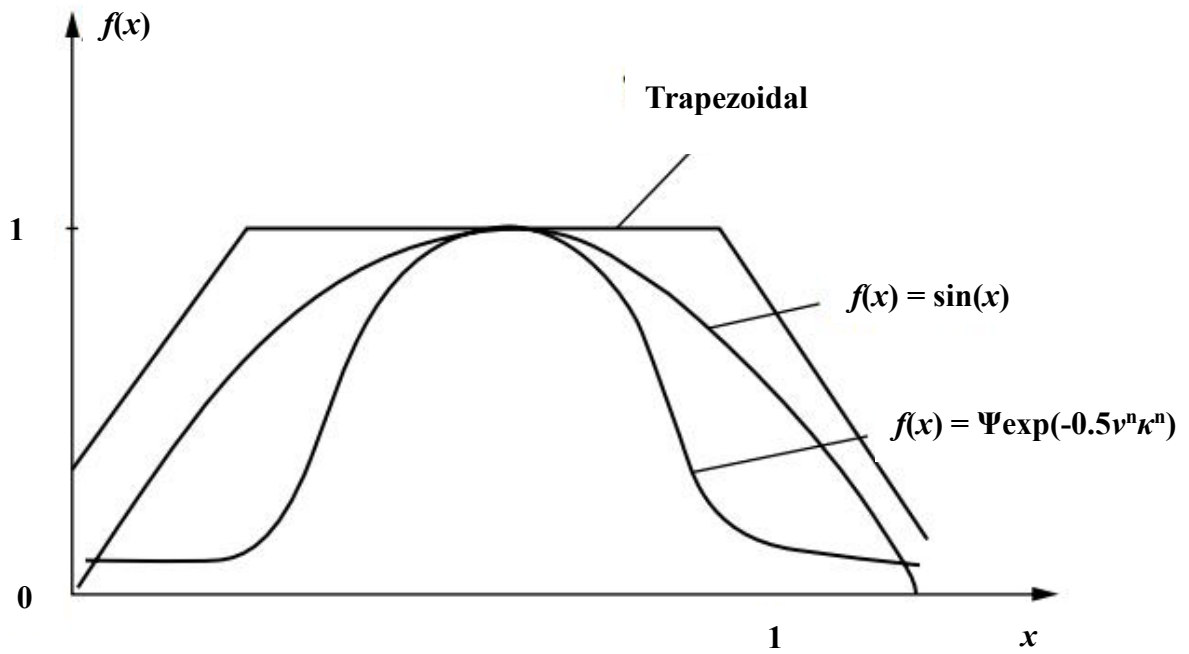


Figure 2.3 Various shapes of $f(x)$ (Cheng and Lau 2008).

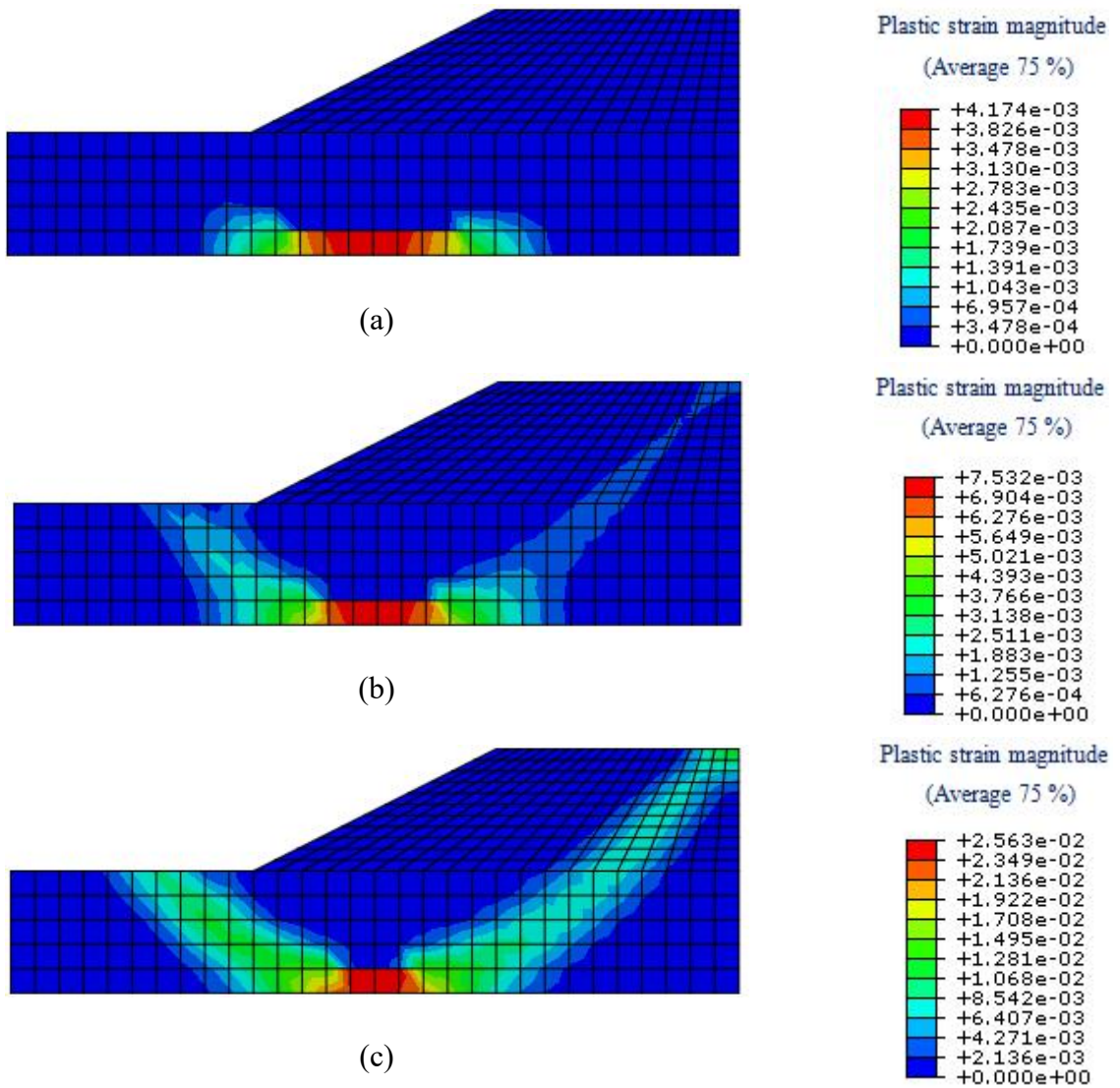
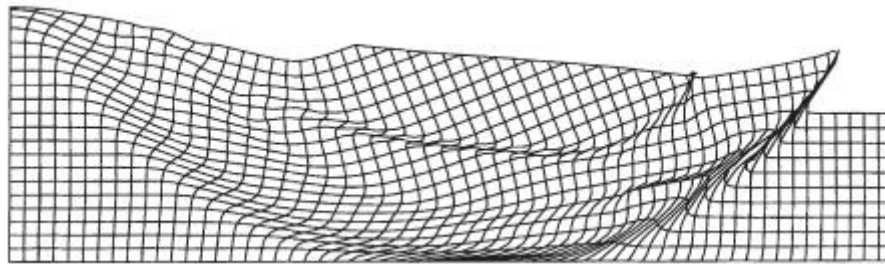
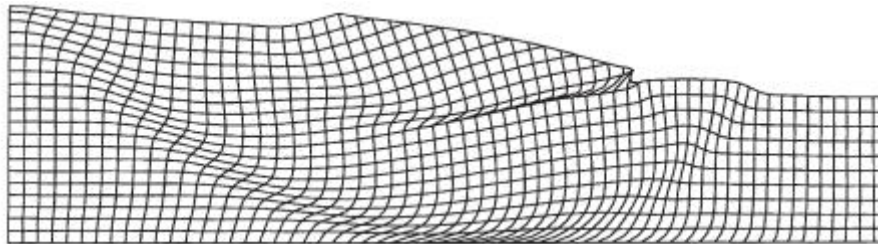


Figure 2.4 Progressive formation of the continuous plastic zone.



(a)



(b)

Figure 2.5 (a) Multiple failure surfaces in a slope with thick weak layer under undrained conditions by SRM; (b) multiple failure surfaces in a slope with weak foundation layer under undrained conditions by SRM (Griffiths and Lane 1999).

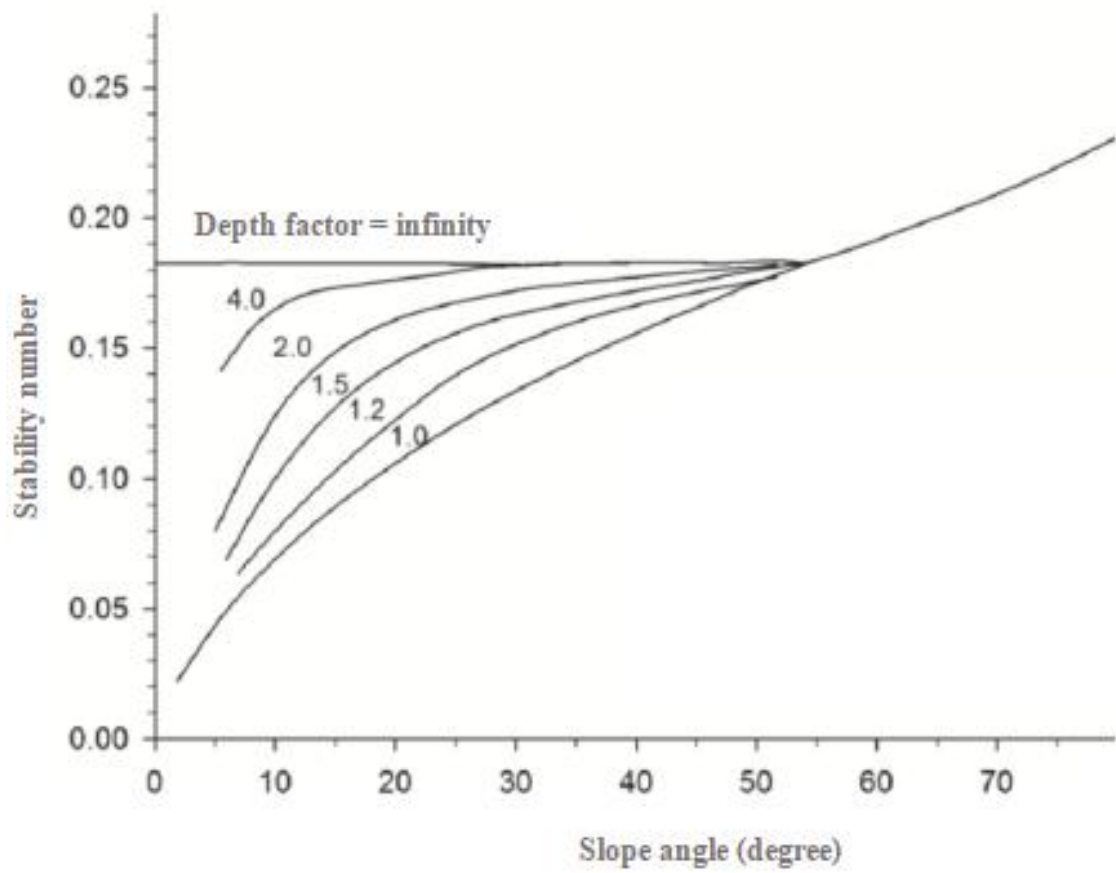


Figure 2.6 Taylor's stability chart for cohesive slope (Taylor 1937; Barnes 1995).

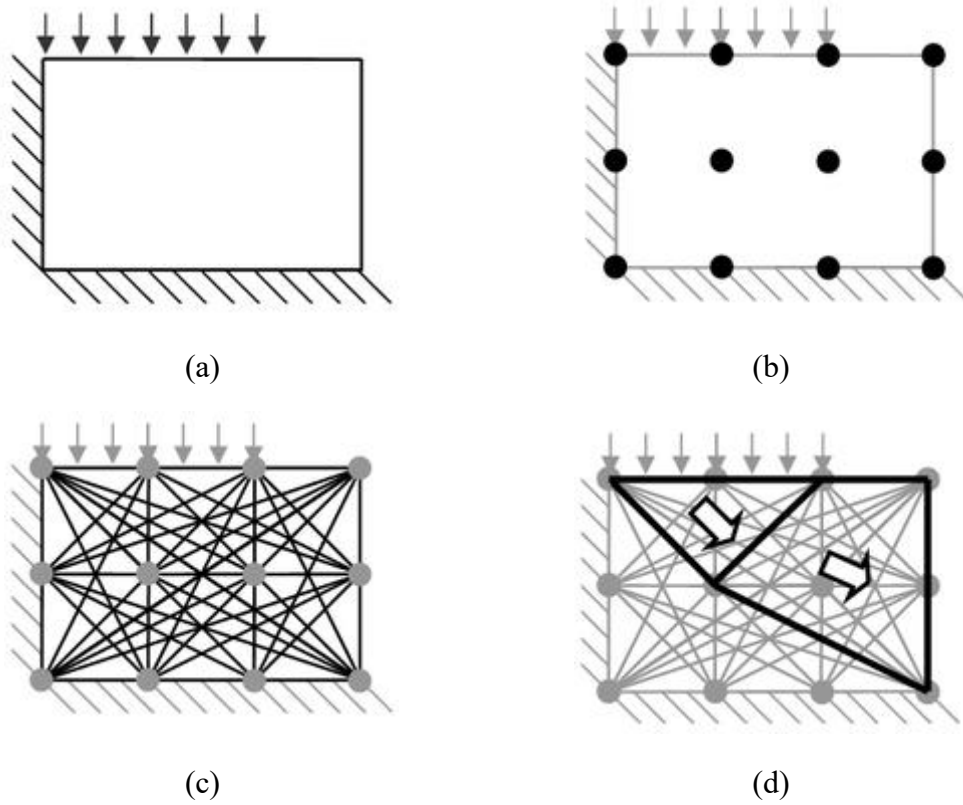


Figure 2.7 Implementation procedure of DLO: (a) define problem domain; (b) discretise the domain by nodes; (c) interconnect the nodes to produce discontinuities; (d) find the critical mechanism with the minimum energy dissipation by optimization (Smith and Gilbert 2010).

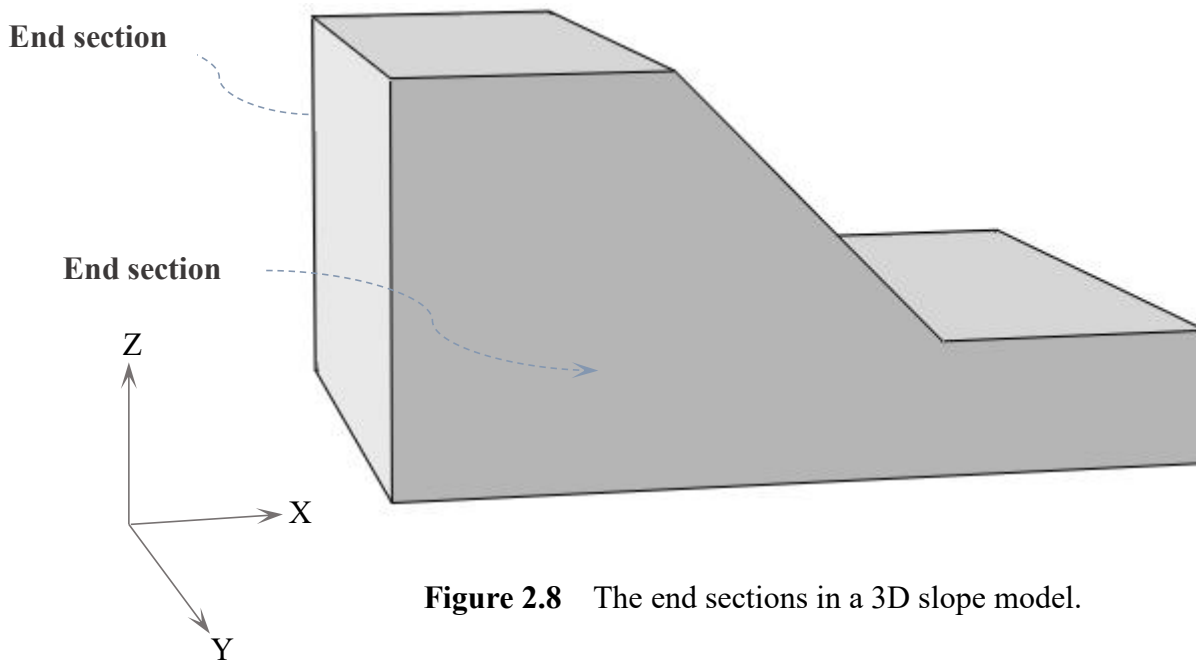


Figure 2.8 The end sections in a 3D slope model.

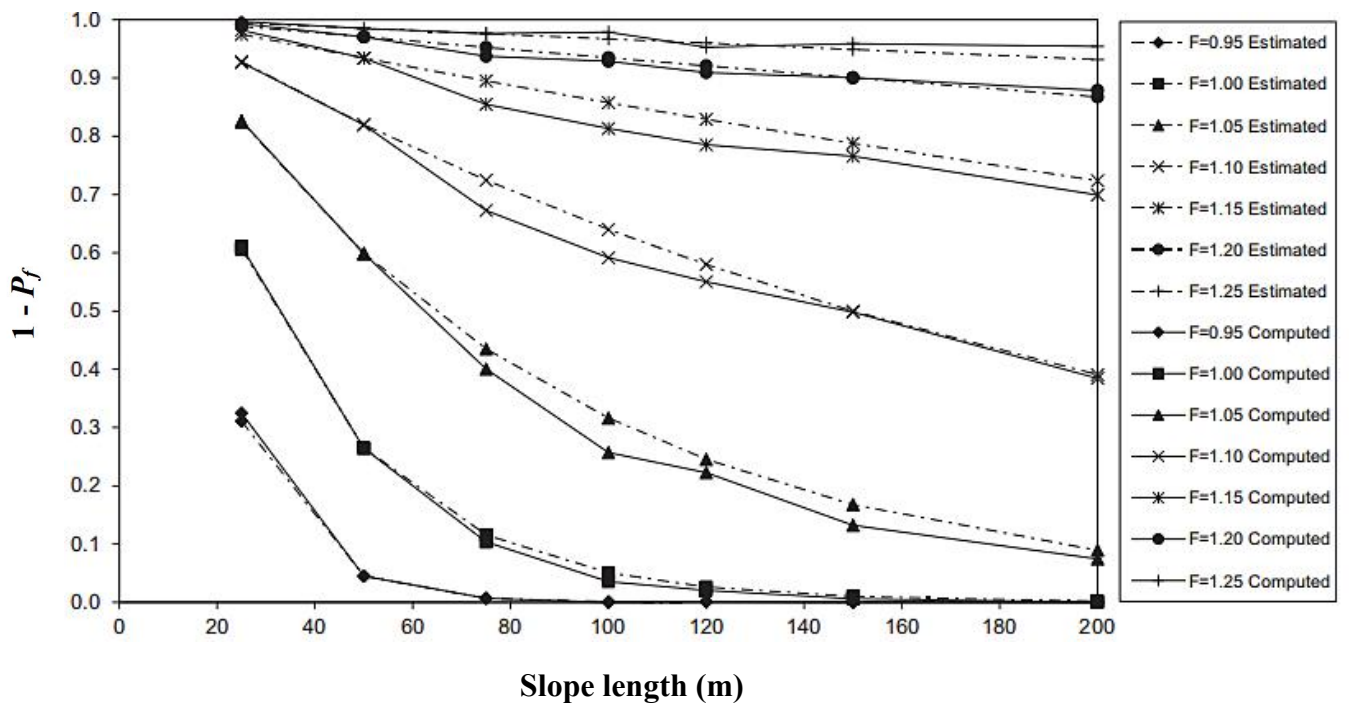
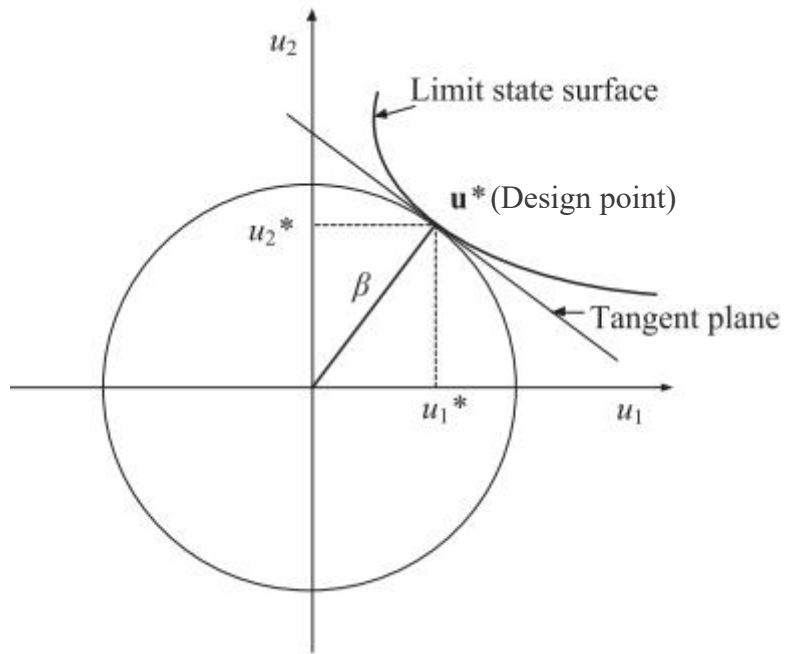
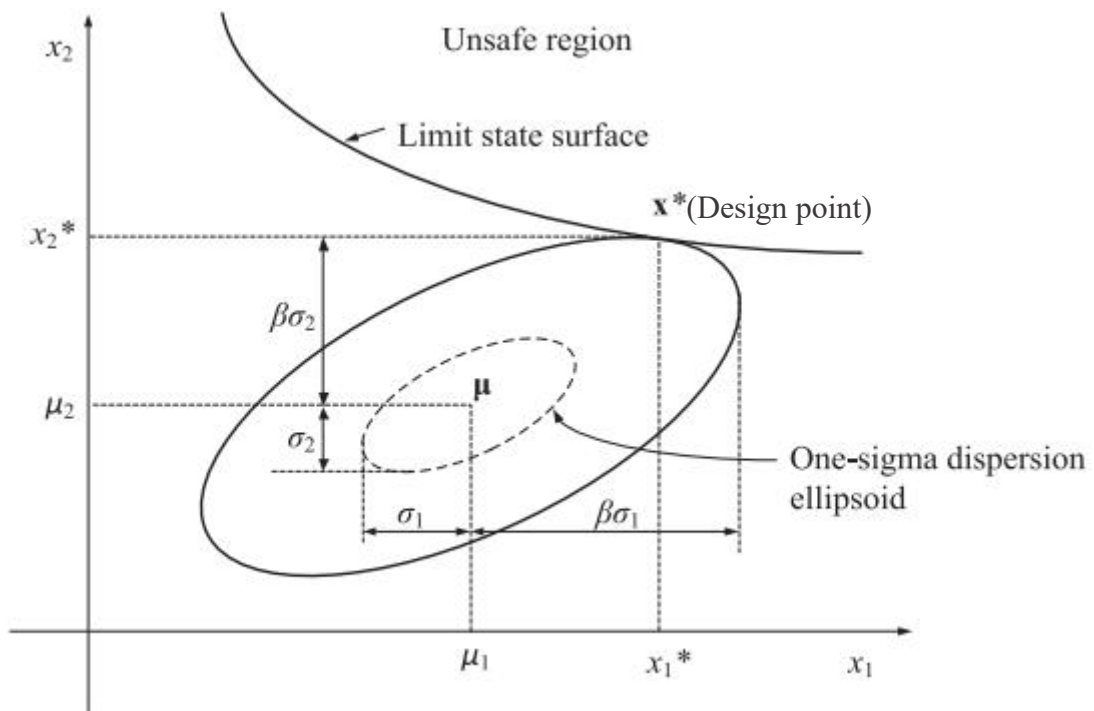


Figure 2.9 Slope reliability versus slope length using random finite element method (RFEM) and the method based on the probability theory (Hicks and Spencer 2010).



(a)



(b)

Figure 2.10 Limit state surface and design point in FORM: (a) in the normal space; (b) in the space of original variable (Ji *et al.* 2019).

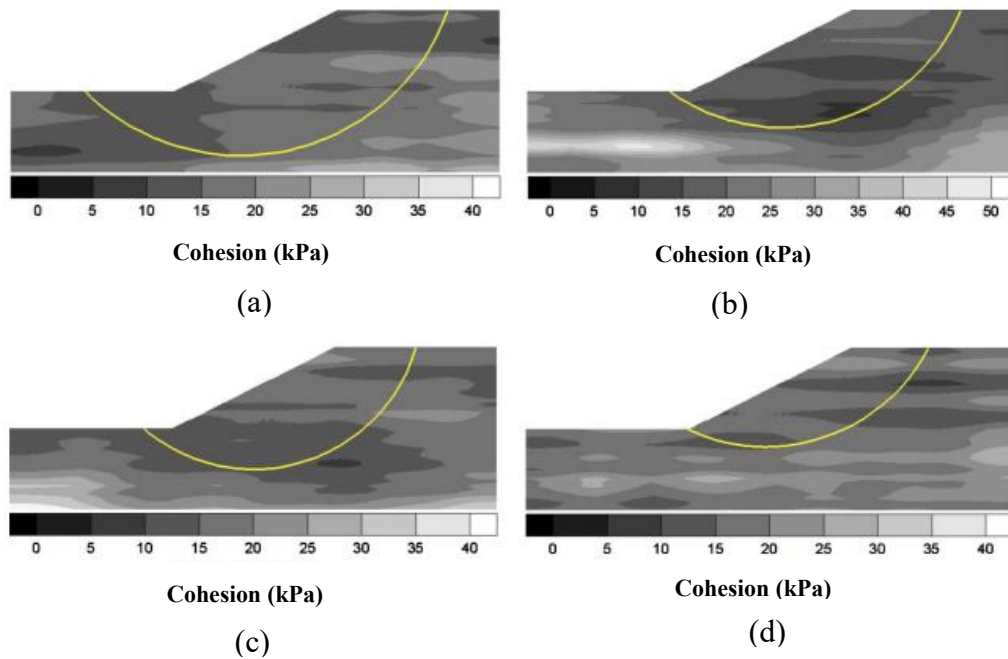


Figure 2.11 Typical realisations of random fields in a slope under undrained conditions and the analysis results by Bishop method ($\theta_h = 20$ m and $\theta_v = 2$ m): (a) FS = 0.905; (b) FS=0.927; (c) FS=0.834; (d) FS=0.983 (Cho 2010).

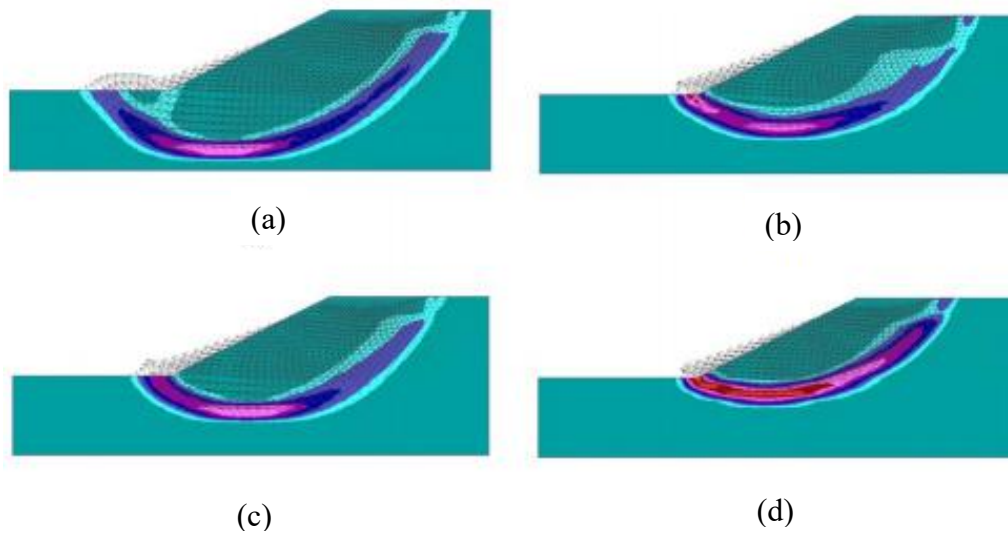
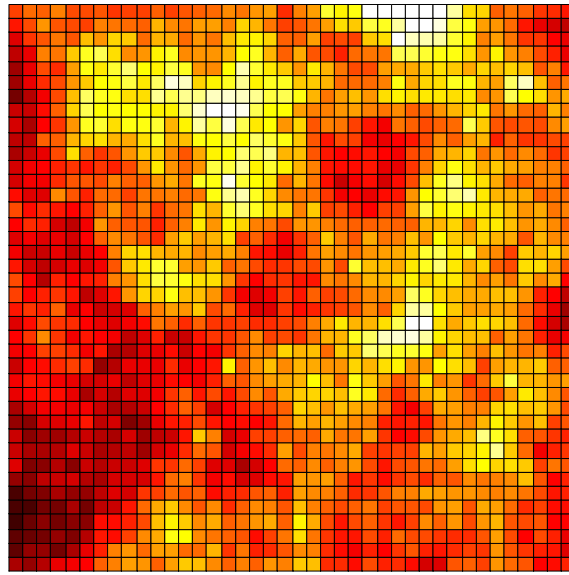
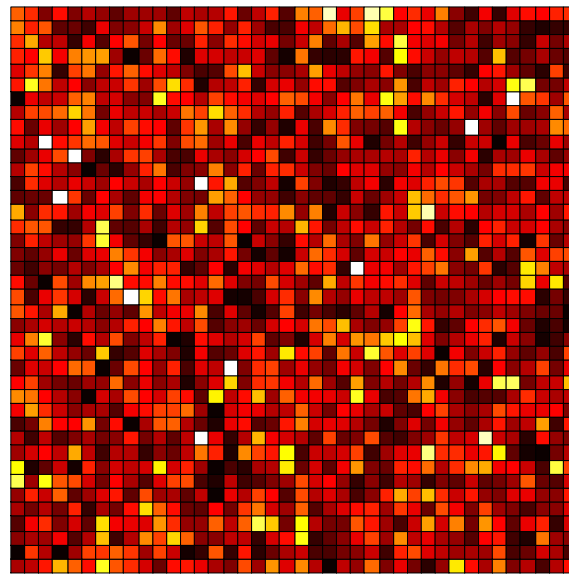


Figure 2.12 Analysis results for the same realisations of random fields in Figure 2.11 by SRM using FLAC: (a) FS = 0.881; (b) FS = 0.889; (c) FS = 0.811; (d) FS = 0.9575 (Cho 2010).



(a)



(b)

Figure 2.13 Isotropic random fields in a square domain of length = 20 m with different spatial autocorrelation distances: (a) $\theta = 15$ m; (b) $\theta = 0.5$ m.

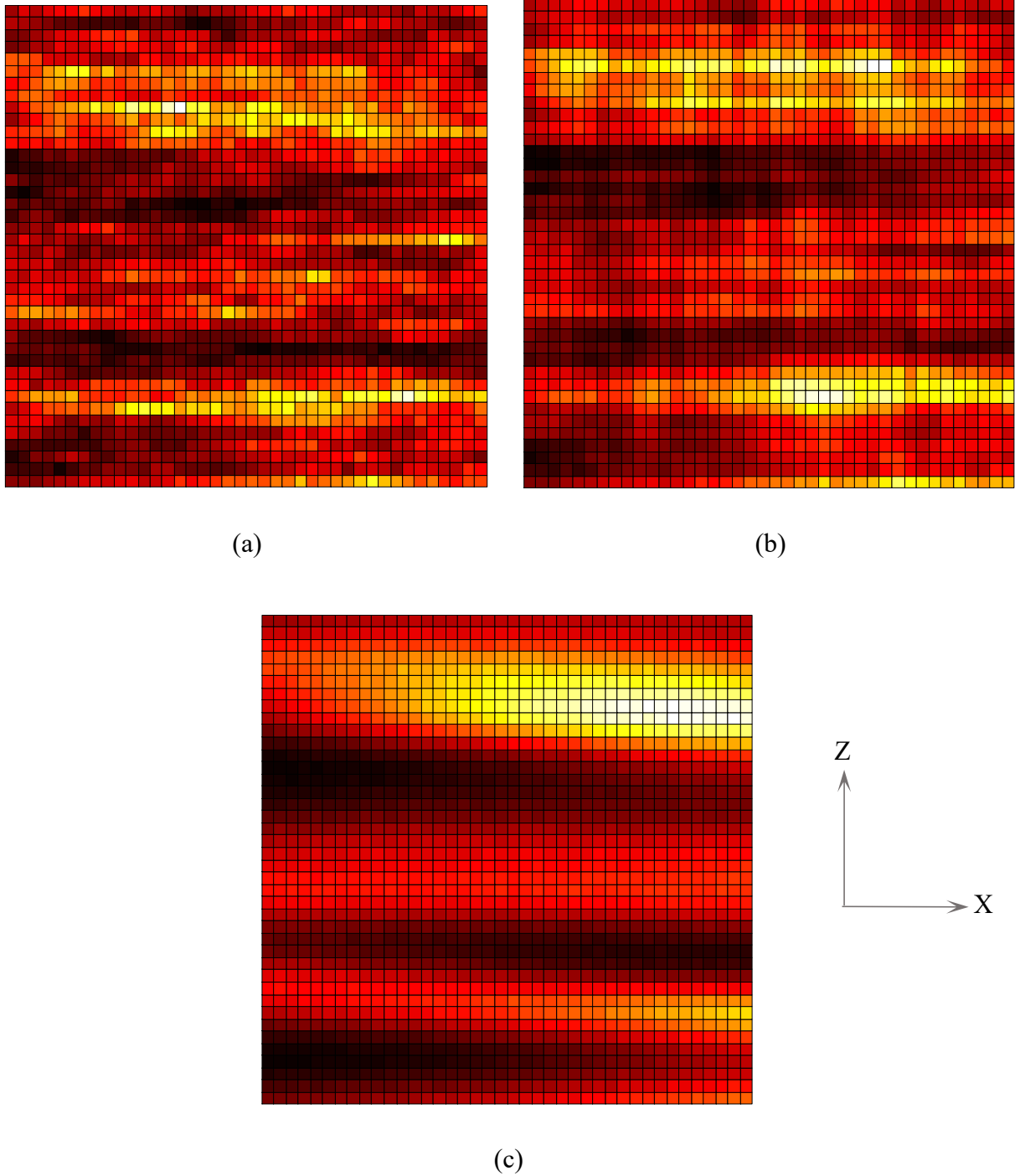


Figure 2.14 Typical realisations of 2D random fields using different autocorrelation functions with $\theta_x = 20$ m and $\theta_z = 2$ m: (a) exponential function; (b) separated single exponential function; (d) Gaussian function.

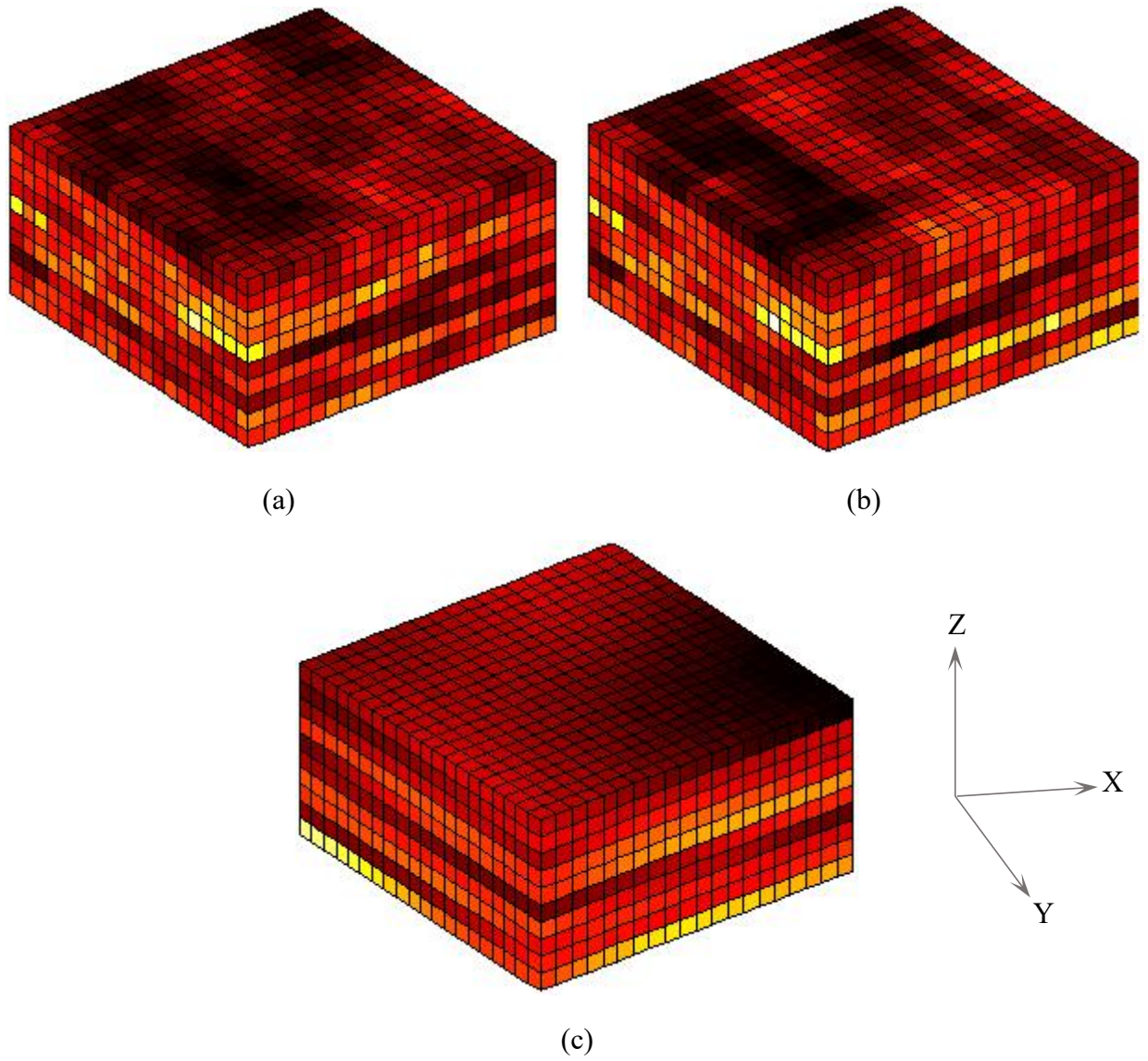
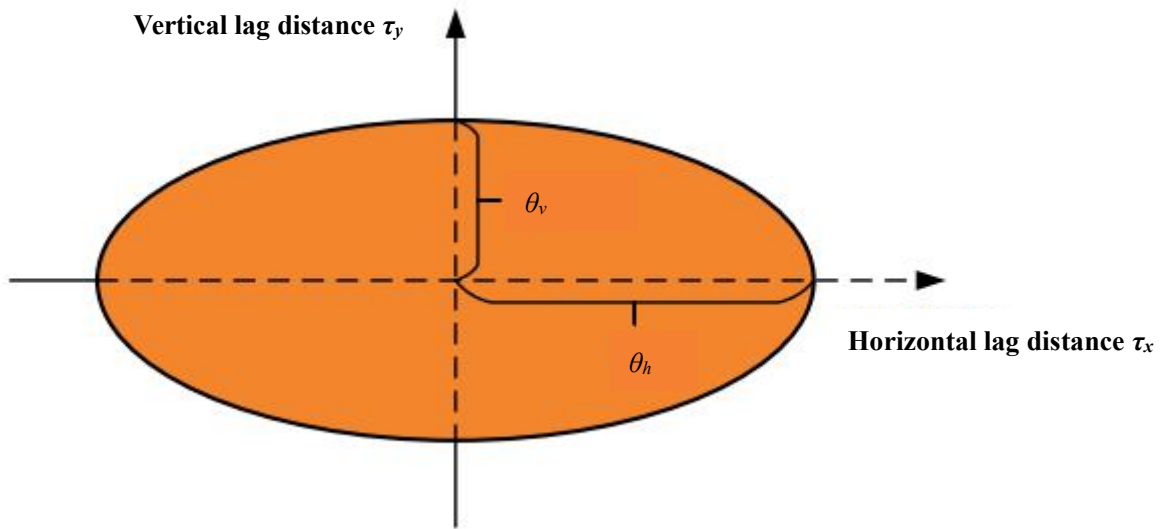
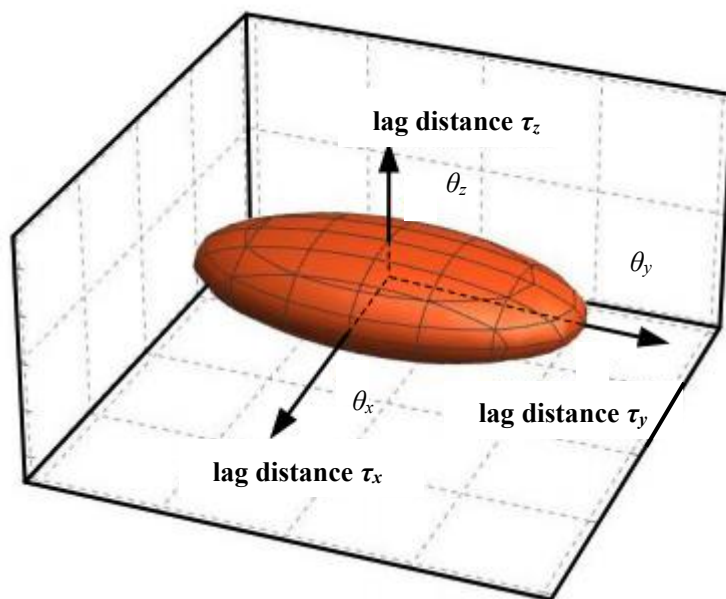


Figure 2.15 Typical realisations of 3D random fields using different autocorrelation functions with $\theta_x = \theta_y = 20$ m and $\theta_z = 1$ m: (a) exponential function; (b) separated single exponential function; (d) Gaussian function.



(a)



(b)

Figure 2.16 Spatial autocorrelation structure: (a) ellipse for 2D soil anisotropy; (b) ellipsoid for 3D soil anisotropy (Liu 2018).

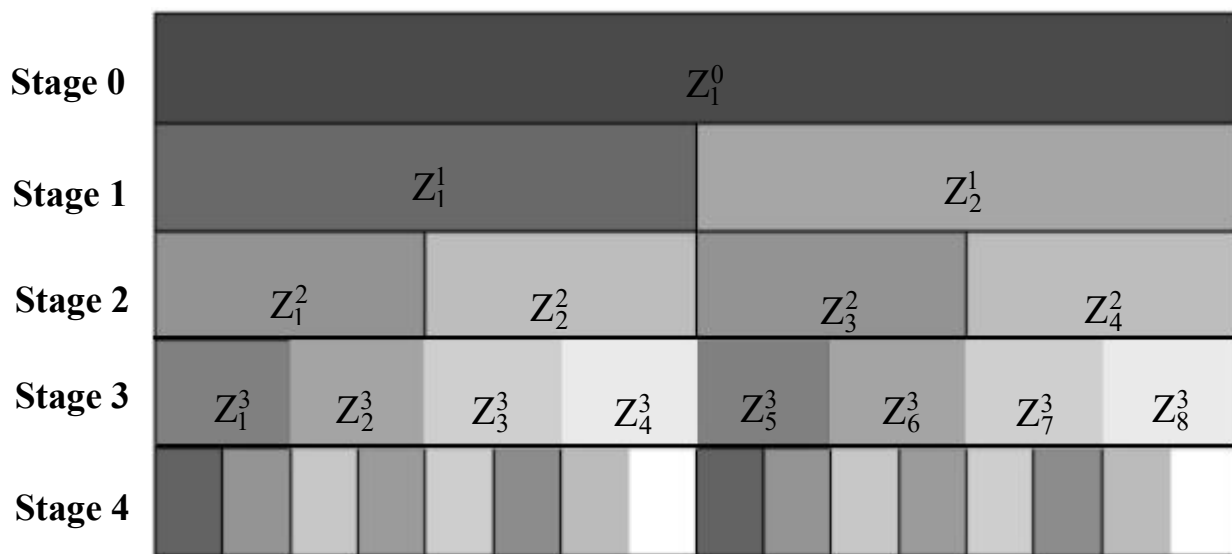
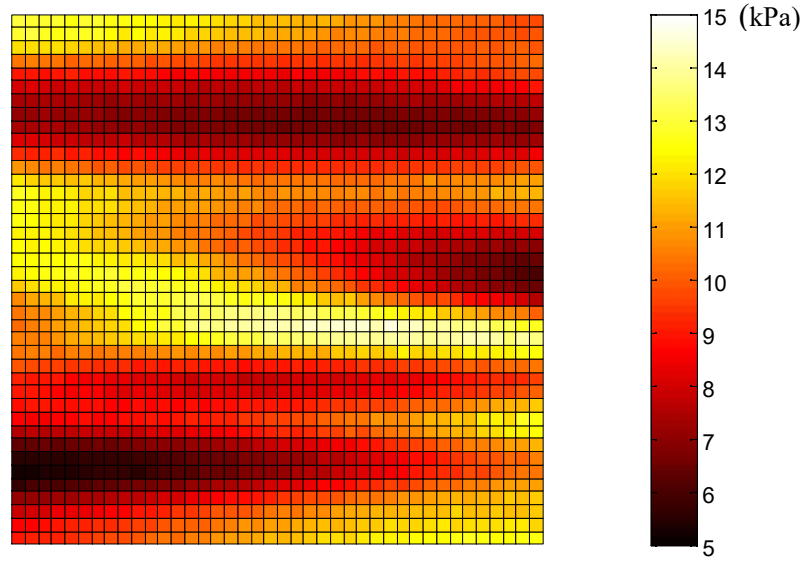
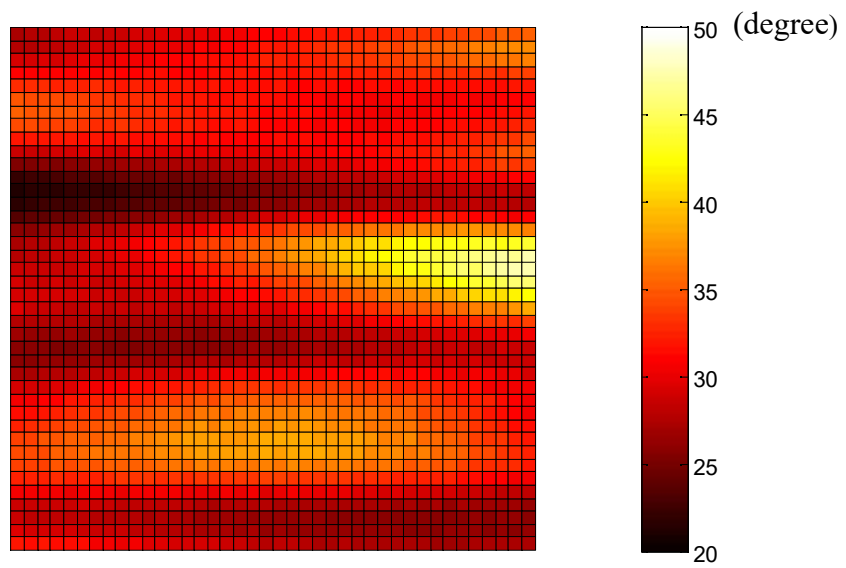


Figure 2.17 Subdivision process in LAS (Fenton and Vanmarcke 1990).



(a)



(b)

Figure 2.18 Realisations of cross-correlated random fields by Gaussian function with $\rho_{c,\varphi} = -0.5$: (a) cohesion; (b) friction angle.

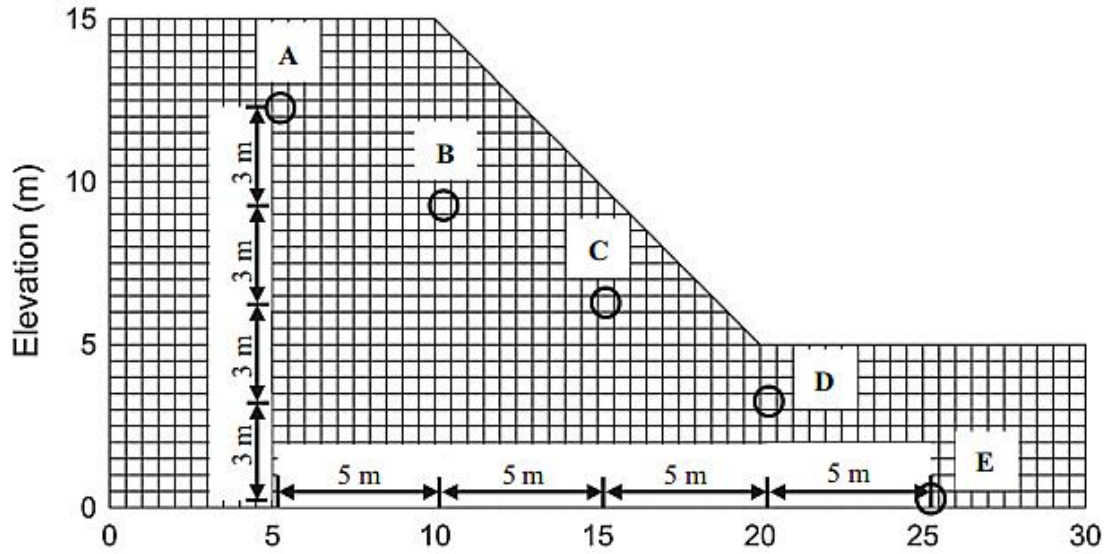


Figure 2.19 A slope under drained conditions and layout of the sampling points (Liu *et al.* 2017b).

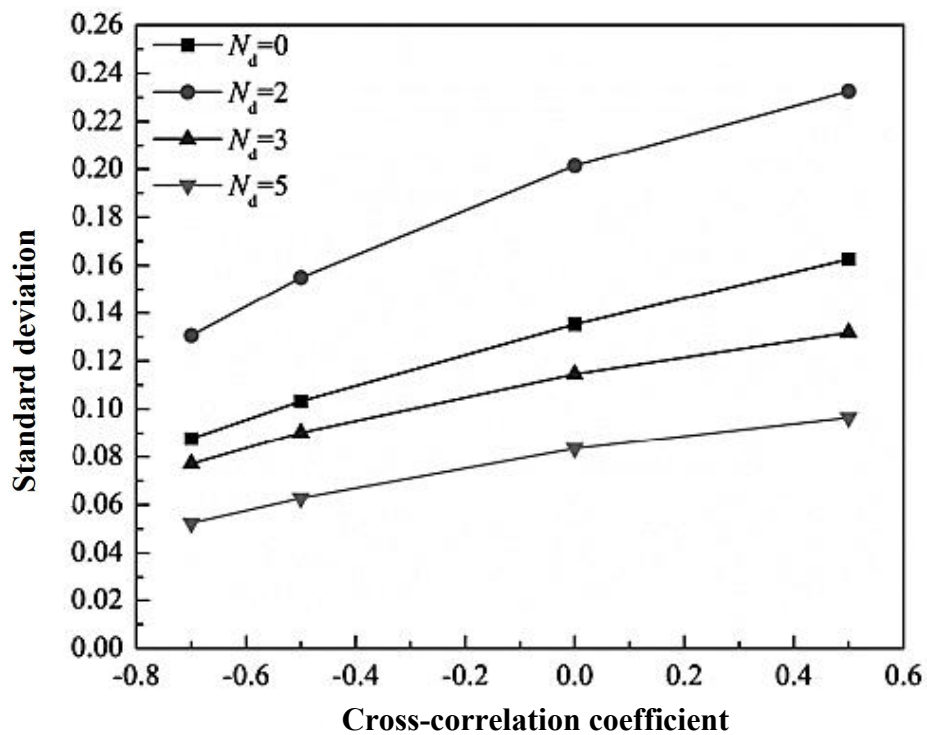


Figure 2.20 Standard deviation of FS by conditional random field simulation method and unconditional random field simulation method versus various cross-correlation coefficients $\rho_{c,\varphi}$ (Liu *et al.* 2017b).

CHAPTER 3 2D Probabilistic Slope Stability Analyses with Rotated Transverse Anisotropy and Non-stationarity in Soil Properties

3.1 Introduction

Due to various geological processes (soil deposition, tectonic movement, etc.), rotated soil strata are often observed in natural slopes (Zhu and Zhang 2013). The influences of rotated transverse anisotropy on slope reliability considering 2D slope models have been investigated previously (Griffiths *et al.* 2009c; Zhu *et al.* 2019), and slopes with a dip direction of strata being opposite to the dip direction of the slope (i.e., reverse slope) were found to have a higher reliability than slopes with a dip direction of the strata being along the dip direction of the slope (i.e., dip slope). Such a finding is consistent with engineering experiences, and the rationale behind that was illustrated through the 2D slope failure mechanism by Griffiths *et al.* (2009c), where the slope failure that occurs along the bedding orientation would result in a smaller FS. Zhu *et al.* (2019) found that the dip angle of strata is influential to the potential failure mechanism of a $c - \varphi$ slope, and the change of failure mechanism would be sensitive to the dip angle of the strata in dip slopes. In the previous studies, a stationary RF was adopted to simulate spatially variable soils with a rotated transverse anisotropy, where the mean and variance of a soil property are assumed to be constant. However, in-situ

soil measurements usually show increasing trends of soil properties for natural soils (Jaksa *et al.* 1997; Hicks and Samy 2002; Elkateb *et al.* 2003; Kulatilake and Um 2003; Wu *et al.* 2012; Wilson *et al.* 2013).

For more realistic simulation of spatially variable soil properties, it is desirable to consider both rotated transverse anisotropy and non-stationarity of soils (i.e., the mean and variance of a soil property vary spatially). To this end, two scenarios are considered in this chapter combining the rotated transverse anisotropy and non-stationarity in soil properties, where the orientations of the increasing trends are different (Figure 3.1). For the type 1 [Figure 3.1(a)], the trend of soil property increases vertically with depth. This usually occurs on originally inclined soil strata, where the soil accumulation is inclined from the beginning. For example, on the edge of sedimentary basin, soils may be deposited obliquely. Also, such a scenario can be found in residual, alluvial, aeolian, and glacial soils, while lava and volcanic debris around a crater are usually found to accumulate in an inclined direction originally. In this case, the increasing trend is caused by in-situ overburden stress. For the type 2 [Figure 3.1(b)], the trend of soil property increases along the direction perpendicular to the bedding, which can be observed in rotated strata caused by tectonic movement or deltaic deposit. For example, the soil bedding was originally in a horizontal orientation and then rotated due to tectonic movements. In this chapter, the two scenarios are considered to estimate the slope reliability. A slope model under undrained conditions is considered (Figure 3.2). Besides, the slope failure mechanism

is investigated by quantifying the depth of slip surface (h_c) under a Monte Carlo framework, where h_c in each Monte Carlo realisation is measured from the slope crest to the rupture surface, as shown in Figure 3.2. Meanwhile, the distributions of slip surfaces obtained in the Monte Carlo process are presented.

3.2 Methodology

3.2.1 Random Limit Equilibrium Method (RLEM)

As mentioned in Section 2.3.4, the random equilibrium method (RLEM) is a probabilistic slope stability analysis approach that combines the traditional limit equilibrium method with a random field. The computational cost of RLEM is lower than that of RFEM, and information in relation to the failure mechanism can be easily obtained by RLEM. When a considering non-circular failure surface, RLEM may suffer from the difficulty in searching the slip surface by global optimization, and convergence problems would arise (Section 2.3.4). Therefore, the Bishop method is used in this chapter. The justification for the use of Bishop method in probabilistic slope stability analysis was discussed previously in Section 2.3.4.

In this chapter, the non-intrusive RLEM is conducted by Slope/W, where the slope stability analysis model can be output by the “.xml” file. That means the random

fields of material properties can be assigned into the slope stability model, by generating and processing “.xml” files in batches. In the current work, the random field is generated by a MATLAB code. The flowchart of the RLEM is shown in Figure 3.3.

3.2.2 Non-stationarity and Rotated Transverse Anisotropy

The random field for rotated transverse anisotropy can be simulated by incorporating the autocorrelation function that represents anisotropic spatial variation of soils. Zhu *et al.* (2019) used the following autocorrelation function to simulate the spatially variable soils under rotated transverse anisotropy. Such an autocorrelation function is also considered in this chapter, where a positive α indicates anti-clockwise rotation and a negative α indicates clockwise rotation:

$$\rho(\tau_x, \tau_y) = \exp \left(-2 \sqrt{ \frac{(\tau_x \cos \alpha + \tau_y \sin \alpha)^2}{\theta_1^2} + \frac{(-\tau_x \cos \alpha + \tau_y \sin \alpha)^2}{\theta_2^2} } \right) \quad (3.1)$$

The non-stationary RF model by Li *et al.* (2014) [Eq. (2.20)] is adopted in this chapter. When soil strength increases with depth, the non-stationary random field considering rotated transverse anisotropy can be directly simulated using Eq. (2.20) coupled with Eq. (3.1), which is named RF Type 1. In addition, soils can be originally deposited in the horizontal orientation and then rotated, leading to a new anisotropy pattern of soil spatial variability. In this situation, the direction of the increasing trend is changed,

and the non-stationary RF Type 2 can be simulated by rotating the non-stationary random field under horizontal transverse anisotropy, the equation of which is derived as Eqs. (3.2a) and (3.2b) for clockwise or anti-clockwise rotations, respectively:

$$z_n = z_0 + a\gamma[(W - x) \sin \alpha_0 + d_0 \cos \alpha_0] \quad (3.2a)$$

$$z_n = z_0 + a\gamma(x \sin \alpha_0 + d_0 \cos \alpha_0) \quad (3.2b)$$

In the above equations, W denotes the slope width (Figure 3.2), α_0 is the rotational angle of the direction of the increasing trend ($0^\circ \leq \alpha_0 \leq 90^\circ$). Figures 3.4(a), (b) and (c) show typical realisations of a stationary RF, RF Type 1 and RF Type 2, respectively.

The non-stationary random field models presented in Table 2.5 are all based on a linearly increasing trend. The Eq. (2.20) derived by Li *et al.* (2014) is based on an empirical function proposed by Kulhawy and Mayne (1999), where the undrained shear strengths for low plasticity and medium plasticity soils increase linearly with depth. Asaoka and A-Grivas (1982) observed that undrained shear strength of an over-consolidated soil can increase linearly with depth.

3.2.3 Implementation Procedure of Non-stationary Random Field Generation

In this chapter, the soil properties are simulated considering rotated transverse anisotropy and non-stationarity. One-thousand Monte Carlo simulations are conducted

for each parametric group (e.g., θ_1 , θ_2 , and α), where the Latin hyper-cube sampling technique is adopted. The procedures for generating the stationary and non-stationary random fields are summarised as follows:

Step 1: Define the inputs for the non-stationary random field, such as probability distribution, mean and standard deviation of a in Eqs. (3.2a) and (3.2b), spatial autocorrelation function, etc.

Step 2: Construct the slope stability model using Slope/W and discretise the domain into elements (Figure 3.2).

Step 3: Extract the mid-point coordinates of each element in the slope domain.

Step 4: Perform stationary random field simulation for a by Eq. (2.19) using the coordinate information obtained in the above step, where Eq. (3.1) is used to represent the spatial autocorrelation.

Step 5: Use Eqs. (3.2a) or (3.2b) to generate N_T non-stationary random fields.

3.3 Case Description

Figure 3.2 shows the slope model investigated in this chapter. The slope height is 15 m, and the slope angle is 45° . To map the random field, the slope domain is discretised into 1365 elements that are mainly squares with 0.5 m length or truncated into triangles along the slope face. This slope is analysed under undrained conditions with the undrained shear strength characterised statistically by a log-normal distribution. When considering a non-stationary RF, the mean and *COV* of a in Eqs. (3.2a) and (3.2b) are equal to 0.3 and 0.4, respectively (Cao *et al.* 2016). As reported by Rackwitz (2000), the undrained shear strength at the ground face (i.e., z_0) was observed to be in the range of 10 - 20 kPa for soft inorganic plastic cohesive soils. Therefore, z_0 is set to 15 kPa. For the purpose of comparison, the mean and standard deviation of the undrained shear strength in the stationary RF are set to be the same as $\mu_n(d_0)$ and $\sigma_n(d_0)$ of RF Type 1 in the mid-height of slope [Eqs. (2.21) and (2.22)], respectively. Such a way to obtain the statistical characteristics for stationary RF is also adopted in Li *et al.* (2014) and Jiang and Huang (2018) when conducting comparative studies between the stationary RF and non-stationary RF. The reason for using such statistical characteristics in the stationary RF is that if the linearly increasing mean of RF Type 1, $\mu_n(d_0)$, is averaged by depth, the averaged result will be equal to the $\mu_n(d_0)$ at mid-depth (Li *et al.* 2014). Therefore, the statistical characteristics at the mid-depth of RF Type 1 seems to be a reasonable assumption with respect to the mean and standard deviation in stationary RF.

The unit weight is assumed to be constant and set as 20 kN/m^3 , as the COV is usually small (Phoon and Kulhawy 1999). For the spatial autocorrelation distance, the major autocorrelation distance is often observed to be much larger than the minor autocorrelation distance. Meanwhile, the minor autocorrelation distance (i.e., vertical autocorrelation distance in horizontally deposited soils) for undrained shear strength is generally in the range of $0.1 - 6 \text{ m}$ (Table 2.6). Therefore, in this study, θ_1 varies as $\{10 \text{ m}, 15 \text{ m}, 20 \text{ m}, 25 \text{ m}, 30 \text{ m}\}$, while θ_2 varies as $\{1.0 \text{ m}, 1.5 \text{ m}, 2.0 \text{ m}, 2.5 \text{ m}, 3.0 \text{ m}, 3.5 \text{ m}, 4.0 \text{ m}\}$. The autocorrelation distances $\theta_1 = 20 \text{ m}$ and $\theta_2 = 2 \text{ m}$ are taken as the base set. The deterministic slope stability analysis is implemented using the Bishop method within Slope/W, with the input shear strength equal to the mean value in the stationary RF (i.e., 60 kPa). The deterministic factor of safety is 1.211. For probabilistic slope stability analysis, the non-intrusive RLEM is adopted, which was presented in Section 3.2.1 above.

3.4 Results

3.4.1 Slope Reliability and Sliding Area

In this chapter, the reliability of the slope is expressed by the reliability index β , which can be estimated using Eqs. (2.10) and (2.11). Since the undrained shear strength is

the only parameter modeled as a random variable, and is assumed to be log-normally distributed, Eq. (2.11) is adopted to determine β .

Figures 3.5 and 3.6 show the change of slope reliability by Eq. (2.11) with θ_1 and θ_2 , respectively. Three dip angles of strata are considered, where $\alpha = 0^\circ$ [Figures. 3.5(a) and 3.6(a)] represents a slope with horizontal bedding; $\alpha = 45^\circ$ [Figures. 3.5(b) and 3.6(b)] represents a dip slope; and $\alpha = -45^\circ$ [Figures. 3.5(c) and 3.6(c)] represents a reverse slope. As can be observed from the figures, the slope reliability marginally changes with major autocorrelation distance for all the slope scenarios, whereas it changes more significantly with minor autocorrelation distance. The possible reason for these observations is that generally a slip surface would pass through several soil strata, and with higher minor autocorrelation distance, a continuous weak zone is easier to be formed through various soil bedding planes. By contrast, a slip surface seldom passes through only one soil bedding especially in the reverse slope and slope with horizontal bedding. Although it is possible for the dip slope to display slip surfaces mainly passing through a single bedding, the major autocorrelation distance is large compared to the 2D slope dimension, and thus its influence on slope reliability is relatively insignificant. According to Table 2.3, the expected performance levels of the slope are significantly different under different RF models, as shown in Figure 3.6 (thresholds for different expected performance levels are indicated by the dashed lines). In addition, it can be noted that for each α the slope reliability under RF Type 1 is higher than that for the stationary RF for all the slope scenarios. Li *et al.*

(2014) found a similar phenomenon when investigating a slope with horizontally deposited soils. For the dip slope ($\alpha = 45^\circ$), the reliability estimated for RF Type 1 is higher than that for RF Type 2. Conversely, for the reverse slope ($\alpha = -45^\circ$), it can be found that RF Type 2 would indicate higher slope reliability than that for RF Type 1. That is, because in the dip slope with RF Type 2, the weak soil layers are close and generally parallel to the slope face, meaning that a slip surface readily forms through the weak zone. By contrast, in the reverse slope with RF Type 2, the strong soil layers are close to the slope toe and the direction of the strata is generally perpendicular to the slope face. That means a slip surface has to pass through several strong soil strata.

Figure 3.7 shows the change of slope reliability with the strata dip angle. Figure 3.8 shows the change in mean of the sliding area (i.e., area of the 2D sliding block) with various dip angles of strata. Generally, in 2D slope stability analyses, the sliding area can be used to represent sliding consequence (Li *et al.* 2016a), which is significant for slope risk assessment. In this work, the major autocorrelation distance is 20 m, and the minor autocorrelation distance is 2 m. As shown in Figure 3.7, considering various dip angles of strata, slope reliability for the reverse slopes (i.e., $\alpha < 0^\circ$) with respect to RF Type 2 is higher than that relevant RF Type 1, while for the dip slopes the reliability for RF Type 1 is higher than that for RF Type 2 in most cases. Such an observation echos the previous findings shown by Figures 3.5 and 3.6. Figure 3.7 also shows that the reliability of the reverse slope is higher than that of the dip slope for each RF scenario. In addition, it can be observed that both the slope reliability and

sliding consequence estimated in RF Type 2 are sensitive to α (Figures 3.7 and 3.8). For a dip slope under RF Type 2, the slip surface would mostly pass through the bedding with the weakest soil strength, meaning that the change of the dip angle of the strata would have a significant influence on the location of the slip surface. Although the slip surface for a reverse slope would pass through several strata, the location of the slip surface can also be significantly influenced by the dip angle under RF Type 2, since the strata with different dip angles would indicate significantly different weak paths of soil strength. As the failure mechanism can be significantly influenced by the dip angle of strata under RF Type 2, the slope reliability and sliding consequence would be sensitive to α . In this case, a slight change in the dip angle of the strata can result in a significant change of slope reliability and sliding consequence, indicating that an accurate estimation for the dip angle of the strata is critical in this scenario. However, the accuracy in estimating the dip angle of the strata is difficult to guarantee for several reasons. For example, when the dip angle of the strata is obtained by geological survey, sometimes the dip angle of the exposed strata may not be the real dip angle of the strata within the slope body. Site characterisation techniques (Section 2.4) can be used to obtain the spatial autocorrelation structure of soils with α , but limited sampling data from drilling boreholes may cause inaccurate estimations. Therefore, when it comes to the soil scenario of RF Type 2, the data set of soil samples needs to be large enough for an accurate estimation of the dip angle of the strata using site characterisation techniques. From Figure 3.8, it can be found that the mean sliding area of a stationary RF is larger than that for RF type 1. With respect

to RF Type 1, soils are weaker in the upper part of slope, leading to slope failures that tend to occur in the upper part. The mean sliding area for RF Type 2 is larger than that for RF Type 1 when $\alpha < 0^\circ$ (i.e., reverse slope) and smaller than that for RF Type 1 when $\alpha > 0^\circ$ (i.e., dip slope). In a reverse slope with respect to RF Type 2, a slip surface must pass through several bedding planes, which usually indicates a large area of sliding mass. On the contrary, in a reverse slope for RF Type 1, weak soils tend to occur in the upper part of the slope, which usually indicates a smaller scale of the sliding mass. For a dip slope with respect to RF Type 2, a slip surface mainly passes through single bedding close to the slope face. In this situation, the scale of the sliding mass would be small. It is also interesting to observe that the critical rotational angles related to the slope reliability are different under different soil scenarios (Figure 3.7). When the undrained shear strength increases along the direction perpendicular to the bedding, the critical angle of rotation is equal to the slope angle (45°).

3.4.2 Depth and Distribution of Slip Surface

The depth of slip surface h_c is investigated using 1000 Monte Carlo simulations. Figure 3.9 shows the histograms and probability distributions of h_c , while Table 3.1 presents the percentage of h_c within each depth range. The multiple slip surfaces obtained by Monte Carlo simulations are presented in Figures 3.11, 3.12, and 3.13. As shown in Figure 3.2, the critical failure surface obtained in the deterministic slope

stability analysis goes deep and passes through the slope toe. However, it is likely that shallow slope failure can occur on a single-layer slope under undrained conditions considering a non-stationary random field, as the weak zone of the soil property could exist in the upper part of slope. Also, rotated transverse anisotropy may lead to shallow slope failures, since the location of the slip surface can be influenced by the dip angle of the strata. For example, in a dip slope for RF Type 2, the slip surface may mainly pass through a single weak soil bedding that is close to the slope face, and thus a shallow slope failure occurs. In this section, the statistical characteristics of h_c are adopted to quantify the occurrence probability of a shallow failure in a single-layer slope under undrained conditions.

For a stationary RF, the deep failure mechanism (i.e., $h_c \geq 10$ m) still mainly dominates, as presented in Figure 3.9(a) and Table 3.1. However, for a non-stationary RF, the probability of occurrence for a shallow failure increases, except for the reverse slope ($\alpha = -45^\circ$) with RF Type 2. For the reverse slope, when RF Type 2 is considered, the deep failure mechanism dominates [Figure 3.9(h) and Table 3.1]. On the contrary, for the dip slope ($\alpha = 45^\circ$), considering RF Type 2 leads to a significant increase in shallow failure [Figure 3.9(e) and Table 3.1]. Generally, the occurrence probability for shallow failure with respect to RF Type 1 is higher than that in a stationary RF for each slope scenario. On the other hand, for RF Type 2 and a stationary RF, it can be observed that shallow failure is more likely to occur on dip slopes, while it is less likely to occur on reverse slopes. Results of h_c by deterministic slope stability analysis

and probabilistic slope stability analysis considering stationary RFs cannot indicate the significant occurrence of shallow slope failures. When considering the non-stationarity of soils, the number of shallow slope failures would significantly increase, especially in a dip slope involving RF Type 2.

Although, the occurrence probability of shallow slope failure in each RF scenario can be obtained by analysing h_c , the different types of shallow slip surfaces cannot be observed by only quantifying the depth of slip surface, as shown in Figure 3.10. In Figure 3.10, the three types of shallow slip surfaces have the same h_c , but their features are different and associated with different locations of entry and exit points (Figure 3.2), which may indicate different formation mechanisms for shallow landslides. Locating the potential slip surface of a slope is significant in risk management, as the slip surfaces passing through the slope face and slope toe would result in significantly different consequences (failure scales), as shown in Figure 3.10. Soil samples from site investigation would be more useful around the location of the potential slip surface. In this work, the entry and exit points of the slip surfaces obtained by Monte Carlo simulations are investigated. Figures 3.11, 3.12 and 3.13 show the distributions of slip surfaces for the slope with horizontal bedding ($\alpha = 0^\circ$), the dip slope ($\alpha = 45^\circ$) and the reverse slope ($\alpha = -45^\circ$), respectively. As shown in Figures 3.11(a) and (b), when the soil bedding is horizontal, the exit points of the slip surfaces are near the slope toe considering a stationary RF, while the exit points are distributed more diffusely along the slope face under a non-stationary RF. For the

entry points of the slip surfaces, there are more entry points close to the slope crest for a non-stationary RF [Figure 3.11(b)] compared with those in a stationary RF [Figure 3.11(a)]. As shown in Figure 3.12, a number of slip surfaces passing through the slope face can be observed for the dip slope, when soil strength increases with depth vertically. By contrast, when undrained shear strength increases along the direction perpendicular to the bedding in a dip slope, exit points of the slip surfaces would concentrate around the slope toe. Generally, entry points of slip surfaces for the dip slope are distributed diffusely on the slope crest under each soil scenario. For the reverse slope (Figure 3.13), the exit points of slip surfaces are centralised at the slope toe for a stationary RF [Figure 3.13(a)], while the entry points of slip surface tend to recede from the slope crest. This observation is similar to that for RF Type 2 [Figure 3.13 (c)]. By contrast, there are more entry points close to the slope crest of RF type 1 in the reverse slope [Figure 3. 13 (b)].

The results of the distributions of slip surfaces show that, when the soil strength increases with depth vertically, a number of slip surfaces passing through the slope surface can be observed. However, when the soil strength increases in the perpendicular direction to the soil strata in the dip slope, most of the slip surfaces still pass through the slope toe. These results indicate the mechanisms of shallow slope failures are different between slopes of RF Type 1 and the dip slopes of RF Type 2. The shallow slip surfaces of RF Type 1 would pass through several soil layers with the exit points generally located on the slope face, which is caused by the existence of

weak soils at shallow depth. For the dip slope of RF Type 2, the shallow slip surfaces mainly pass through a single layer close and parallel to the slope face with weak soil strength, and the exit points are close to the slope toe.

3.5 Summary

In this chapter, the rotated transverse anisotropy is combined with a non-stationary random field to investigate the reliability and failure pattern of a slope under undrained conditions. Two scenarios of non-stationary RF are considered: (a) the trend of the soil property increases with depth; and (b) the trend increases along the direction perpendicular to the soil bedding. A stationary RF is also implemented to simulate spatially variable soils. Performance of the different RF models using probabilistic slope stability analyses is investigated. In addition, different slope scenarios (i.e., slope with horizontal bedding, dip slope, and reverse slope) are considered when estimating the slope reliability and sliding consequence, while the failure mechanism is investigated by analysing the depth and distribution of the slip surfaces. The main findings are summarised as follows:

(1) In slope reliability analysis, the expected performance levels of a slope are significantly different under the different scenarios of RF. Generally, for each α , considering RF Type 1 results in higher slope reliability than that considering a stationary RF. For the dip slope, the reliability of a slope of RF Type 1 is higher than

that for RF Type 2. Conversely, for the reverse slope the slope reliability for RF Type 1 is smaller than that for RF Type 2. In addition, it was found that under RF Type 2, slope reliability and sliding consequence are sensitive to α . When it comes to a slope with soil strength increasing in the direction perpendicular to bedding, the estimation of the dip angle of the strata should be accurate enough for reliable assessments of slope reliability and failure scale. However, the dip angle of the strata obtained from a geological survey may not always be accurate enough, as the dip angle of the exposed strata may not be the dip angle of the strata within the slope body. Site characterisation techniques can be alternatives to obtain the dip angle of the strata, but the accuracy of α obtained by these methods would be affected by limited sampling data. Therefore, for an accurate estimation of the dip angle of the strata the sampling size of the soil samples should be large enough when using site characterisation techniques.

(2) Considering non-stationarity and anisotropic spatial variation of soils, the minor autocorrelation distance is more influential to slope reliability than the major autocorrelation distance in the various scenarios examined. In addition, the reverse slope is found to have a higher reliability than the dip slope under the different RF models treated.

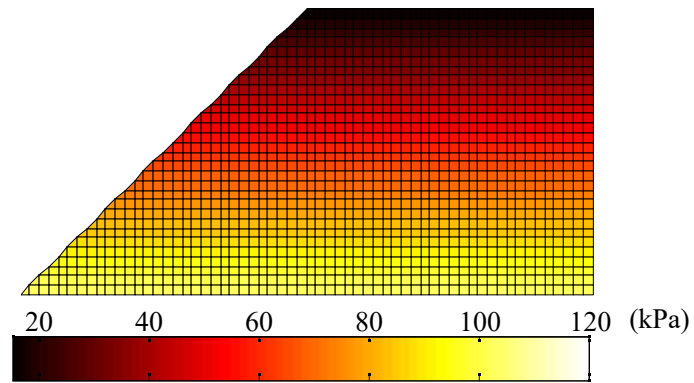
(3) When considering RF Type 1, the percentage of shallow slope failures would increase compared with that in a stationary RF. When RF Type 2 is considered in a

dip slope, the occurrence probability for shallow failure would be high. On the contrary, the deep failure mechanism is dominant in the reverse slope of RF Type 2. The results for the depth of slip surface show that, considering non-stationarity and rotated transverse anisotropy, the number of shallow slope failures can also be significant in a single-layer slope under undrained conditions. By contrast, the potential slip surface of a single-layer slope under undrained conditions can only be deep-seated in the traditional slope stability analysis.

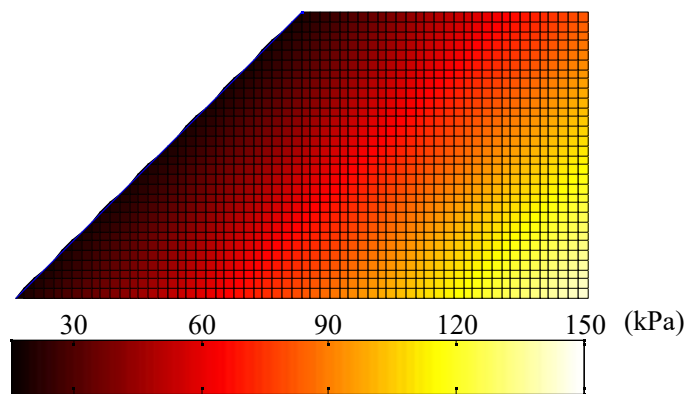
(4) As indicated in the distributions of slip surfaces, a number of slip surfaces passing through the slope surface can be observed of RF Type 1 for each slope scenario, meaning that the reason for shallow failures in slopes under RF Type 1 is the existence of weak soils in the upper section of the slopes. Meanwhile, most of the slip surfaces pass through the slope toe in the dip slope of RF Type 2. This means the reason for shallow failures in the dip slope of RF Type 2 is that the slip surface mainly passes through a single weak soil layer close to the slope face.

Table 3.1 Proportion of h_c within each depth range with $\theta_1 = 20$ m and $\theta_2 = 2$ m.

α (°)	RF type	$h_c < 5$ m	$5 \text{ m} \leq h_c < 10$ m	$h_c \geq 10$ m
0	Stationary RF	0 %	3.8%	96.2%
	Non-stationary RF	0.8 %	42.4%	56.8%
45	Stationary RF	0 %	12.7%	87.3%
	RF Type 1	1%	39%	60%
	RF Type 2	10.1%	71%	18.9%
-45	Stationary RF	0%	0%	100%
	RF Type 1	0.3%	29.2%	70.5%
	RF Type 2	0%	0.6%	99.4%



(a)



(b)

Figure 3.1 Two orientations of the trend for mean shear strength with rotational angle of soil bedding = 45° : (a) Type 1; (b) Type 2.

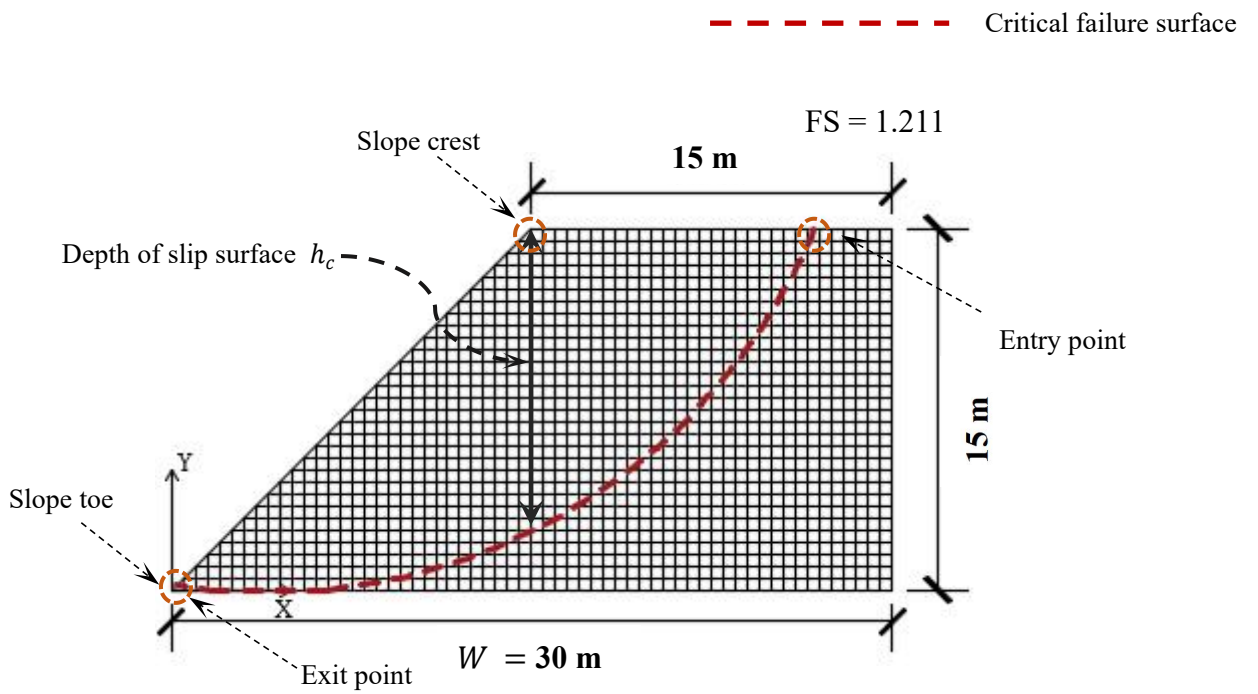


Figure 3.2 Geometry of the slope model.

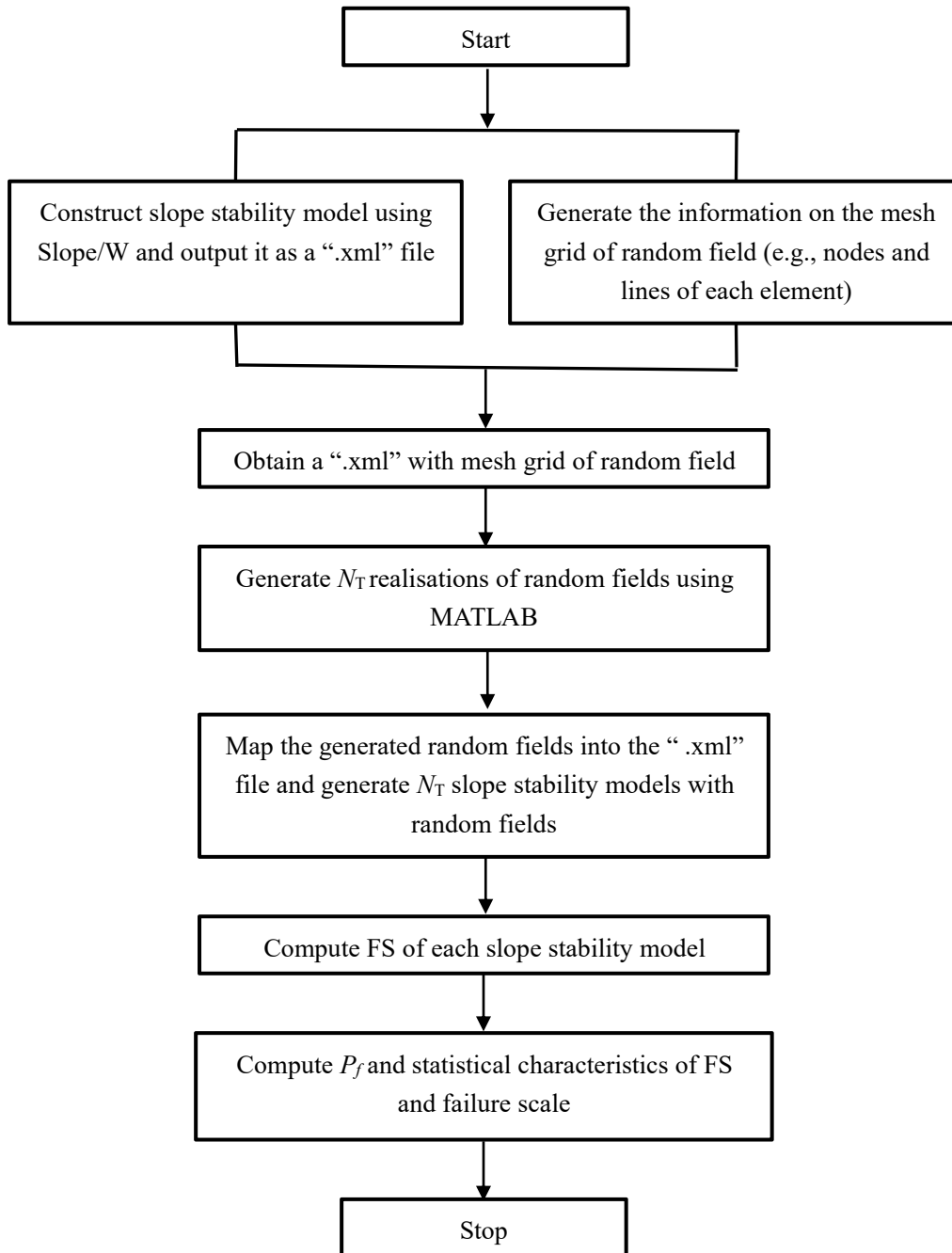
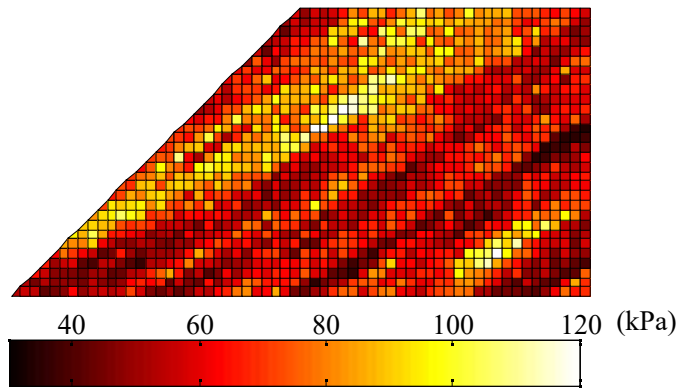
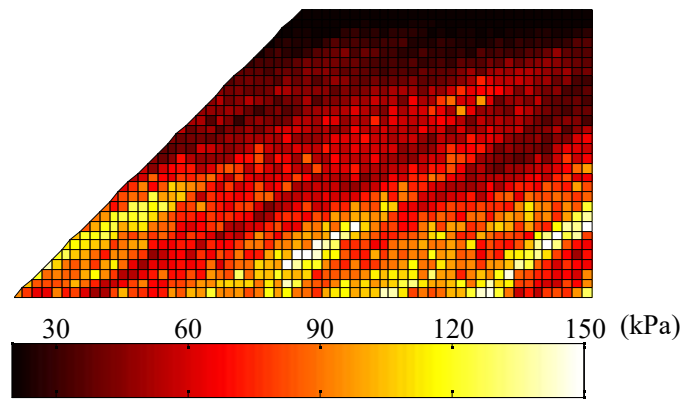


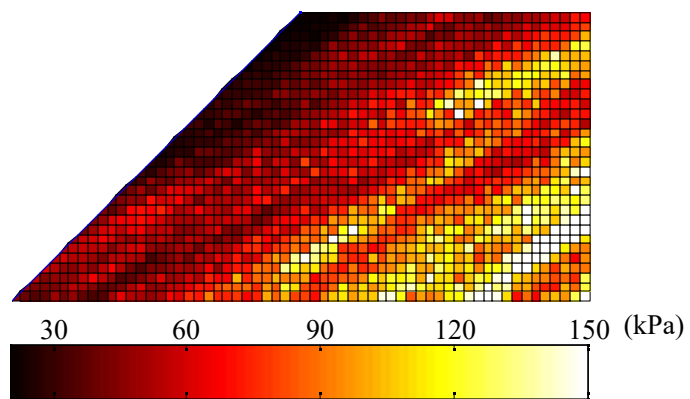
Figure 3.3 Flowchart of non-intrusive RLEM.



(a)

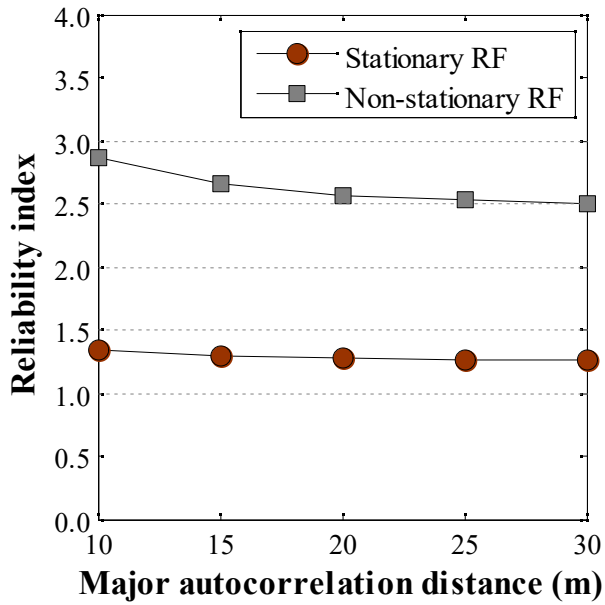


(b)

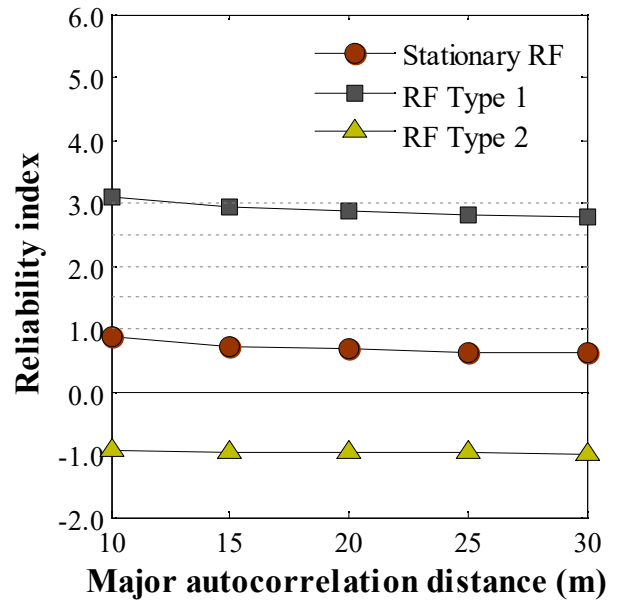


(c)

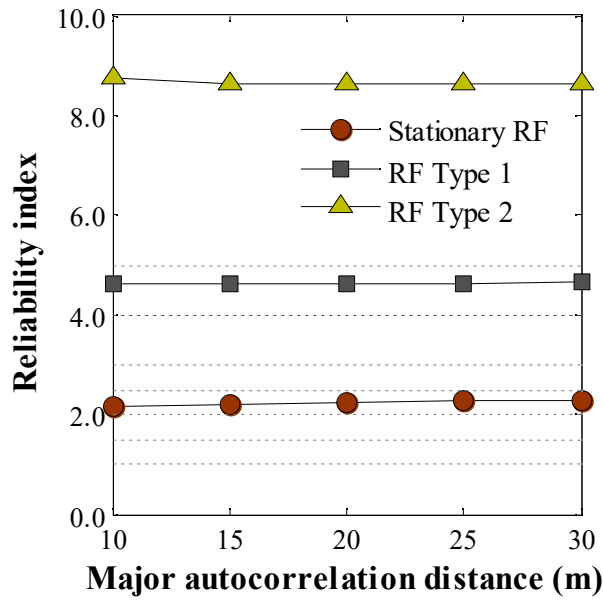
Figure 3.4 Typical realisations of random fields with $\alpha = 30^\circ$: (a) stationary RF; (b) RF Type 1; (c) RF Type 2.



(a)

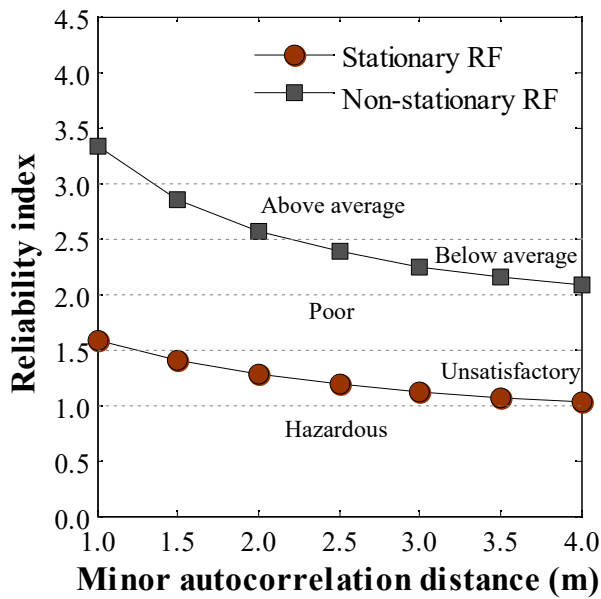


(b)

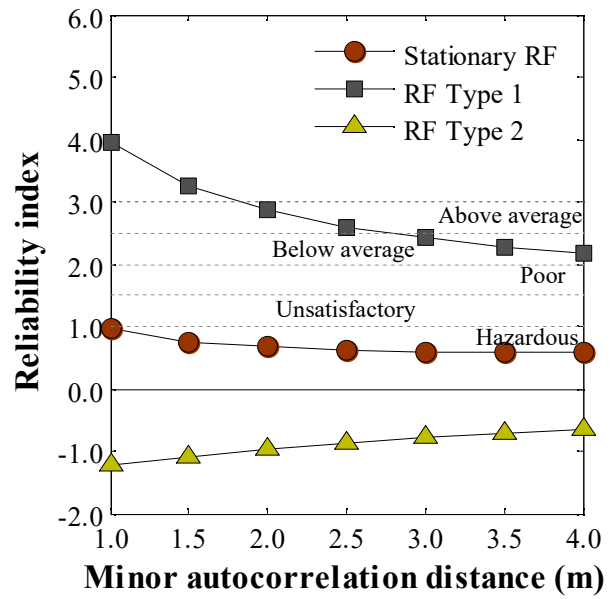


(c)

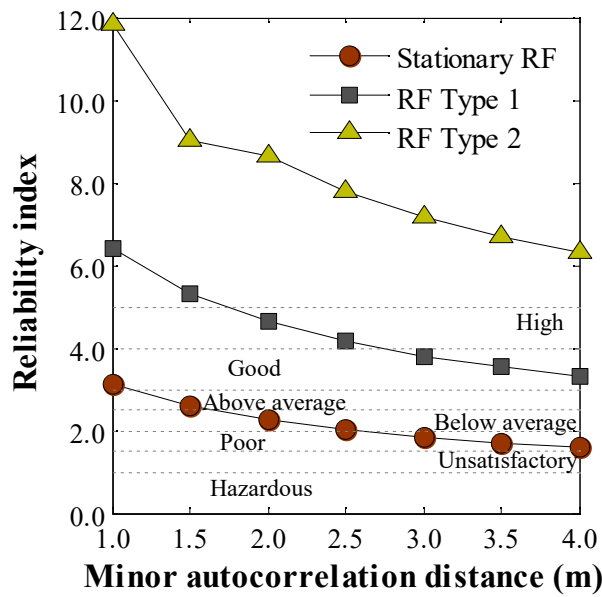
Figure 3.5 Reliability index versus major autocorrelation distance by Eq. (2.11) with $\theta_2 = 2$ m: (a) $\alpha = 0^\circ$; (b) $\alpha = 45^\circ$; (c) $\alpha = -45^\circ$.



(a)



(b)



(c)

Figure 3.6 Reliability index versus minor autocorrelation distance by Eq. (2.11) with $\theta_1 = 20$ m: (a) $\alpha = 0^\circ$; (b) $\alpha = 45^\circ$; (c) $\alpha = -45^\circ$.

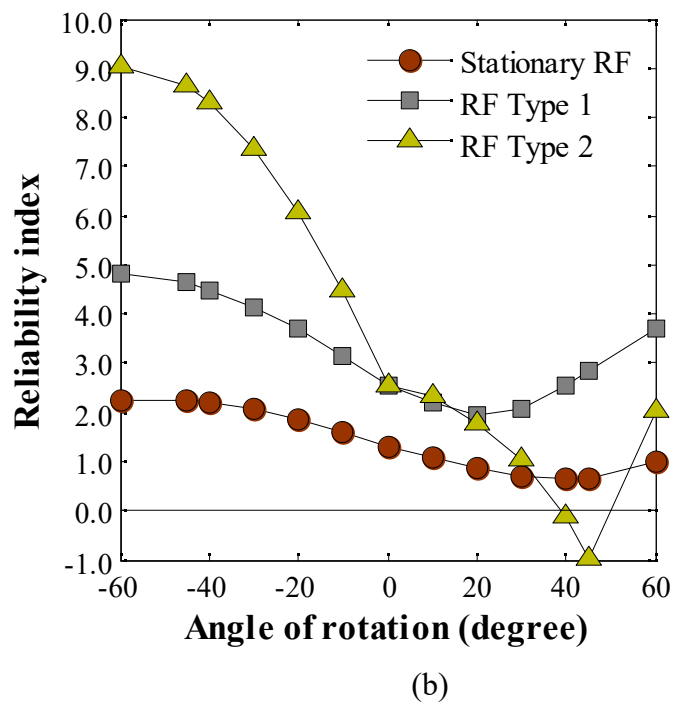


Figure 3.7 Reliability index versus rotational angle of soil bedding using Eq. (2.11).

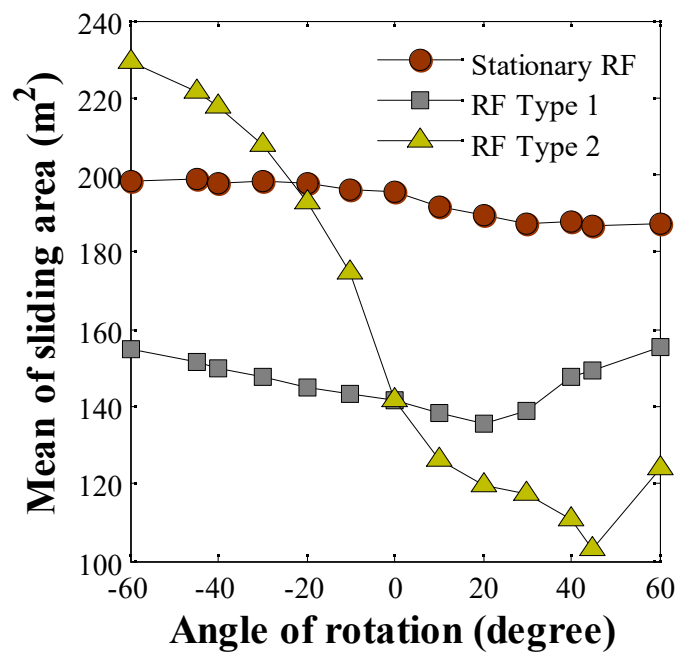
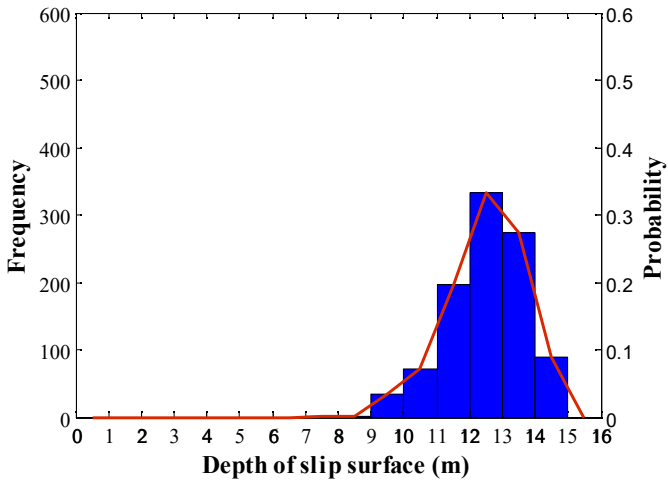
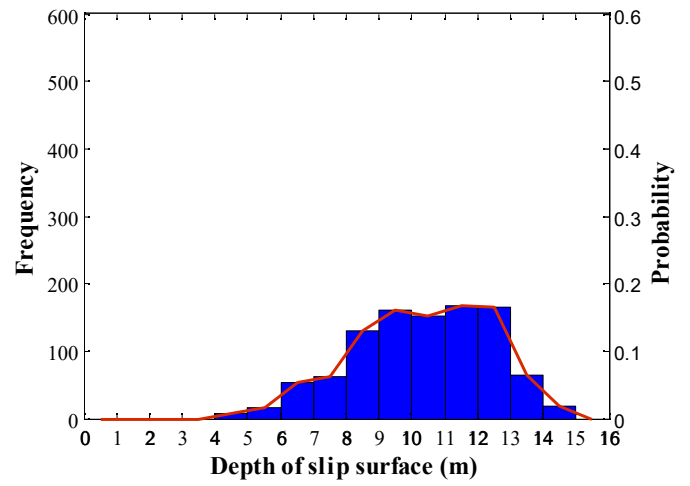


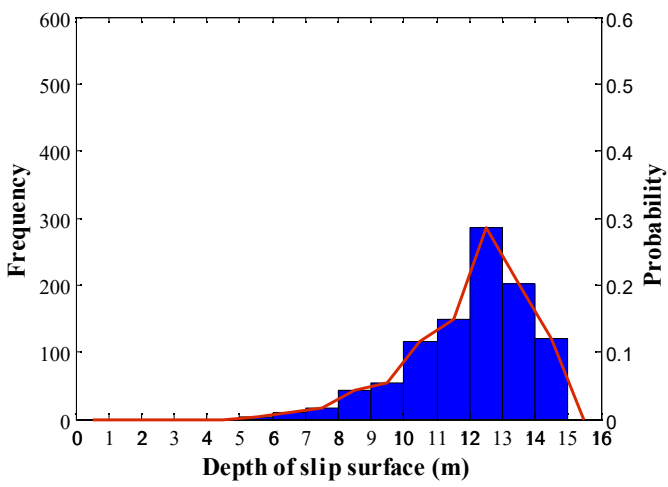
Figure 3.8 Mean of sliding area versus rotational angle of soil bedding.



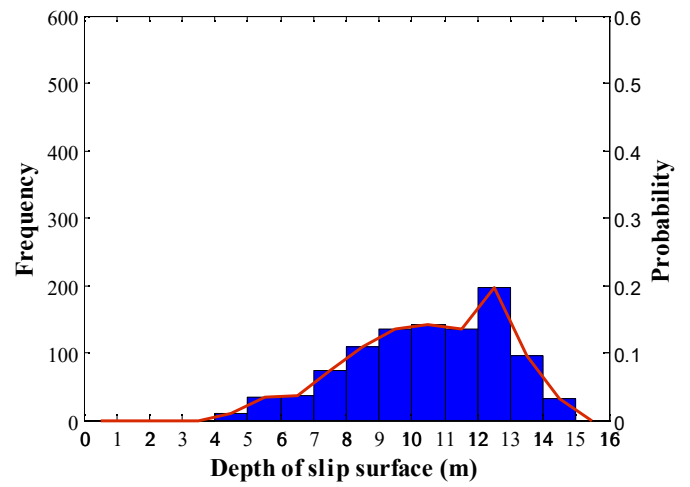
(a)



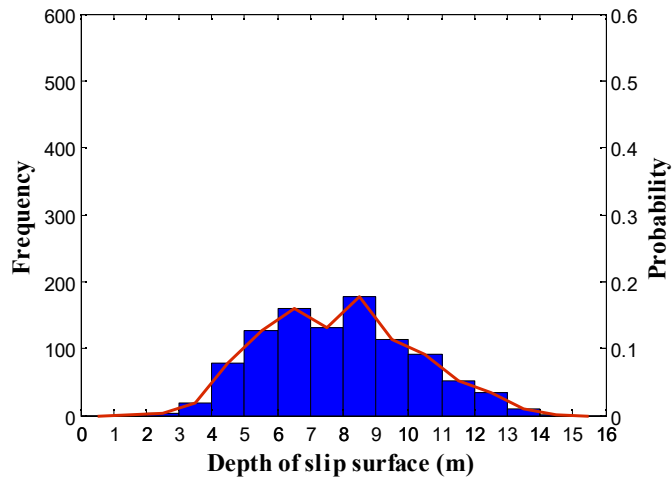
(b)



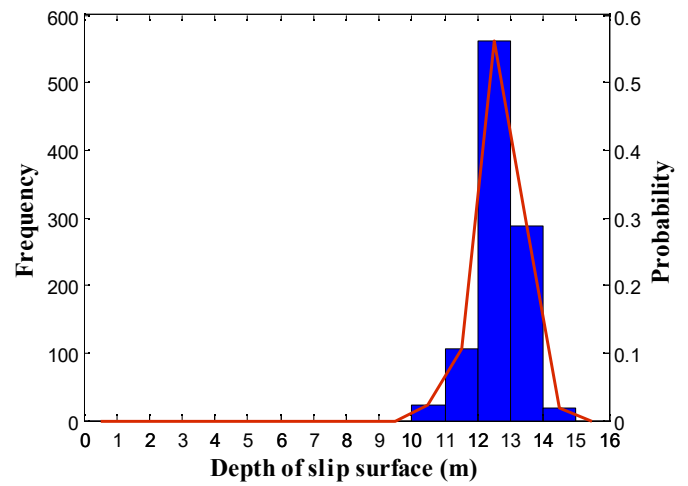
(c)



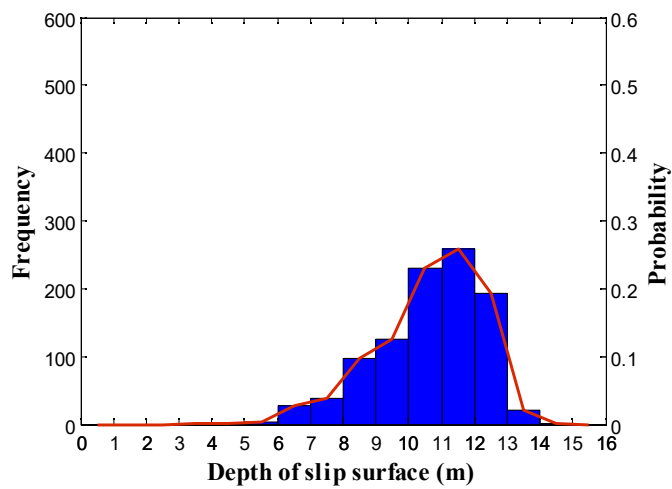
(d)



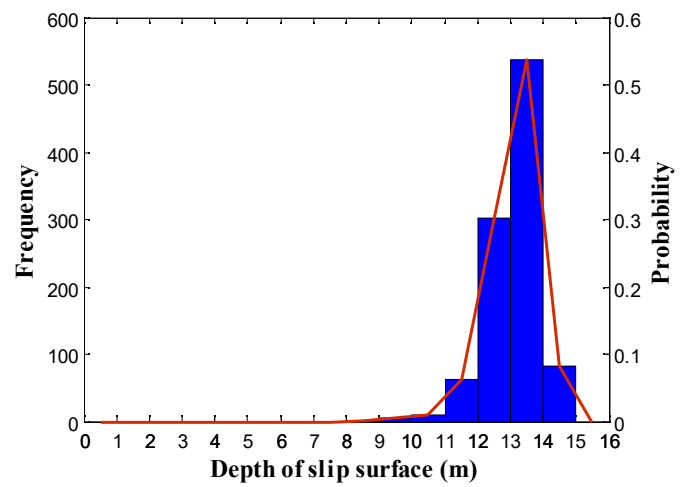
(e)



(f)



(g)



(h)

Figure 3.9 Histograms and probability distributions of h_c : (a) stationary RF ($\alpha = 0^\circ$); (b) non-stationary RF ($\alpha = 0^\circ$); (c) stationary RF ($\alpha = 45^\circ$); (d) RF Type 1 ($\alpha = 45^\circ$); (e) RF Type 2 ($\alpha = 45^\circ$); (f) stationary RF ($\alpha = -45^\circ$); (g) RF Type 1 ($\alpha = -45^\circ$); (h) RF Type 2 ($\alpha = -45^\circ$).

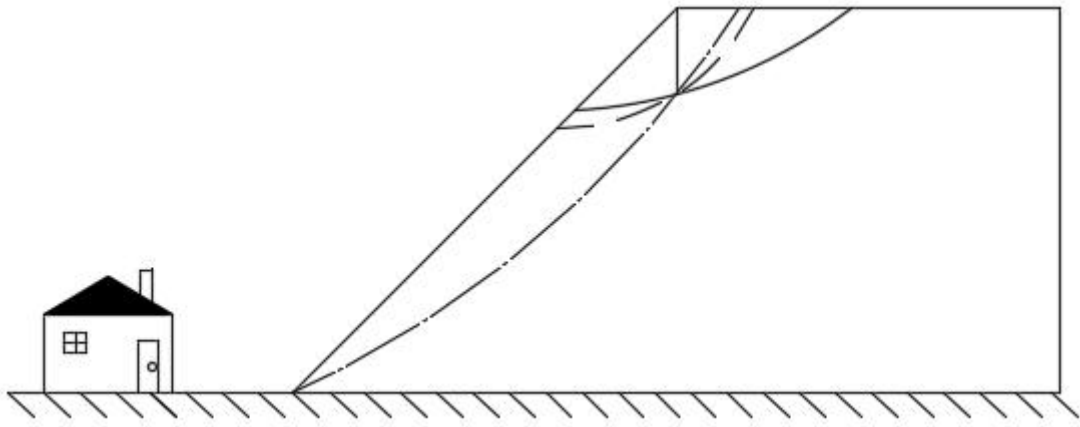
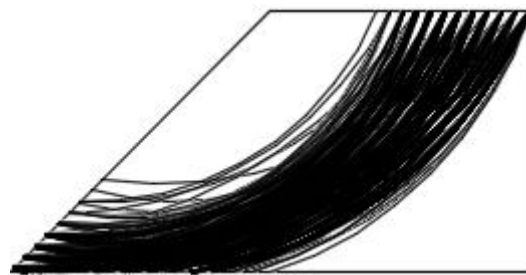
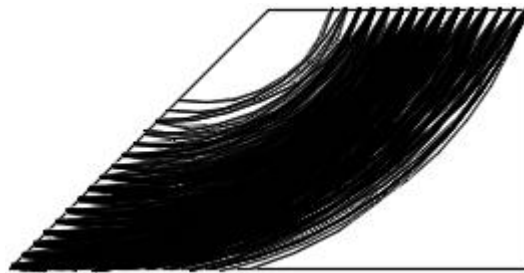


Figure 3.10 Consequences (failure scales) caused by shallow slip surfaces passing through slope face and slope toe, respectively.

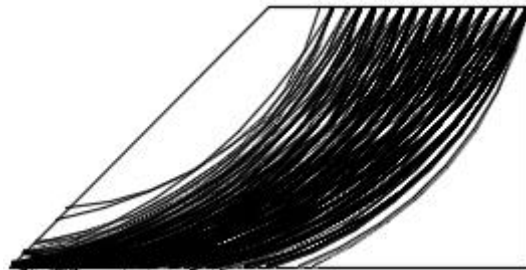


(a)

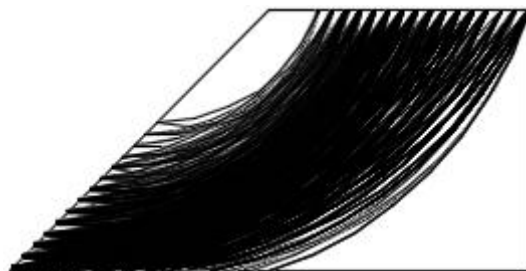


(b)

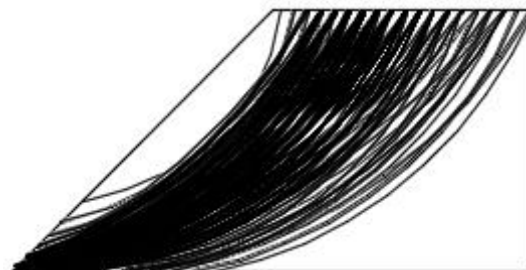
Figure 3.11 1000 slip surfaces within the slope in horizontally deposited soils ($\alpha = 0^\circ$): (a) stationary RF; (b) non-stationary RF.



(a)

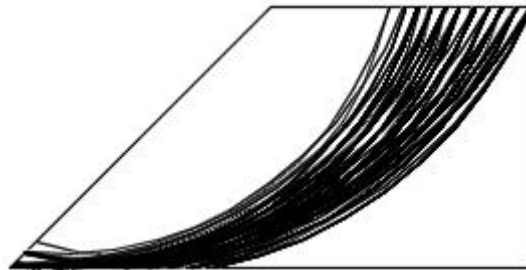


(b)

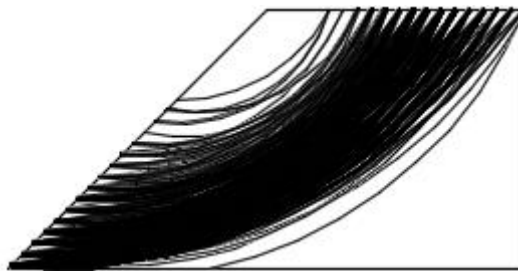


(c)

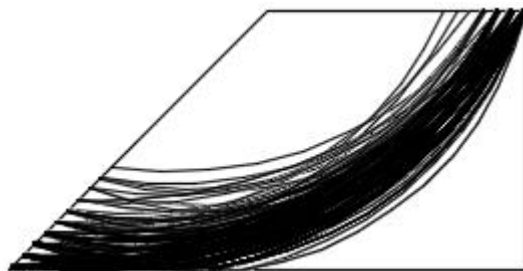
Figure 3.12 1000 slip surfaces within the dip slope ($\alpha = 45^\circ$): (a) stationary RF; (b) RF Type 1; (c) RF Type 2.



(a)



(b)



(c)

Figure 3.13 1000 slip surfaces within the reverse slope ($\alpha = -45^\circ$): (a) stationary RF; (b) RF Type 1; (c) RF Type 2.

CHAPTER 4 3D Probabilistic Slope Stability Analyses with Rotated Transverse Anisotropy in Soil Properties

4.1 Introduction

Chapter 3 investigated the influence of rotated transverse anisotropy and non-stationarity of soils on slope reliability and the failure mechanism in 2D probabilistic slope stability analyses, where various 2D scenarios of slope section were considered, including slopes with horizontal bedding, reverse slopes and dip slopes. When it comes to 3D slope models, slope scenarios can generally be divided into four categories based on stratigraphic occurrence [i.e., strike direction, dip direction and dip angle (Figure 4.1)]: (a) cross-dip slope (i.e., dip direction of strata is perpendicular to that of the slope) [Figure 4.1(a)]; (b) dip slope (i.e., dip direction of strata is the same as that of the slope) [Figure 4.1(b)]; (c) reverse-dip slope (i.e., dip direction of strata is in the opposite direction to that of the slope) [Figure 4.1(c)]; and (d) slope with horizontal bedding. In engineering practice, cross-dip and reverse-dip slopes are often considered as favorable scenarios for slope safety, whereas the dip slope usually constitutes adverse conditions. Despite the previous investigations involving 2D probabilistic slope stability analyses, the influence of 3D rotated transverse anisotropy on slope reliability has not yet been investigated or reported in

detail.

Horizontal transverse anisotropy (i.e., where soils display a horizontally deposited fabric pattern) has been considered in 3D probabilistic slope stability analyses in a number of studies (e.g., Hicks and Spencer 2010; Hicks *et al.* 2014; Hicks and Li 2018; and Varkey *et al.* 2019). In general, three failure modes can be observed, depending on the ratio of the horizontal autocorrelation distance [i.e., major autocorrelation distance (θ_1)] to the slope length (L) and slope height (H): (a) when the ratio is small, e.g., $\theta_1 < H$ as suggested by Hicks and Spencer (2010), the result of 3D probabilistic slope stability analysis is similar to conventional 2D deterministic analysis, and this is referred to failure mode 1; (b) when the ratio falls within an intermediate range of $H < \theta_1 < L/2$, discrete failure zones can be observed along the slope length, and this is known as failure mode 2; (c) when the ratio is large enough, e.g., $\theta_1 > L/2$, the soil properties are similar among different locations along the horizontal direction, and this leads to failure mode 3, where the 3D probabilistic slope stability analyses tend to produce similar results to the 2D counterparts under plane strain conditions. However, the 3D slope scenarios shown in Figure 4.1 cannot be considered by assuming horizontally deposited soil strata, which are influential to slope reliability. In addition, the findings regarding the three failure modes in 3D probabilistic slope stability analyses may be different when considering rotated transverse anisotropy, since the soil bedding planes are no longer in the horizontal orientation.

This chapter considers three categories of 3D rotated transverse anisotropy: (1) where the strike direction of the strata is perpendicular to the out-of-plane direction of the slope [“rotated anisotropy around the x axis” as shown in Figure 4.1(a)]; (2) where the strike direction of strata is along the out-of-plane direction of the slope [“rotated anisotropy around the y axis” as shown in Figures 4.1(b) and (c)]; and (3) “rotated anisotropy around the z axis” as shown in Figure 4.1(d). Also, slopes with horizontal bedding are investigated. Compared to categories (1) and (2), category (3) may be less common, but can be found in saprolitic soils which originates from preferential weathering of rocks (Liu and Leung 2018). In this chapter, 3D slope stability analyses are conducted considering the soil idealised as a Tresca material. Effects of soil variability are investigated using the 3D random finite element method which combines the finite element method with random field modelling under a Monte Carlo framework.

4.2 Methodology

4.2.1 3D Random Finite Element Method

As discussed in Section 2.3.4, soil spatial variability can be considered in probabilistic slope stability analyses by RFEM, RFDM and RLEM. However, there are few studies using 3D RLEM in the literature. That is possibly because limited mature 3D LEM

procedures can be used for coupling with random fields. By contrast, some commercial procedures using 3D SRM (e.g., ABAQUS and FLAC3D) can be adopted to couple with random fields. In this chapter, 3D RFEM is adopted to conduct probabilistic slope stability analyses using the commercial finite element software (i.e. ABAQUS). In ABAQUS, the slope stability model can be constructed and then output as a “.inp” file. The “.inp” file contains information regarding the finite element mesh, slope geometry, boundary conditions, and material properties. The random fields can be assigned the elements of the finite element mesh, through processing and generating the “.inp” files in batches. The implementation procedure of RFEM is show by a flowchart in Figure 4.2.

4.2.2 Soil Spatial Variability Considering 3D Rotated Transverse Anisotropy

In this chapter, spatially variable soils are simulated using the Cholesky decomposition method, where the autocorrelation function considering 3D rotated transverse anisotropy can be directly incorporated into random field generation. The mid-point method is considered for random field discretisation, where the mid-point coordinates are used to evaluate representative properties for the element. Under rotated transverse anisotropy, the autocorrelation structure can be derived through rotation of the coordinate system (Zhu and Zhang 2013; Liu and Leung 2018). For

instance, for rotated anisotropy around the x axis, the autocorrelation function is expressed as:

$$\rho = \exp \left[-2 \sqrt{\frac{\tau_x^2}{\theta_1^2} + \frac{(\tau_y \cos \alpha + \tau_z \sin \alpha)^2}{\theta_1^2} + \frac{(-\tau_y \sin \alpha + \tau_z \cos \alpha)^2}{\theta_2^2}} \right] \quad (4.1)$$

For rotated anisotropy around the y axis, the autocorrelation function is given by:

$$\rho = \exp \left[-2 \sqrt{\frac{(\tau_x \cos \alpha + \tau_z \sin \alpha)^2}{\theta_1^2} + \frac{\tau_y^2}{\theta_1^2} + \frac{(-\tau_x \sin \alpha + \tau_z \cos \alpha)^2}{\theta_2^2}} \right] \quad (4.2)$$

For rotated anisotropy around the z axis, the autocorrelation function is given by:

$$\rho = \exp \left[-2 \sqrt{\frac{(\tau_x \cos \alpha + \tau_y \sin \alpha)^2}{\theta_1^2} + \frac{(-\tau_x \sin \alpha + \tau_y \cos \alpha)^2}{\theta_2^2} + \frac{\tau_z^2}{\theta_1^2}} \right] \quad (4.3)$$

Some typical realisations of random fields of the rotated transverse anisotropy around the x and y axes are shown in Figures 4.3 and 4.4, respectively.

4.3 Case Description

Figure 4.5(a) shows a cross-section of the 3D slope model. The slope has a height of 5 m and a slope angle of 45° . The base case involves slope length of 60 m, while various other slope lengths are also considered later. As shown in Figure 4.5(b), the finite element mesh with slope length of 60 m contains 9,300 elements, and each element size is 0.5 m \times 0.5 m \times 1 m (y - direction). Griffiths and Marquez (2007)

suggested that a finer mesh would always result in a smaller FS in 3D finite element analysis of slopes, but the difference is slight. Meanwhile, for random field generation, a smaller element size would lead to a more realistic simulation of spatially variable soils. Huang and Griffiths (2015) recommended that the element size in RFEM should be less than half of the spatial autocorrelation distance using the element-level averaging method. However, they also pointed out that only a 2D random field of undrained shear strength (s_u) was simulated in their research, and the recommendations on element size could be different in more general cases (e.g., 3D model). Besides, their study only considered an isotropic random field. In contrast, Ching and Phoon (2013) considered both isotropic and anisotropic random fields to investigate the influence of element size on the mobilised shear strength, which is defined by the yield stress recorded before FEM fails to converge. They found that when discretising the random field with a single exponential autocorrelation structure, the element size should be smaller than $0.05\theta_2$ to avoid excessive spatial averaging in the element-level averaging method, and a similar element size requirement also applied for the mid-point method. Since θ_2 is usually small in practice, this requirement would be computationally demanding for RFEM, especially for 3D problems where the requirement may not be realistic. Although the element size adopted in this study is larger than $0.05\theta_2$, Ching and Phoon (2013) described that in such cases, the mid-point method leads to conservative estimates of the mobilised shear strength than reality when assigning shear strengths to elements, while the element-level averaging method would produce unconservative estimates. Therefore,

the mid-point method is suggested for engineering practice.

In the RFEM analyses, the base of the model is fully fixed, and the back face is prevented to move in the x - direction through roller boundaries (Figure 4.5). For the two end sections along the y - direction, three kinds of boundary conditions are usually adopted (Chugh 2003; Shen and Karakus 2014), which are discussed in Section 2.2.5. Hicks and Spencer (2010) discussed that when smooth boundaries are adopted, the two end conditions would tend to exaggerate the failure zones over a suite of Monte Carlo simulations, and biases would occur in these areas. Therefore, they adopted the boundary condition with movements fixed in the x and y directions. This boundary condition is also adopted in this chapter.

In this chapter, the soil is modeled as an elastic-perfectly plastic Tresca material. The undrained shear strength s_u is characterized statistically by a log-normal distribution with the mean and coefficient of variation being 19 kPa and 0.3, respectively. The unit weight, Young's modulus (E) and Poisson's ratio (ν) are 20 kN/m³, 100 MPa and 0.3, respectively. For slope stability analysis under undrained conditions, $\nu = 0.5$ is more appropriate for total stress analysis. This study considers a combination of $E = 100$ MPa and $\nu = 0.3$, as this was used in many previous studies of probabilistic slope stability analyses (Hicks and Spencer 2010; Hicks *et al.* 2014; Xiao *et al.* 2016; Hicks and Li 2018). Indeed, E and ν have little influences on the FS results by finite element

analysis with the strength reduction method (Griffiths and Lane 1999; Griffiths and Marquez 2007). For comparison, simulations of a 60 m long slope ($\theta_1 = 12$ m) are performed using $E = 20$ MPa and $\nu = 0.495$, and the results for the standard deviation of FS are almost identical to the corresponding cases with $E = 100$ MPa and $\nu = 0.3$, as shown in Figure 4.6. In addition, the results of mean FS under the two settings (i.e., $E = 20$ MPa; $\nu = 0.495$, and $E = 100$ MPa; $\nu = 0.3$) are very close (not shown). In this study, the minor autocorrelation distance is fixed to 1 m, while the major autocorrelation distance varies from {2 m, 12 m, 24 m, 60 m}. The dip angle of the strata varies from $\{-30^\circ, -60^\circ, 0^\circ, 30^\circ, 60^\circ, 90^\circ\}$, where the negative values represent a clockwise rotation, while the positive rotational angle represents an anticlockwise rotation. For each parametric setting (i.e., α , θ_1 , and L), 500 realisations are generated by the Monte Carlo approach with the Latin hyper-cube sampling technique. Generally, 500 Monte Carlo simulations are sufficient for determining the statistical characteristics of FS (i.e., mean and standard deviation of FS) (Tabarroki *et al.* 2013; Li *et al.* 2016b; Liu *et al.* 2017b), but when determining P_f , more simulations are usually needed.

Deterministic slope stability analysis is first conducted as a benchmark using SRM. For the definition of slope failure in SRM, there are mainly three criteria (Cheng and Lau 2008), which were discussed previously in Section 2.2.3. In the current work, under the Monte Carlo framework, option (3) (i.e., formation of a continuous plastic zone) is not applicable, since the plastic strain contour of each simulation needs to be

checked manually. For option (1) (i.e., a sudden increase in the nodal displacement), the nodal displacement should be obtained from some feature points, but it is difficult to select those points especially in a 3D slope problem. Therefore, option (2) (i.e., non-convergence of the finite element solution) is adopted in this study. More details about the non-convergence option is given by Griffiths and Lane (1999). A deterministic slope stability analysis is first conducted as a benchmark, using the strength reduction method with the non-convergence criteria. The undrained shear strength is set to be the mean value (i.e. $s_u = 19$ kPa), and the deterministic FS is 1.214 for the 2D model and 1.244 for the 3D model. It is deemed to be reasonable that the FS by 3D analysis is slightly larger than that by 2D analysis, due to the additional constraints imposed by the boundary conditions in the 3D model.

4.4 Results

4.4.1 Statistical Characteristics of FS

Figures 4.6 and 4.7 show the standard deviation and mean of FS for various scenarios of strata rotation, respectively. Considering the rotation around the x and z axes, the statistical characteristics of FS tend to be symmetrical about $\alpha = 0^\circ$. This is expected, as the same angles with opposite directions of rotation would lead to scenarios that are mirror images of each other, around the plane parallel to the slope cross-section

[Figures 4.8(a) and (b)]. Besides, Figures 4.7(a) and (c) show that the mean of FS decreases with larger major autocorrelation distances, for rotated anisotropies around the x and z axes (except with $\alpha = 90^\circ$ around the z axis, which is equivalent to $\alpha = 90^\circ$ around the y axis, and $\alpha = 0^\circ$ around the x axis, which indicates horizontal transverse anisotropy). This phenomenon can be explained by the influence of θ_1 on the failure mechanism, which will be discussed in later sections.

For rotated anisotropy around the y axis, a maximum value of standard deviation (Figure 4.6) and a minimum value of the mean FS [Figure 4.7(b)] can be observed for all θ_1 when the rotational angle is 30° . This indicates that the critical angle of rotation would be around 30° , considering the slope angle of 45° in this study. In contrast, the negative angles of rotation would lead to smaller standard deviations and higher mean FS, which correspond to a lower risk level. For dip slopes with positive angles of rotation around the y axis, failure through a weak zone occurs more easily (compared to cross-dip or reverse-dip slope) since it would pass through fewer bedding planes, or mainly one bedding plane in some cases. Therefore, a dip slope generally constitutes to an adverse condition for slope stability. This is also consistent with the observations from 2D probabilistic slope stability analyses reported in Chapter 3 and Zhu *et al.* (2019).

When $\theta_h = 1.5$ m and 2 m, the means and standard deviations of FS show small differences at various rotational angles and among the three scenarios of rotated

transverse anisotropy. With a small value of θ_h , a continuous weak zone is more difficult to develop, and the potential failure surface would pass through both weak and strong zones alike. Therefore, there would be significant averaging effects on the soil property over the large 3D failure surface, and the average s_u over the failure surface would be close to the mean value over the entire soil mass (i.e., 19 kPa in this study). Consequently, there are smaller dispersions of FS estimates, with the 3D probabilistic results approaching those of the deterministic analyses. In addition, when the value of θ_h approaches θ_v (i.e., 1 m), the spatially variability pattern becomes similar to the isotropic pattern, and this is also reflected in the trends of the statistics of FS as θ_h decreases (Figures 4.6 and 4.7). This explains why the different scenarios of rotated transverse anisotropy lead to similar results at small values of θ_h . Figure 4.7 shows that the means of FS for small θ_h values (i.e., $\theta_h = 1$ m, 1.5 m and 2 m) are slightly below the FS from 3D deterministic analyses, with the differences generally less than 4%. Despite the averaging of s_u over the failure surface, the sliding mass would still pass through the weakest path in each realization of the probabilistic analyses, leading to lower FS values than the deterministic estimates. Similar phenomena are also observed in various probabilistic assessments of geotechnical systems (e.g., Cho 2010; Kasama and Whittle 2011; Xiao *et al.* 2016).

4.4.2 Reliability Index

This section investigates the influences of major autocorrelation distance and the length of the slope model on the results of reliability assessments, through the reliability index (β). The 3D results are also compared with those by 2D probability analyses, to shed insights on the potential limitations of plane strain assumptions. As the only random variable (i.e., s_u) is assumed to be log-normally distributed, the reliability index is calculated by Eq. (2.11).

Effects of major autocorrelation distance

Figure 4.9 (a) shows the reliability index versus various rotational angles when $\theta_1 = 2$ m, and the values of β are found to be very high ($\beta > 6$) in the 3D analyses for all scenarios of rotated transverse anisotropy. When $\beta > 5$, the corresponding probability of failure is smaller than 3×10^{-7} , and the expected performance level of a structure can be defined as “High” (Table 2.3). This is consistent with the previous discussions that 3D probabilistic slope stability analyses would resemble deterministic analyses when θ_1 and θ_2 are small enough, and with the deterministic FS exceeding 1.2, there is a very small chance of slope failure. In contrast, the β values estimated by 2D probabilistic slope stability analyses are much smaller. For both 2D and 3D slope model geometries, failure through a weak zone is difficult to develop when spatial autocorrelation distances are small, as the soil properties vary rapidly among adjacent

elements. Such averaging effects are more pronounced within the failure surface of a 3D slope geometry, compared to that of the corresponding 2D cross-section, since the 3D rupture surface involves a much larger area (arising from the additional dimension) than the 2D slip line. Hence, when θ_1 is small, the response of 3D probabilistic slope stability analysis is similar to that by deterministic analysis.

Figures 4.9(b), (c) and (d) show that, when $\theta_1 \geq 12$ m and considering rotated anisotropy around the x and z axes, two slopes yield similar β values when the same degrees of strata rotation are involved with opposite rotational directions (i.e., symmetrical about $\alpha = 0$). For rotated anisotropy around the y axis, the results of β , by 3D probabilistic slope stability analyses, approach those of the corresponding 2D probabilistic analysis results when θ_1 is large. This is because when θ_1 is large, the soil strata would appear as a continuous layer. Considering rotated anisotropy around the y axis, slope failures tend to occur along the entire slope length (y - direction) through weak layers, and therefore become similar to those by 2D probabilistic slope stability analyses (Hicks and Spencer 2010) (i.e., failure mode 3). In contrast, considering rotated anisotropy around the x and z axes, the β values estimated by 3D probabilistic slope stability analyses are significantly larger than those by 2D slope analyses, showing no tendency to approach the 2D results, even with large θ_1 values.

In practice, and as mentioned above, the cross-dip slope [Figure 4.1(a)] and reverse-dip slope [Figure 4.1(c)] are generally favorable scenarios in slope stability

assessment, while the dip slope [Figure 4.1(b)] constitutes an adverse condition. Figure 4.10 also shows that the reliability indices for dip slopes are smaller than those in reverse-dip and cross-dip slopes. Meanwhile, it can be seen from Figure 4.9 that when $\theta_1 \geq 12$ m, for a given α the reliability of a cross-dip slope is higher than the dip and reverse-dip slopes. Also, for most of the cases shown in Figure 4.10, for a given θ_1 , cross-dip slopes generally have higher reliability than reverse-dip slopes.

Effects of slope length

In 3D probabilistic slope stability analysis considering isotropy and horizontal transverse anisotropy in soil spatial variability, slope reliability was found to be sensitive to the length of slope model (in the y - direction). Generally, the increase of slope length would lead to a reduction in slope reliability, due to the diminished constraining effects from the boundaries and the increased probability of occurrence of a critical weak zone (Griffiths *et al.* 2009a; Hicks and Spencer 2010). In this chapter, various slope lengths are considered with $\theta_1 = 24$ m, as shown in Figures 4.11(a) and (b). According to Figure 4.11(a), with horizontal soil strata (i.e. $\alpha = 0^\circ$) and rotated anisotropy around the y axis, the reliability index decreases as the slope length increases, and β values from 3D analyses would eventually fall below the results from 2D analyses. In contrast, β values estimated by 3D analysis under rotated anisotropy around the x axis are much larger than those by 2D analysis even when the slope length is large, and the change of β with various slope lengths is more modest.

4.4.3 Mean of Slide Length

Figure 4.12 illustrates the definition of the length of the sliding mass (or slide length), while its mean value can be obtained over a suite of Monte Carlo simulations. In this study, a slide length in each realization is obtained by the total number of elements along the y - direction, located in the row immediately above the slope toe, that have an average nodal x - displacement exceeding a threshold value. To determine this threshold value, an approach conceptually similar to that by Hicks *et al.* (2014) is adopted. A 3D slope model is first constructed with homogeneous soil properties ($s_u = 19$ kPa), and the cross-section at mid-length ($L/2$) is considered in the 3D analyses. Making use of the displacement response at this mid-length cross-section, a relationship (Figure 4.13) can be established between a certain displacement δ_0 (expressed as percentage of the maximum nodal x -displacement) and the number of elements (or percentage of elements in the cross-section) with average x -displacement exceeding δ_0 .

Meanwhile, the volume of the sliding mass in this cross-section can be defined as the volume (or area in 2D) of soil above the slip surface. Herein, the slip surface is determined by a polynomial curve fitting the points of maximum plastic strain in each column of the strain contour. In this case, as shown in Figure 4.14, the volume of the

sliding mass is estimated to be 58.9% of the entire mesh volume. According to Figure 4.13, this volume corresponds to the value of δ_0 which is 32% of the maximum displacement in the model. This δ_0 value is then treated as the threshold when determining the length of the sliding mass.

The mean slide lengths estimated by this approach are compared against previous studies by Li *et al.* (2015b) for horizontally deposited soils, as shown in Table 4.1. Apart from the homogeneous benchmark model, additional simulations are performed with spatially variable soils of different α values. For these cases, 2D slope models are adopted since the cross-sections of the 3D models at mid-length may not always provide representative information of the slip surface due to the spatially variable and uncertain nature of the soil properties. Using these 2D models of different α values, it is found that the thresholds for various cases are within the range of 31% - 34% of the maximum nodal displacement. This means that in general, adopting the calibrated threshold value (32%) would not affect the trends of slide length variations under different α .

Under horizontal transverse anisotropy, Hicks *et al.* (2014) proposed that when θ_1 is large relative to slope height H , the mean of slide length is positively correlated to θ_1 . This is because in this case, a sliding mass is attracted to a pocket of weak soils, and a large value of θ_1 usually indicates a larger extent of a weak zone (Griffiths *et al.* 2009a). In this study, the mean estimates of slide length and influences of θ_1 and α

are investigated under rotated transverse anisotropy.

Figures 4.15(a), (b), and (c) show the mean estimates of slide length with various rotational angles under rotated anisotropy around the x , y , and z axes, respectively. Similar to previous results of reliability indices, under rotated anisotropy around the x and z axes, the mean of the slide length is similar between two slopes having the same degrees of strata rotation but in opposite rotational directions. Considering rotated anisotropy around the y axis, the rotation of strata (i.e., $\alpha \neq 0^\circ$) can result in larger mean values for the slide length. Figure 4.15 also shows the changes in slide lengths with different major autocorrelation distances. It can be seen from Figure 4.15(b) that under rotated anisotropy around the y axis, when $\theta_1 \geq 12$ m (i.e., failure modes 2 and 3), the mean of slide length increases with larger major autocorrelation distance, which is consistent with the above-mentioned observations for a horizontal fabric pattern. A similar pattern is also observed with $\alpha = 0^\circ$ around the x axis in Figure 4.15(a) and $\alpha = 90^\circ$ around the z axis in Figure 4.15(c). In these cases, the soil variations along the y - direction are controlled by θ_1 , and a larger value of θ_1 leads to a longer mean slide length. On the contrary, when considering other cases of rotated anisotropy around the x and z axes [Figures 4.15(a) and (c)], an increase in major autocorrelation distance would lead to smaller mean estimates of slide length. In these cases, soil variability along the y - direction is controlled by θ_2 . As θ_2 is usually too small for a continuous weak zone to develop along the direction of slide length, the formation of a potential sliding mass would be mainly controlled by the cumulative

effects of a weak paths from all the cross-sections within the sliding mass. In this case, a larger major autocorrelation distance would usually result in easier formation of weak path for each cross-section, and hence fewer cross-sections may be involved to form a sliding mass. Consequently, for cases of strata rotation around the x and z axes, the mean value of the slide length usually decreases modestly as θ_1 increases. Moreover, as the formation of a rupture surface is generally easier with larger θ_1 , the reliability of the slope tends to decrease, manifested as lower mean estimates of FS shown in Figures 4.7(a) and (c).

4.5 Discussion

In engineering practice, the safety of a slope is usually estimated by 2D slope stability analysis. The main reason is that the estimated results of slope safety by the 2D method would usually be conservative. Therefore, when the difference between the 2D and 3D estimates of FS is not large, the 2D slope stability analysis method can be adopted. Otherwise, the use of the 2D method is undesirable due to the economic losses, when FS is significantly underestimated. The results in this chapter reveal that, when the major autocorrelation distance is very small (i.e., failure mode 1) or the 3D slope model is a cross-dip slope (Figure 4.9), the 2D probabilistic slope stability analyses would significantly underestimate the slope reliability. By contrast, when one considers reverse and dip slopes, and slopes with horizontal bedding, 2D probabilistic slope stability analyses would result in similar estimations of slope reliability to those

by the 3D method with large autocorrelation distances.

Furthermore, reverse-dip and cross-dip slopes are usually regarded as favourable scenarios for road construction and alignment. In this chapter, considering soil spatial variability, a cross-dip slope is found to be a more favourable scenario regarding slope reliability than a reverse-dip slope. Meanwhile, a slope with horizontally deposited soils is observed to be a more adverse scenario than a cross-dip slope and a reverse-dip slope (Figure 4.10). Therefore, the cross-dip slope would be a better scenario, when constructing roads and selecting road routes. These conclusions can assist engineers make primary decisions when assessing slope stability and performing engineering designs.

4.6 Summary

Previous probabilistic slope stability analyses considering rotated transverse anisotropy of soils only focused on 2D problems. Meanwhile, the influence of soil variability on 3D slope reliability evaluation has only been investigated for soils that display isotropic spatial variability features or anisotropic horizontal fabric patterns. However, the plane-strain condition or horizontal transverse anisotropy are extreme cases of a whole spectrum of slope problems. In this chapter, 3D rotated transverse anisotropy is considered to constitute to a more comprehensive perspective of slope

reliability, considering various possible scenarios of spatially variable soils. Herein, three categories of 3D rotated transverse anisotropy are considered (i.e., rotated anisotropy around the x , y and z axes, respectively) together with three slope scenarios (i.e., dip, reverse-dip and cross-dip slopes). It was found that the rotated transverse anisotropy is an important factor that can affect the 3D slope reliability evaluation in spatially variable soils. More specific conclusions can be made in the following:

(1) When the major autocorrelation distance (θ_1) is small compared to the slope dimensions, the potential slip surface would pass through weak and strong elements and it is more difficult for a continuous weak zone to emerge. Consequently, the soil properties, when averaged over a large rupture surface, would approach their mean value. Meanwhile, the spatial variability pattern also approaches the isotropic pattern, and hence the effects of rotated transverse anisotropy are mitigated.

(2) As θ_1 increases, a continuous, or semi-continuous, weak zone of soils can form within a slope. For rotated anisotropy around the x and z axes, the reliability indices of two slopes are similar if their soil strata are rotated to the same angles but in opposite directions. The slope reliability revealed by 3D analyses shows no tendency to approach that of the 2D analyses. Besides, under these scenarios, when the major autocorrelation distance increases, the mean value of the slide length would slightly decrease. These findings differ from those for horizontal transverse anisotropy reported in previous studies.

(3) For rotated anisotropy around the y axis, the slope reliability by 3D analyses tends to be similar to that of 2D analyses with large values of θ_1 . The mean slide length in this case would increase with the major autocorrelation distance. These observations are similar to previous studies considering horizontal transverse anisotropy. In addition, at this situation, when the dip angle of the strata increases, the mean slide length would be increased.

(4) Considering rotated anisotropy around the x axis, the changes in the slope reliability are relatively insensitive to the length of the slope in the out-of-plane direction. Conversely, the reliability of a slope would reduce significantly with slope length, when soils display a horizontally deposited fabric pattern or with pronounced rotated anisotropy around the y axis.

(5) Cross-dip and reverse-dip slopes are usually regarded as favorable features for slope stability. In this chapter, it is found that in general, cross-dip slopes could be more favorable scenarios for slope reliability, when spatial variability of soil properties in various directions are considered.

Table 4.1 Comparison of mean slide lengths of slopes in horizontally deposited soils under undrained conditions with $\theta_2 = 1$ m.

θ_1 (m)	Current study of a 60 m slope (% of total slope length)	Li <i>et al.</i> (2015b) of a 50 m slope (% of total slope length)
2	60.84	Around 60
12	38.97	Around 38
24	41.7	Around 40

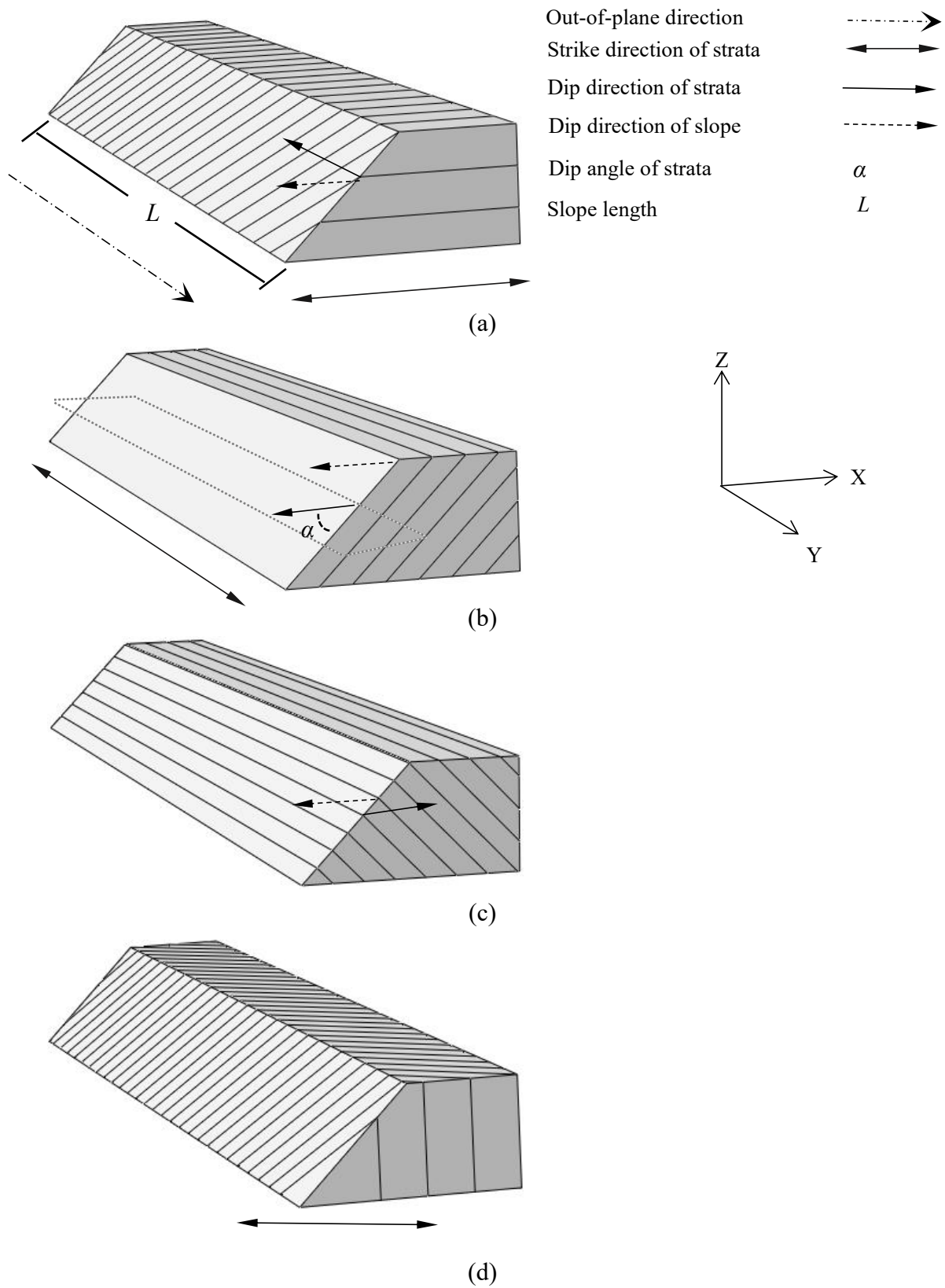


Figure 4.1 (a) Strata rotating around the x axis (cross-dip slope); (b) strata rotating around the y axis (dip slope); (c) strata rotating around the y axis (reverse-dip slope); (d) strata rotating around the z axis.

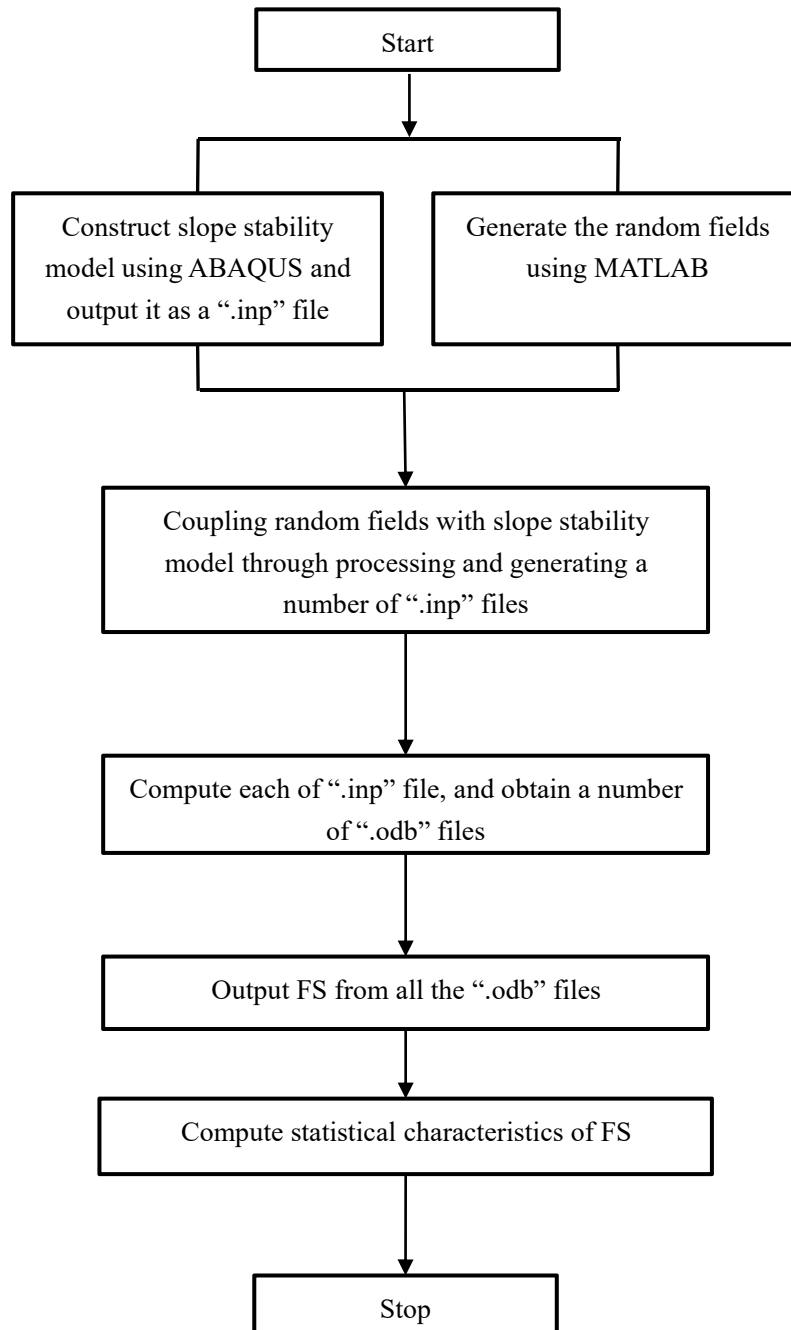


Figure 4.2 Flowchart of non-intrusive 3D RFEM using ABAQUS.

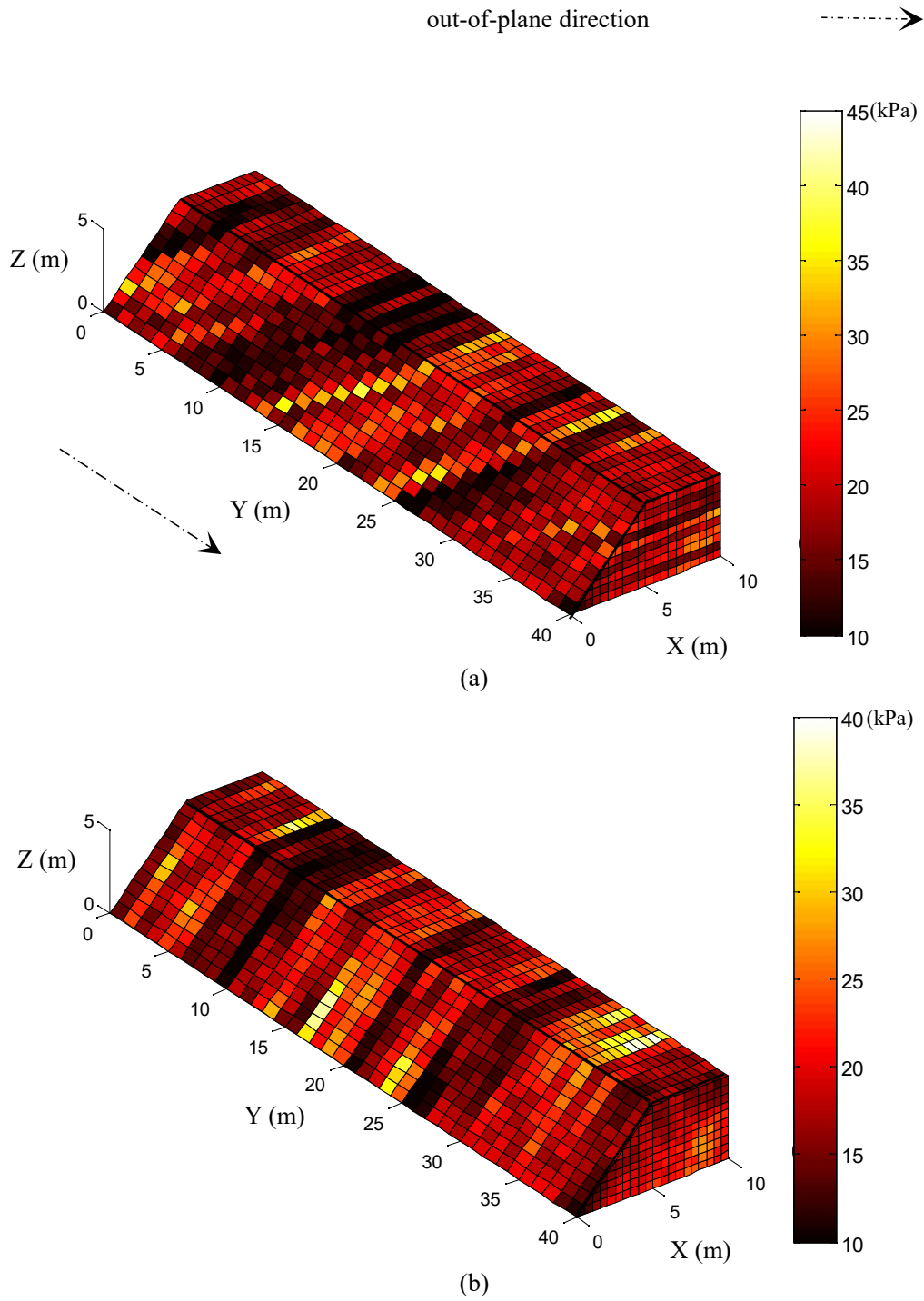


Figure 4.3 Typical realisations of random fields of undrained shear strength under rotation around the x axis: (a) $\alpha = 30^\circ$; (b) $\alpha = 90^\circ$.

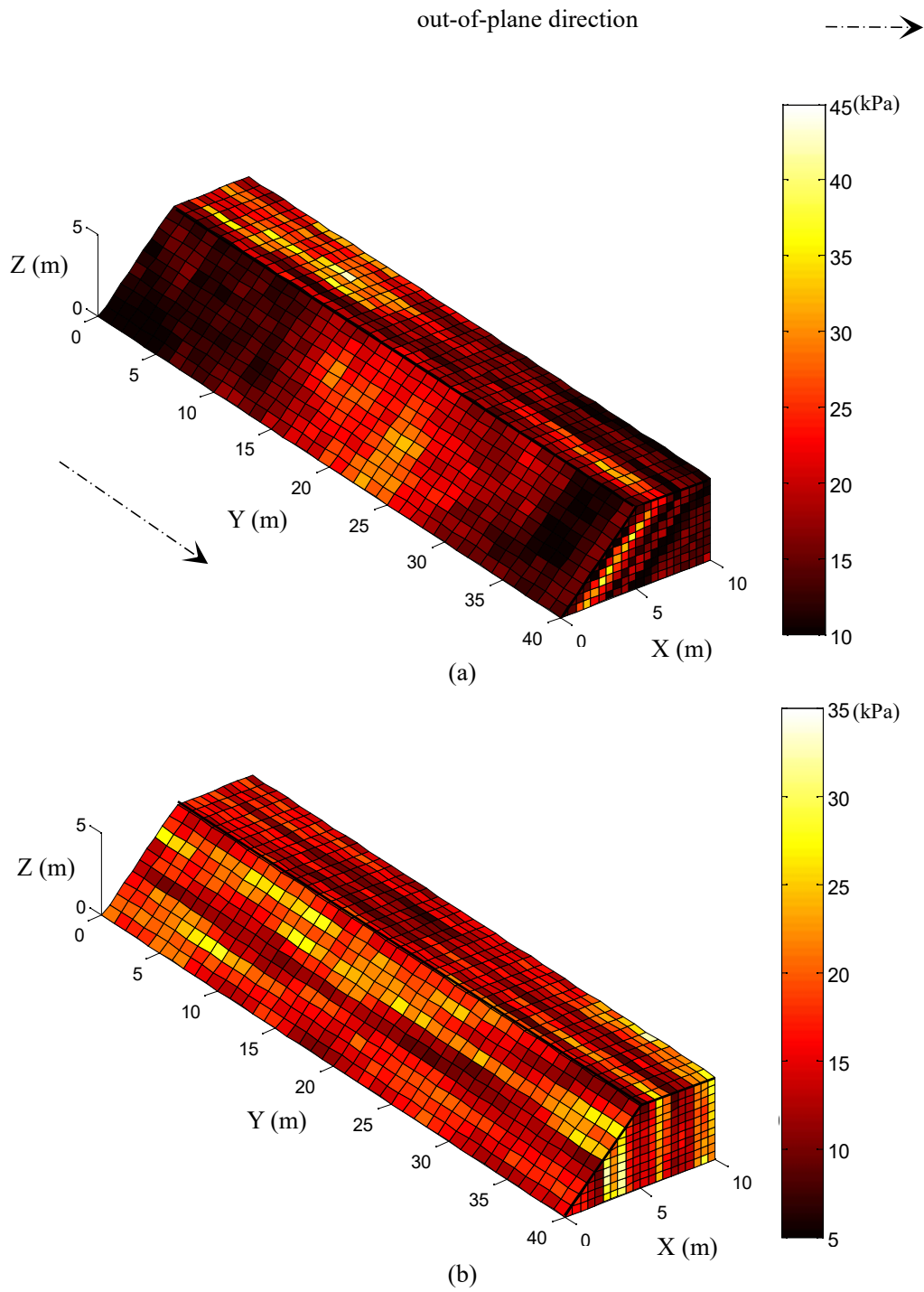
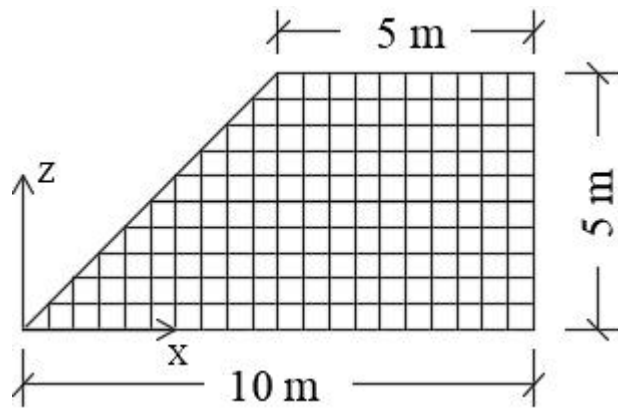
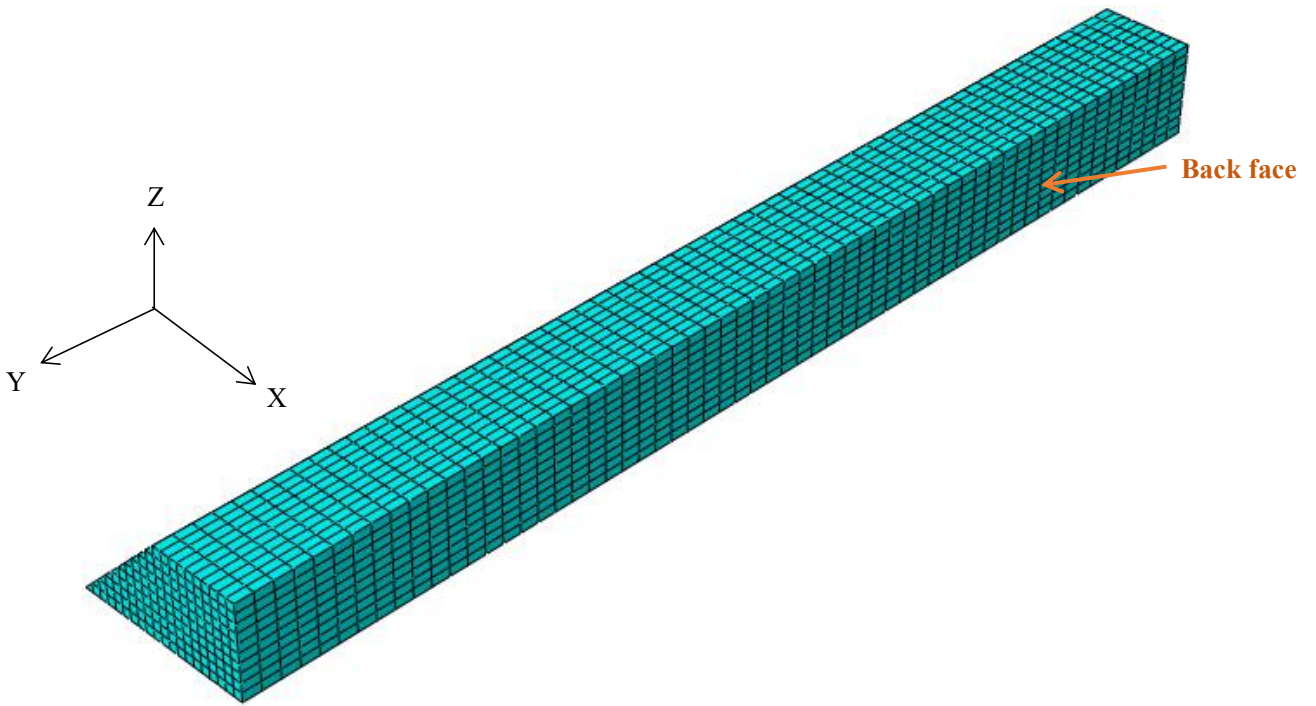


Figure 4.4 Typical realisations of random fields of undrained shear strength under rotation around the y axis: (a) $\alpha = 45^\circ$; (b) $\alpha = 90^\circ$.



(a)



(b)

Figure 4.5 Slope geometry and finite element mesh: (a) cross-section through mesh; (b) finite element mesh for a 3D slope model.

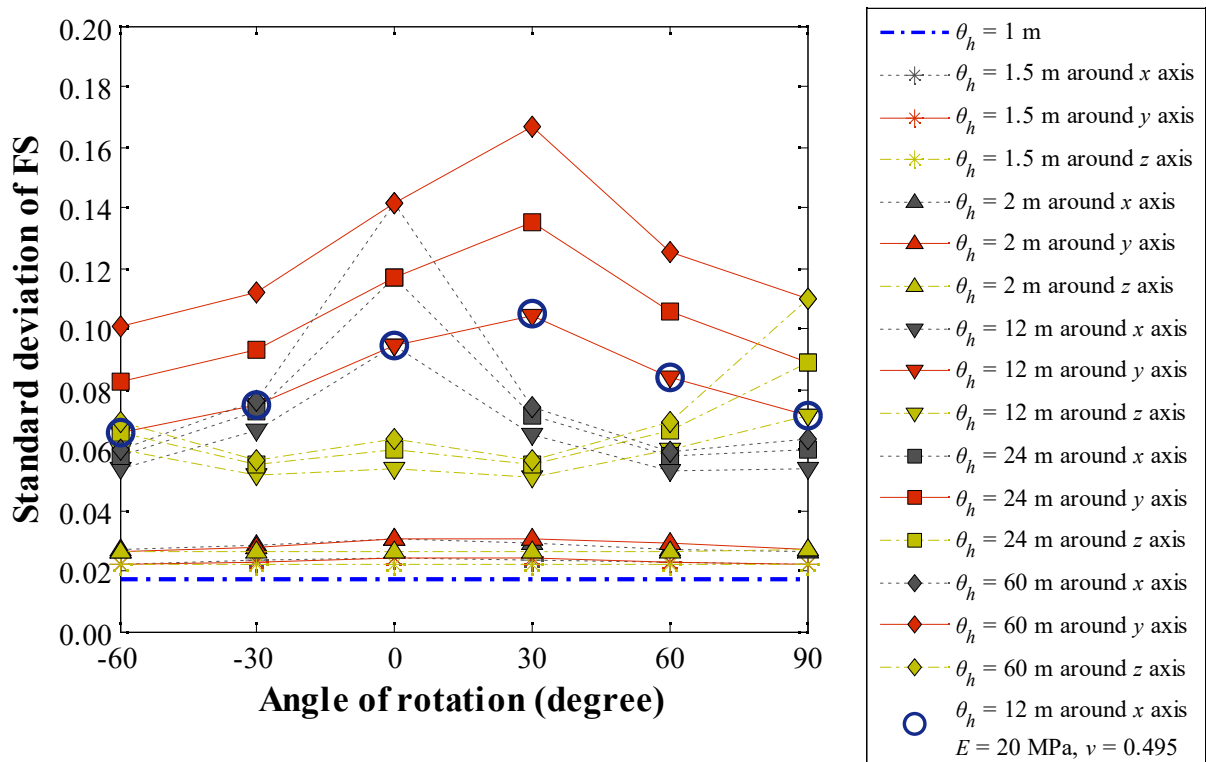
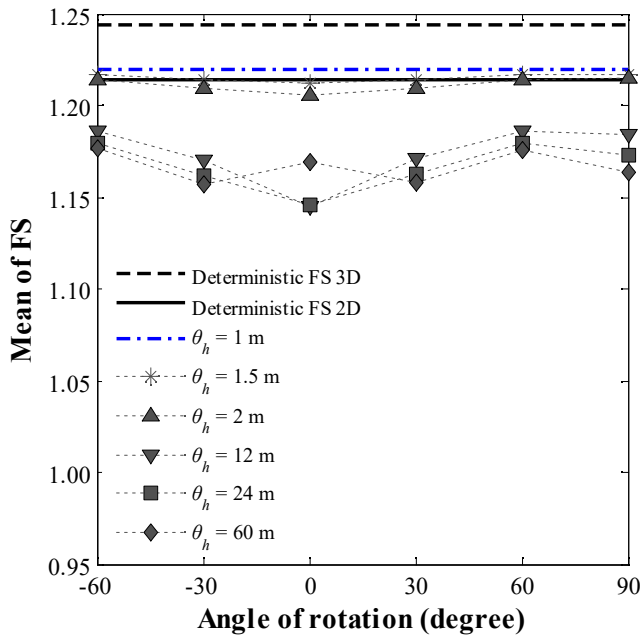
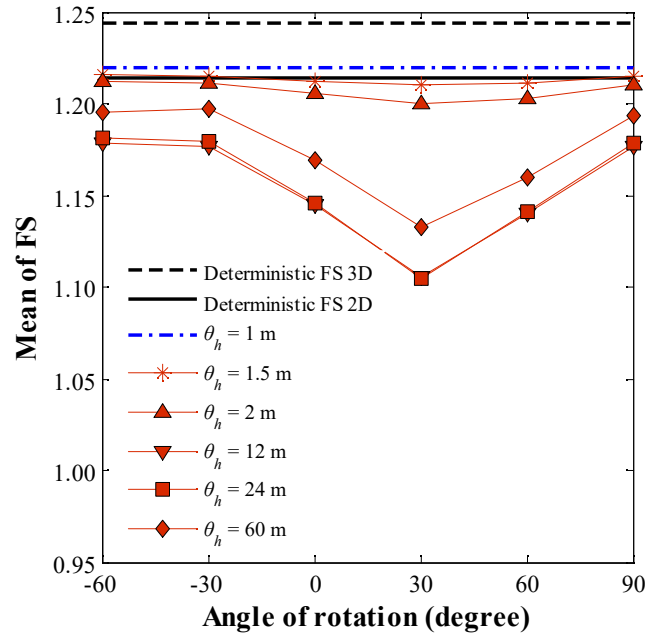


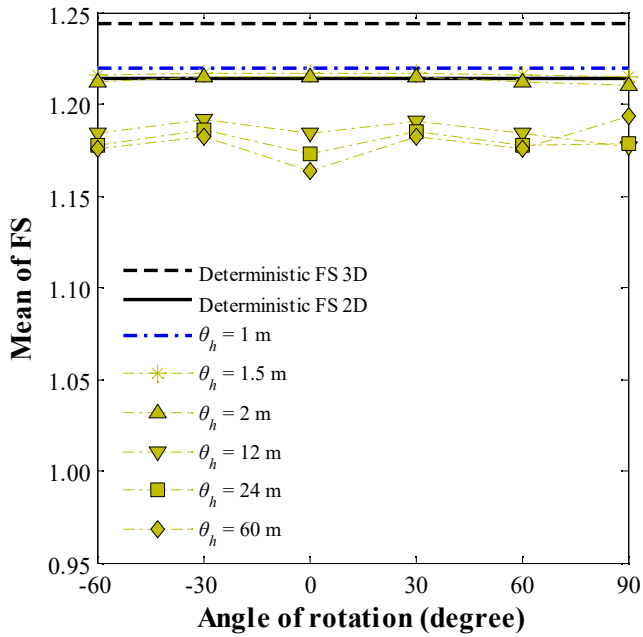
Figure 4.6 Standard deviation of FS versus angle of rotation.



(a)



(b)



(c)

Figure 4.7 Mean of FS versus angle of rotation under: (a) rotated anisotropy around the x axis; (b) rotated anisotropy around the y axis; (c) rotated anisotropy around the z axis.

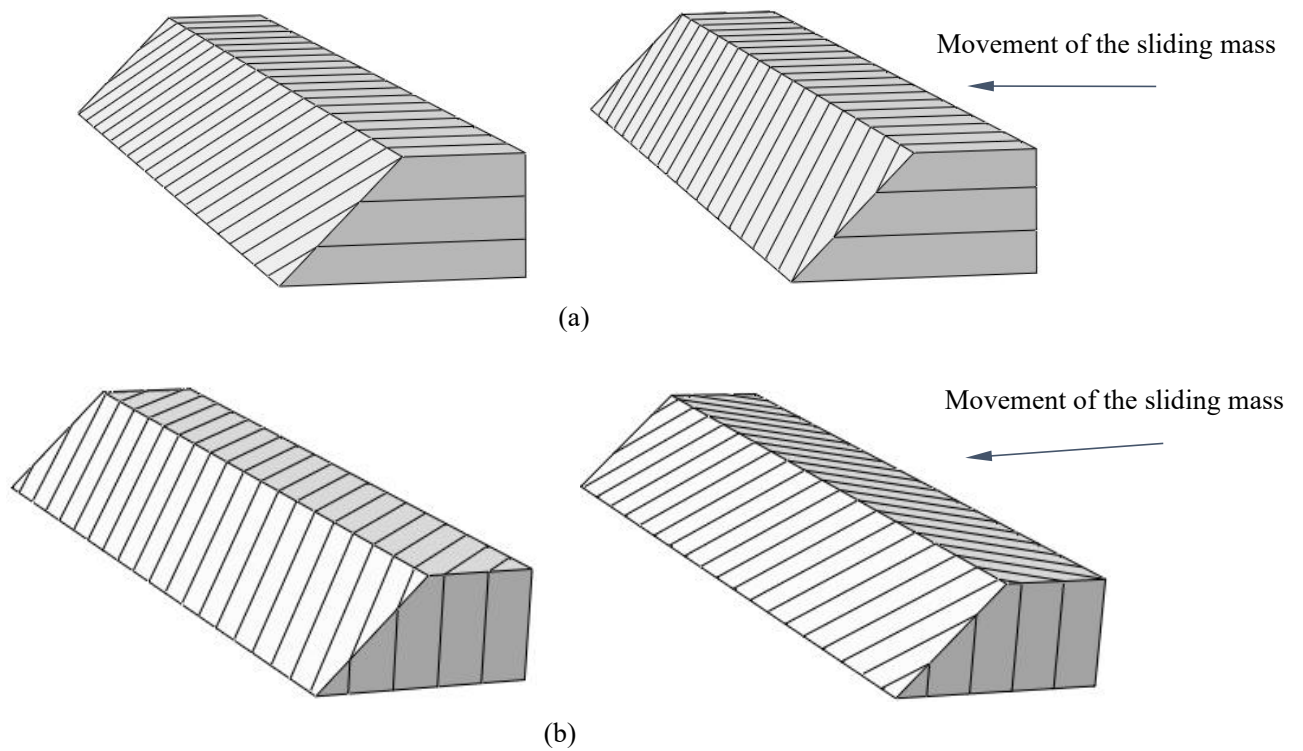
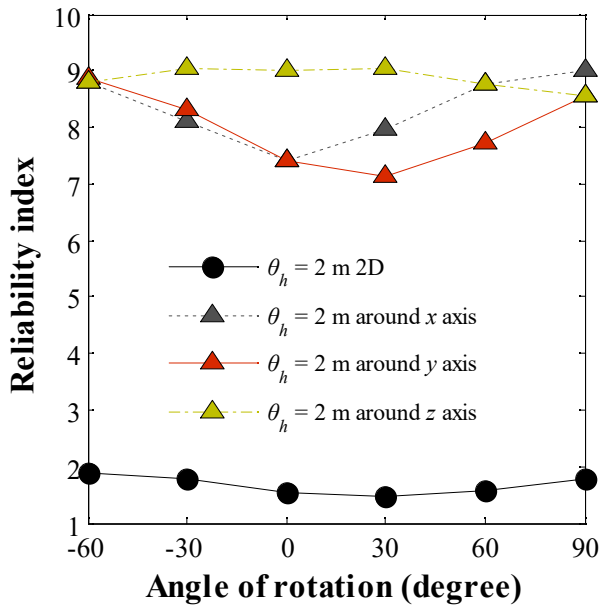
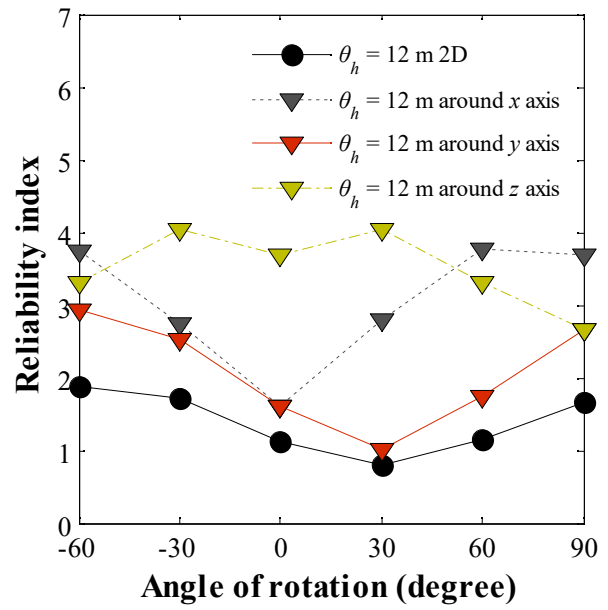


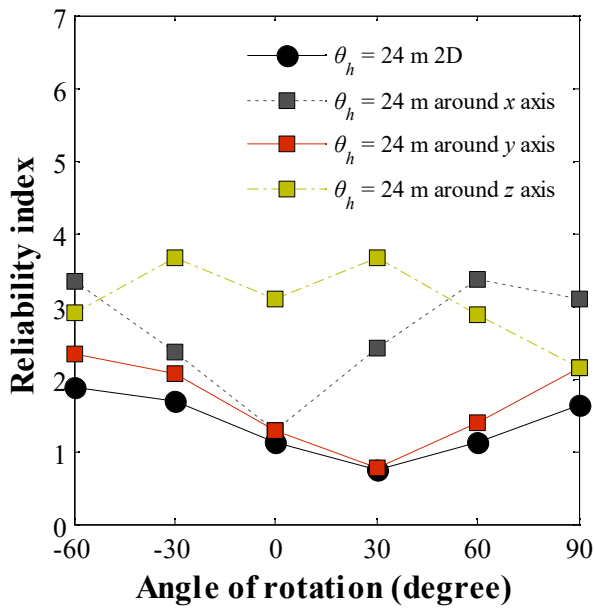
Figure 4.8 (a) Two slopes under rotated anisotropy around the x axis with the same degrees of rotation and opposite rotational directions; (b) two slopes under rotated anisotropy around the z axis with the same degrees of rotation and opposite rotational directions.



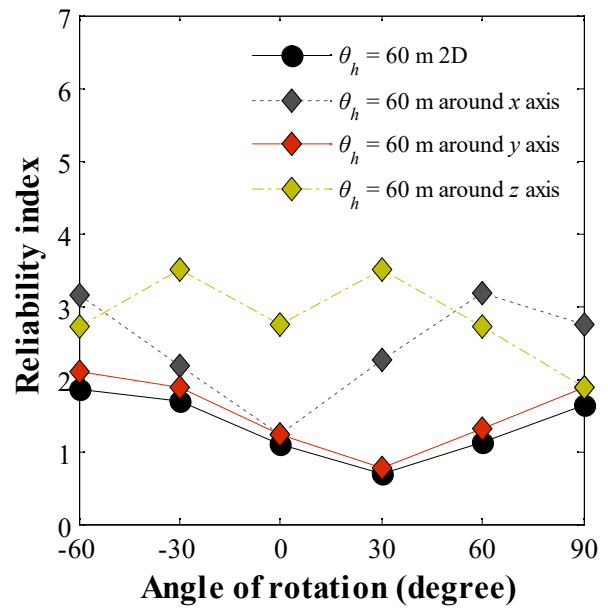
(a)



(b)



(c)



(d)

Figure 4.9 Reliability index versus angle of rotation: (a) $\theta_1 = 2$ m; (b) $\theta_1 = 12$ m; (c) $\theta_1 = 24$ m; (d) $\theta_1 = 60$ m.

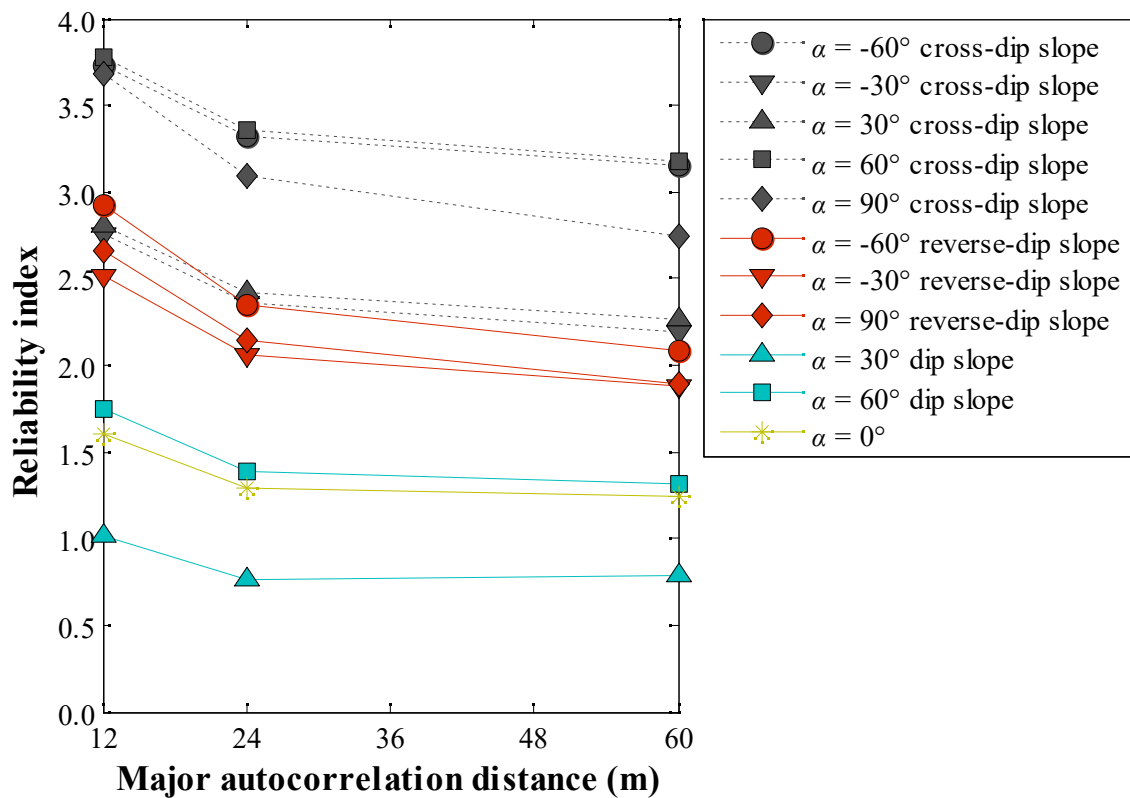
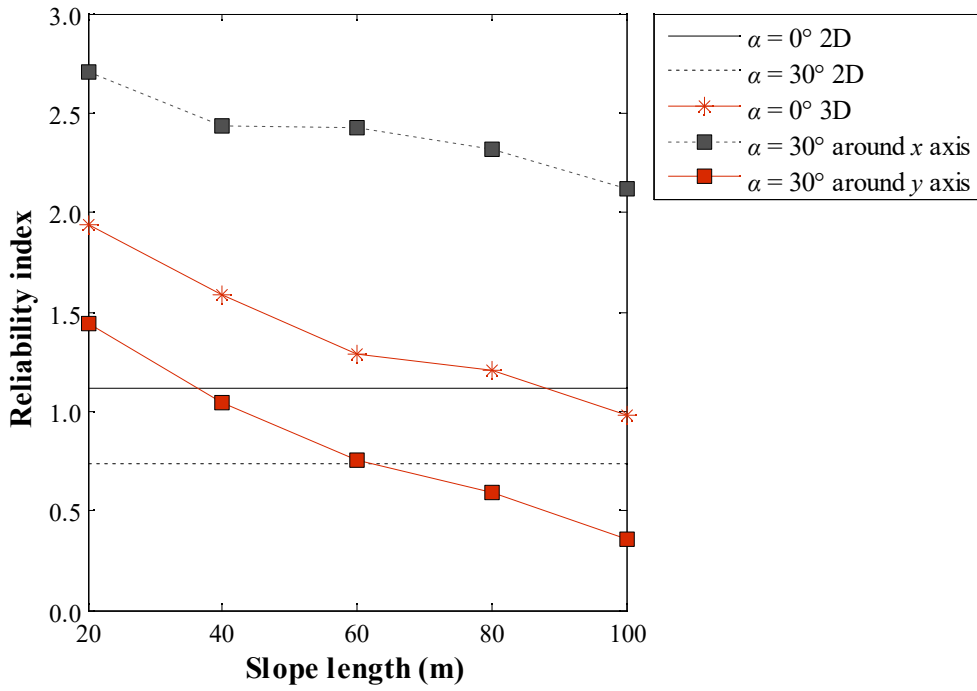
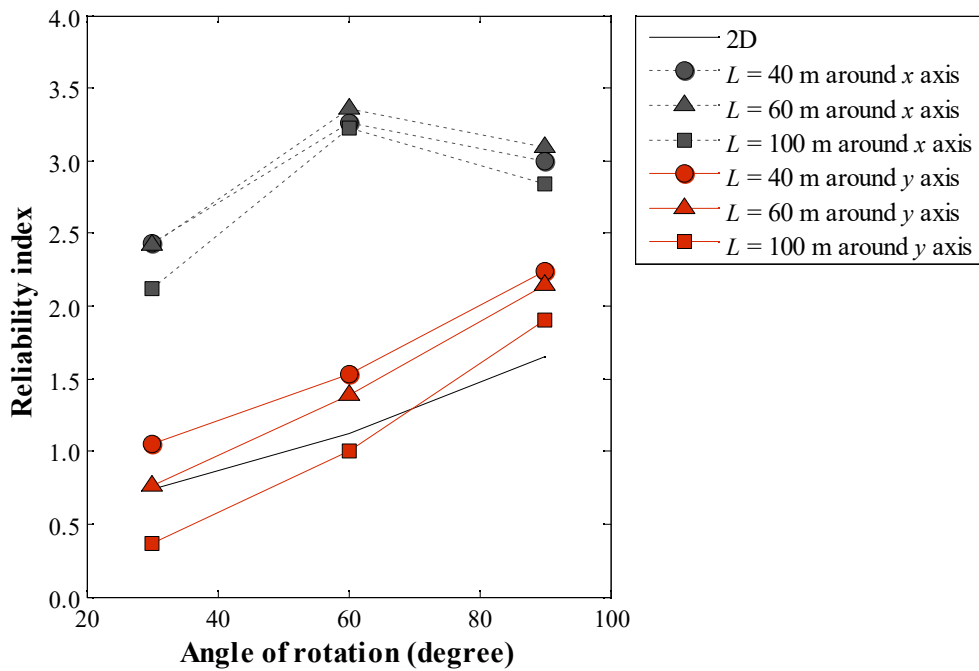


Figure 4.10 Reliability index β versus major autocorrelation distance.



(a)



(b)

Figure 4.11 Reliability index β with $\theta_1 = 24$ m versus: (a) slope length; (b) angle of rotation.

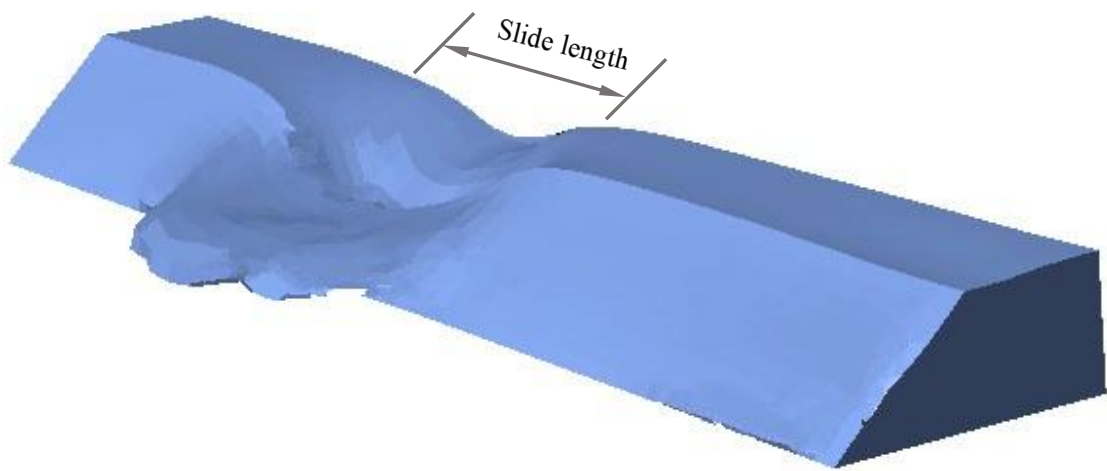


Figure 4.12 Slide length of a slope.

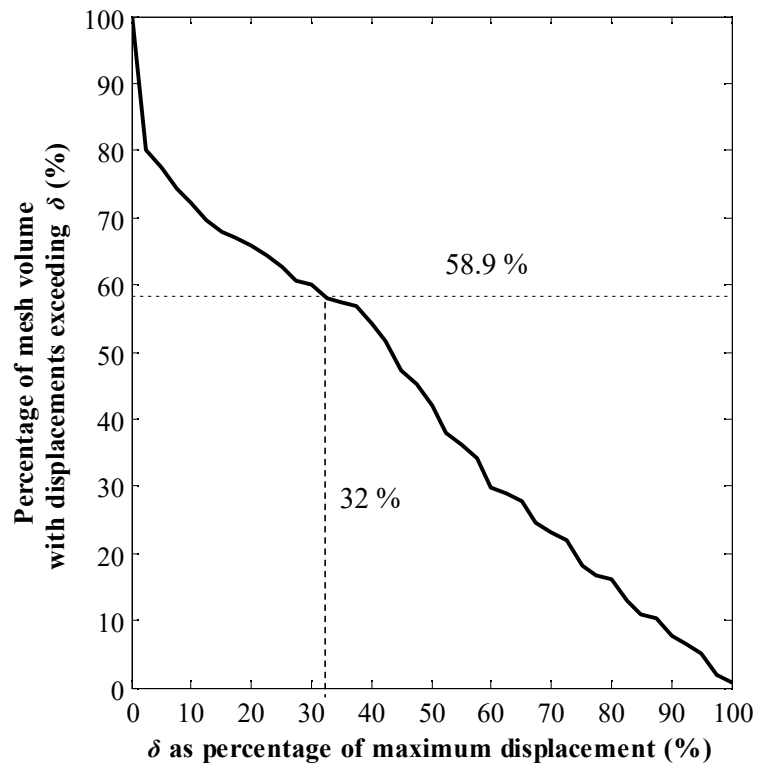


Figure 4.13 Relationship between displacement δ_0 and the volume of soil mass with displacements exceeding δ_0 .

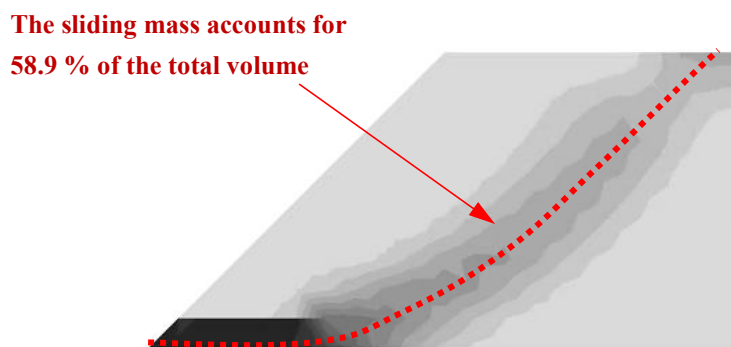
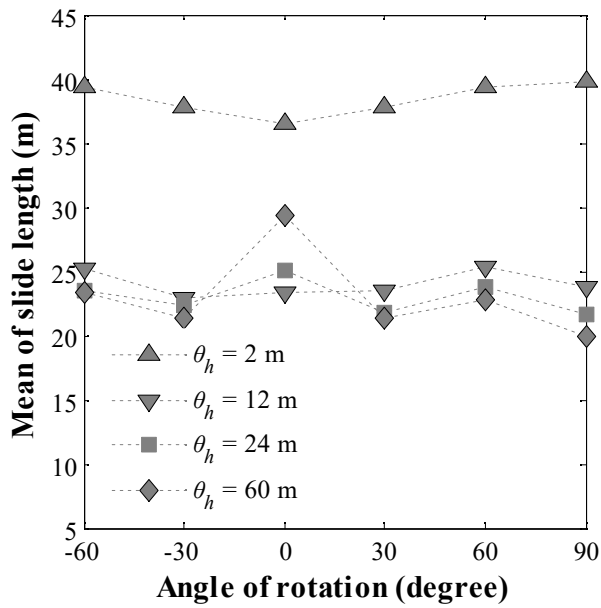
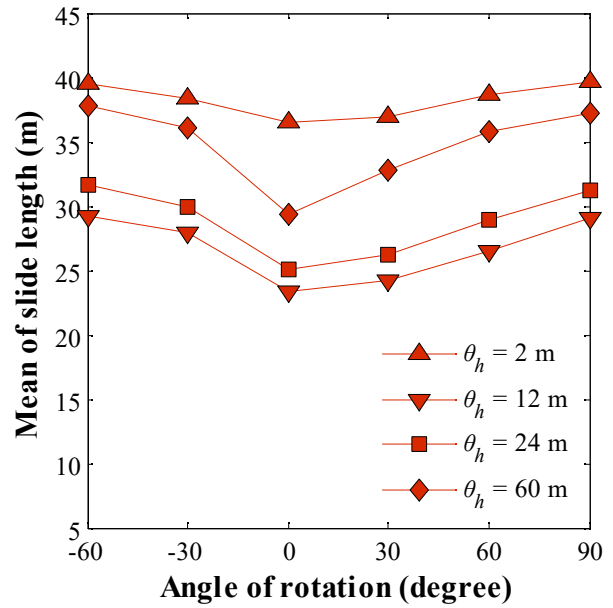


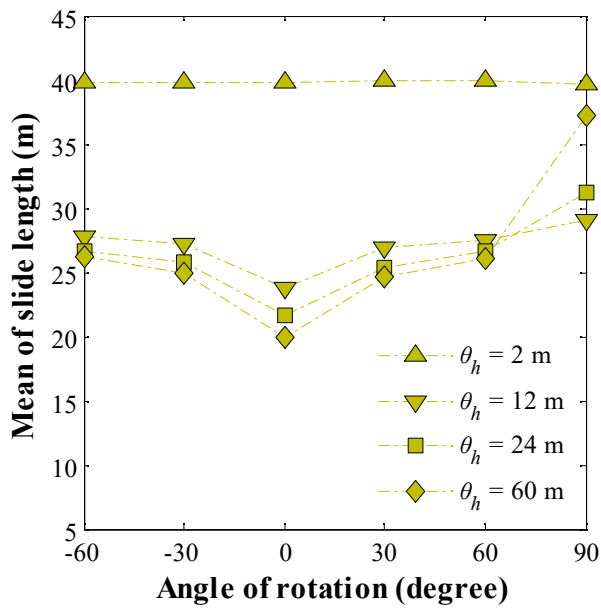
Figure 4.14 Slip surface and plastic strain contour (darker parts indicate higher shear strain).



(a)



(b)



(c)

Figure 4.15 Mean of slide length versus angle of rotation considering the threshold of 32 % of the maximum computed displacement: (a) rotated anisotropy around the x axis; (b) rotated anisotropy around the y axis; (c) rotated anisotropy around the z axis.

CHAPTER 5 Sampling Effects in 2D Probabilistic Slope Stability Analyses

5.1 Introduction

The previous chapters investigated the slope reliability using unconditional random fields. In engineering practice, sampling points with known soil properties are usually obtained in geotechnical site investigations. The use of unconditional random fields cannot consider those known points in slope reliability analysis. To incorporate the sampling effects in geotechnical reliability analyses, conditional random field can be adopted (Lloret-Cabot *et al.* 2014; Li *et al.* 2016b; Liu *et al.* 2017b, etc.). In these studies, the conditional random field model reported by Frimpong and Achireko (1998) was adopted [i.e., Eq. (2.32)], where ordinary Kriging is employed and the prediction error at each spatial point is simulated by Monte Carlo simulation (i.e., conditional RF model 1). The effects of sampling strategy on the variance of system response can be quantified by the magnitude of uncertainty reduction, $\sigma_{\text{cond}}(\text{FS}) / \sigma_{\text{uncond}}(\text{FS})$, where a smaller value of $\sigma_{\text{cond}}(\text{FS}) / \sigma_{\text{uncond}}(\text{FS})$ indicates a higher magnitude of uncertainty reduction. However, Liu *et al.* (2017b) found that when using the conditional RF model 1, the standard deviation of FS after conditioning, $\sigma_{\text{cond}}(\text{FS})$, may be estimated to be higher than that obtained by the unconditional random field simulation method, $\sigma_{\text{uncond}}(\text{FS})$. Such an issue may occur when the sampling points are quite sparse with

small spatial autocorrelation distances. Liu *et al.* (2017b) did not systematically study the issue of $\sigma_{\text{cond}}(\text{FS}) > \sigma_{\text{uncond}}(\text{FS})$ by conditional RF model 1, and the reason for this problem was not discussed in detail. Moreover, Liu *et al.* (2017b) only considered horizontally deposited soils with a separated single exponential function. It is worthwhile to investigate the sampling effects and the problem of $\sigma_{\text{cond}}(\text{FS}) > \sigma_{\text{uncond}}(\text{FS})$ associated with other patterns of soil spatial variability.

Lo and Leung (2017) proposed a conditional random field model that is based on covariance matrix decomposition technique, where the spatial autocorrelation matrix after conditioning is considered (i.e., conditional RF Model 2) [Eqs. (2.36) and (2.37)]. Both conditional random field simulation methods can be used to quantify the uncertainty reduction of system response after conditioning for a given sampling pattern. However, as discussed in Section 2.7.3, when determining the sampling pattern with the maximum magnitude of uncertainty reduction (i.e., optimal sampling pattern), the computational effort would be extensive by conditional random field simulation methods. In order to determine the optimal sampling pattern in an efficient way, Lo and Leung (2018) proposed a method based on the Sobol sensitivity index, which can consider spatially correlated random variables. Using the extended Sobol index formulation, the Sobol index for each sampling pattern can be obtained, where a higher Sobol index indicates higher sampling efficiency. The optimal sampling pattern can then be defined as sampling pattern with the maximum Sobol index value.

In this chapter, the methods mentioned in the previous paragraphs (i.e., conditional RF models 1 and 2, Sobol index method) are adopted in 2D probabilistic slope stability analyses. The random limit equilibrium method associated with the Bishop method is used under the Monte Carlo framework, due to the low computational cost and acceptable accuracy in probabilistic slope stability analysis, as discussed in Section 2.3.4. A slope under undrained conditions is considered, together with various sampling strategies and spatial correlations in soil properties. Also, rotated transverse anisotropy in the soil properties is considered associated with various rotational angles of the strata. Based on the comparison of the results, the merits and limitations of each method are discussed.

5.2 Methodology

5.2.1 Conditional Random Field Modelling and Stationarity Assumptions

The conditional RF model 1 by Frimpong and Achireko (1998) is based on Kriging interpolation. For the Kriging interpolation method, stationarity is an essential precondition. Meanwhile, in the conditional RF model 2, the use of Eqs. (2.36) and (2.37) should also be based on stationarity assumptions. That means the original formulations for conditional RF models 1 and 2 can only be adopted to simulate the

random field based on a normal distribution. However, if a normal distribution is considered in simulating soil properties, meaninglessly negative values can be obtained. In order to simulate a log-normal random by the conditional RF model 1, where negative values are not possible, a simple transformation can be made as follows:

$$\mathbf{z}_{\logcr} = \mathbf{z}_{\logkm} + (\mathbf{z}_{\logur} - \mathbf{z}_{\logks}) \quad (5.1)$$

$$\mathbf{z}_{cr} = \exp(\mathbf{z}_{\logcr}) \quad (5.2)$$

In Eq. (5.1), \mathbf{z}_{\logcr} is the conditional random field under log-transformation; \mathbf{z}_{\logur} is the logarithm of the unconditional random field, while \mathbf{z}_{\logkm} and \mathbf{z}_{\logks} are the Kriging fields based on the logarithm of the measured values and the Kriging field based on the simulated values of \mathbf{z}_{\logur} at the sampling locations, respectively. The implementation of Eq. (5.1) indicates the random field is first generated using a logarithmic transformation, which can then be back-transformed to the original space through exponential transformation by Eq. (5.2). Similar to the conditional RF model 1, the conditional RF model 2 is also generated first under the log-transformation, where the soil properties at the sampling locations are transformed to the logarithmic form and the variance under log-transformation is considered. After that, the random fields in the log-space are also transformed to the original space through exponential transformation [Eq. (5.2)].

5.2.2 Polynomial Chaos Expansion

In this chapter, the model response incorporated in the Sobol index method is

constructed by the response surface method, where the 2nd order PCE function [Eq. (2.17)] is adopted. The PCE function is used to approximate the complex deterministic model representing the relation between FS and spatially variable soil properties (i.e., spatially correlated random variables of a random field). As the number of spatially correlated random variables for a random field is usually large, if all the random variables are incorporated, the required number of training samples for determining the PCE coefficients would significantly increase. That would indicate the significant increase in the number of calls of the slope stability analysis. As proposed by Lo and Leung (2017), considering the significant terms in PCE can lead to sufficient accuracy for predicting model response. In this chapter, only the elements corresponding to the first M terms in the diagonal matrix Λ_d [Eq. (2.40)] are considered, which is determined by (Lo and Leung 2017):

$$\min_M \sum_{i=1}^M \lambda_i > v_p d \quad (5.3)$$

where v_p is the preserved percentage of total variance; and λ_i is the i th eigenvalue in the diagonal matrix Λ_d [Eq. (2.40)]. In this chapter, $v_p > 90\%$ is considered. The 2nd order PCE coefficient vector \mathbf{a} can be obtained by regression analysis as follows:

$$\mathbf{a} = (\mathbf{\Theta}^T \mathbf{\Theta})^{-1} \mathbf{\Theta}^T \boldsymbol{\eta} \quad (5.4)$$

where $\mathbf{\Theta}$ is a matrix containing polynomials constructed by ξ [Eqs. (2.17) and (2.41)], corresponding to N_T random field realisations. In this chapter, $\boldsymbol{\eta}$ is a vector containing N_T values of FS by slope stability analysis under Monte Carlo simulation, and N_T should result in the coefficient of determination $Q^2 > 0.95$. The Q^2 is based on leave-one-out cross validation, which can indicate better prediction capability of PCE

than the traditional R^2 in linear regression (Blatman and Sudret 2010).

5.2.3 Sobol Index Method

The extended formulations of the Sobol index method by Lo and Leung (2018) that can consider spatially correlated random variables were reported previously in Section 2.7.2. This section will discuss the implementation procedure for the Sobol index method.

In the Sobol index method, the performance function between the model response (i.e., FS) and spatially variable soil properties should be constructed using the training samples by the unconditional random field simulation method. For reducing the number of random variables in the performance function, sparse polynomial chaos expansion is adopted. Firstly, the eigenvectors and eigenvalues of the spatial autocorrelation matrix can be obtained through eigen decomposition [Eq. (2.40)]. The PCE coefficient can be determined through Eq. (5.4), considering a number of training samples by Monte Carlo simulation. The Sobol index can then be obtained and used to quantify the magnitude of uncertainty reduction, $\sigma_{\text{cond}}(\text{FS}) / \sigma_{\text{uncond}}(\text{FS})$, using Eq. (2.39). The implementation procedure for the Sobol index method can be summarised as follows:

Step 1: Define the settings for generating the unconditional random field (e.g., mean

and standard deviation of the soil properties, probability distribution, and autocorrelation structure).

Step 2: Conduct eigen decomposition of spatial autocorrelation matrix using Eq. (2.40) and then determine the number of significant items, M , in the PCE using Eq. (5.3).

Step 3: Generate the unconditional random fields, and conduct RLEM to obtain a number of training samples.

Step 4: Construct the model response through the 2nd order PCE function [Eq. (2.17)] considering M significant random variables, and the PCE coefficients are obtained by Eq. (5.4).

Step 5: Determine the original variance of the model response (i.e., FS) by Eq. (2.42), and the variance after conditioning for a given sampling pattern by Eq. (2.44).

Step 6: Sobol index $S(\mathbf{X})$ for a given sampling pattern is determined by Eq. (2.38), while the magnitude of uncertainty reduction can be obtained by Eq. (2.39).

5.3 Case Description

A slope under undrained conditions is investigated (Figure 5.1). The height of the

slope is 5 m with a firm base at 10 m below the top of the slope, and the slope gradient is 1:2. For coupling with random fields, this slope is discretised into 910 elements, which are mainly 0.5 m × 0.5 m square with the elements along the slope face truncated to fit the geometry. The undrained shear strength s_u is assumed to be statistically characterised by a log-normal distribution, and the mean and COV of s_u are equal to 23 kPa and 0.3, respectively. The saturated unit weight γ_{sat} is assumed to be a constant value equal of 20 kN/m³, as the COV of the unit weight is usually small. A Gaussian autocorrelation function is considered in this chapter, where a rotational angle of strata, α , is incorporated for simulating rotated transverse anisotropy, which is given as follows:

$$\rho(\tau_x, \tau_y) = \exp \left[- \left(\frac{(\tau_x \cos \alpha + \tau_y \sin \alpha)^2}{\theta_1^2} + \frac{(-\tau_x \cos \alpha + \tau_y \sin \alpha)^2}{\theta_2^2} \right) \right] \quad (5.5)$$

As discussed in Section 3.3, θ_2 for undrained shear strength is generally in the range of 0.1 - 6 m, and θ_1 is far larger than θ_2 , according to the literature. In this chapter, $\theta_1 = 20$ m and $\theta_2 = 2$ m are taken as the base set, while various θ_2 in {1 m, 1.5 m, 2 m, 2.5 m, 3 m} are also considered. It should be noted that measured values at known points should be used in simulating the conditional RF. In the current work, the mean soil property is assigned to the sampling locations. That is because there is no real measurement data, and investigated results by different methods should be compared considering various sampling strategies. It should be noted that since the conditional RF simulations are implemented under a log-transformation first, the adopted mean values should be the mean of the logarithm of the soil property. The mean and

standard deviation of the soil properties (e.g., s_u) in log space can be given as follows (Griffiths *et al.* 2004):

$$\sigma_{\ln s_u} = \sqrt{\ln(1 + COV_{s_u}^2)} \quad (5.6)$$

$$\mu_{\ln s_u} = \ln \mu_{s_u} - \frac{1}{2} \sigma_{\ln s_u}^2 \quad (5.7)$$

The slope stability analysis is implemented by the Bishop method considering the mean shear strength, and the FS is found to be 1.358 which is close to the result by Cho (2010) (FS = 1.356). For the probabilistic slope stability analysis, the non-intrusive approach (Section 3.2.1) that combines the random field with the limit equilibrium method (i.e., the Bishop method) is used.

5.4 Results

In this section, comparative studies are conducted on the methods that can consider sampling effects (i.e., conditional RF models 1 and 2, Sobol index method). In Section 5.4.1, the magnitude of uncertainty reduction is investigated by the various methods, considering various sampling strategies under horizontal transverse anisotropy (i.e., $\alpha = 0^\circ$). Meanwhile, the influences of rotated transverse anisotropy on the standard deviation of FS after conditioning and ratio of $\sigma_{\text{cond}}(\text{FS}) / \sigma_{\text{uncond}}(\text{FS})$ are investigated in Section 5.4.2. The rotational angle of soil bedding is varied in the range of $-90^\circ < \alpha < 90^\circ$. It should be noted that the strata with $\alpha = -90^\circ$ is equivalent to

that with $\alpha = 90^\circ$ in this chapter, since stationary RF is considered. The advantages and disadvantages of each method are discussed in Section 5.4.3.

In order to obtain the magnitude of uncertainty reduction $[\sigma_{\text{cond}}(\text{FS}) / \sigma_{\text{uncond}}(\text{FS})]$, 2,000 Monte Carlo simulations are considered for the unconditional random field simulation method and the conditional random field simulation methods. When using the Sobol index method, the model response is constructed considering 2,000 Monte Carlo simulations with the use of the unconditional random field, and $\sigma_{\text{cond}}(\text{FS}) / \sigma_{\text{uncond}}(\text{FS})$ can be obtained by Eq. (2.39). Generally, $\sigma_{\text{cond}}(\text{FS}) / \sigma_{\text{uncond}}(\text{FS}) < 1$ is expected, which means the performance uncertainty is reduced through considering sample points.

5.4.1 Influence of Sampling Strategy on Magnitude of Uncertainty Reduction

In this section, sampling strategies with various sampling densities are considered to investigate the influence of the sampling pattern on the performance of the methods in slope reliability evaluation.

Firstly, sampling strategies with different numbers of sample points along the inclined direction are considered, where $n = 2, 3$ and 5 denotes that the soil samples are taken from $\{A, E\}$, $\{A, C, E\}$ and $\{A, B, C, D, E\}$, respectively, in Figure 5.1. In site

investigations, a number of boreholes can be drilled, but limited samples are usually taken from the boreholes due to the relatively high cost of laboratory. Figures 5.2(a), (b), and (c) show the ratio of $\sigma_{\text{cond}}(\text{FS}) / \sigma_{\text{uncond}}(\text{FS})$ versus the minor autocorrelation distance θ_2 for $n = 2, 3$, and 5 , respectively. As can be observed from Figure 5.2, the results from the conditional RF model 2 and the Sobol index method are close, and the $\sigma_{\text{cond}}(\text{FS}) / \sigma_{\text{uncond}}(\text{FS})$ is overestimated by the conditional RF model 1. When $n = 2$ with $\theta_2 = 1$ to 3 m and $n = 3$ with $\theta_2 = 1$ m, $\sigma_{\text{cond}}(\text{FS}) / \sigma_{\text{uncond}}(\text{FS})$ is larger than 1 by the conditional RF model 1. The issue of $\sigma_{\text{cond}}(\text{FS}) / \sigma_{\text{uncond}}(\text{FS}) > 1$ cannot be observed when using the conditional RF model 2 and the Sobol index method. When $n = 5$, $\sigma_{\text{cond}}(\text{FS}) / \sigma_{\text{uncond}}(\text{FS})$ is smaller than 1 by all the methods. These results show that the sparse distribution of sample points may be a cause of the issue of $\sigma_{\text{cond}}(\text{FS}) / \sigma_{\text{uncond}}(\text{FS}) > 1$ by conditional RF model 1, but Figure 5.2(b) also shows that with higher minor autocorrelation distance, such a problem may disappear. Table 5.1 presents the results of $\sigma_{\text{cond}}(\text{FS}) / \sigma_{\text{uncond}}(\text{FS})$ with $\theta_2 = 10$ m. It can be seen that with a large minor autocorrelation distance, the ratio of $\sigma_{\text{cond}}(\text{FS}) / \sigma_{\text{uncond}}(\text{FS})$ would be smaller than 1 under $n = 2$ by conditional RF model 1, and the differences of $\sigma_{\text{cond}}(\text{FS}) / \sigma_{\text{uncond}}(\text{FS})$ are small using the various methods. Besides, as shown in Figure 5.2, the $\sigma_{\text{cond}}(\text{FS}) / \sigma_{\text{uncond}}(\text{FS})$ decreases with higher minor autocorrelation distance. That is because, when the autocorrelation distance increases, the Kriging variance [i.e., $\mathbf{z}_{ur} - \mathbf{z}_{ks}$ in conditional RF model 1 and σ_z^2 in conditional RF model 2 (Section 2.7.1)] would decrease, which indicates the larger reduction effects on the spatial uncertainty and thus the smaller $\sigma_{\text{cond}}(\text{FS})$ (Li *et al.* 2016b).

Secondly, vertical boreholes at various locations are considered, with different numbers of sample points taken from each borehole. The best sampling location among the various borehole positions can be obtained through finding the borehole position with the smallest $\sigma_{\text{cond}}(\text{FS}) / \sigma_{\text{uncond}}(\text{FS})$. Figure 5.3 shows the magnitude of uncertainty reduction for each borehole location shown in Figure 5.1 (the borehole position numbers are from 1 to 10), with $\theta_1 = 20$ m and $\theta_2 = 2$ m. Two sampling strategies are considered in each borehole, where $n = 2$ [Figure 5.3(a)] indicates the sampling points are taken at the elevations of a and e in Figure 5.1, and $n = 5$ [Figure 5.3(b)] indicates the sampling points are taken at the five elevation levels. As shown in Figure 5.3(a), when taking sparse sampling points within each borehole, the ratio of $\sigma_{\text{cond}}(\text{FS}) / \sigma_{\text{uncond}}(\text{FS})$ by conditional RF model 1 is larger than 1 and much higher than the results estimated by conditional RF model 2 and the Sobol index method. By contrast, the ratio of $\sigma_{\text{cond}}(\text{FS}) / \sigma_{\text{uncond}}(\text{FS})$ by conditional RF model 2 is smaller than 1 considering each sampling location, and close to that by the Sobol index method. Also, it can be observed that the magnitudes of uncertainty reduction by conditional RF model 2 and the Sobol index method would become smaller (i.e., $\sigma_{\text{cond}}(\text{FS}) / \sigma_{\text{uncond}}(\text{FS})$ becomes higher) when the borehole position recedes from the slope crest, but such a tendency cannot be shown by the curve of conditional RF model 1 when $n = 2$. When five sampling points are taken within each borehole [Figure 5.3(b)], the ratios of $\sigma_{\text{cond}}(\text{FS}) / \sigma_{\text{uncond}}(\text{FS})$ estimated by the various methods are close. Meanwhile, in this situation, all the curves can show gradually increasing tendencies when the sampling

position recedes from the slope crest, meaning that the optimal sampling location among the 10 borehole positions is around the slope crest. Therefore, findings from Figure 5.3 also indicate that under a sparse sampling pattern, conditional RF model 1 may produce inaccurate estimation of the best sampling location.

The results in this section show that the difference between $\sigma_{\text{cond}}(\text{FS}) / \sigma_{\text{uncond}}(\text{FS})$ by conditional RF model 2 and that by the Sobol index method is slight, considering various sampling strategies and spatial correlations in soil property. By contrast, the conditional RF model 1 would generally produce higher $\sigma_{\text{cond}}(\text{FS}) / \sigma_{\text{uncond}}(\text{FS})$ ratios than those by the other methods. When considering sparse sampling patterns with small θ_2 , the results by conditional RF model 1 would be significantly different from those by the other methods, while with sufficient sampling points or a large θ_2 , the difference would be small. Besides, the issue of $\sigma_{\text{cond}}(\text{FS}) > \sigma_{\text{uncond}}(\text{FS})$ may occur when using conditional RF model 1 under a sparse sampling pattern with a small θ_2 , while such a problem cannot be observed when using conditional RF model 2 and the Sobol index method. The reasons why conditional RF model 1 would produce higher ratios of $\sigma_{\text{cond}}(\text{FS}) / \sigma_{\text{uncond}}(\text{FS})$ than those by the other methods and may indicate $\sigma_{\text{cond}}(\text{FS}) / \sigma_{\text{uncond}}(\text{FS}) > 1$, will be discussed later in Section 5.4.3, so as to integrate the findings considering rotated transverse anisotropy, which is examined in the following section.

5.4.2 Influence of Rotated Transverse Anisotropy on Magnitude of Uncertainty Reduction

In this section, the influence of rotated transverse anisotropy on the slope reliability evaluation is investigated by the various methods, where various rotational angles of the strata, α , and two sampling patterns (Figure 5.4) are considered with $\theta_1 = 20$ m and $\theta_2 = 2$ m. The vertical sampling pattern can often be encountered in engineering practice when a single vertical borehole is drilled, while a inclined borehole can also be found in some engineering cases (He *et al.* 2010; Wei and Liu 2015).

The standard deviation of FS can be used to quantify the performance uncertainty of the system response in slope reliability analysis (Li *et al.* 2016b; Liu *et al.* 2017b), where a higher standard deviation of FS means a higher performance uncertainty. Figures 5.5(a) and (b) show the results of standard deviation of FS by the various methods under the vertical sampling pattern and inclined sampling pattern, respectively. Figure 5.5 shows that changes in the standard deviation of FS with rotational angle are different under different sampling patterns. It can be noted that for each sampling pattern, the highest standard deviation of FS occurs when the layout of sample points is along the orientation of the soil bedding. The standard deviation of FS generally becomes higher when α approaches 90° and 45° for vertical sampling pattern and inclined sampling, respectively. It should be noted that, as the rotations under $\alpha = -90^\circ$ and $\alpha = 90^\circ$ are equivalent in this chapter, in the horizontal axes of the figures, α also approaches 45° from 0° to -90° to 45° (i.e., in an opposite direction to

the horizontal axis). That means the performance uncertainty of the slope would increase when the angle of the drilling direction of the borehole approaches the dip angle of the strata.. As discussed in Sections 2.5.3 and 5.3, rotated transverse anisotropy of soil spatial variability is simulated by rotating the horizontally rectangular coordinate system for horizontal transverse anisotropy. With the rotation of the coordinate system, the lag distance in the direction of θ_2 between any two points would become smaller (Figure 5.6). This is equivalent to the sampling points gathering to a spot gradually. Since the reduction effects on the spatial uncertainty of soil properties are more pronounced near the known points, the gathering of the sampling points would indicate the higher spatial uncertainty of the total domain, and thus the higher performance uncertainty. Figures 5.5(a) and (b) also show that the results by conditional RF model 2 and the Sobol index method are close, considering various rotational angles of strata. By contrast, conditional RF model 1 would significantly overestimate the standard deviation of FS after conditioning in most cases considering rotated transverse anisotropy (i.e., $\alpha \neq 0^\circ$). The difference between the results by conditional RF model 1 and the other methods would be more pronounced when the angle of the drilling direction of the borehole approaches the dip angle of the strata. The reason for this phenomenon will be discussed in Section 5.4.3.

Figures 5.7(a) and (b) show the change of $\sigma_{\text{cond}}(\text{FS}) / \sigma_{\text{uncond}}(\text{FS})$ with rotational angle of strata from -90° to 90° under the vertical sampling pattern and inclined sampling

pattern, respectively. As can be observed from the figures, $\sigma_{\text{cond}}(\text{FS}) / \sigma_{\text{uncond}}(\text{FS})$ by the various methods would become higher when the dip angle of the strata approaches the angle of the drilling direction of the borehole. As the sampling points are distributed along the bedding orientation, the magnitude of uncertainty reduction is the smallest. As discussed in the above paragraph, the rotation of the strata would indicate the decrease of the lag distance in the direction of θ_2 , which is equivalent to the sampling points gathering to a spot gradually. Consequently, the constraining effects on the spatial uncertainty imposed by the sampling points would gradually reduce, which cause the increase of $\sigma_{\text{cond}}(\text{FS}) / \sigma_{\text{uncond}}(\text{FS})$. Such a finding indicates that the angle of the drilling direction of the boreholes should not be along or near the dip angle of the strata. From these figures, it can also be seen that $\sigma_{\text{cond}}(\text{FS}) / \sigma_{\text{uncond}}(\text{FS})$ ratios by conditional RF model 2 and the Sobol index method are close and smaller than 1 with various angles of rotation. By contrast, conditional RF model 1 would significantly overestimate $\sigma_{\text{cond}}(\text{FS}) / \sigma_{\text{uncond}}(\text{FS})$ ratio and result in $\sigma_{\text{cond}}(\text{FS}) / \sigma_{\text{uncond}}(\text{FS}) > 1$, when the angle of the drilling direction of the borehole is near the dip angle of the strata, the reason for which will be discussed in the following section.

5.4.3 Discussion

In this section, the reason why $\sigma_{\text{cond}}(\text{FS})$ estimated by conditional RF model 1 might be larger than $\sigma_{\text{uncond}}(\text{FS})$ is examined. Besides, the advantages and limitations of each of the methods that can consider sampling effects are discussed.

The issue of $\sigma_{\text{cond}}(\text{FS}) / \sigma_{\text{uncond}}(\text{FS}) > 1$ is unexpected in slope reliability evaluation. Theoretically, the sampling points would provide known information in simulating spatially variable soils and thus reduce the spatial uncertainty. However, results in this chapter show that $\sigma_{\text{cond}}(\text{FS})$ may be estimated to be larger than $\sigma_{\text{uncond}}(\text{FS})$ by conditional RF model 1, when considering a sparse sampling pattern with a small θ_2 or rotated transverse anisotropy of soils. The cause of this problem can be demonstrated through the rationale of the formulation of conditional RF model 1 [i.e., Eq. (2.32)]. In Eq. (2.32), the deterministic component of the random field is represented by \mathbf{z}_{km} , which is determined by Kriging interpolation of the sample points. In addition, the fluctuation component of the random field is denoted by $\mathbf{z}_{\text{ur}} - \mathbf{z}_{\text{ks}}$, which indicates the Kriging prediction error for \mathbf{z}_{km} simulated in each random field realisation. Herein, \mathbf{z}_{ur} represents a field predicted by \mathbf{z}_{ks} using Kriging interpolation of the simulated values at the sample locations. Hence, the better accuracy of the Kriging interpolation in $\mathbf{z}_{\text{ur}} - \mathbf{z}_{\text{ks}}$ would indicate a smaller Kriging prediction error for \mathbf{z}_{km} in each random field realisation, which results in the smaller fluctuation of the random field and the higher magnitude of uncertainty reduction. However, Kriging interpolation can only be effective with a reasonable layout of the sampling points in consideration of autocorrelation distance. In some cases, there is generally no benefit derived from Kriging interpolation from known points to unknown points. Figure 5.8 shows such cases, including scenarios for a single sample point [Figure 5.8(b)], two very close sample points [Figure 5.8(c)] and two very sparse sample points [Figure

5.8(d)]. The scenario for a single sample point is actually equivalent to the situation when the drill angle of the borehole is the same as that of the dip angle of the strata. In Figure 5.8, the zones where the prediction is ineffective are highlighted by dashed lines. In these zones, the correlations between the unknown and known points cannot act effectively using the Kriging interpolation, indicating that the efficacy of those unknown points is negligible. That means in this situation, the Kriging interpolation performs poorly. Herein, the standard deviation of the resulting conditional random fields with those zones may be higher than that of the unconditional random fields. That is because in those zones, the soil properties at the corresponding elements in \mathbf{z}_{ks} are generally the same in each random field realisation. However, for different random field realisations the value of the soil properties will change, depending on the simulated soil properties at the sample locations. Therefore, when the area of the zone without effective prediction is large enough, the performance uncertainty by conditional RF model 1 can be larger than that by the unconditional RF simulation method. In addition, due to the existence of the zone, estimates of the standard deviation of FS by conditional RF model 1 would generally be larger than those by conditional RF model 2 and the Sobol index method [indicating larger $\sigma_{\text{cond}}(\text{FS}) / \sigma_{\text{uncond}}(\text{FS})$ by conditional RF model 1]. When the number of sample points increases and the distribution of the sample points is set properly considering the dip angle of the strata, the area of the zone would reduce, meaning that the differences between the estimated results by conditional RF model 1 and the other methods would decrease.

The conditional RF model 1 may result in $\sigma_{\text{cond}}(\text{FS}) / \sigma_{\text{uncond}}(\text{FS}) > 1$ under a sparse sampling strategy with a small θ_2 or rotated transverse anisotropy. In these cases, the $\sigma_{\text{cond}}(\text{FS}) / \sigma_{\text{uncond}}(\text{FS})$ would be significantly overestimated. By contrast, the results of $\sigma_{\text{cond}}(\text{FS}) / \sigma_{\text{uncond}}(\text{FS})$ by conditional RF model 2 and the Sobol index method have good agreement under various sampling patterns and rotational angles of the strata. The limitation of conditional RF model 2 is that such a method can only be coupled with the matrix decomposition technique, while under some circumstances (e.g., a very large slope model) other random field generation techniques (e.g., LAS) may indicate less computational time for generating random fields (Section 2.6). Nevertheless, in general, the computational effort for generating random fields is relatively insignificant in geotechnical reliability analysis, when compared to that for thousands of Monte Carlo simulation runs. The Sobol index method is an efficient way to estimate the magnitude of uncertainty reduction for each sampling pattern and thus determine the optimal sampling strategy. However, P_f and the failure scale of the slopes after conditioning cannot be determined by the Sobol index method. That means the Sobol index method is unable to be used in slope risk assessment, where the risk is estimated by the probability of failure multiplied by the failure consequence (i.e., volume of the failure mass) (Liu *et al.* 2017a; Li *et al.* 2016a). Therefore, in general, conditional RF model 2 is suggested to be adopted in slope reliability evaluation and risk assessment, when sampling effects need to be incorporated in engineering practice.

5.5 Summary

In this chapter, sampling effects have been investigated in 2D probabilistic slope stability analyses. The magnitude of uncertainty reduction [$\sigma_{\text{cond}}(\text{FS}) / \sigma_{\text{uncond}}(\text{FS})$] has been investigated considering various sampling strategies and rotated transverse anisotropy. Comparative studies have been conducted using various methods (i.e., conditional RF models 1 and 2, the Sobol index method), while the merits and limitations of each method have been discussed.

Generally, the difference between $\sigma_{\text{cond}}(\text{FS}) / \sigma_{\text{uncond}}(\text{FS})$ by conditional RF model 2 and that by the Sobol index method is small, considering various sampling patterns and rotational angles of the strata. When the sampling pattern is sparse with a small θ_2 or the angle of the drilling direction of the borehole is near the dip angle of the strata, $\sigma_{\text{cond}}(\text{FS}) / \sigma_{\text{uncond}}(\text{FS})$ by conditional RF model 1 would be significantly larger than that by the other methods. In addition, when the sample points are sparsely distributed or the angle of the drilling direction of the borehole is near the dip angle of the strata, $\sigma_{\text{cond}}(\text{FS})$ may be estimated to be larger than $\sigma_{\text{uncond}}(\text{FS})$ by conditional RF model 1, which is unexpected in slope reliability evaluation. This issue is not observed when using conditional RF model 2 and the Sobol index method.

Furthermore, when the distribution orientation of the sample points approaches the dip angle of the strata, $\sigma_{\text{cond}}(\text{FS})$ would increase, and $\sigma_{\text{cond}}(\text{FS}) / \sigma_{\text{uncond}}(\text{FS})$ would also

increase. This is because the lag distance between the sampling points in the direction of θ_2 would change in the rotated coordinate system. As the distribution orientation of the sample points approaches the bedding orientation, the lag distance between the sampling points tends to zero in the direction of θ_2 , and thus the constraining effects imposed by the known points on the spatial uncertainty would reduce gradually.

As conditional RF model 1 may be inaccurate under sparse sampling patterns or rotated transverse anisotropies, conditional RF model 2 and the Sobol index method are better alternatives when conducting slope reliability analysis. However, the Sobol index method cannot produce the probability of failure and the failure scale after conditioning. In conclusion, when compared against conditional RF model 1 and the Sobol index method, conditional RF model 2 provides superior performance in slope risk assessment when considering sampling effects.

Table 5.1 $\sigma_{\text{cond}}(\text{FS}) / \sigma_{\text{uncond}}(\text{FS})$ by the various methods considering sampling effects with $\theta_2 = 10$ m.

n	Methods	$\sigma_{\text{cond}}(\text{FS}) / \sigma_{\text{uncond}}(\text{FS})$	Difference of $\sigma_{\text{cond}}(\text{FS}) / \sigma_{\text{uncond}}(\text{FS})$
2	Conditional RF model 1	0.5848	-2.34%
	Conditional RF model 2	0.5714	
	Sobol index method	0.5952	-4.17%
3	Conditional RF model 1	0.3058	-1.23%
	Conditional RF model 2	0.3021	2.91%
	Sobol index method	0.2933	
5	Conditional RF model 1	0.3106	-4.05%
	Conditional RF model 2	0.2985	3.18%
	Sobol index method	0.2890	

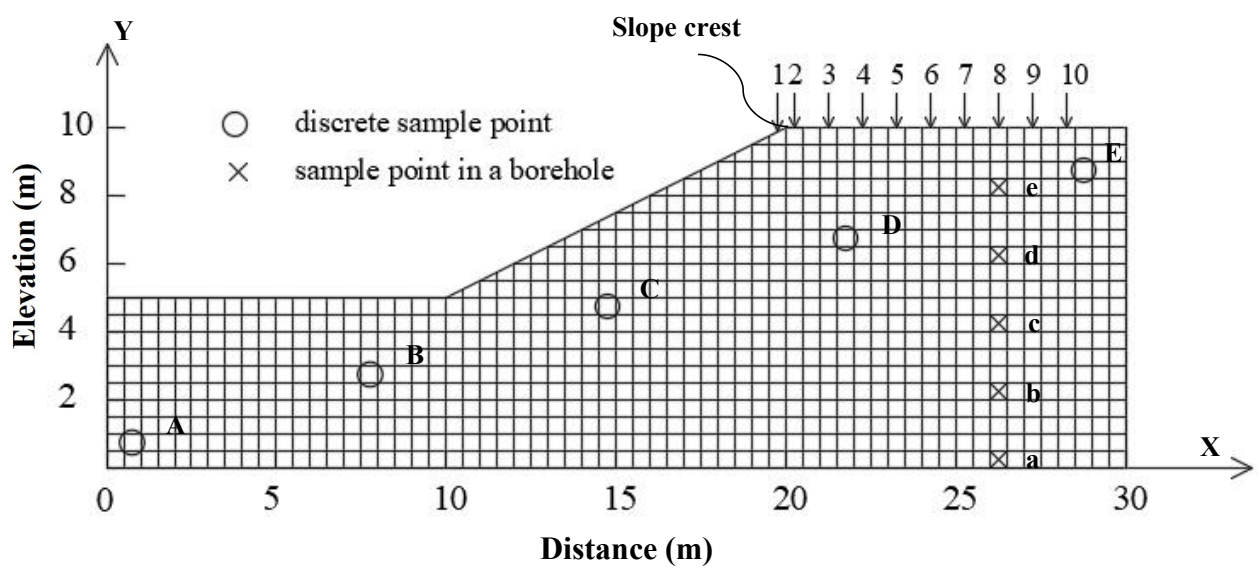
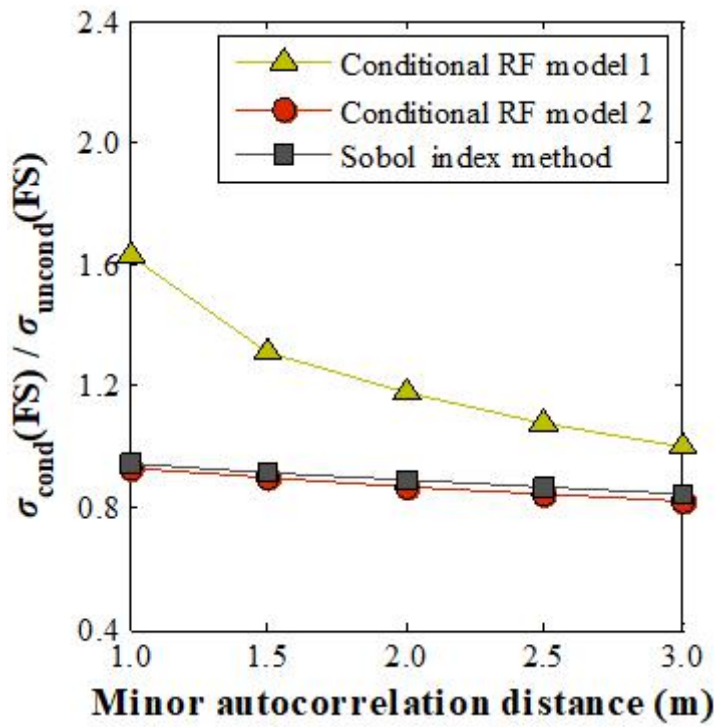
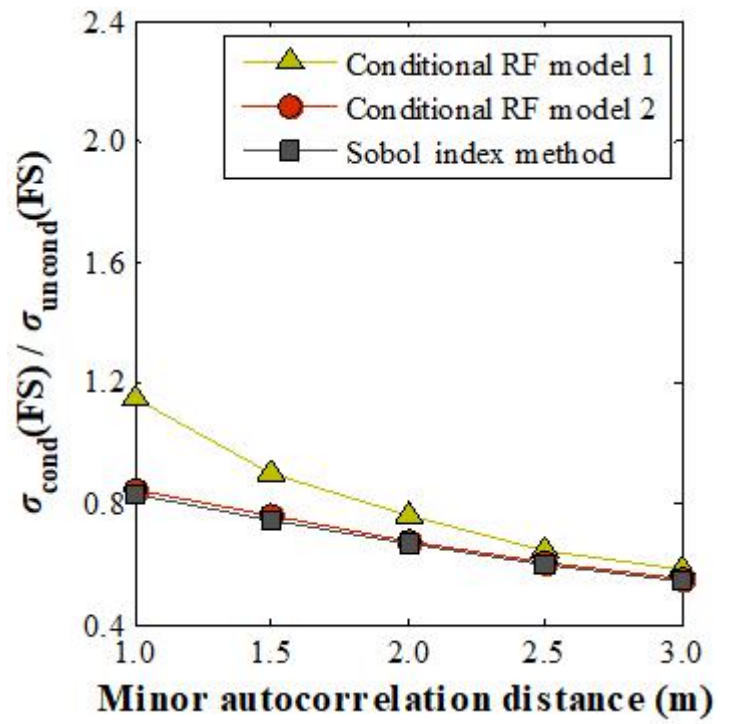


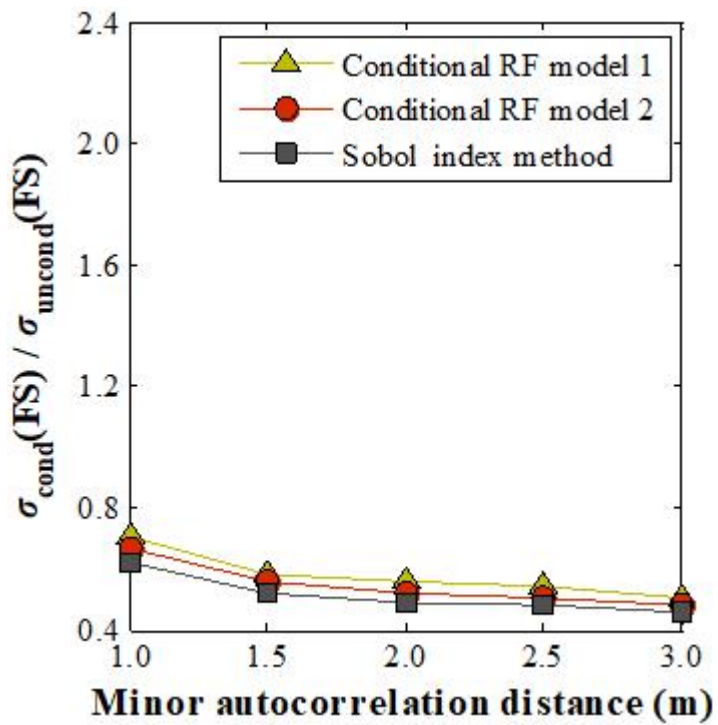
Figure 5.1 Geometry of the slope model and random field discretisation.



(a)

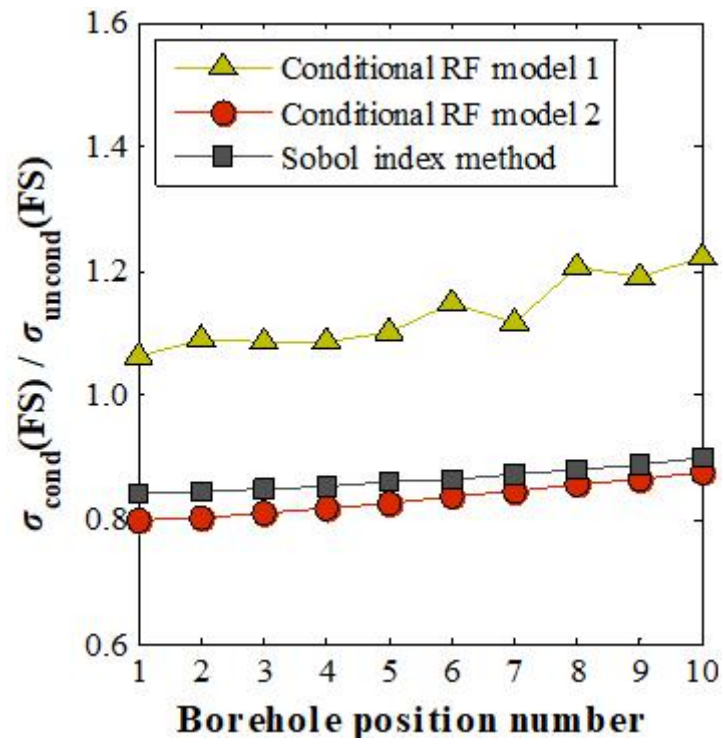


(b)

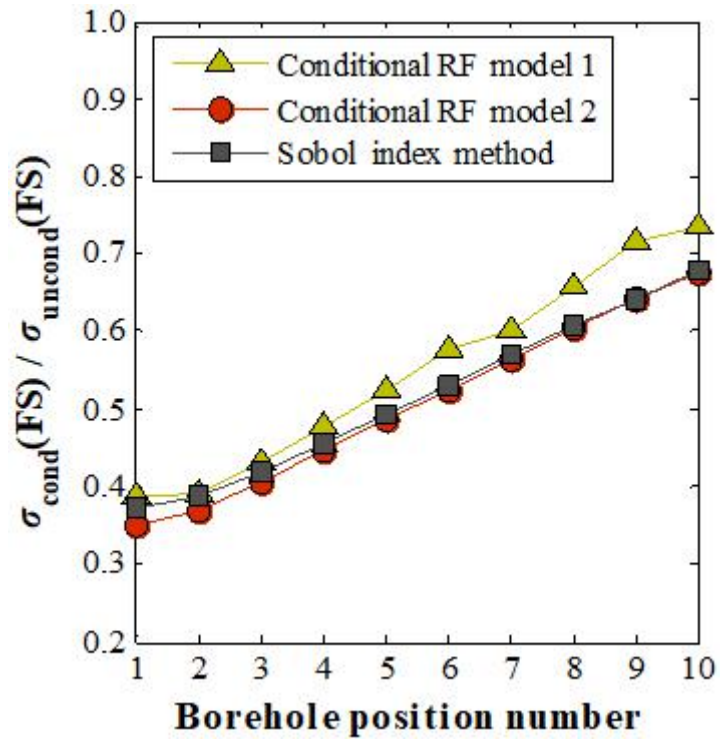


(c)

Figure 5.2 $\sigma_{\text{cond}}(\text{FS}) / \sigma_{\text{uncond}}(\text{FS})$ versus minor autocorrelation distance: (a) $n = 2$; (b) $n = 3$; (c) $n = 5$.



(a)



(b)

Figure 5.3 Magnitude of uncertainty reduction for each borehole location: (a) $n = 2$; (b) $n = 5$.

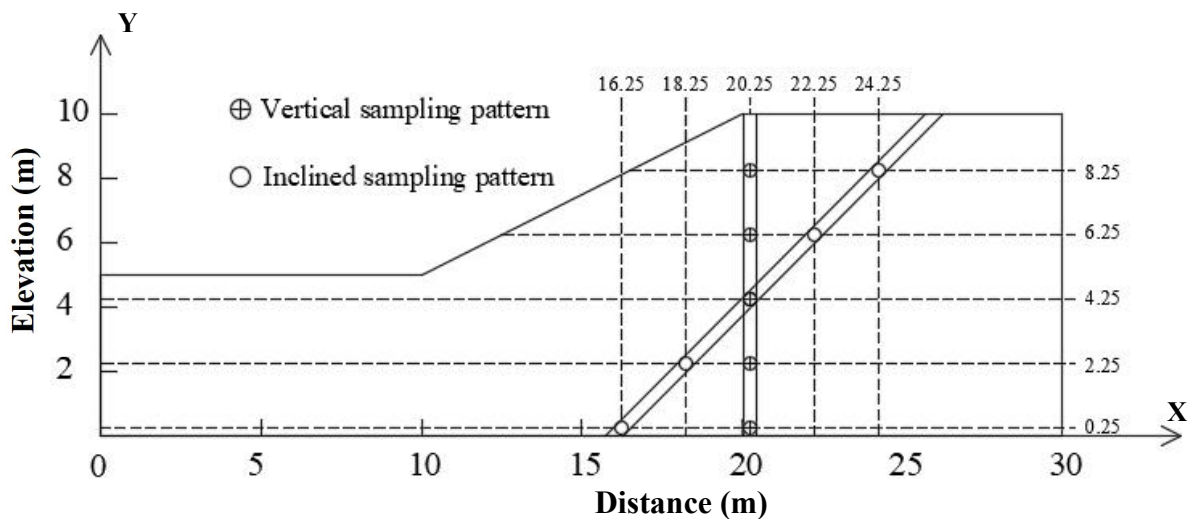
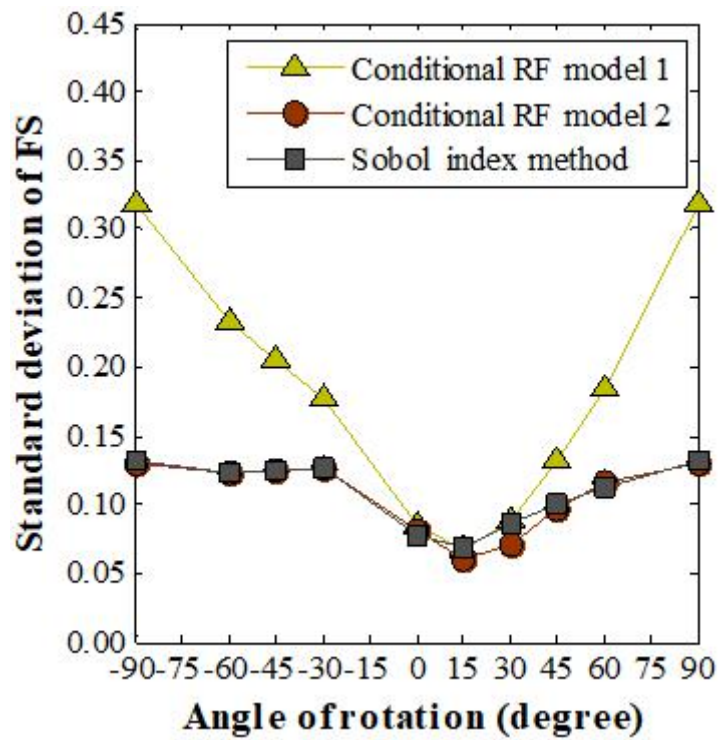
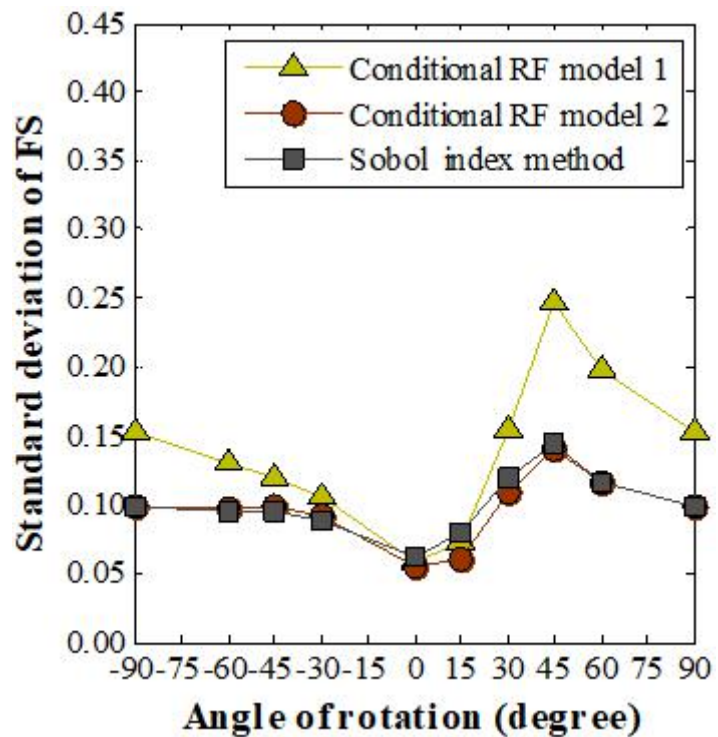


Figure 5.4 The two sampling patterns.



(a)



(b)

Figure 5.5 Standard deviation of FS versus angle of rotation of strata under: (a) vertical sampling pattern; (b) inclined sampling pattern.

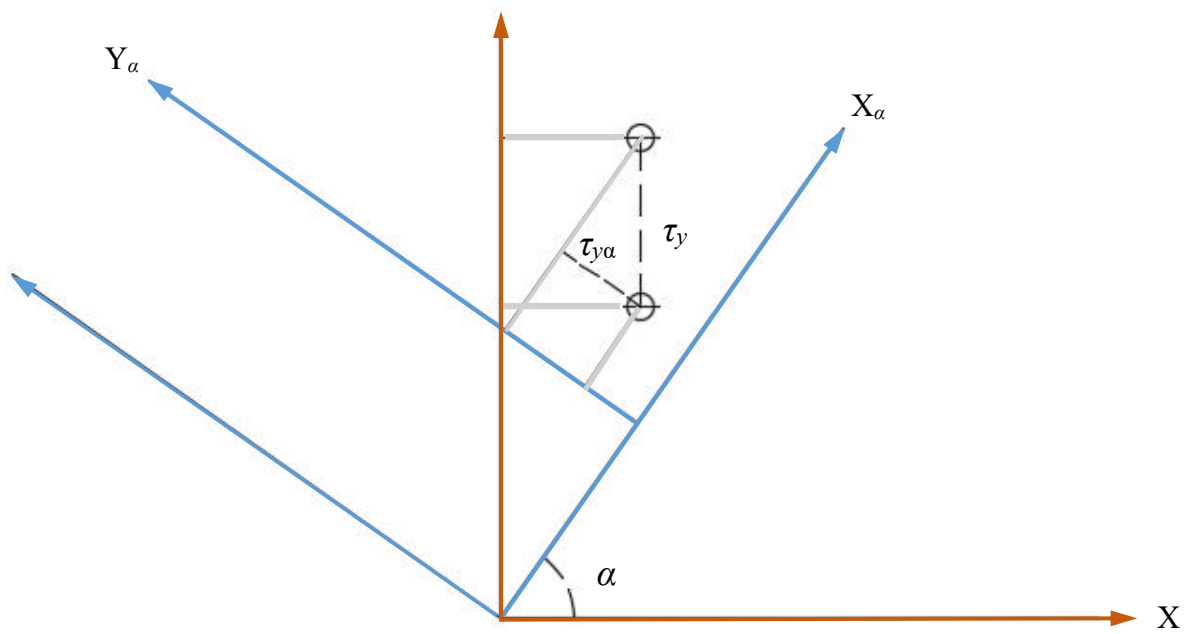
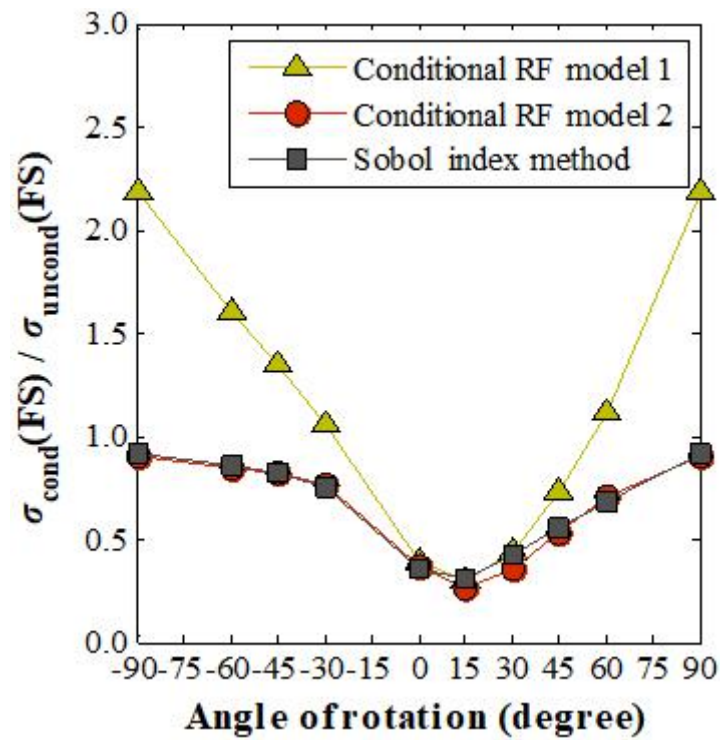
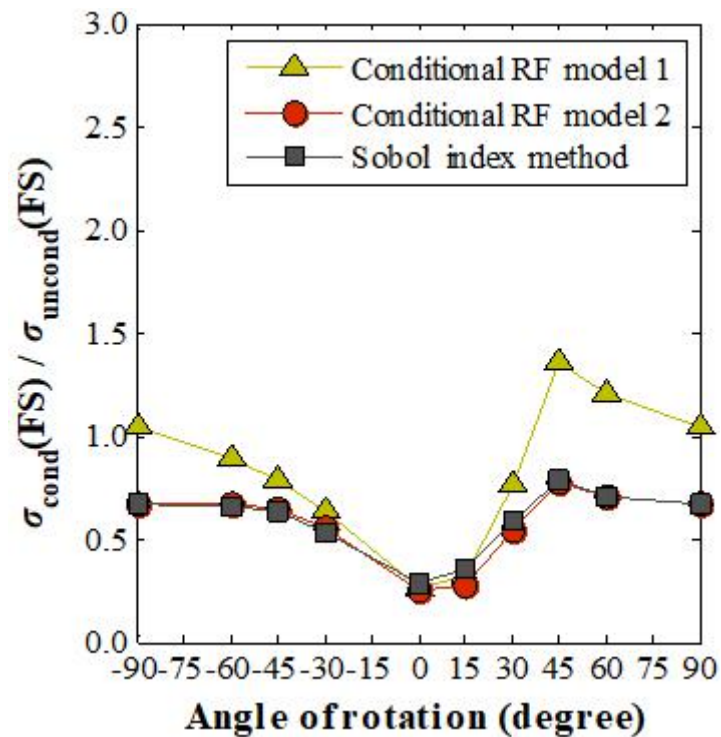


Figure 5.6 Original vertical lag distance τ_y , and lag distance in the rotated coordinate system $\tau_{y\alpha}$.



(a)



(b)

Figure 5.7 $\sigma_{\text{cond}}(\text{FS}) / \sigma_{\text{uncond}}(\text{FS})$ versus angle of rotation of strata under: (a) vertical sampling pattern; (b) inclined sampling pattern.

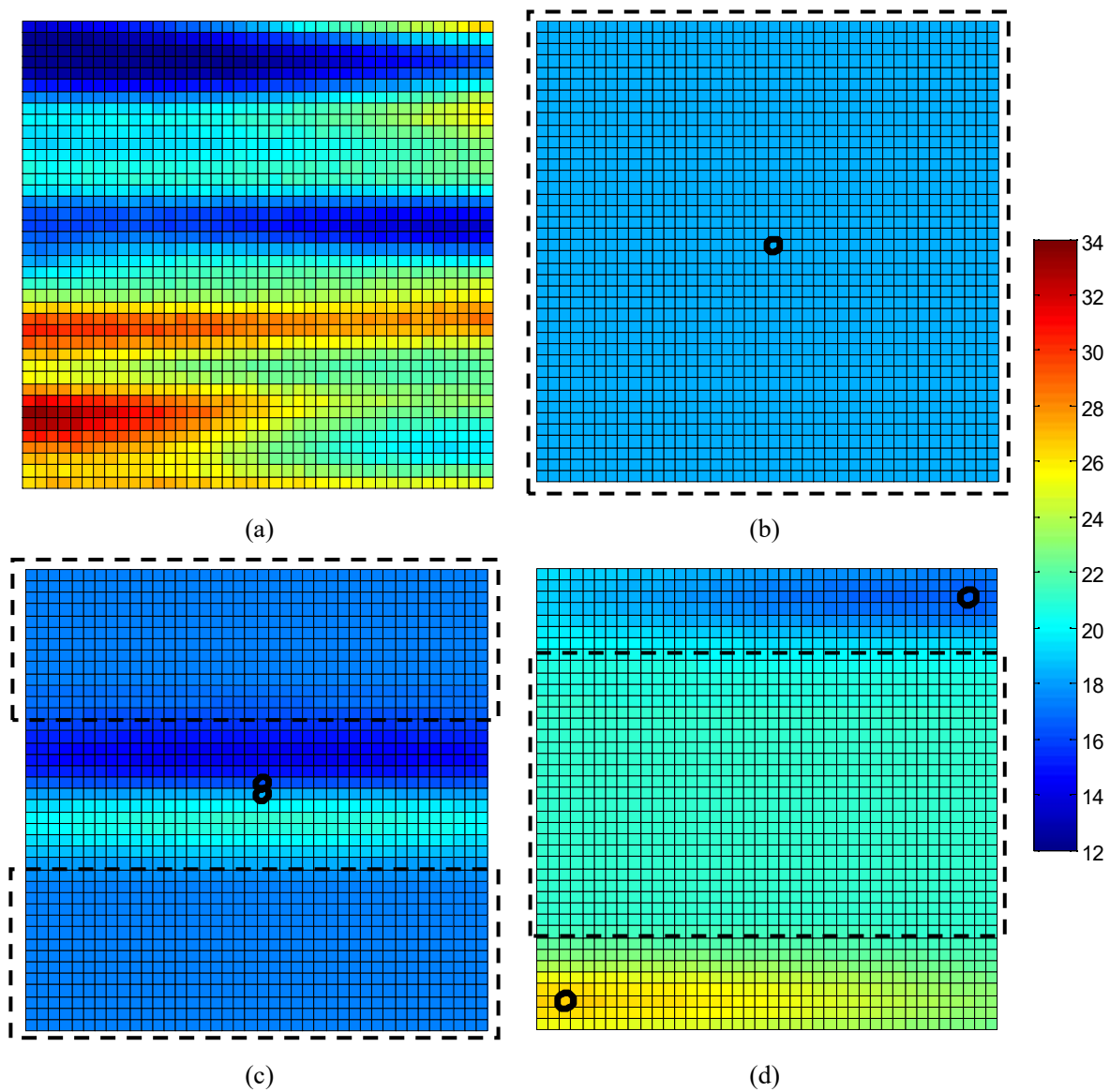


Figure 5.8 The unconditional random field \mathbf{z}_{ur} and the prediction field by ordinary Kriging \mathbf{z}_{kr} with $\theta_1 = 20$ m and $\theta_2 = 2$ m (the sample points are marked by black circles): (a) the field \mathbf{z}_{ur} ; (b) the prediction field considering single sample point; (c) the prediction field considering two very close sample points; (d) the prediction field considering two sparse sample points.

CHAPTER 6 Sampling Effects in 3D Probabilistic Slope Stability Analyses

6.1 Introduction

Chapter 5 investigated the influence of sampling strategy on 2D slope reliability evaluation. Also, previous studies of sampling effects in probabilistic slope stability analyses were mainly based on 2D models, where the spatial variability along the slope length was unaccounted for. For more realistic designs and assessments of slopes, sampling effects in 3D slope reliability analysis should be investigated. Previous investigations on 3D probabilistic slope stability analyses revealed failure modes that cannot be captured in 2D slope models (Hicks *et al.* 2010; Hicks *et al.* 2014; Hicks *et al.* 2018). The failure mode of a 3D slope was found to be associated with the relation between the spatial autocorrelation distance (θ) and slope geometry [i.e., slope height (H) and length (L)]. The thresholds for different failure modes in 3D probabilistic slope stability analyses were discussed previously in Section 4.1. Generally, when failure mode 1 occurs in a slope with spatially variable soils, the 3D slope failure is analogous to the slope failure in a deterministic analysis based on the mean shear strength. Under failure mode 2, a slope would fail in a discrete and localised sliding mass in 3D probabilistic slope stability analysis. In relation to failure

mode 3, the soil properties at different locations are similar in the direction of the major autocorrelation distance. In this situation, the 3D probabilistic slope stability analyses would be similar to single random variable probabilistic analyses considering isotropic spatial variation of soils (Griffiths *et al.* 2009b) or 2D stochastic slope stability analyses in reverse-dip and dip slopes, and those with horizontal bedding (Chapter 4; Hicks *et al.* 2010). Although, the influence of the failure mode on slope reliability has been reported previously, it has not yet been considered in 3D probabilistic slope stability analyses that consider sampling effects.

Furthermore, in 3D slope models with spatially variable shear strength, the boundary conditions of the two end sections can affect the shape and location of the critical failure zone, which in turn affect the optimal sampling strategy. The end boundary conditions in 3D slope stability analysis have been previously discussed in detail in Section 2.2.5, which are summarised as follows: (1) only preventing movement in the y – direction (smooth boundary), which can be adopted when the investigated slope is a portion of a longer slope (Ji and Chan 2014); (2) preventing movement in the (x, y) – direction [boundary fixed in the (x, y) - direction], which is adopted to consider the side shear resistance; and (3) preventing movement in the (x, y, z) – direction (fully fixed boundary), which means no movement at the two ends. The influences of the end boundary condition on the failure mode and deterministic FS of a slope were shown previously in Figure 1.2. Under the same profile of spatially variable undrained shear strength, boundary conditions (1) and (3) would lead to markedly different

failure zones and FS values.

Despite the importance of failure modes and boundary conditions, there have been limited discussions on their effects on sampling strategies. Li *et al.* (2016b) was the first to study the three-dimensional sampling efficiency in probabilistic slope stability analyses by integrating conditional random field simulation and the random finite element method. However, the effects of failure modes and boundary conditions have not been addressed in detail, possibly due to the large computational demand associated with the conditional random field simulation method. Under conditional random field simulation, the sample locations must be specified prior to the slope analyses (Lo and Leung 2018; Lo 2019). That means, in order to obtain a sampling pattern with the best sampling efficiency, many trial sampling patterns are necessary to consider all of the possible options, and each sampling pattern involves hundreds of realisations. If more than one borehole needs to be considered, the number of the trial sampling patterns will be compounded. In three-dimensional finite element analysis, the computation would be further increased due to the high computational cost and the large geometry of a 3D slope model.

In this chapter, various combinations of spatial autocorrelation distances, slope lengths, and the end boundary conditions are considered to investigate the sampling effects in 3D probabilistic slope stability analyses. A slope under undrained conditions is considered, while the random finite element method is used within a Monte Carlo

framework.

6.2 Methodology

6.2.1 Quantification on Sampling Efficiency in Three-dimensional Problem

Sections 2.7 and 5.2 discussed the methods that can be used to quantify sampling efficiency in slope reliability analysis. For the conditional random field simulation methods, hundreds of simulation runs are needed to quantify the magnitude of uncertainty reduction for a given sampling pattern. In this chapter, a number of analyses need to be conducted considering various borehole locations and parametric settings (e.g., slope geometries, autocorrelation distances, and end boundary conditions) in 3D problems. In addition, the optimal sampling pattern should be determined. The computational effort will be quite extensive if conditional random field simulation methods are used. Therefore, the Sobol index method discussed in Sections 2.7.2 and 5.2.3 is adopted.

When using the Sobol index method, the performance function between the model response and spatially variable soil properties should be constructed using the training samples by the unconditional random field simulation method (Section 2.7.2). In this

chapter, the 3D slope failure modes and the corresponding thresholds (Section 4.1) proposed by Hicks and Spencer (2010) and Hicks *et al.* (2014) are considered in the investigation of sampling effects. The form of the autocorrelation function may affect the thresholds, as it corresponds to the pattern of soil spatial variability (Section 2.5.2). Therefore, this chapter uses the same autocorrelation function used by Hicks and Spencer (2010):

$$\rho(\tau_x, \tau_y, \tau_z) = \exp \left[-2 \left(\frac{\sqrt{\tau_x^2 + \tau_y^2}}{\theta_h} + \frac{|\tau_z|}{\theta_v} \right) \right] \quad (6.1)$$

In addition, and consistent with Hicks and Spencer (2010), the random field is generated by LAS considering element averaging effects, which is also used in this chapter when considering various ratios of θ / L and failure modes. As discussed in Section 2.6.2, the subdivision algorithm itself in LAS is unable to preserve anisotropy. Hicks and Spencer (2010) proposed that the thresholds for the 3D slope failure modes are applicable under both isotropic and horizontally anisotropic random fields. Therefore, the spatially variable undrained shear strength, s_u , is simulated with $\theta = \theta_h = \theta_v$, when investigating the influences of ratio of θ / L and the corresponding failure modes.

In addition, influences of anisotropic patterns of soil spatial variability are also studied in this chapter, considering various end boundary conditions. When considering anisotropic patterns of soil spatial variability, the Cholesky decomposition method is adopted to generate the random fields. The value of M in Eq. (5.3) is large

when considering a single exponential function for a 3D problem, which indicates quite demanding computational efforts in obtaining PCE coefficients; therefore, the Gaussian autocorrelation function is used, which results from rotation of the coordinate system for horizontal transverse anisotropy, as discussed in Section 2.5.3.

6.2.2 Differential Evolution

In this chapter, if only one borehole is considered, the sample location \mathbf{X} can be represented as $(x_1, y_1)^T$, while the depths of the samples are described in Table 6.1. As shown in Table 6.1, 4 samples will be obtained from each borehole, and the depths of the samples depend on the borehole location. If the borehole is drilled behind the slope crest (Figure 6.1), the samples will be spaced at 1 m intervals. Otherwise, the samples will be more closely spaced. By evaluating the Sobol index, $S(\mathbf{X})$, for all possible borehole locations, the optimal location is identified as the location with the maximum $S(\mathbf{X})$.

If two or three boreholes are considered, then the sample location \mathbf{X} can be represented as the locations of the two $[(x_1, y_1)^T, (x_2, y_2)^T]$ or three boreholes $[(x_1, y_1)^T, (x_2, y_2)^T, (x_3, y_3)^T]$, respectively. In a 3D problem, a direct search for the maximum $S(\mathbf{X})$ would be tedious and infeasible, as there are a large number of possible combinations for the multiple borehole locations due to the large geometry of a 3D

model. Therefore, a global optimization algorithm known as Differential Evolution (Storn and Price 1997) can be adopted to maximize $S(\mathbf{X})$. When conducting Differential Evolution, an initial population is generated first:

$$\mathbf{PAR}_{0i,j} = \mathbf{pl}_j + \text{random}[0, 1] \times (\mathbf{pu}_j - \mathbf{pl}_j) \quad (6.2)$$

In Eq. (6.2), \mathbf{PAR}_0 is a matrix containing the initial population. $i = (1, 2, \dots, N_{\text{pop}})$ and $j = (1, 2, \dots, N_{\text{de}})$, where N_{pop} denotes the size of the initial population ($N_{\text{pop}} = 50$ in this chapter) and N_{de} denotes the dimension of the variable. The parameters \mathbf{pu}_j and \mathbf{pl}_j are the upper limit and lower limit of the population, respectively.

After generating the initial population, a new generation of the population will be created by mutation and crossover in the existing population:

$$\mathbf{PAR}_M^{(i)} = \mathbf{PAR}_0^{(\mathbf{mu}_1)} + F_a \times \left\{ \mathbf{PAR}_0^{(\mathbf{mu}_2)} - \mathbf{PAR}_0^{(\mathbf{mu}_3)} \right\} \quad (6.3)$$

$$\mathbf{PAR}_{Ci,j} = \begin{cases} \mathbf{PAR}_{Mi,j} & \text{if } \mathbf{Rand}_{i,j} < CR \text{ or } (i/j) \in \mathbf{I}_r \\ \mathbf{PAR}_{0i,j} & \text{otherwise} \end{cases} \quad (6.4)$$

In the above equations, $\mathbf{PAR}_M^{(i)}$ denotes the i th row of the matrix containing the mutated population; \mathbf{mu} is a vector containing three random samples, which range from 1 to N_{pop} ; F_a is a mutation amplification factor taken from 0 to 2; \mathbf{PAR}_C represents a matrix containing the population by crossover; \mathbf{Rand} is a matrix containing random samples taken from 0 to 1; CR is a crossover constant taken from 0 to 1; and \mathbf{I}_r is a identity matrix that makes sure the crossover can occur on each individual in the existing population.

After the mutation and crossover, the fitness value of each individual in \mathbf{PAR}_C will be

calculated by an objective function, and then compared to that in the initial population \mathbf{PAR}_0 . The individual in \mathbf{PAR}_C with an improved fitness value will be retained in the population, otherwise it will be discarded. The procedures are iterated until the fitness values of every individuals in the population converge to the global maximum, and hence the optimal solution can be obtained. In this chapter, the code of Differential Evolution is written using MATLAB. The number of iterations is set to 1,000, while F_a and CR are set to 1 and 0.5, respectively. When determining the optimal sampling pattern by Differential Evolution, the fitness value is denoted by the Sobol index of each sampling pattern, and the population is represented by various combinations of borehole locations.

6.3 Case Description

In the current study, the finite element analysis software ABAQUS is used to model the slope. The strength reduction method is adopted to determine the FS, considering the non-convergence criteria (Griffiths and Lane 1999). The geometry of the slope is shown in Figure 6.1. The slope is 45° with slope height $H = 5$ m, while the slope length L is varied from 20 m to 100 m. The soil is modeled as an elastic-perfectly plastic Tresca material. The undrained shear strength is treated as a spatial variable and assumed to be log-normally distributed to avoid simulating negative values, with the mean and COV equal to 22.54 kPa and 0.5, respectively. The deterministic FS

with the soil strength equal to the mean undrained shear strength is 1.4. The autocorrelation distance θ is varied across a wide range (from $\theta / L = 0.05$ to 1.125). The mesh comprises of brick elements of dimensions $0.5 \text{ m} \times 0.5 \text{ m} \times 1 \text{ m}$ (y - direction), while the elements along the slope face are truncated to fit the geometry [Figure 6.1(b)]. In the finite element analysis, the base of the slope model is fully fixed, while the back face is only fixed in the x - direction. For the boundary conditions of the two end sections, the three boundary conditions [i.e., smooth boundary, boundary fixed in the (x, y) direction and fully fixed boundary conditions] are considered.

6.4 Results

In the current work, various combinations of θ and L are considered, as shown in Table 6.2. Three types of end boundary conditions are investigated for each combination, resulting in a total of 24 cases. Table 6.2 also presents the x - coordinate of the optimal sample location for each parametric setting under different end boundary conditions. It is observed that the optimal sampling borehole is generally around the slope crest in the x - direction (i.e., $x / W = 0.5$ for the slope model in Figure 6.1). Such an observation is consistent with the finding by Li *et al.* (2016b). As shown in Table 6.2, when the x - coordinate of the sampling borehole is fixed on the slope crest, the change of the Sobol index is slight for the fully fixed boundary

condition. Other boundary conditions also indicate a negligible change in the Sobol index in most cases (not shown). Therefore, to provide simple guidelines on the sampling borehole locations, in Sections 6.4.2, 6.4.3 and 6.4.4, the x – coordinate of all the boreholes are fixed at the slope crest.

Figure 6.2 shows the Sobol index along the slope length using two sampling sizes (1,000 and 2,000) for constructing PCE, with $L = 40$ m, $\theta / L = 0.5$, and end boundaries fixed in the (x, y) direction. In Figure 6.2, the sampling location is represented by $\Delta y / L$, where Δy denotes the distance between the borehole location and the end section in the y – direction [Figure 6.1(a)]. Meanwhile, Table 6.3 presents the difference of the Sobol index between any two symmetrical locations in Figure 6.2. Theoretically, since the geometry and the end boundary condition of the slope are both symmetrical about the middle of the slope length, the values of the Sobol index should also be symmetrical. However, when the simulation size is small, the curve of the Sobol index would be obviously asymmetric (Figure 6.2), possibly due to the under-representation of the response surface when evaluating the Sobol index. With larger simulation size, nearly symmetrical results can be obtained, as can be seen in Figure 6.2 and Table 6.3. Therefore, a sufficient number of realisations are ensured in each setting to produce a symmetric Sobol index map, which is presented in Table 6.4.

6.4.1 Sampling Strategies Considering Two and Three Boreholes

In this section, the sampling strategies with two and three boreholes are investigated considering isotropic soil spatial variability. When two sampling boreholes are considered, the optimal sampling pattern is determined by two different approaches. In Approach 1, the two optimal locations are randomly searched throughout the whole domain. In Approach 2, the x - coordinate is fixed at the crest of the slope with the two borehole locations being symmetrical about the middle of the slope length. The Differential Evolution method outlined in Section 6.2.2 is adopted in the two approaches. Five combinations of θ and L are considered, and the differences between the Sobol index by Approaches 1 and 2 are presented in Table 6.5. It can be observed that the differences are small (all the differences are under 10 %). That suggests that obtaining optimal samples that are along the slope crest and symmetrical around the middle of the slope can lead to a similar magnitude of uncertainty reduction by a randomised search of the samples throughout the whole domain.

Figure 6.3 shows the change of $\Delta y_0 / \theta$ with θ / L using Approach 2 considering two sampling boreholes, where Δy_0 represents the distance between one of the symmetrical boreholes and the nearer boundary. As can be noted from Figure 6.3, generally, with the increase of θ / L the normalised distance ($\Delta y_0 / \theta$) would decrease,

and the results of the boundary which is fixed in the (x, y) direction are close to the results of the fully fixed boundary. In relation to three sampling boreholes, one of the boreholes is fixed at the middle of the slope length, and the other two boreholes are symmetrical around the middle. The change of $\Delta y_0 / \theta$ with θ / L considering three sampling boreholes is shown in Figure 6.4. As indicated in the figure, when three sampling boreholes are considered, the normalised distance ($\Delta y_0 / \theta$) would also decrease with the higher value of θ / L . Besides, the results under the boundary condition fixed in the (x, y) direction and the fully fixed boundary condition yield good agreements in most cases.

6.4.2 Sampling Efficiency Considering Single Borehole

In this section, the sampling efficiency considering one borehole is investigated. The Sobol index values for different locations along the slope length under the three boundary conditions are presented in Figure 6.5. It can be observed from Figures 6.5(a), (b) and (c) that in general, the Sobol index, and hence sampling efficiency increases with larger θ / L . That means the ratio of θ / L mainly contributes to the sampling efficiency. In general, with a higher value of θ , more areas of the domain in the direction of slope length would be significantly influenced by the conditioning effects imposed by the sampling points. Hence, for a given sampling pattern and slope length, the higher value of θ can indicate the smaller spatial uncertainty of soil

properties, and thus result in the higher sampling efficiency. On the other hand, with a higher slope length, there would be more areas that cannot be significantly influenced by the conditioning effects. Therefore, the proportion of the domain under significant conditioning effects is controlled by the ratio of θ / L . Herein, the higher value of θ / L would indicate the higher proportion, and thus the higher sampling efficiency. Such a finding corroborates the previous observation by Li *et al.* (2016b) that the sampling efficiency is positively associated with the horizontal autocorrelation distance in 3D probabilistic slope stability analyses.

Figure 6.6 further compares the sampling efficiency under different failure modes and end boundary conditions. The slope length is fixed at 40 m, while three different autocorrelation distances (i.e. 2 m, 15 m and 45 m) are considered corresponding to the failure modes 1, 2 and 3, respectively. It is found that under failure mode 1, the Sobol index values for all the three boundary conditions are very small and negligible. That is because in this situation, the autocorrelation distance is so small that the sampling effects are insignificant. For failure modes 2 and 3, the Sobol index values under the smooth boundary condition are larger than those under the fully fixed boundary condition near the boundary, and smaller than those near the middle. Meanwhile, the Sobol index values under the boundary condition fixed in the (x, y) direction are close to those under the fully fixed boundary condition. As proposed by Spencer (2007), slope failures tend to be attracted to the end boundaries under the smooth boundary condition in spatially variable soils, leading to the higher sampling

efficiency near the end sections. In contrast, preventing movements at the end sections tends to push the sliding mass to the middle and hence results in higher sampling efficiency.

6.4.3 Optimal Sampling Location and Uncertainty Reduction Considering Single Borehole

In this section, the optimal sampling location and the corresponding magnitude of uncertainty reduction are discussed. In Figure 6.7, the location of the optimal borehole is represented by y_0 / L , where y_0 denotes the distance between the borehole location and the nearer end section in the y – direction. As can be observed from the figure, when the two end sections are fully fixed and preventing movement in the (x, y) - direction, the optimal sampling boreholes are around the middle of the slope in most failure modes. By contrast, for the slope with the smooth boundary condition, the optimal locations display a trend with θ / L : the optimal locations are near the middle of the slope when θ / L is larger than 0.5 corresponding to the failure mode 3, while with other values of θ / L the optimal locations are near the ends [For the smooth end boundary condition with $\theta / L = 1.125$, the optimal sampling location is around $y_0 / L = 0.68$, as shown in Figure 6.7, the Sobol index value of which (0.576) is quite close to that at $y_0 / L = 0.51$ (0.571)]. The reasons behind those results are associated with the failure modes and boundary effects. Under fixed boundary conditions, the effect

of the end boundary condition would push the failure to the middle of the slope. Under smooth boundary conditions, the slope will fail in a discrete mass for failure mode 2 ($\theta / L < 0.5$), and the failure tends to occur at the mesh ends (Spencer 2007). On the other hand, when $\theta / L > 0.5$ (failure mode 3), the slope failure tends to occur along the whole slope length, leading to the optimal sampling location in the middle for both the fixed boundary and smooth boundary conditions.

It should also be noted that when $\theta / L = 0.125$, two different settings of slope length and autocorrelation distance are considered (i.e., [$L = 100$ m, $\theta = 12.5$ m] and [$L = 40$ m and $\theta = 5$ m]), which result in two significantly different optimal sampling strategies for slopes with fully fixed boundaries. As proposed by Hicks *et al.* (2014), at the transition from failure mode 1 to failure mode 2, multiple potential sliding masses (Figure 6.8) are more likely to occur in a slope. That means there would be more than one critical zone of a slope, and it may cause two optimal locations distributed around the two ends. When $\theta = 5$ m (i.e., value of the slope height H), the slope failure mode is closer to the transition point, because the threshold for the failure mode 1 is based on the height of a slope. By contrast, when $\theta = 12.5$ m, the possibility for the occurrence of the multiple potential sliding masses would reduce, and the fixed boundary condition would push the failures to the middle.

Figure 6.9 shows the magnitude of uncertainty reduction [i.e. $\sigma_{\text{cond}}(\text{FS}) / \sigma_{\text{uncond}}(\text{FS})$] corresponding to the optimal sampling borehole. As can be noted from the figure,

with the increase of θ / L the $\sigma_{\text{cond}}(\text{FS}) / \sigma_{\text{uncond}}(\text{FS})$ would decrease (higher magnitude of performance uncertainty reduction), due to the larger conditioning effect of the soil samples. It is interesting to note that when $\theta / L = 0.125$, under the fully fixed boundary condition, the difference in $\sigma_{\text{cond}}(\text{FS}) / \sigma_{\text{uncond}}(\text{FS})$ between the two cases (i.e., $[L = 100 \text{ m}, \theta = 12.5 \text{ m}]$ and $[L = 40 \text{ m and } \theta = 5 \text{ m}]$) is small, although their optimal sampling locations are different. That is because, as discussed in the previous sections, the same θ / L ratios can be associated with similar sampling efficiencies.

6.4.4 Sampling Effects under Rotated Transverse Anisotropy Considering Single Borehole

In this section, rotated transverse anisotropy is considered under various end boundary conditions with $\theta_1 = 15 \text{ m}$ and $\theta_2 = 1 \text{ m}$. Figures 6.10 (a), (b), (c) and (d) show the variations of the Sobol index value along the slope length for a slope with horizontal bedding, a dip slope, a reverse-dip slope and a cross-dip slope, respectively. Meanwhile, Table 6.6 presents the magnitude of uncertainty reduction, $\sigma_{\text{cond}}(\text{FS}) / \sigma_{\text{uncond}}(\text{FS})$, considering the optimal sampling location for each slope scenario. In this section, 2,000 simulations are considered for each slope scenario.

As shown in Figures 6.10 (a) (b) and (c), the Sobol index values are generally symmetrical about the middle of slope length for the slope with horizontal bedding, dip slope and reverse-dip slope. Also, the observations on the influences of end

boundary conditions on the variation of the Sobol index are similar to those considering the isotropic soil spatial variability with $\theta = 15$ m shown in Figure 6.6. That is, the Sobol index values under the boundary condition which is fixed in the (x, y) direction are close to those with the fully fixed boundary condition. The Sobol index values under the smooth boundary condition are larger than those under the fully fixed boundary condition near the boundary, and smaller than those near the middle. However, when considering the cross-dip slope, the symmetrical feature cannot be observed when examining the variation of the Sobol index values under the smooth boundary condition and the boundary condition which is fixed in (x, y) direction. That is because the strata orientation in cross-dip slope leads to the asymmetrical feature of soil spatial variability. Besides, the variation of the Sobol index values along slope length under the fixed boundary condition in the (x, y) direction is significantly different from that under the fully fixed boundary condition for the cross-dip slope. As can be seen from Table 6.6, the fully fixed boundary conditions can lead to the maximum magnitude of uncertainty reduction (i.e., the smallest $\sigma_{\text{cond}}(\text{FS}) / \sigma_{\text{uncond}}(\text{FS})$) among various boundary conditions for the slope with horizontal bedding, dip slope, and reverse-dip slope. Such an observation is consistent with that considering the isotropic random field. By contrast, the $\sigma_{\text{cond}}(\text{FS}) / \sigma_{\text{uncond}}(\text{FS})$ considering optimal sampling location is the smallest under the smooth boundary condition for the cross-dip slope.

6.5 Discussion

In this chapter, the ratio of spatial autocorrelation distance (θ) to slope length (L) and the boundary condition at the end sections are found to be influential to sampling efficiency. Both factors cannot be explicitly incorporated in probabilistic slope stability analyses when a 2D slope model is adopted. In addition, the sampling efficiency and optimal sampling strategy are influenced by the failure modes in 3D probabilistic slope stability analyses. These findings reveal the significance of considering 3D models when performing probabilistic slope stability analysis incorporating sampling effects.

In engineering practice, a slope being analysed is usually taken from a longer slope or a part of a region. That means historical data of ground investigation may be available from neighbouring sites, which can be used to obtain the autocorrelation distance for the region in general. When the autocorrelation distance is obtained, some findings in this chapter can help engineers to make primary decisions in ground investigation and engineering designs. The suggestions for engineering practice are presented as follows: (1) as the sampling efficiency is positively correlated with the θ / L ratio, an engineer can decide whether it is worthwhile to drill sampling boreholes based on the θ / L ratio of a slope considering economic benefits; (2) when two boreholes need to be drilled, it is suggested to drill two symmetrical boreholes along the slope crest, and the distance between the borehole location and boundary, Δy_0 , can generally be

obtained referring to the results shown in Figure 6.3; (3) when failure mode 2 is decided to be the potential failure mode of a slope, a single sampling borehole is suggested to be drilled near the boundary of a slope along crest, if the end boundary condition can be assumed to be smooth. On the other hand, if the end boundary condition can be assumed to be fixed, then the borehole should be drilled near the middle. However, when the potential failure mode is failure mode 3, it is suggested to drill a borehole in the middle of a slope, regardless of the end boundary condition.

In engineering practice, a number of boreholes (usually more than 3 boreholes) are usually drilled in the ground investigation for a slope project. That means the scenarios of considering one or two boreholes might not be practical. Although more than 3 boreholes are usually taken in the site investigation stage, some of them may be used to characterize the soil type and profile. Therefore, the smaller number of boreholes may be considered to obtain the soil parameters, which are needed in simulating spatially variable soils in slope reliability evaluation. Especially, when laboratory tests (e.g., triaxial tests) are used to obtain the soil parameters, the limited number of boreholes may be considered due to the high cost of the tests.

6.6 Summary

This chapter investigated the sampling efficiency using 3D probabilistic slope

stability analyses considering soil spatial variability by the Sobol sensitivity index. Compared with the conditional random field simulation method, the use of the Sobol index method significantly reduces the computational effort in 3D problems. Various slope lengths L , autocorrelation distances θ and end boundary conditions have been considered. The slope stability analyses were conducted using 3DRFEM under different boundary conditions of the end sections. In consideration of the various slope dimensions and autocorrelation distances, the following observations are obtained:

(1) If two boreholes are adopted, searching two symmetrical locations about the middle of slope length along the slope crest can lead to similar results by a randomised search of the optimal sampling pattern within the whole slope domain. Therefore, when it is needed to consider two sampling boreholes, for simplicity, two symmetrical boreholes around the middle of slope can be drilled along the slope crest. In addition, it is found that when considering the two symmetrical locations, the normalised distance ($\Delta y_0 / \theta$) tends to decrease with larger θ / L ratio. Such a phenomenon can also be observed, when considering three sampling boreholes with one of the boreholes fixed at the middle of the slope length and the other two boreholes being symmetrical around the middle. Hence, if the autocorrelation distance can be obtained from the neighbouring sites, the distance between the borehole location and the nearer end boundary can be generally determined based on the relation between $\Delta y_0 / \theta$ and θ / L shown in Figures 6.3 and 6.4.

(2) Considering one borehole, the end boundary conditions and potential failure modes of a slope can affect the optimal sampling location. Generally, the optimal sampling location for a slope with boundary conditions preventing movement in the (x, y, z) - direction is near the middle of slope length, while for a slope with a smooth boundary condition the optimal sampling location is near the middle under failure mode 3 and near the boundaries in the other situations. In addition, the ratio of θ / L is found to influence the sampling efficiency. In general, with an increase of the ratio, the sampling efficiency increases. Also, the boundary conditions can affect the sampling efficiency. Under failure modes 2 and 3, sampling locations around the ends with smooth boundary conditions can indicate higher sampling efficiency than those of sampling locations with fixed boundary conditions. However, for the sampling locations around the middle, the sampling efficiency with fixed boundary conditions is higher. The slope length in the out-of-plane direction and the boundary condition of the end sections cannot be explicitly considered in probabilistic slope stability analyses when using a 2D slope model, which reveals the significance for using 3D slope model in slope reliability evaluation considering sampling effects. When considering anisotropic patterns of soil spatial variability, observations on the variation of the Sobol index along the slope length and the influence of the end boundary condition for the slope with horizontal bedding, dip slope and reverse-dip slope are similar to those considering isotropic soil spatial variability. However, such observations are significantly different when considering the cross-dip slope, due to the asymmetrical nature of the soil spatial variability in the cross-dip slope.

Table 6.1 Depth of samples according to the borehole location.

<i>x</i> - coordinate of borehole (m)	<i>z</i> - coordinate of samples (m)
5	(4, 3, 2, 1)
4	(3.5, 2.5, 1.5, 0.5)
3.5	(3, 2.5, 1.5, 0.5)
3	(2.5, 2, 1.5, 0.5)
2.5	(2, 1.5, 1, 0.5)

Table 6.2 Parametric settings, the optimal sampling location and the optimal Sobol index value.

L (m)	θ (m)	θ/L	x/W of the optimal sampling location Smooth boundary	x/W of the optimal sampling location Boundary fixed in (x , y) direction	x/W of the optimal sampling location Fully fixed boundary	Sobol index with x - coordinate by randomised search Fully fixed boundary	Sobol index with x - coordinate fixed in the slope crest Fully fixed boundary
40	2	0.05	0.6	0.4	0.4	0.0366	0.0347
100	12.5	0.125	0.55	0.5	0.4	0.0858	0.0836
40	5	0.125	0.5	0.55	0.5	0.0920	0.0920
60	15	0.25	0.55	0.5	0.55	0.2390	0.2388
40	15	0.375	0.45	0.55	0.55	0.3810	0.3801
40	20	0.5	0.55	0.55	0.5	0.4360	0.4360
20	15	0.75	0.5	0.45	0.45	0.6580	0.6585
40	45	1.125	0.5	0.5	0.5	0.6960	0.6960

Table 6.3 Difference of Sobol index for any two symmetrical boreholes considering two different simulation sizes in Figure 6.2.

Borehole group No.	Difference for the 1,000 simulations (%)	Difference for the 2,000 simulations (%)
1	9.10	0.86
2	8.84	1.63
3	8.82	2.26
4	8.93	2.43
5	9.01	2.28
6	9.23	1.94
7	9.90	1.31
8	10.85	0.38
9	11.52	0.64
10	11.48	1.47
11	10.85	2.02
12	9.87	2.15
13	8.54	1.67
14	6.81	0.71
15	5.00	0.25
16	3.63	0.83
17	2.71	1.10
18	1.90	1.20
19	1.07	1.00
20	0.33	0.39

Table 6.4 Simulation size for each setting.

L (m)	θ (m)	Number of	Number of	Number of
		realisations	realisations	realisations
		Smooth boundary	Boundary fixed in (x, y) direction	Fully fixed boundary
40	2	1,000	1,000	1,000
100	12.5	1,000	1,000	1,000
40	5	1,000	1,000	1,000
60	15	2,000	1,000	1,000
40	15	2,000	1,000	1,000
40	20	2,000	2,000	2,000
20	15	500	500	500
40	45	1,000	500	500

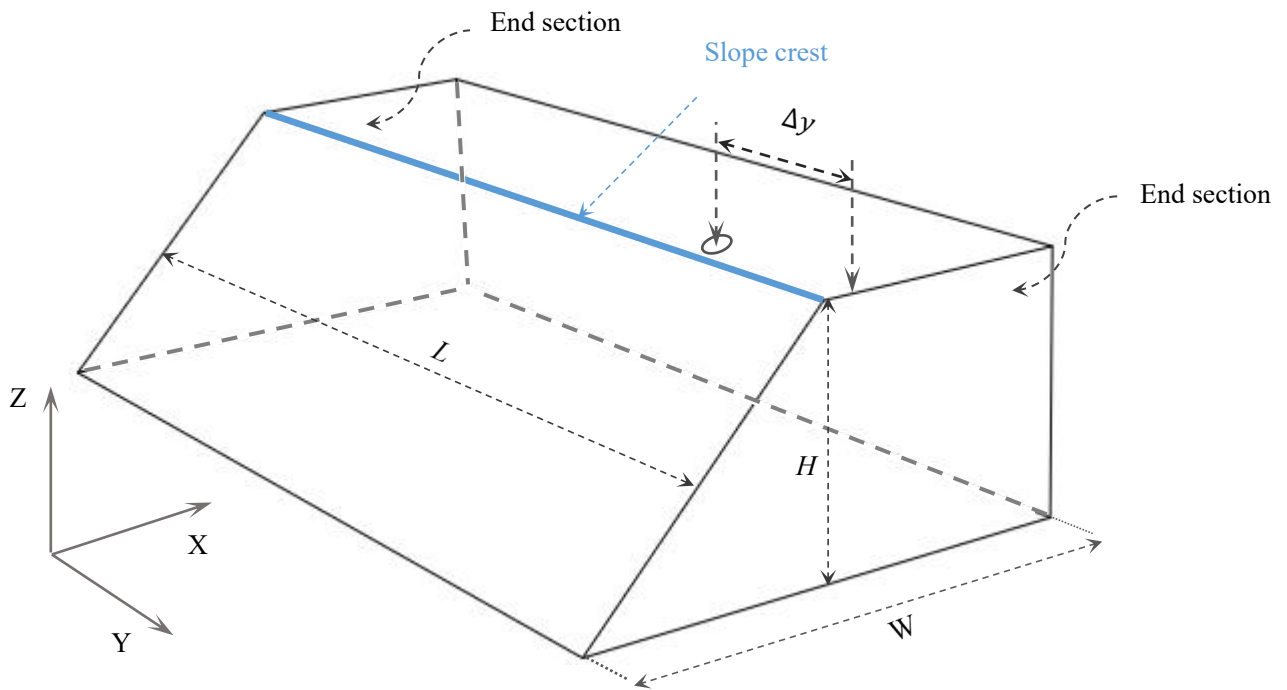
Table 6.5 Difference of Sobol index by the two approaches.

<i>L</i> (m)	<i>θ</i> (m)	Difference of Sobol index (Approach 1 and Approach 2, %)	Difference of Sobol index (Approach 1 and Approach 2, %)	Difference of Sobol index (Approach 1 and Approach 2, %)
		Smooth boundary	Boundary fixed in (x, y) direction	Fully fixed boundary
20	15	1.96	1.43	1.63
40	15	3.60	2.12	4.66
40	20	7.34	0.14	0.43
40	45	3.32	0.36	1.18
60	15	5.86	2.91	3.60

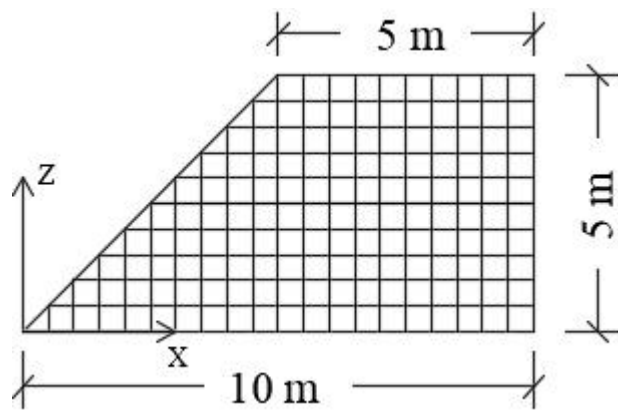
Note: The difference = [(Sobol index by Approach 1 - Sobol index by Approach 2) / (Sobol index by Approach 1)] × 100%.

Table 6.6 Magnitude of uncertainty reduction, $\sigma_{\text{cond}}(\text{FS}) / \sigma_{\text{uncond}}(\text{FS})$, considering the optimal sampling pattern under different slope scenarios.

Slope type	Smooth boundary	Boundary fixed in (x, y) direction	Fully fixed boundary
Slope with horizontal bedding	0.77	0.71	0.69
Dip slope ($\alpha = 30^\circ$)	0.68	0.56	0.54
Reverse-dip slope ($\alpha = -30^\circ$)	0.86	0.82	0.81
Cross-dip slope ($\alpha = 30^\circ$)	0.85	0.88	0.89



(a)



(b)

Figure 6.1 (a) Geometry of the 3D slope model; (b) the cross-section of finite element mesh.

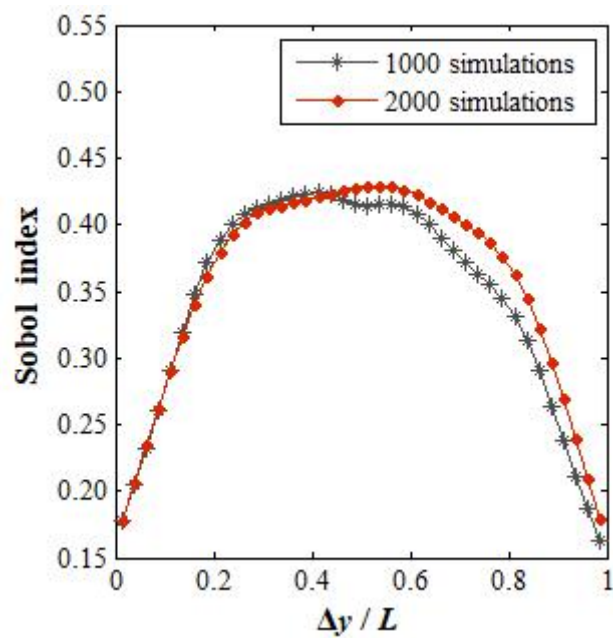


Figure 6.2 Sobol index using 1,000 simulations and 2,000 simulations for constructing PCE.

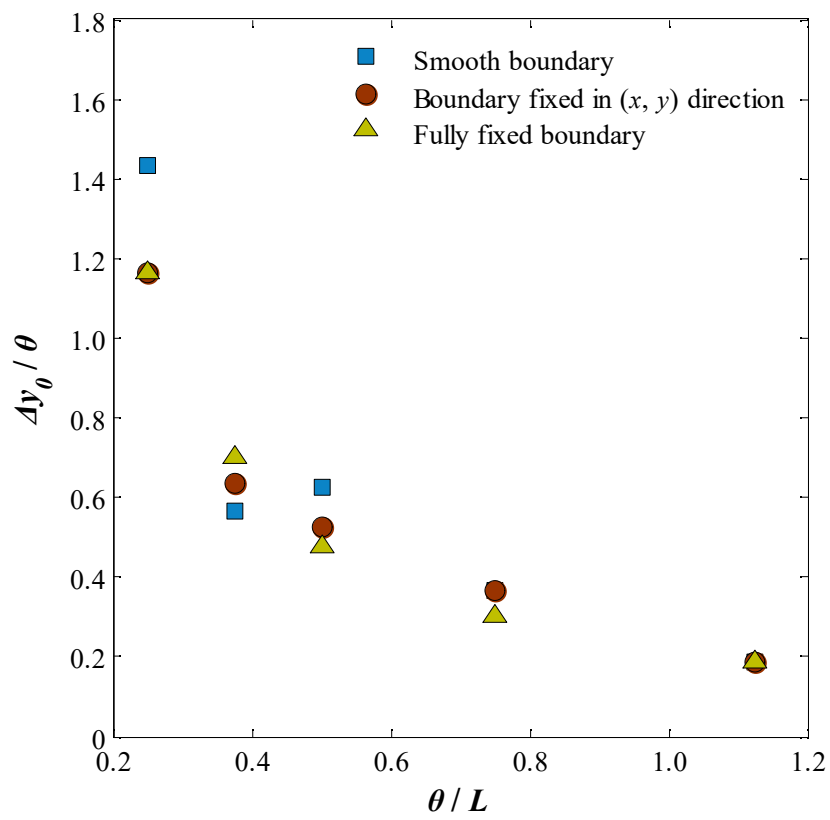


Figure 6.3 Distance between the optimal borehole location and the nearer end boundary divided by θ versus θ / L considering two sampling boreholes.

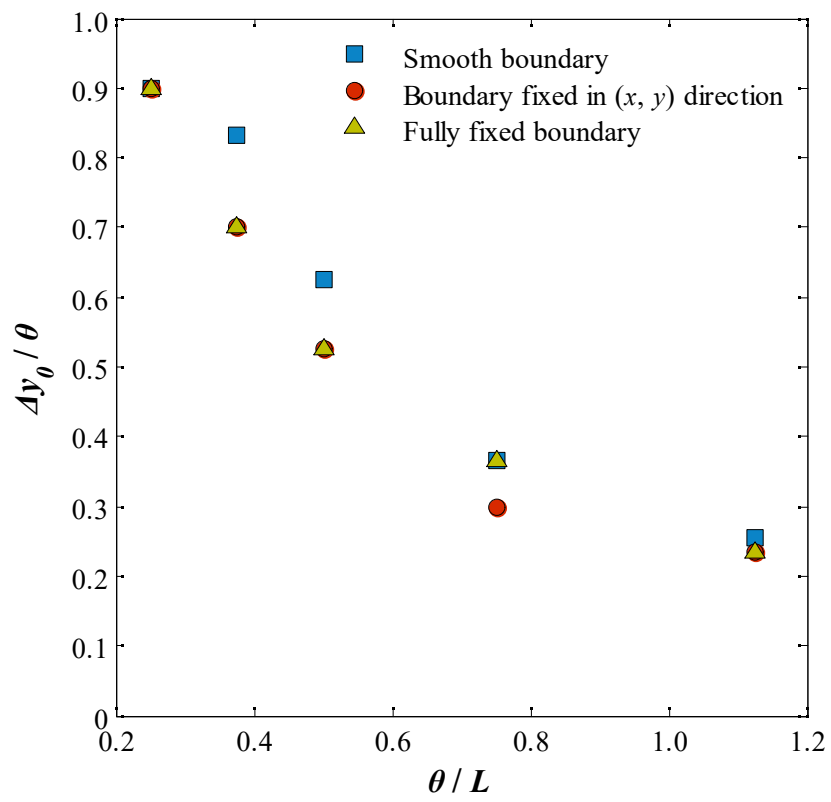
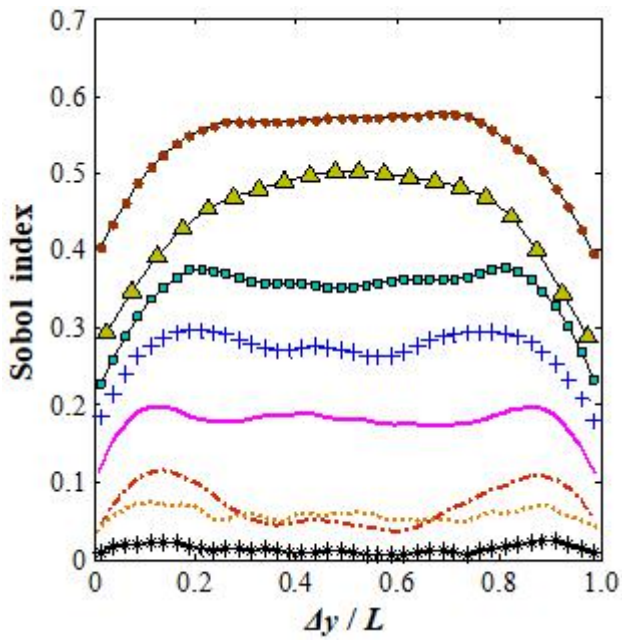
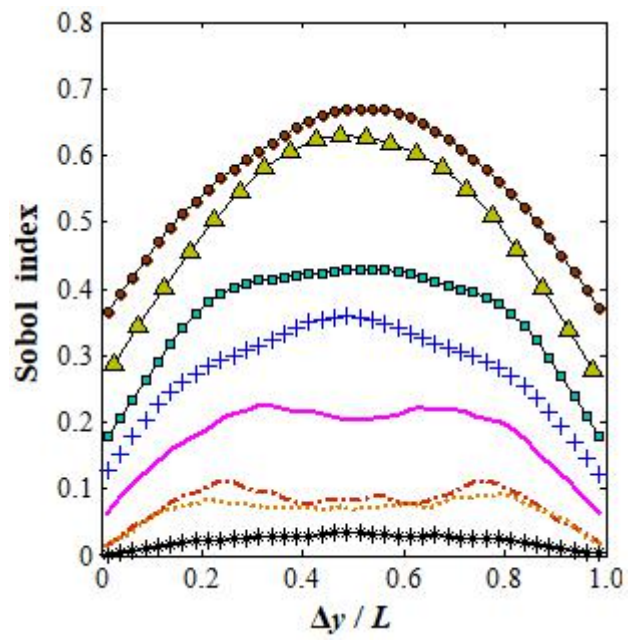


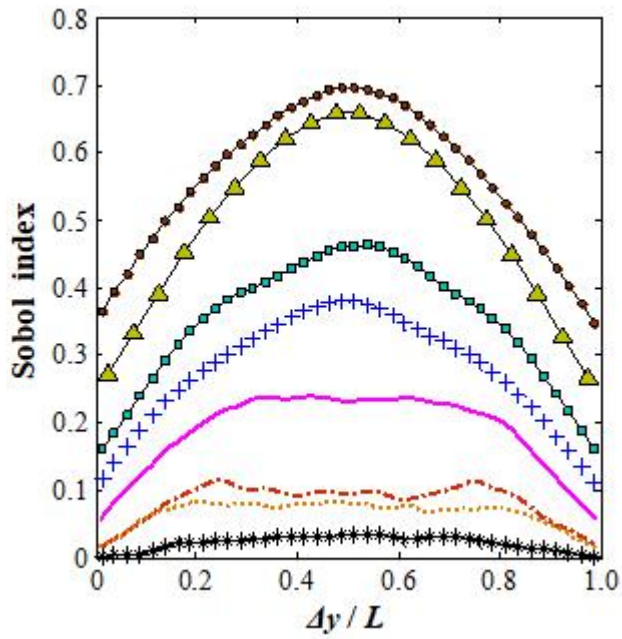
Figure 6.4 Distance between the optimal borehole location and the nearer end boundary divided by θ versus θ / L considering three sampling boreholes.



(a)



(b)



(c)

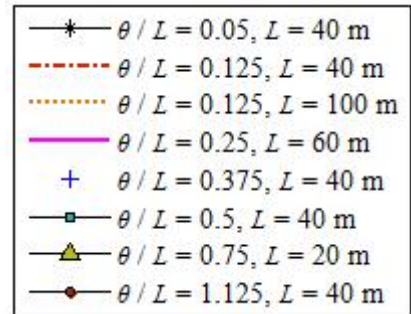


Figure 6.5 Sobol index along the slope length under different boundary conditions: (a) smooth boundary; (b) boundary fixed in (x, y) direction; (c) fully fixed boundary.

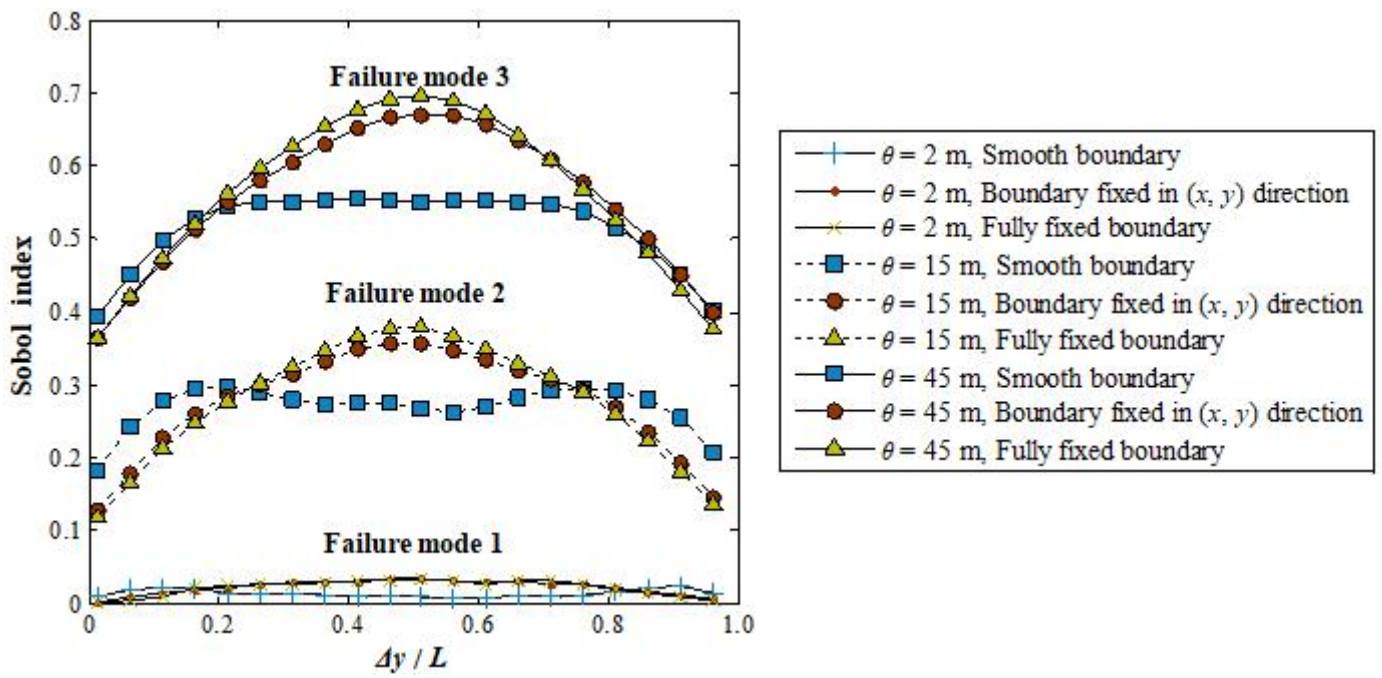


Figure 6.6 Comparison of Sobol index under the three boundary conditions with $L = 40$ m.

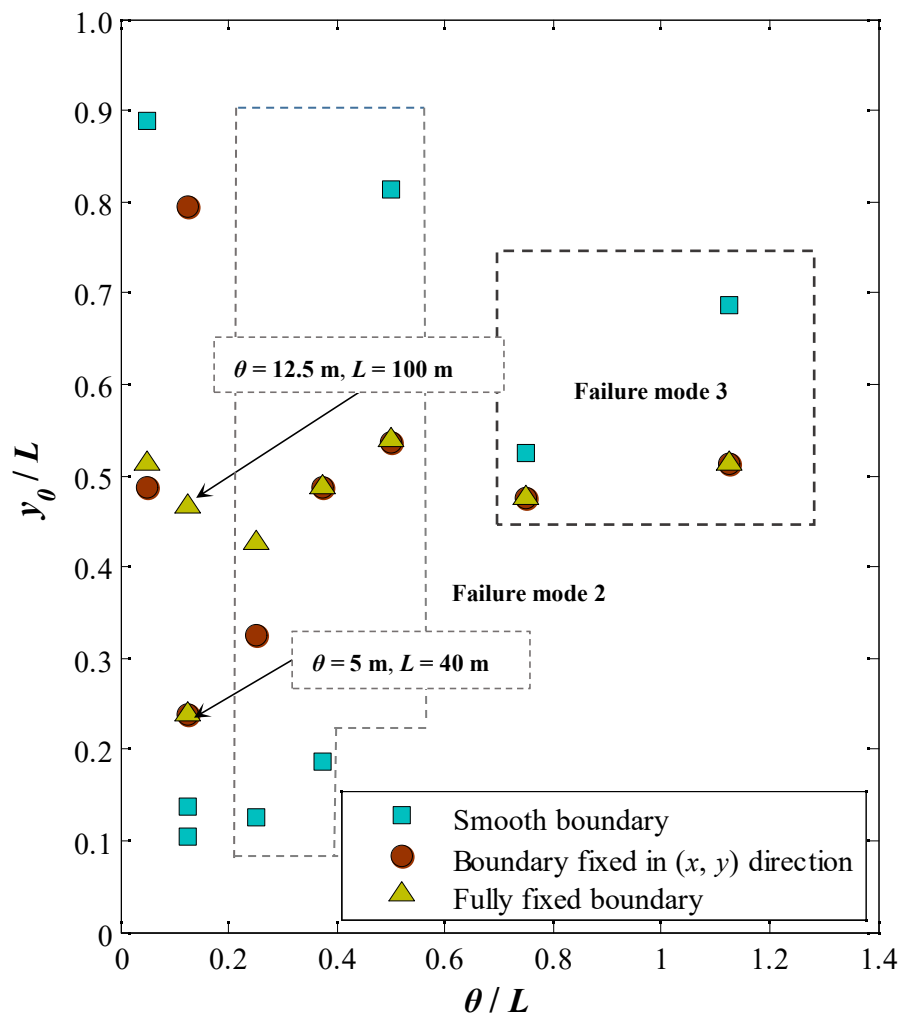


Figure 6.7 Optimal sampling location with one borehole.

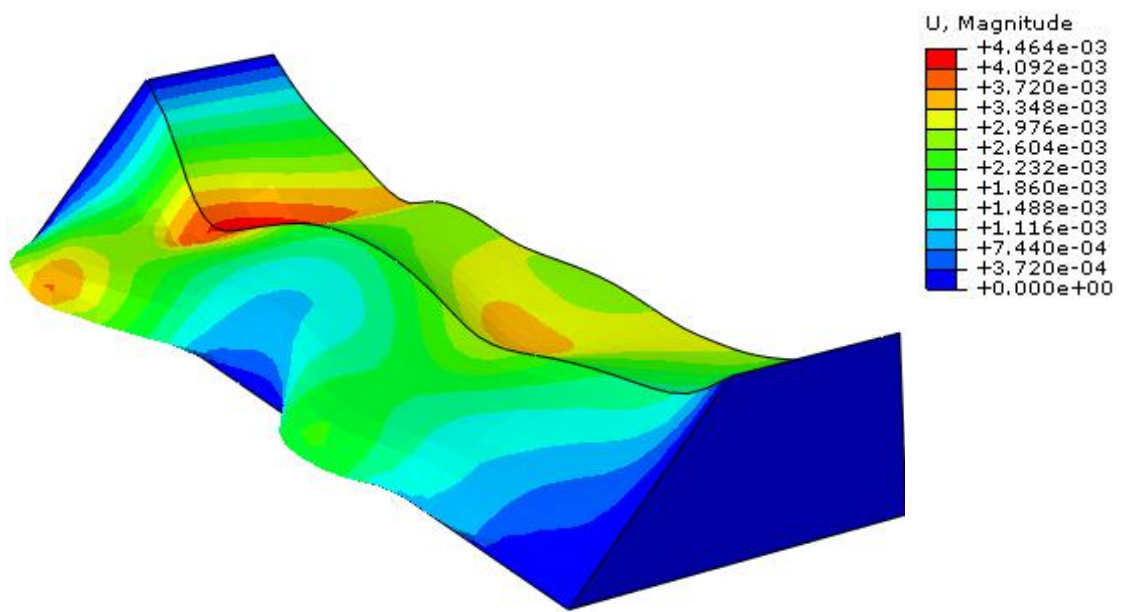


Figure 6.8 Multiple potential sliding volumes.

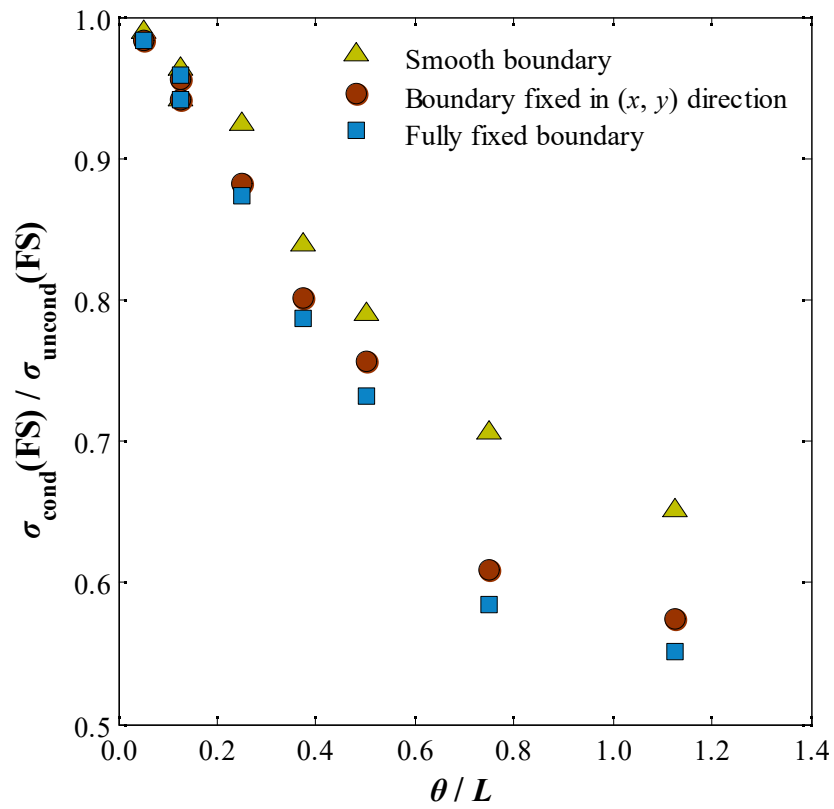
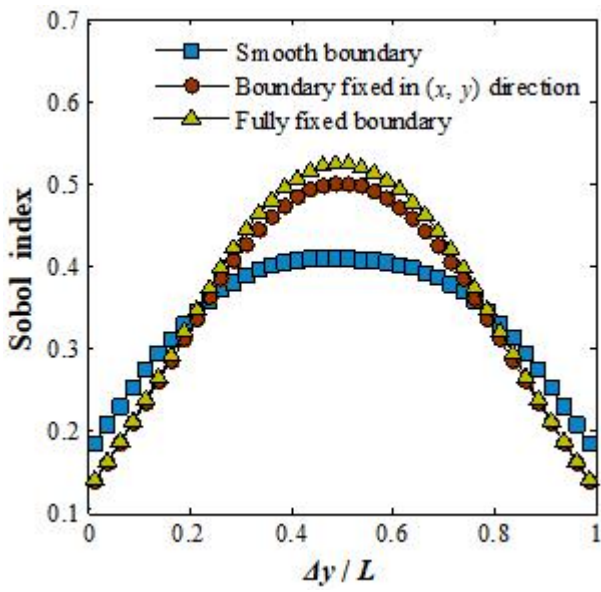
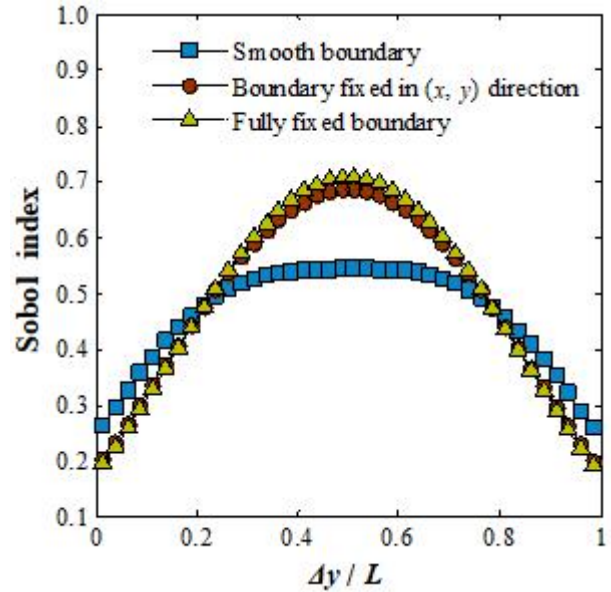


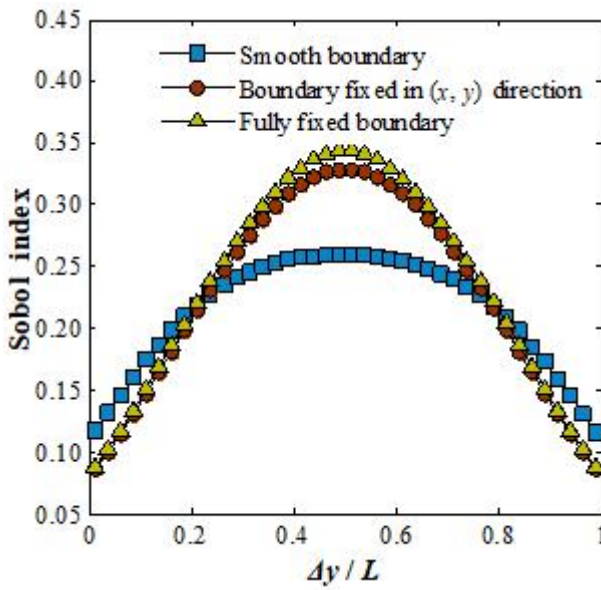
Figure 6.9 Magnitude of uncertainty reduction considering the optimal sampling pattern versus θ / L .



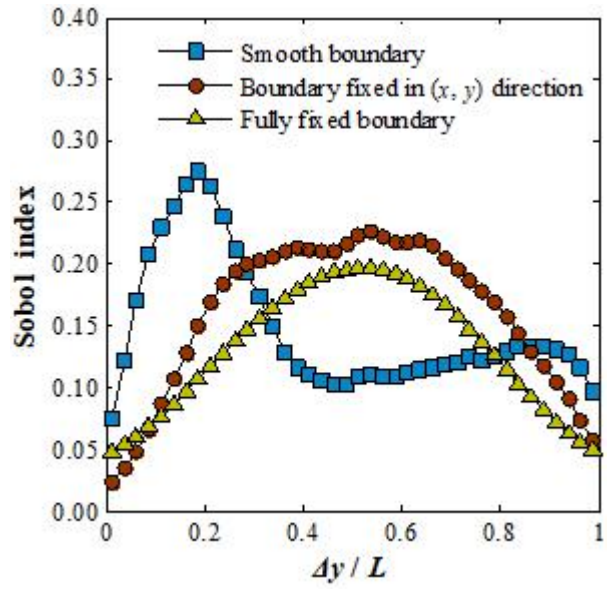
(a)



(b)



(c)



(d)

Figure 6.10 Sobol index along the slope length considering anisotropic patterns of soil spatial variability under different end boundary conditions: (a) slope with horizontal bedding; (b) dip slope ($\alpha = 30^\circ$); (c) reverse-dip slope ($\alpha = -30^\circ$); (d) cross-dip slope ($\alpha = 30^\circ$).

CHAPTER 7 Conclusion and Recommendations

7.1 Conclusion

In this thesis, the influences of anisotropic spatial variation of soils and sampling strategy were investigated in slope reliability evaluation. Non-stationary random fields considering rotated transverse anisotropy was adopted to simulate the spatially variable soils in the 2D probabilistic slope stability analyses. In addition, the 3D probabilistic slope stability analyses were conducted considering rotated transverse anisotropy of the soil properties. Investigations of sampling effects were also implemented in 2D and 3D problems. In the 2D study, various sampling strategies and rotated transverse anisotropies were considered, while comparative studies were conducted on three methods that can incorporate sampling effects in slope reliability analysis. For the 3D problem, various end boundary conditions and ratios of spatial autocorrelation distance to slope length were considered. Main findings of this thesis are presented in this section.

7.1.1 Influence of Non-stationarity and Rotated Transverse Anisotropy in Slope Reliability Evaluation

In nature, soil properties usually display non-stationarity features. Through combining non-stationarity with rotated transverse anisotropy of the soil properties, two scenarios of soils were simulated in the 2D probabilistic slope stability analyses, where the soil strength increases with depth or along the direction perpendicular to the bedding. A Stationary random field was also adopted to simulate the spatially variable soils. In this study, a saturated fine-grained slope under undrained conditions is considered, and it was found that the direction of the increasing trend has significant effects on the estimation of slope reliability and the failure mechanism considering rotated transverse anisotropy. For slope reliability analysis, the safety levels of a slope are significantly different under the different soil scenarios. When soil strength increases with depth, the slope reliability is usually higher than that considering a stationary random field. In addition, in a dip slope, the slope reliability under soil strength increasing with depth is higher than that with soil strength increasing along the perpendicular direction to the bedding. However, in the reverse slope, soil strength increasing along the direction perpendicular to the bedding would lead to higher reliability than that under soil strength increasing with depth. Furthermore, when the undrained shear strength increases along the direction perpendicular to the bedding, the slope reliability and potential failure consequence are sensitive to the dip angle of the strata. In this case, an accurate estimation of the dip angle of the strata is crucial in

slope reliability analysis and risk assessment. However, due to the complexity of the geological conditions in most engineering cases, obtaining an accurate dip angle of the strata may be difficult in normal geological surveys. For example, the bedding exposed may not display the actual orientation of the bedding within the slope body, which may cause inaccurate estimation of the dip angle of the strata. Site characterisation techniques (Section 2.4.1) can also be used to determine the dip angle of the strata through estimating the spatial autocorrelation structure of the soil properties. However, for an accurate estimation, a large number of site investigation data are needed.

Regarding the failure mechanism, it was found that when soil strength increases with depth, the probability of occurrence of a shallow slope failure would increase compared with that in a stationary random field. When the soil strength increases along the direction perpendicular to the bedding, the probability of occurrence of a shallow failure would be high in dip slopes. On the contrary, such a scenario of soils would lead to a deep failure mechanism being dominant in reverse slopes. After investigating the locations of multiple slip surfaces obtained by Monte Carlo simulations, it is found that the shallow slip surfaces occurring on slopes with soil strength increasing with depth mainly pass through the slope surface. By contrast, the shallow slip surfaces in the dip slope ($\alpha = 45^\circ$), with soil strength increasing perpendicularly to the bedding, mainly pass through the slope toe. These two scenarios of shallow slip surface can indicate significantly different consequences

(Figure 3.10). Generally, when the slip surface passes through the slope toe, the consequence caused by the landslide would be more severe.

7.1.2 Influence of 3D Rotated Transverse Anisotropy in Slope Reliability Evaluation

The effects of 3D rotated transverse anisotropy on slope reliability and failure mechanisms were investigated considering the slope under undrained conditions. Three kinds of 3D rotated transverse anisotropy [i.e., “rotated transverse anisotropy around the x axis”, “rotated transverse anisotropy around the y axis”, and “rotated transverse anisotropy around the z axis” (Figure 4.1)] were considered, associated with three slope scenarios [i.e., dip slope, reverse-dip slope and cross-dip slope (Figure 4.1)]. When the major autocorrelation distance is small relative to the slope length and height, the influence of the rotated transverse anisotropy is mitigated. That is because in this situation, the solution of the 3D probabilistic slope stability analysis is similar to that of the deterministic analysis, and the spatially variability pattern also approaches the isotropic case. When considering rotated anisotropy around the x and z axes, the same dip angles of the strata would lead to similar results of slope reliability and the mean slide length regardless of the rotational direction. In addition, in these cases, the mean FS and mean slide length decrease with higher major autocorrelation distance. On the other hand, in the cross-dip slope, the slope reliability is relatively

insensitive to the change of slope length. Those findings in relation to the cross-dip slope are different from previous findings in relation to the slope reliability and failure mechanism in 3D probabilistic slope stability analyses based on horizontal transverse anisotropy.

In relation to “rotated transverse anisotropy around the y axis” (i.e., dip and reverse-dip slopes), a critical dip angle of the strata corresponding to the lowest slope reliability can be found, and a reverse-dip slope usually has a higher reliability than that of a dip slope. When the major autocorrelation distance is large enough, the 3D estimates of the reliability of the dip slope or reverse-dip slope would be close to that estimated in the plane strain condition. However, such a phenomenon cannot be observed in a cross-dip slope. For mean slide lengths, when the major autocorrelation distance is larger than the slope height, the higher major autocorrelation distance can result in an increase in the mean slide length in a dip slope and a reverse-dip slope. These observations in relation to the slope reliability and mean slide length are similar to the findings in previous studies, where the soil bedding is assumed to be horizontal.

7.1.3 Influence of Sampling Strategies in 2D Slope Reliability Evaluation

For the investigations on sampling effects in 2D probabilistic slope stability analyses,

various sampling strategies and rotated transverse anisotropies were considered. The conditional random field simulation methods and the Sobol index method were adopted to calculate the magnitude of uncertainty reduction. It was found that when the distribution of sample points is sparse with small θ_2 or the angle of the drilling direction of the borehole is near the dip angle of the strata, the magnitudes of uncertainty reduction estimated by conditional RF model 1 are significantly smaller than those estimated using the other methods. By contrast, the estimated results by conditional RF model 2 and the Sobol index method are close. In those situations, the issue of $\sigma_{\text{cond}}(\text{FS}) > \sigma_{\text{uncond}}(\text{FS})$ may occur using conditional RF model 1. Theoretically, such an issue is unexpected in slope reliability evaluation, because sample points can provide known information on simulating the spatially variable soils and thus reduce the spatial uncertainty. The cause of this problem is the inaccurate Kriging interpolation involved in the formulation [Eq. (2.32)] of conditional RF model 1 (Section 5.4.3). By contrast, this problem is not found when using the conditional RF model 2 and the Sobol index method. Generally, when sample points are distributed properly considering the autocorrelation distance and the dip angle of the strata, the differences in the magnitude of uncertainty reduction by the three methods are small.

In addition, rotated transverse anisotropy has a significant influence on the sampling efficiency, as the lag distance in the direction of the minor autocorrelation distance between sample points would change in the rotated coordinate system. When the dip angle of the strata approaches the angle of the layout of the sample points, the lag

distance between the sample points in the direction of the minor autocorrelation distance would reduce. That means the range for effective prediction with smaller error by Kriging interpolation tends to be narrowed. Therefore, the magnitude of uncertainty reduction would decrease with the angle of the drilling direction of the borehole approaching the dip angle of the strata. When the dip angle of the strata is the same to the drilling direction of the borehole, the lag distance between the sample points in the direction of the minor autocorrelation distance is zero, which results in the highest standard deviation of FS after conditioning and the smallest magnitude of uncertainty reduction.

7.1.4 Influence of Sampling Strategies in 3D Slope Reliability Evaluation

In 3D probabilistic slope stability analyses considering sampling effects, the Sobol sensitivity index was adopted to quantify the sampling efficiency, while the optimal sampling strategy is also investigated. Compared with the conditional random field simulation methods, the method based on the Sobol index does not require given sampling points, and thus the computational effort can be significantly reduced. This is particularly significant when 3D analyses need to be performed or more than one borehole should be considered. Through considering different end boundary conditions, together with varied combinations of spatial autocorrelation distance θ and

slope length L , the sampling efficiency, optimal sampling strategy and the magnitude of uncertainty reduction are investigated.

Sampling strategies with two and three boreholes were firstly discussed. When considering two sampling boreholes, two approaches for selecting the two optimal sampling locations were considered. Approach 1 considered a randomised search of the two sampling locations throughout the whole domain, while Approach 2 considered the two locations along the slope crest being symmetrical around the middle of the slope length. It was observed that the difference in the sampling efficiency using the two approaches is small. In addition, considering Approach 2, the ratio of the distance between the sampling point and the nearer end section to the spatial autocorrelation distance generally decreases with higher ratio of θ / L . Such a phenomenon can also be found, when considering three sampling boreholes with one of the boreholes fixed at the slope middle and the other two boreholes being symmetrical around the middle.

When considering a single sampling borehole, it was found that with the increase of ratio of θ / L , the sampling efficiency for each borehole location along the slope crest increases. Also, the sampling efficiency can be affected by the end boundary conditions. Near the end sides of a slope the sampling efficiency considering the smooth boundary condition is higher than that considering the fully fixed boundary condition, whereas the observations are contrary near the middle of a slope. On the

other hand, for a slope with end boundary conditions preventing the movement in (x , y , z) direction, the optimal sampling location is around the middle of slope length in most cases. With respect to, under the smooth boundary condition, the optimal sampling location is near the middle of slope length under failure mode 3, but near the ends under failure mode 2. When considering anisotropic spatial variation of soils, observations on the variation of the Sobol index along the slope length and the influence of end boundary conditions for a slope with horizontal bedding, dip slope and reverse-dip slope are similar to those considering isotropic soil spatial variability. However, when considering cross-dip slopes, such observations are significantly different from those considering an isotropic random field.

7.1.5 Suggestions for Engineering Practice

In this thesis, both 2D and 3D probabilistic slope stability analyses were conducted. Findings in the investigations on 3D slope problems revealed the significance for considering 3D slope models in slope reliability evaluation. For example, the results in Chapter 4 showed that when the autocorrelation distance is small or the strata rotate around the x and z axes, the slope reliability would be significantly underestimated considering 2D slope models. That is because in these situations, the 3D slope features or failure modes cannot be explicitly considered in 2D slope model. In addition, the results in Chapter 6 showed that the ratio of the autocorrelation distance

to the slope length and the end boundary condition have a significant influence on slope reliability evaluation considering sampling effects. However, the slope length and end boundary conditions cannot be modeled in 2D probabilistic slope stability analyses.

Based on the findings using the unconditional simulation methods in Chapters 3 and 4, there are some points that should be noted for engineering practice. Rotated transverse anisotropy should be carefully considered with non-stationarity of soil properties, as the trend direction has a significant influence on the estimation of slope reliability. In addition, it should be noted that, when the soil strength increases along the direction perpendicular to the bedding, a slight change of the dip angle of the strata can cause a significant change in the slope reliability and potential sliding consequence. That means an accurate estimation of the dip angle of the strata is significant in this case. In this situation, advanced site characterisation techniques (e.g., Liu and Leung 2018) are suggested to be used with a large number of sampling data to assure the accurate estimation of the autocorrelation structure. In the 3D probabilistic slope stability analyses, results by comparing the slope reliability of dip, reverse-dip, cross-dip slopes and those with horizontal bedding show that the cross-dip slope can be the optimal scenario when conducting road construction and alignment. That is because the reliability of the cross-dip slope is generally the highest among these slope scenarios. Findings for the investigations on the 3D problems also showed that when the strata rotate around the y axis (i.e., dip and reverse-dip slopes), the reliability

estimated by 2D stochastic slope stability analyses would be similar to that considering the 3D slope model, if the major autocorrelation distance is large enough. However, in relation to slopes under rotated anisotropy around the x and z axes, the 3D slope model should be adopted. Otherwise, the slope reliability would be significantly underestimated, and thus economic benefits would reduce.

In addition, suggestions for engineering practice can also be given from the findings in Chapters 5 and 6. When it is needed to obtain soil samples from slopes with rotated transverse anisotropies, the borehole orientation should not be close to the bedding orientation. In addition, the issue of $\sigma_{\text{cond}}(\text{FS}) > \sigma_{\text{uncond}}(\text{FS})$ may occur in conditional RF model 1, when the sampling pattern is sparse or the angle of the drilling direction of the borehole is near the dip angle of the strata. In these situations, conditional RF model 1 would also produce a significantly higher standard deviation of FS than that by conditional RF model 2 and the Sobol index method. Estimated results of the magnitude of uncertainty reduction by conditional RF model 2 and the Sobol index method are close, but the Sobol index method cannot be used to compute the probability of failure and failure consequence after conditioning. Therefore, in slope reliability analysis and risk assessment, conditional RF model 2 is suggested to be adopted. In 3D probabilistic slope stability analyses considering sampling effects, the results of sampling efficiency by a randomised search of two optimal borehole locations is close to the result by selecting two symmetrical locations (about the middle) on the slope crest. If the spatial autocorrelation distance can be obtained from

historical site investigation data in the neighbouring sites, the locations of the two symmetrical boreholes can be primarily determined based on the relation between $\Delta y_0 / \theta$ and θ / L . Also, as θ / L value is positively proportional to sampling efficiency, engineers can decide whether it is worthwhile to drill boreholes and conduct conditional simulations based on θ / L , considering economic benefits.

7.2 Recommendations

7.2.1 Recommendations on Study of Non-stationarity in Soil Properties

Formulations for modelling non-stationary random fields have been developed by Li *et al.* (2014), Griffiths *et al.* (2015) and Jiang and Huang (2018), as shown in Table 2.5. In this thesis, the formulation by Li *et al.* (2014) was used to generate non-stationary random fields in the 2D probabilistic slope stability analyses. However, all the formulations in Table 2.5 are based on linearly increasing trends of the soil property. The justification for using a linearly increasing trend to simulate shear strength parameters has been discussed in Li *et al.* (2014). Also, a linearly increasing trend for soil strength parameters can be found in site characterisation (Asaoka and A-Grivas 1982; Liu and Leung 2018). However, non-linearly increasing trend can

often be observed in undrained shear strength through CPT data (e.g., Jaksa *et al.* 1999; Stuedlein *et al.* 2012a). Therefore, formulations for non-stationary random fields with a higher-order trend structure are desirable to be derived.

In addition, the non-stationary random field is seldom adopted in three-dimensional probabilistic slope stability analysis. When considering the 3D problem, the spatial variation of soil property in the planar orientation (i.e., x and y directions in Figure 1.2) should be involved in the trend structure. That is because the spatial autocorrelation along the slope length is significant in three-dimensional probabilistic slope stability analysis, whereas the change of the major autocorrelation distance has a little effect on the slope reliability in the 2D problem. Also, the direction of the increasing trend (i.e., increasing trend with depth and the direction perpendicular to the bedding) can be combined with the three 3D slope scenarios (i.e., cross-dip, reverse-dip and dip slopes) to investigate the reliability and failure pattern of a slope.

7.2.2 Recommendations on Study of Anisotropic Patterns of Soil Spatial Variability

This thesis only considered the anisotropic patterns of soil spatial variability for shear strength parameters. However, since most landslides are induced by rainfalls, parameters in relation to unsaturated soil parameters are also significant for slope

reliability. The permeability coefficient and saturated water content are significant to the stability of a slope, as those parameters can affect the matric suction of soils and hence the unsaturated soil strength. Considering the 3D features of slopes (e.g., cross-dip, reverse-dip and dip slopes), the rotation of the strata is expected to influence the processes of rainfall infiltration and seepage, which can result in different performance levels of slope reliability. Therefore, the spatially variable soils under rotated transverse anisotropy should be simulated considering the spatial variations of the permeability coefficient and saturated water content in probabilistic slope stability analyses. Also, the difference between the results using 2D and 3D models is worthwhile to be discussed.

Furthermore, only rotated transverse anisotropy of soil properties is investigated in this thesis. In nature, there are many anisotropic patterns of soil spatial variability [i.e., horizontal transverse anisotropy, rotated transverse anisotropy, general anisotropy, general rotated transverse anisotropy, and combinations of these (Figure 1.1)]. Zhu and Zhang (2013) have derived the autocorrelation functions for the various 2D anisotropic patterns. The autocorrelation function for 3D anisotropic patterns of soil spatial variability was also studied by Liu and Leung (2018) and Liu (2018). Based on these findings, the slope reliability and failure mechanism can be investigated considering the different patterns of anisotropy. In 3D analyses, the relation between the strike direction of the strata and the direction of the slope length should be involved in probabilistic slope stability analysis considering the different anisotropic

patterns. In addition, various slope lengths, α and η (Tables 2.9 and 2.10) should be considered together with the spatial autocorrelation distance.

7.2.3 Recommendations on Study of Sampling Effects in Probabilistic Slope Stability Analyses

In the 2D probabilistic slope stability analyses considering sampling effects and rotated transverse anisotropy, the sampling patterns were given in the current work. Herein, the optimal sampling strategy was not studied considering rotated transverse anisotropy. As the rotation of the soil bedding was found to be influential to the slope failure mechanism (Chapter 3), it is expected that the optimal sampling strategy can be affected by rotated transverse anisotropy of the soil properties. To determine the optimal sampling strategy, the computational efforts for conditional random field simulation methods are extensive. Therefore, the Sobol index method is suggested to be adopted.

The investigation on sampling effects in the 3D probabilistic slope stability analysis only focused on situations of the small number of boreholes. The situation for a large number of sampling boreholes can also be considered using the Sobol index method and Differential Evolution methods. With respect to a larger number of sampling boreholes, apart from the maximum sampling efficiency, the economic benefit should

also be considered when determining the optimal sampling strategy. That is because, when the number of sampling boreholes exceeds a threshold, the increase in sampling efficiency may be slight by adding more boreholes, while the cost of performing site investigations is usually high. Therefore, an optimal combination of the magnitude of uncertainty reduction and the economic benefit is desirable.

7.2.4 Recommendations on Study of the Influence of Groundwater Level in Probabilistic Slope Stability Analyses

In the present study, the groundwater effects are not considered. However, in engineering practice, the groundwater level is a significant factor in slope stability analysis. The increase of the groundwater level is usually the trigger of slope failure. In probabilistic slope stability analyses, the influence of soil spatial variability on slope reliability might be masked by the groundwater effects. Therefore, the influence of groundwater level is desirable to be investigated considering slopes with spatially variable soils.

In relation to the studies considering the groundwater effects, the unsaturated soil characteristics should be incorporated. When generating random fields, the spatial variability of the unsaturated soil characteristics should be considered for the soils above the groundwater level. Also, various spatial autocorrelations of soil properties

should be considered in the probabilistic slope stability analyses. In addition, it is interesting to find how high the groundwater level is can mask the influence of soil spatial variability.

References

Akbas, S.O., and Kulhawy, F.H. 2010. Characterization and estimation of geotechnical variability in Ankara clay: A case history. *Geotechnical and Geological Engineering*, 28: 619-631.

Alonso, E.E. 1976. Risk analysis of slopes and its application to slopes in Canadian sensitive clays. *Géotechnique*, 26(3): 453-472.

Ang, H.S., and Tang, W.H. 1984. Probability concepts in engineering planning and design. *Decision, Risk, and Reliability*, vol. 2., John Wiley and Sons, New York.

Arellano, D., and Stark, T.D. 2000. Importance of three-dimensional slope stability analysis in practice. In *ASCE Geotechnical Special Publication No. 101: Slope Stability 2000*, Griffiths, D.V., Fenton, G.A., and Martin, T.R. (eds). ASCE, New York: 18-32.

Asaoka, A., and A-Grivas, D. 1982. Spatial variability of the undrained strength of clays. *Journal of the Geotechnical Engineering Division*, 108(5): 743-756.

Auvinet, G., and Gonzalez, J.L. 2000. Three-dimensional reliability analysis of earth

slopes. *Computers and Geotechnics*, 26: 247-261.

Baecher, G.B., and Christian, J.T. 2003. *Reliability and statistics in geotechnical engineering*. John Wiley and Sons, New York.

Baligh, M.M., and Azzouz, A.S. 1975. End effects on the stability of cohesive soils. *Journal of the Geotechnical Engineering Division*, 101(11): 1105-1117.

Barnes, G. 1995. *Soil mechanics: principles and practice*. Macmillan International Higher Education, London.

Bishop, A.W. 1955. The use of the slip circle in the stability analysis of earth slopes. *Géotechnique*, 10(4): 129-150.

Blatman, G., and Sudret, B. 2010. An adaptive algorithm to build up sparse polynomial chaos expansions for stochastic finite element analysis. *Probabilistic Engineering Mechanics*, 25(2): 183-197.

Bucher, C.G., and Bourgund, U., 1990. A fast and efficient response surface approach for structural reliability problems. *Structural Safety*, 7(1): 57-66.

Cafaro, F., and Cherubini, C. 2002. Large sample spacing in evaluation of vertical

strength variability of clayey soil. *Journal of Geotechnical and Geoenvironmental Engineering*, 128 (7): 558-568.

Cao, Z.J., Wang, Y., and Li, D.Q. 2016. Quantification of prior knowledge in geotechnical site characterization. *Engineering Geology*, 203: 107-116.

Chang, C.S. 1992. Discrete element method for slope stability analysis. *Journal of Geotechnical Engineering*, 118(12): 1889-1905.

Chen, R.H., and Chameau, J.L. 1982. Three-dimensional limit equilibrium analysis of slopes. *Géotechnique*, 32: 31-40.

Chen, W.F. 1970. Limit analysis and limit equilibrium solutions in soil mechanics. *Soils and Foundations*, 10(3): 13-49.

Cheng, Q., Luo, S.X., and Gao, X.Q. 2000. Analysis and discuss of calculation of scale of fluctuation using correlation function method. *Chinese Journal of Rock Soil Mechanics*, 21 (3): 281-283 (in Chinese).

Cheng, Y.M., and Lau, C.K. 2008. *Slope stability analysis and stabilization*. Routledge, London.

Cheng, Y.M., and Yip, C.J. 2007. Three-dimensional asymmetrical slope stability analysis extension of Bishop's, Janbu's, and Morgenstern-Price's techniques. *Journal of Geotechnical and Geoenvironmental Engineering*, 133(12): 1544-1555.

Cheng, Y.M., Liu, H.T., and Au, S.K. 2005. Location of critical three-dimensional nonspherical failure surface by NURBS functions and ellipsoid with applications to highway slopes. *Computers and Geotechnics*, 32: 387-399.

Cheng, Y.M., Lansivaara, T., and Wei, W.B. 2007. Two-dimensional slope stability analysis by limit equilibrium and strength reduction methods. *Computers and Geotechnics*, 34: 137-150.

Cheng, Y.M., Zhao, Z.H., and Sun, Y.J. 2010. Evaluation of interslice force function and discussion on convergence in slope stability analysis by the lower bound method. *Journal of Geotechnical and Geoenvironmental Engineering*, 136(8): 1103-1113.

Ching, J.Y., and Phoon, K.K. 2013. Effect of element sizes in random field finite element simulations of soil shear strength. *Computers and Structures*, 126: 120-134.

Ching, J.Y., Phoon, K.K., and Chen, Y.C. 2010. Reducing shear strength uncertainties in clays by multivariate correlations. *Canadian Geotechnical Journal*, 47(1): 16-33.

Ching, J.Y., Hu, Y.G., Yang, Z.Y., Shiau, J.Q., Chen, J.C., and Li, Y.S. 2011. Reliability-based design for allowable bearing capacity of footings on rock masses by considering angle of distortion. *International Journal of Rock Mechanics and Mining Science*, 48 (5): 728-740.

Cho, S.E. 2009. Probabilistic stability analyses of slopes using the ANN-based response surface. *Computers and Geotechnics*, 36 (5): 787-797.

Cho, S.E. 2010. Probabilistic assessment of slope stability that considers the spatial variability of soil properties. *Journal of Geotechnical and Geoenvironmental Engineering*, 136(7): 975-984.

Cho, S.E. 2013. First-order reliability analysis of slope considering multiple failure modes. *Engineering Geology*, 154: 98-105.

Chowdhury, R.N., and Xu, D.W. 1993. Rational polynomial technique in slope-reliability analysis. *Journal of the Geotechnical Engineering Division*, 119(12): 1910-1928.

Chowdhury, R.N., and Xu, D.W. 1995. Geotechnical system reliability of slopes. *Reliability Engineering and System Safety*, 47: 141-151.

Christian, J.T., Charles, C., Ladd, C.C., and Baecher, B.G. 1994. Reliability applied to slope stability analysis. *Journal of Geotechnical Engineering*, 120(12): 2180-2207.

Chugh, A.K. 2003. On the boundary conditions in slope stability analysis. *International Journal for Numerical and Analytical Methods in Geomechanics*, 27: 905-926.

Cooley, J.W., and Turkey, J.W. 1965. An algorithm for the machine calculation of complex Fourier series. *Mathematics of Computation*, 19(90): 297-301.

Cornell, C.A. 1971. First-order uncertainty analysis of soils deformation and stability. In *Proceedings of the 1st International Conference on Application of Probability and Statistics in Soil and Structural Engineering (ICAPI)*. Hong Kong: 129-144.

Corps of Engineers. 2003. "Appendix G - Procedures and Examples for Rapid Drawdown". *Engineering Manual*, EM 1110-2-1902. Department of the U.S Army Corps of Engineers.

Dawson, E.M., Roth, W.H., and Drescher, A. 1999. Slope stability analysis by strength reduction. *Géotechnique*, 49(6): 835-840.

DeGroot, D.J., and Baecher, G.B. 1993. Estimating autocovariance of in-situ soil

properties. *Journal of Geotechnical engineering*, 119(1): 147-166.

Deng, J. 2006. Structural reliability analysis for implicit performance function using radial basis function network. *International Journal of Solids Structure*, 43(3): 255-291.

Deng, J., Gu, D., Li, X., and Yue, Q.Z. 2005. Structural reliability analysis for implicit performance functions using artificial neural network. *Structural Safety*, 27(1): 25-48.

Deng, Z.P., Li, D.Q., Qi, X.H., Cao, Z.J., and Phoon, K.K. 2017. Reliability evaluation of slope considering geological uncertainty and inherent variability of soil parameters. *Computers and Geotechnics*, 92: 121-131.

Deodatis, G. 1996. Simulation of ergodic multivariate stochastic processes. *Journal of Engineering Mechanics*, 122(8): 778-787.

Detournay, C., Hart, R., and Varona, P. 2011. Factor of safety measure for Hoek-Brown material. In *Proceedings of Continuum and Distinct Element Numerical Modeling in Geomechanics-2011*. ITASCA Consulting Group, 2008, Melbourne, Australia. Edited by Sainsbury, Hart, Detournay, and Nelson: 765-772.

Ditlevsen, O. 1981. Uncertainty modeling: with applications to multidimensional civil engineering systems. McGraw-Hill, New York.

Donald, I.B., and Giam, S.K. 1988. Application of the nodal displacement method to slope stability analysis. In Proceedings of the 5th Australia-New Zealand Conference on Geomechanics. Institution of Engineers, Australia, Sydney, Australia: 456-460.

Drucker, D.C., and Prager, W. 1952. Soil mechanics and plastic analysis for limit design. Quarterly of Applied Mathematics, 10(2): 157-165.

Duncan, J.M. 1996. State of the art: Limit equilibrium and finite element analysis of slopes. Journal of Geotechnical Engineering, 122(7): 577-596.

Elkateb, T., Chalaturnyk, R., and Robertson, P.K. 2003. Simplified geostatistical analysis of earthquake-induced ground response at the wildlife site, California, U.S.A. Canadian Geotechnical Journal, 40(1): 16-35.

El-Ramly, H., Morgenstern, N.R., and Cruden, D.M. 2002. Probabilistic slope stability analysis for practice. Canadian Geotechnical Journal, 39(3): 665-683.

El-Ramly, H., Morgenstern, N.R., and Cruden, D.M. 2003. Probabilistic stability analysis of a tailing dyke on presheared clay-shale. Canadian Geotechnical Journal,

40(1): 192-208.

Fan, K., Fredlund, D.G., and Wilson, G.W. 1986. An interslice force function for limit equilibrium slope stability analysis. *Canadian Geotechnical Journal*, 23(3): 287-296.

Fellenius, W. 1936. Calculation of the stability of earth dam. In *Proceedings of the Second Congress of Large Dams. International Congress on Large Dam, Washington, D.C.*: 445-463.

Fenton, G.A. 1990. Simulation and analysis of random fields. PhD thesis, Princeton University, Princeton, N.J.

Fenton, G.A. 1994. Error evaluation of three random-field generators. *Journal of Engineering Mechanics*, 120(12): 2478-2497.

Fenton, G.A., and Griffiths, D.V. 2003. Bearing-capacity prediction of spatially random $c - \phi$ soils. *Canadian Geotechnical Journal*, 40(1): 54-65.

Fenton, G.A., and Griffiths, D.V. 2008. Risk assessment in geotechnical engineering. John Wiley & Sons, New York.

Fenton, G.A., and Vanmarcke, E.H. 1990. Simulation of random fields via local

average subdivision. *Journal of Engineering Mechanics*, 116(8): 1733-1749.

Firouzianbandpey, S., Griffiths, D.V., Ibsen, L.B., and Andersen, L.V. 2014. Spatial correlation length of normalized cone data in sand: Case study in the north of Denmark. *Canadian Geotechnical Journal*, 51(8): 844-857.

Foye, K.C., Abou-Jaoude, G.G., and Salgado, R. 2004. Limit states design (LSD) for shallow and deep foundations. Report, Joint Transportation Research Program. West Lafayette (Indiana): Indiana Department of Transportation and Purdue University; Report No.: FHWA/IN/JTRP-2004/21.

Frimpong, S., and Achireko, P.K. 1998. Conditional LAS stochastic simulation of regionalized variables in random fields. *Computer & Geoscience*, 2: 37-45.

Gao, D.Z. 1996. Safety index of geotechnical design and its application. *Chinese Journal of Geotechnical Investigation Survey*, 1: 1-6 (in Chinese).

Georgakakos, A., Kitanidis, P., and Loaiciga, H. 1990. Review of geostatistics in geohydrology. I: basic concepts. *Journal of Hydraulic Engineering*, 116(5): 612-632.

GEO-SLOPE International Ltd. 2012. Stability modelling with SLOPE/W 2012 version: an engineering methodology [computer program]. GEO-SLOPE International

Ltd., Calgary, Alberta, Canada.

Geotechnical Engineering Office. 1984. Geotechnical Manual of Slopes. Civil Engineering and Development Department, Hong Kong: Hong Kong Government, the HKSAR Government.

Gharti, H.N., Komatitsch, D., Oye, V., Martin, R., and Tromp, J. 2012. Application of an elastoplastic spectral-element method to 3D slope stability analysis. *International Journal for Numerical Methods in Engineering*, 91(1): 1-26.

Gomes, H.M., and Awruch, A.M. 2004. Comparison of response surface and neural network with other methods for structural reliability analysis. *Structural Safety*, 26 (1): 49-67.

Griffiths, D.V., and Fenton, G.A. 2001. Bearing capacity of spatially random soil: the undrained clay Prandtl problem revisited. *Géotechnique*, 51(4): 351-359.

Griffiths, D.V., and Fenton, G.A. 2004. Probabilistic slope stability analysis by finite elements. *Journal of Geotechnical and Geoenvironmental Engineering*, 130(5): 507-518.

Griffiths, D.V., and Lane, P.A. 1999. Slope stability analysis by finite elements.

Géotechnique, 49(3): 387-403.

Griffiths, D.V., and Marquez, R.M. 2007. Three-dimensional slope stability analysis by elasto-plastic finite elements. *Géotechnique*, 57: 537-546.

Griffiths, D.V., and Marquez, R.M. 2008. Reply to discussion by P.R. Vaughan on three-dimensional slope stability analysis by elasto-plastic finite elements. *Géotechnique*, 58: 683-685.

Griffiths, D.V., Huang, J., and Fenton, G.A. 2009a. Influence of spatial variability on slope reliability using random fields. *Journal of Geotechnical and Geoenvironmental Engineering*, 135(10): 1367-1378.

Griffiths, D.V., Huang, J., and Fenton, G.A. 2009b. On the reliability of earth slopes in three dimensions. *Proceedings of the Royal Society A-Mathematical Physical & Engineering Sciences*, 465(2110): 3145-3164.

Griffiths, D.V., Schiermeyer, R.P., Huang, J., and Fenton, G.A. 2009c. Influence of anisotropy and rotation on probabilistic slope stability analysis by RFEM. In *Proceedings of GeoHalifax*. Canadian Geotechnical Society (CGS) and the International Association of Hydrogeologists (IAH), Paper 408, (CD-ROM).

Griffiths, D.V., Huang, J., and Fenton, G.A. 2015. Probabilistic slope stability analysis using RFEM with non-stationary random fields. In *Geotechnical Safety and Risk V*, Schweckendiek, T., van Tol, A.F., Pereboom, D., *et al.* (Eds.). pp: 704-709.

Haldar, A., and Mahadevan, S. 1999. *Probability, reliability and statistical methods in engineering design*. John Wiley and Sons, New York.

Haldar, S., and Sivakumar Babu, G.L. 2009. Design of laterally loaded piles in clays based on cone penetration test data: a reliability-based approach. *Géotechnique*, 59 (7): 593-607.

Hasofer, A.M., and Lind, N.C. 1974. Exact and invariant second-moment code format. *Journal of Engineering Mechanics*, 100: 111-121.

Hassan, A.M., and Wolff, T. F. 1999. Search algorithm for minimum reliability index of earth slopes. *Journal of Geotechnical and Geoenvironmental Engineering*, 125(4): 301-308.

He, X., Hu, H.S., and Guan, W. 2010. Fast and slow flexural waves in a deviated borehole in homogeneous and layered anisotropic formations. *Geophysical Journal International*, 181(1): 417-426.

Hicks, M.A., and Li, Y. 2018. Influence of length effect on embankment slope reliability in 3D. *International Journal for Numerical and Analytical Methods in Geomechanics*, 42(1): 891-915.

Hicks, M.A., and Samy, K. 2002. Influence of heterogeneity on undrained clay slope stability. *Quarterly Journal of Engineering Geology and Hydrogeology*, 35 (1): 41-49.

Hicks, M.A., and Spencer, W.A. 2010. Influence of heterogeneity on the reliability and failure of a long 3D slope. *Computers and Geotechnics*, 37: 948-955.

Hicks, M.A., Nuttall, J.D., and Chen, J. 2014. Influence of heterogeneity on 3D slope reliability and failure consequence. *Computers and Geotechnics*, 61(3): 198-208.

Hoeg, K., and Tang, W. 1977. Probabilistic considerations in the foundation engineering for offshore structures. In *Proceedings of the Second International Conference on Structural and Reliability*. Technische Universitat Munchen, Munich, Germany: 267-296.

Houmadi, Y., Ahmed, A., and Soubra, A.H. 2012. Probabilistic analysis of a one-dimensional soil consolidation problem. *Georisk: Assessment and Management of Risk for Engineered Systems and Geohazards*, 6(1): 36-49.

Huang, C.C., Tsai, C.C., and Chen, Y.H. 2002. Generalized method for three-dimensional slope stability analysis. *Journal of Geotechnical and Geoenvironmental Engineering*, 128(10): 836-848.

Huang, J., and Griffiths, D.V. 2015. Determining an appropriate finite element size for modelling the strength of undrained random soils. *Computers and Geotechnics*, 69: 506-513.

Huang, J., Griffiths, D.V., and Fenton, G.A. 2010. System reliability of slopes by RFEM. *Soils and Foundations*, 50(3): 343-353.

Huang, S.P., Liang, B., and Phoon, K.K. 2009. Geotechnical probabilistic analysis by collocation-based stochastic response surface method: an Excel add-in implementation. *Georisk: Assessment and Management of Risk for Engineered Systems and Geohazards*, 3(2): 75-86.

Hungr, O. 1987. An extension of Bishop's simplified method of slope stability analysis to three dimensions. *Géotechnique*, 37: 113-117.

Hutchinson, J.N., and Sarma, S.K. 1985. Discussion on three-dimensional limit equilibrium analysis of slopes. *Géotechnique*, 35: 215-216.

Itasca. 1999. PFC2D/3D – Particle flow code in 2 dimensions. Itasca Consulting Group Inc, Minneapolis.

Jaksa, M.B., Brooker, P.I., and Kaggwa, W.S. 1997. Inaccuracies associated with estimating random measurement errors. *Journal of Geotechnical and Geoenvironmental Engineering*, 123 (5): 393-401.

Jaksa, M.B., Kaggwa, W.S., and Brooker, P.I. 1999. Experimental evaluation of the scale of fluctuation of a stiff clay. In 8th International Conference on Application of Statistics and Probability (ICASP8). Balkema, Sydney: 415-422.

Janbu, N. 1957. Earth pressure and bearing capacity by generalized procedure of slices. In *Proceedings of the Fourth International Conference on Soil Mechanics*. Butterworths, London, U.K.: 207-212.

Janbu, N. 1973. Slope stability computations. In *Embankment-Dam Engineering*, Hirschfeld, R.C., and Poulos, S.J. (eds.). John Wiley, New York: 47-86.

Javankhoshdel, S., Luo, N., and Bathurst, R.J. 2017. Probabilistic analysis of simple slopes with cohesive soil strength using RLEM and RFEM. *Georisk: Assessment and Management of Risk for Engineered Systems and Geohazards*, 11(3): 231-246.

Jha, S.K., and Ching, J.Y. 2013. Simplified reliability method for spatially variable undrained engineered slopes. *Soils and Foundations*, 53(5): 708-719.

Ji, J. 2014. A simplified approach for modelling spatial variability of undrained shear strength in out-plane failure mode of earth embankment. *Engineering Geology*, 183: 315-323.

Ji, J., and Chan, C.L. 2014. Long embankment failure accounting for longitudinal spatial variation - A probabilistic study. *Computers and Geotechnics*, 61: 50-56.

Ji, J., and Low, B.K. 2012. Stratified response surface for system probabilistic evaluation of slopes. *Journal of Geotechnical and Geoenvironmental Engineering*, 138(11): 1398-1406.

Ji, J., Liao, H.J., and Low, B.K. 2012. Modeling 2-D spatial variation in slope reliability analysis using interpolated autocorrelations. *Computers and Geotechnics*, 40: 135-146.

Ji, J., Zhang, C.B., Gao, Y.F., and Kodikara, J. 2019. Reliability-based design for geotechnical engineering: An inverse FORM approach for practice. *Computers and Geotechnics*, 111: 22-29.

Jiang, J.C., and Yamagami, T. 1999. Determination of the sliding direction in three-dimensional slope stability analysis. In Proceedings of the 44th Symposium on Engineering Geology and Geotechnical Engineering. University of Nevada, Reno, Nevada, 193-200.

Jiang, S.H., and Huang, J.S. 2016. Efficient slope reliability analysis at low-probability levels in spatially variable soils. *Computers and Geotechnics*, 75: 18-27.

Jiang, S.H., and Huang, J.S. 2018. Modeling of non-stationary random field of undrained shear strength of soil for slope reliability analysis. *Soils and Foundations*, 58(1): 185-198.

Jiang, S.H., Li, D.Q., Zhang, L.M., and Zhou, C.B. 2014. Slope reliability analysis considering spatially variable shear strength parameters using a non-intrusive stochastic finite element method. *Engineering Geology*, 168(1): 120-128.

Jiang, S.H., Li, D.Q., Cao, Z.J., Zhou, C.B., and Phoon, K.K. 2015. Efficient system reliability analysis of slope stability in spatially variable soils using Monte Carlo simulation. *Journal of Geotechnical and Geoenvironmental Engineering*, 141(2): 04014096.

Kang, F., and Li, J. 2016. Artificial bee colony algorithm optimized support vector regression for system reliability analysis of slopes. *Journal of Computing in Civil Engineering*, 30(3): 04015040.

Kang, F., Xu, Q., and Li, J. 2016. Slope reliability analysis using surrogate models via new support vector machines with swarm intelligence. *Applied Mathematical Modelling*, 40(11-12): 6105-6120.

Kasama, K., and Whittle, A.J. 2011. Bearing capacity of spatially random cohesive soil using numerical limit analyses. *Journal of Geotechnical and Geoenvironmental Engineering*, 137(11): 989-996.

Kerry, R., and Oliver, M.A. 2007. Comparing sampling needs for variograms of soil properties computed by the method of moments and residual maximum likelihood. *Geoderma*, 140(4): 383-396.

Kim, J.M., and Sitar, N. 2013. Reliability approach to slope stability analysis with spatially correlated soil properties. *Soils and Foundations*, 53(1): 1-10.

Kulatilake, P.H.S.W., and Um, J.G. 2003. Spatial variation of cone tip resistance for the clay site at Texas A&M University. *Geotechnical and Geological Engineering*, 21(2): 149-165.

Kulhawy, F.H., and Mayne, P.W. (Cornell University, Geotechnical engineering group). 1990. In Manual on estimating soil properties for foundation design, Final report. Palo Alto (CA): Electric Power Research Institute; Report No.: EL-6800.

Lam, H., Leung, J., and Lo, D. 2014. Review of landslides in 2011. Civil Engineering and Development Department, The Government of the Hong Kong Special Administrative Region, Report No. LSR 1/2013.

Lark, R.M. 2000. Estimating variograms of soil properties by the method-of-moments and maximum likelihood. *European Journal of Soil Slopes*, 51(4): 717-728.

Lee, R., and Lo, D. 2017. Review of landslides in 2013. Civil Engineering and Development Department, The Government of the Hong Kong Special Administrative Region, Report No. LSR 2/2014.

Lee, R., Leung, J., and Lo, D. 2015. Review of landslides in 2012. Civil Engineering and Development Department, The Government of the Hong Kong Special Administrative Region, Report No. LSR 1/2014.

Lee, R., Law, R., and Lo, D. 2017. Review of landslides in 2014. Civil Engineering and Development Department, The Government of the Hong Kong Special

Administrative Region, Report No. LSR 1/2015.

Leshchinsky, D., Baker, R., and Silver, M.L. 1985. Three-dimensional analysis of slope stability analysis. *International Journal for Numerical and Analytical Methods in Geomechanics*, 9: 199-223.

Li, A., Lau, J., Cheung, L., and Lam, C. 2012. Review of landslides in 2008. Civil Engineering and Development Department, The Government of the Hong Kong Special Administrative Region, Report No. LSR 15/2009.

Li, A., Lau, J., Cheung, L., and Lam, C. 2013. Review of landslides in 2009. Civil Engineering and Development Department, The Government of the Hong Kong Special Administrative Region, Report No. LSR 1/2011.

Li, A., Leung, J., and Lam, H. 2014. Review of landslides in 2010. Civil Engineering and Development Department, The Government of the Hong Kong Special Administrative Region, Report No. LSR 1/2012.

Li, C.C., and Der Kiureghian, A. 1993. Optimal discretization of random fields. *Journal of Engineering Mechanics*, 119(6): 1136-1154.

Li, D.Q., Qi, X.H., Phoon, K.K., Zhang, L.M., and Zhou, C.B. 2014. Effect of

spatially variable shear strength parameters with linearly increasing mean trend on reliability of infinite slopes. *Structural Safety*, 49: 45-55.

Li, D.Q., Jiang, S.H., Cao, Z.J., Zhou, W., Zhou, C.B., and Zhang, L.M. 2015. A multiple response-surface method for slope reliability analysis considering spatial variability of soil properties. *Engineering Geology*, 187: 60-72.

Li, D.Q., Xiao, T., Cao, Z.J., Zhou, C.B., and Zhang, L.M. 2016a. Enhancement of random finite element method in reliability analysis and risk assessment of soil slopes using subset simulation. *Landslides*, 13(2): 293-303.

Li, D.Q., Zheng, D., Cao, Z.J., Tang, X.S., and Phoon, K.K. 2016c. Response surface methods for slope reliability analysis: Review and comparison. *Engineering Geology*, 203: 3-14.

Li, L., and Chu, X.S. 2015. Multiple response surfaces for slope reliability analysis. *International Journal for Numerical and Analytical Methods in Geomechanics*, 39(2): 175-192.

Li, L., and Chu, X.S. 2016. Risk assessment of slope failure by representative slip surfaces and response surface function. *KSCE journal of civil engineering*, 39(2): 175-192.

Li, L., and Chu, X.S. 2019. Failure mechanism and factor of safety for spatially variable undrained soil slope. *Advances in Civil Engineering*, 2019: 8575439.

Li, L., Wang, Y., Cao, Z.J., and Chu, X.S. 2013. Risk de-aggregation and system reliability analysis of slope stability using representative slip surfaces. *Computers and Geotechnics*, 53(3): 95-105.

Li, X.Y., Xie, K.H., and Yu, Y. 2003. Research of the characteristics of correlation distance on soil properties indexes. *China Civil Engineering Journal*, 36 (8): 91-95 (in Chinese).

Li, Y.J., Hicks, M.A., and Nuttall, J.D. 2015b. Comparative analyses of slope reliability in 3D. *Engineering Geology*, 196: 12-23.

Li, Y.J., Hicks, M.A., and Vardon, P.J. 2016b. Uncertainty reduction and sampling efficiency in slope designs using 3D conditional random fields. *Computers and Geotechnics*, 79: 159-172.

Liu L.L., and Cheng, Y.M. 2016. Efficient system reliability analysis of soil slopes using multivariate adaptive regression splines-based Monte Carlo simulation. *Computers and Geotechnics*, 79: 41-54.

Liu, L.L., Cheng, Y.M., Wang, X.M., Zhang, S.H., and Wu, Z.H. 2017a. System reliability analysis and risk assessment of a layered slope in spatially variable soils considering stratigraphic boundary uncertainty. *Computers and Geotechnics*, 89: 213-225.

Liu, L.L., Cheng, Y.M., and Zhang, S.H. 2017b. Conditional random field reliability analysis of a cohesion-frictional slope. *Computers and Geotechnics*, 82: 173-186.

Liu, L.L., Cheng, Y.M., and Wang, X.M. 2017c. Genetic algorithm optimized Taylor Kriging surrogate model for system reliability analysis of soil slopes. *Landslides*, 14: 535-546.

Liu, L.L., Deng, Z.P., Zhang, S.H., and Cheng, Y.M. 2018. Simplified framework for system reliability analysis of slopes in spatially variable soils. *Engineering Geology*, 239: 330-343.

Liu, W.F. 2018. Characterisation of soil spatial variability and applications in ground exploration. PhD thesis, The Hong Kong Polytechnic University, Hong Kong.

Liu, W.F., and Leung, Y.F. 2018. Characterising three-dimensional anisotropic spatial correlation of soil properties through in situ test results. *Géotechnique*, 69(9):

805-819.

Liu, W.F., Leung, Y.F., and Lo, M.K. 2017d. Integrated framework for characterization of spatial variability of geological profiles. *Canadian Geotechnical Journal*, 54 (1): 47-58.

Lloret-Cabot, M., Hicks, M.A., and Van Den Eijnden, A.P. 2012. Investigation of the reduction in uncertainty due to soil variability when conditioning a random field using Kriging. *Géotechnique letters*, 2: 123-127.

Lloret-Cabot, M., Fenton, G.A., and Hicks, M.A. 2014. On the estimation of scale of fluctuation in geostatistics. *Georisk: Assessment and Management of Risk for Engineered Systems and Geohazards*, 8(2): 129-140.

Lo, M.K. 2019. Effect of soil spatial variability, sampling strategy and field monitoring on geotechnical reliability. PhD thesis, The Hong Kong Polytechnic University, Hong Kong.

Lo, M.K., and Leung, Y.F. 2017. Probabilistic analyses of slopes and footings with spatially variable soils considering cross-correlation and conditioned random field. *Journal of Geotechnical and Geoenvironmental Engineering*, 143(9): 04017044.

Lo, M.K., and Leung, Y.F. 2018. Reliability assessment of slopes considering sampling influence and spatial variability by Sobol sensitivity index. *Journal of Geotechnical and Geoenvironmental Engineering*, 144(4): 04018010.

Low, B.K. 2014. FORM, SORM, and spatial modelling in geotechnical engineering. *Structural Safety*, 49: 56-64.

Lowe, J., and Karafiath, L. 1960. Stability of Earth Dams Upon Drawdown. In *Proceedings of the 1st Pan-American Conference on Soil Mechanics and Foundation Engineering*. São Paulo: Associação Brasileira de Mecânica dos Solos, Mexico City, 2: 537-552.

Lumb, P. 1970. Safety factors and the probability distribution of soil strength. *Canadian Geotechnical Journal*, 7(3): 225-242.

Matérn, B. 1960. Spatial variation: Stochastic models and their application to some problems in forest surveys and other sampling investigations. *Meddelanden Fran Statens Skogsforskningsinstitut*, 49(5): 1-144.

Mateu, J., Juan, P., and Porcu, E. 2007. Geostatistical analysis through spectral techniques: some words of caution. *Communications in Statistics - Simulation and Computation*, 36(5): 1035-1051.

Matsui, T., and San, K.C. 1992. Finite element slope stability analysis by shear strength reduction technique. *Soils and Foundations*, 32(32): 59-70.

Matsuo, M. 1976. *Reliability in Embankment Design*. Department of Civil Engineering, MIT, Cambridge.

Melchers, R.E. 1999. *Structural reliability analysis and prediction*, 2nd ed. John Wiley and Sons, New York.

Mafi, R., Javankhoshdel, S., Cami, B., Chenari, R.J., and Gandomi, A.H. 2020. Surface altering optimisation in slope stability analysis with non-circular failure for random limit equilibrium method. *Georisk: Assessment and Management of Risk for Engineered Systems and Geohazards*, DOI: [10.1080/17499518.2020.1771739](https://doi.org/10.1080/17499518.2020.1771739).

Miro, S., Hartmann, D., and Schanz, T. 2014. Global sensitivity analysis for subsoil parameter estimation in mechanized tunneling. *Computers and Geotechnics*, 56: 80-88.

Mollon, G., Dias, D., and Soubra, A. 2011. Probabilistic analysis of pressurized tunnels against face stability using collocation-based stochastic response surface method. *Journal of Geotechnical and Geoenvironmental Engineering*, 137(4):

385-397.

Morgenstern, N.R., and Price, V.E. 1965. The analysis of the stability of general slip surfaces. *Géotechnique*, 15(1): 79-93.

Naylor, D.J. 1982. Finite elements and slope stability. *Numerical Methods in Geomechanics*, 92: 229-244.

Ni, W.K., Niu, F.J., and Liu, D.Y. 2002. A study on the spatial self-correlation of loess parameters. *Chinese Journal Xian Engineering University*, 24(2): 4-9 (in Chinese).

Nian, T.K., Huang, R.Q., Wan, S.S., and Chen, G.Q. 2012. Three-dimensional strength-reduction finite element analysis of slopes: geometric effects. *Canadian Geotechnical Journal*, 49(5): 574-588.

Odeh, I.O.A., Mcbratney, A.B., Chittleborough, D.J. 1995. Further results on prediction of soil properties from terrain attributes: heterotopic cokriging and regression-kriging. *Geoderma*, 67(3-4): 215-226.

Phoon, K.K., and Kulhawy, F.H. 1999. Characterization of geotechnical variability. *Canadian Geotechnical Journal*, 36(4): 612-624.

Phoon, K.K., Quek, S.T., and An, P. 2003. Identification of statistically homogeneous soil layers using modified Bartlett statistics. *Journal of Geotechnical and Geoenvironmental Engineering*, 129(7): 649-659.

Qi, X.H., and Li, D.Q. 2018. Effect of spatial variability of shear strength parameters on critical slip surfaces of slopes. *Engineering Geology*, 239: 41-49.

Rackwitz, R. 2000. Reviewing probabilistic soils modelling. *Computers and Geotechnics*, 26: 199-223.

Roberts, C., and Casella, G. 1999. Monte Carlo statistical methods. Springer, Berlin, Germany.

Ronold, M. 1990. Random field modeling of foundation failure modes. *Journal of Geotechnical Engineering*, 166(4): 554-570.

Salgado, R., and Kim, D. 2014. Reliability analysis and load and resistance factor design of slopes. *Journal of Geotechnical and Geoenvironmental Engineering*, 140(1): 57-73.

Samui, P., Lansivaara, T., and Kim, D. 2011. Utilization relevance vector machine for slope reliability analysis. *Applied Soft Computing Journal*, 11(5): 4036-4040.

Samui, P., Lansivaara, T., and Bhatt, M.R. 2013. Least square support vector machine applied to slope reliability analysis. *Geotechnical and Geological Engineering*, 31(4): 1329-1334.

Santra, P., Das, B.S., and Chakravarty, D. 2012. Spatial prediction of soil properties in a watershed scale through maximum likelihood approach. *Environmental Earth Sciences*, 65(7): 2051-2061.

Shahid, S.A., Abdelfattah, M.A., and Taha, F.K. 2013. *Developments in soil salinity assessment and reclamation: Innovative thinking and use of marginal soil and water resources in irrigated agriculture*. Springer, Dordrecht, Netherlands.

Shen, J.Y., and Karakus, M. 2014. Three-dimensional numerical analysis for rock slope stability using shear strength reduction method. *Canadian Geotechnical Journal*, 51: 164-172.

Shinozuka, M. 1983. Basic analysis of structural safety. *Journal of Structural Engineering*, 109(3): 721-740.

Sivakumar Babu, G.L., Srivastava, A., and Murthy, D.S.N. 2006. Reliability analysis of the bearing capacity of a shallow foundation resting on cohesive soil. *Canadian*

Geotechnical Journal, 43(2): 217-223.

Smith, C., and Gilbert, M. 2007. Application of discontinuity layout optimization to plane plasticity problems. In Proceedings of the Royal Society of London A Mathematical Physical & Engineering Sciences, 463(2086): 2461-2484.

Smith, C., and Gilbert, M. 2010. Advances in computational limit state analysis and design. GeoFlorida, Advances in Analysis, Modeling & Design: 119 - 128.

Sobol, I.M. 2001. Global sensitivity indices for nonlinear mathematical models and their Monte Carlo estimates. Mathematics and Computers in Simulation, 55: 271-280.

Spencer, E. 1967. A method of analysis of the stability of embankments assuming parallel inter-slice forces. Géotechnique, 17(1): 11-26.

Spencer, W.A. 2007. Parallel stochastic and finite element modelling of clay slope stability in 3D. PhD thesis, University of Manchester, UK.

Stianson, J.R., Fredlund, D.G., and Chan, D. 2011. Three-dimensional slope stability based on stresses from a stress-deformation analysis. Canadian Geotechnical Journal, 48(6): 891-904.

Storn, R., and Price, K. 1997. Differential evolution: a simple and efficient heuristic for global optimization over continuous spaces. *Journal of Global Optimization*, 11(4): 341-359.

Stuedlein, A.W., Kramer, S.L., Arduino, P., and Holtz, R.D. 2012a. Geotechnical characterization and random field modeling of desiccated clay. *Journal of Geotechnical and Geoenvironmental Engineering*, 138(11): 1301-1313.

Stuedlein, A.W., Kramer, S.L., Arduino, P., and Holtz, R.D. 2012b. Reliability of spread footing performance in desiccated clay. *Journal of Geotechnical and Geoenvironmental Engineering*, 138(11): 1314-1325.

Sudret, B., and Der Kiureghian, A. 2002. Comparison of finite element reliability methods. *Probabilistic Engineering Mechanics*, 17(4): 337-348.

Tabarroki, M., Ahmad, F., Banaki, R., Jha, S.K., and Ching, J.Y. 2013. Determining the factors of safety of spatially variable slopes modeled by random fields. *Journal of Geotechnical and Geoenvironmental Engineering*, 139(12): 2082-2095.

Taylor, D.W. 1937. Stability of earth slopes. *Journal of the Boston Society of Civil Engineers*, 24: 197-246.

Ugai, K., and Leshchinsky, D. 1995. Three-dimensional limit equilibrium and finite element analyses: A comparison of results. *Soils and Foundations*, 35(4): 1-7.

U.S. Army Corps of Engineers. 1997. Engineering and design: introduction to probability and reliability methods for use in geotechnical engineering. Department of the U.S Army, Washington, D.C. Engineer Technical Letter, 1110-2-547.

Uzielli, M., Vannucchi, G., and Phoon, K.K. 2005. Random field characterisation of stress-normalised cone penetration testing parameters. *Géotechnique*, 55(1): 3-20.

Vanmarcke, E.H. 1977. Probabilistic modeling of soil profiles. *Journal of Geotechnical Engineering*, 103(11): 1227-1246.

Vanmarcke, E.H. 1984. *Random fields: Analysis and synthesis*. MIT Press, Cambridge MA.

Vanmarcke, E.H. 2011. Risk of limit-equilibrium failure of long earth slopes: How it depends on length. *Geo-Risk 2011, Risk Assessment and Management*: 1-24.

Varkey, D., Hicks, M.A., and Vardon, P.J. 2019. An improved semi-analytical method for 3D slope reliability assessments. *Computers and Geotechnics*, 111: 181-190.

Wai, R., Lee, R., and Law, R. 2018a. Review of landslides in 2015. Civil Engineering and Development Department, The Government of the Hong Kong Special Administrative Region, Report No. LSR 1/2016.

Wai, R., Lee, R., and Law, R. 2018b. Review of landslides in 2016. Civil Engineering and Development Department, The Government of the Hong Kong Special Administrative Region, Report No. LSR 4/2017.

Wang, Y., Cao, Z.J., and Au, S.K. 2011. Practical reliability analysis of slope stability by advanced Monte Carlo simulations in a spreadsheet. *Canadian Geotechnical Journal*, 48(1): 162-172.

Wei, L., and Liu, L. 2015. Numerical study of mode waves in a deviated borehole penetrating a transversely isotropic formation. *Physics Procedia*, 70: 102-105.

Wei, W.B., Cheng, Y.M., and Li, L. 2009. Three-dimensional slope failure analysis by the strength reduction and limit equilibrium methods. *Computers and Geotechnics*, 36(1-2): 70-80.

Wilson, D.W., Abbo, A.J., Sloan, S.W., and Lyamin, A.V. 2013. Undrained stability of a square tunnel where the shear strength increases linearly with depth. *Computers and Geotechnics*, 49: 314-325.

Wong, F.S. 1985. Slope reliability and response surface method. *Journal of Geotechnical Engineering Division*, 111 (1): 32-53.

Wu, S.H., Ou, C.Y., Ching, J., and Hsein Juang, C. 2012. Reliability-based design for basal heave stability of deep excavations in spatially varying soils. *Journal of Geotechnical and Geoenvironmental Engineering*, 138(5): 594-603.

Wu, T.H., and Kraft, L.M. 1970. Safety analysis of slopes. *Journal of the Soil Mechanics and Foundations Division*, 96(3): 609-630.

Xiao, T., Li, D.Q., Zhou, C.B., and Phoon, K.K. 2014. Non-intrusive reliability analysis of multi-layered slopes using strength reduction FEM (in Chinese). *Journal of Basic Science and Engineering*, 22(4): 718-732.

Xiao, T., Li, D.Q., Cao, Z.J., Au, S.K., and Phoon, K.K. 2016. Three-dimensional slope reliability and risk assessment using auxiliary random finite element method. *Computers and Geotechnics*, 79: 146-158.

Xie, G.H. 2009. Stochastic analysis of geotechnical parameters and study on stable reliability of slope. PhD thesis, Central South University, China (in Chinese).

Xie, M.W., Esaki, T., Zhou, G.Y., and Mitani, Y. 2003. Geographic information systems-based three-dimensional critical slope stability analysis and landslide hazard assessment. *Journal of Geotechnical and Geoenvironmental Engineering*, 129(12): 1109-1118.

Yan, S.W., Zhu, H.X., and Liu, R. 2009. Numerical studies and statistic analyses of correlation distances of soil properties in Tianjin Port. *Chinese Journal of Rock Soil Mechanics*, 30(7): 2179-2185 (in Chinese).

Yang, R., Huang, J.S., Griffiths, D.V., Li, J.H., and Sheng, D.C. 2019. Importance of soil property sampling location in slope stability assessment. *Canadian Geotechnical Journal*, 56(3): 335-346.

Yi, P., Wei, K., Kong, X., and Zhu, Z. 2015. Cumulative PSO-Kriging model for slope reliability analysis. *Probabilistic Engineering Mechanics*, 39: 39-45.

Ying, L. 2012. Application of stochastic response surface method in the structural safety. *Procedia Engineering*, 28: 661-624.

Yucemen, M.S., Tang, W.H., and Ang, A.H. 1973. A probabilistic study of safety and design of earth slopes. Urbana, Illinois: University of Illinois, Structural Research Series Vol. 402.

Zhang, J., Zhang, L.M., and Tang, W.H. 2011. New methods for system reliability analysis of soil slopes. *Canadian Geotechnical Journal*, 48: 1138-1148.

Zhang, J., Huang, H.W., and Phoon, K.K. 2013a. Application of the Kriging-based response surface method to the system reliability of soil slopes. *Journal of Geotechnical and Geoenvironmental Engineering*, 139(4): 651-655.

Zhang, J., Huang, H.W., Jiang, C.H., and Li, D.Q. 2013b. Extension of Hassan and Wolff method for system reliability analysis of soil slopes. *Engineering Geology*, 160: 81-88.

Zhang, X., and Qian, L.X. 1993. Rigid finite element and limit analysis. *Acta Mechanica Sinica (English edition)*, 9(2): 156-162.

Zhang, Y., Chen, G., Zheng, L., Li, Y., and Zhuang, X. 2013. Effects of geometries on three-dimensional slope stability. *Canadian Geotechnical Journal*, 50(3): 233-249.

Zheng, H., Tian, B., Liu, D.F., and Feng, Q. 2005. On definitions of safety factor of slope stability analysis with finite element method. *Chinese Journal of Rock Mechanics and Engineering*, 24(13): 2225-2230.

Zhu, H., and Zhang, L.M. 2013. Characterizing geotechnical anisotropic spatial variations using random field theory. *Canadian Geotechnical Journal*, 50: 723-734.

Zhu, H., Griffiths, D.V., Fenton, G.A., and Zhang, L.M. 2015. Undrained failure mechanisms of slopes in random soil. *Engineering Geology*, 191: 31-35.

Zhu, H., Zhang, L.M., and Xiao, T. 2019. Evaluating the stability of anisotropically deposited soil slopes. *Canadian Geotechnical Journal*, 56: 753-760.

Zienkiewicz, O.C. 1970. The finite element method in engineering science. *International Journal for Numerical Methods in Engineering*, 23(11): 2153-2165.